Institute of
Thermal Engineering

TU Graz

Dipl.-Ing. Vanja Subotić, BSc

Detection of carbon depositions and development of novel regeneration approaches for solid oxide fuel cells

DOCTORAL THESIS

to achieve the university degree of

Doctor of Technical Sciences

submitted to

Graz University of Technology

Faculty of Mechanical Engineering and Economical Sciences

Supervisor

Univ.-Prof. Dipl.-Ing. Dr.tech. Christoph Hochenauer

Evaluator

Prof. Dr. habil. Téko Wilhelmin Napporn

Graz, January 2017

Statutory Declaration

I declare that I have authored this thesis independently, that I have not used other than the declared sources/resources, and that I have explicitly marked all material which has been quoted either literally or by content from the used sources.

Graz, ...
Date

.....
Signature

Eidesstattliche Erklärung

Ich erkläre an Eides statt, dass ich die vorliegende Arbeit selbständig verfasst, andere als die angegebenen Quellen/Hilfsmittel nicht benutzt, und die den benutzten Quellen wörtlich und inhaltlich entnommenen Stellen als solche kenntlich gemacht habe.

Graz, am .....
Datum

.....
Unterschrift

''Nothing makes a man so happy as his fair belief that he has done everything he could by investing his best abilities in his work.'' - Mihajlo Pupin

Acknowledgments

"It is the supreme art of the teacher to awaken joy in creative expression and knowledge." - Albert Einstein.

Therefore, first and foremost, I would like to express my greatest thanks to my supervisor, Univ.Prof. Dipl.Ing. Dr.tech. Christoph Hochenauer. He has always been available to advise me and to encourage my research. I very much appreciate all of his contributions, whether in the form of time, ideas, enthusiasm for research, or his immense knowledge, which was motivational for me and made my PhD time both productive and stimulating. Without his guidance and constant feedback, this work would not have been possible. Thank you very much!

My sincere thanks also go to Prof. Dr. habil. Téko Wilhelmin Napporn. Our highly inspiring discussions of solid oxide fuel cells during the Summer School, both in Yokohama and Graz, allowed me to gain deeper insight into this complex topic, and motivated me for my further research. I am very pleased and grateful that he agreed to evaluate and review my PhD thesis.

Many thanks go to my colleague, Christoph Schluckner, for our very interesting and endless discussions, not only of fuel cells, but all imaginable topics and for the great collaboration on our research project. I am also very grateful to my colleague Bernhard Stoeckl for always being supportive of my work and for his helpfulness. For her support at the beginning of my PhD time, for her help and great friendship, I want to thank Andrea Janics. Many thanks also go to my colleagues Stefan Kleindel and Rene Prieler for their support and friendship at the beginning of my PhD time. For the pleasant atmosphere in our office I want to thank to Martin Landfahrer and Markus Buchmayr. I also wish to thank all of my Bachelor and Master students, especially Johannes Strasser, for their support in the laboratory and during data evaluation. For his support while carrying out microscopic examinations of the cells, as well as the extensive discussions of such, I owe my thanks to Hartmuth Schroettner. For their helpfulness and great assistance in the laboratory, especially during the improvement of the test bench and the SOFC-laboratory renovation project, I want to thank Markus Raiber and Markus Sackl. Many thanks for their support in the laboratory go to Herbert Hartner and Heinz Strauss. I am further thankful to all my

colleagues at the Institute of Thermal Engineering.

This thesis is the result of a three year research project entitled RESOX, carried out by the Institute of Thermal Engineering (IWT) at the Graz University of Technology, in cooperation with the AVL List GmbH, and funded by The Austrian Research Promotion Agency FFG under grunt number 841154 as well as by AVL List GmbH, for which financial support I am very grateful.

I particularly want to thank all my friends and the nice people who have stood by me in the last years and made my life more colourful. Your support was very important for me. Thank you for being there and for your words of encouragement.

Dear parents and brother, thank you for always supporting me, believing in me, and reminding me that everything would work out. Thank you for allowing me to get where I am now. Thank you for the strength and wisdom you have given me my whole life. No amount of ''thank'' is enough to express it. Hvala za sve!

I dedicate this work to my parents and my brother!

Kurzfassung

Festoxidbrennstoffzellen (SOFCs) stellen eine sehr attraktive innovative Technologie für die umweltschonende Stromerzeugung durch direkte Umwandlung chemischer Energie des gasförmigen Brennstoffs in elektrische Energie dar. Aufgrund der hohen Betriebstemperaturen und der sehr guten katalytischen Eigenschaften ist ein Betrieb mit einer Vielzahl von Brenngasen möglich. Daher zählt die SOFC zu den effizientesten Brennstoffzellenarten.

Im Rahmen der vorliegenden Arbeit wurden planare, anodengestütze Festoxidbrennstoffzellen untersucht. Die Zellen wurden unter anwendungsnahen Rahmenbedingungen getestet und mit sowohl alternativen als auch konventionellen Brennstoffen betrieben. Bei Verwendung von kohlenstoffhaltigen Brennstoffen kann es an der brenngasseitigen Elektrode zur Bildung von Kohlenstoff kommen. Je nach Ausmaß können diese Ablagerungen zur Verkürzung der Lebensdauer bis hin zur vollständigen Zerstörung der Zelle führen. Um eine Steigerung der Zelllebensdauer zu erreichen und einen sicheren Betrieb zu gewährleisten, ist es notwendig ein grundlegendes Verständnis dieses Ablagerungsprozesses zu erlangen.

Um die Degradationsphänomene zu verstehen, wurde zunächst eine detaillierte in-situ elektrochemische Analyse der Zellen durchgeführt. Mittels elektrochemischer Impedanzspektroskopie (EIS) wurde der Zustand der Zellen zeitlich aufgelöst und auftretende Degradationsmechanismen wurden identifiziert. Hierfür musste ein passendes Ersatzschaltbild (EC) der eingesetzten Brennstoffzellen entwickelt und experimentell bzw. numerisch validiert werden. Die EIS-Technologie wurde in Kombination mit fortgeschrittener Relaxionszeitverteilung - Methode (DRT) als ein vielversprechendes Verfahren eingesetzt. Diese Kombination ermöglichte Untersuchung von kritischen Betriebszuständen und kann zur Online - Überwachung eingesetzt werden.

In einem nächsten Schritt wurden Kohlenstoffablagerungsmechanismen ausgiebig untersucht. Gleichgewichtsberechnungen wurden herangezogen, um Betriebsbedingungen zu definieren, unter welchen es zur Bildung von Kohlenstoffablagerungen kommt. Als Brenngas wurde ein Dieselreformatgemisch verwendet, welches so auch in technischer Anwendung zu erwarten sein wird. Dabei wurde der Einfluss von unvollständig reformiertem

Methan auf die Bildung von Kohlenstoff in der Brenngaselektrode eingehend untersucht. Eine frühzeitige Erkennung von Kohlenstoffablagerungen konnte mittels elektrochemischer Impedanzspektroskopie, Polarisationskurvenmessung, Temperaturmessung und Gasanalyse bewerkstelligt werden. In post-mortem Analyse wurde der gebildete Kohlenstoff mittels Rasterelektronenmikroskopie (REM) nachgewiesen.

Abschließend wurden unterschiedliche Ansätze entwickelt, die eine vollständige und zellschonende Entfernung dieser Kohlenstoffablagerungen ermöglichen und somit die ursprüngliche Leistung erzielen. Die entwickelten Ansätze beruhen auf: (1) der Verwendung von Gasgemischen zur Entfernung von abgelagertem Kohlenstoff und (2) dem Einsatz von elektrochemischen Methoden, die durch einen definierten Strom, bzw. Spannung die Kohlenstoffentfernung ermöglichen. Der Betrieb mit Wasserstoff, Wasserdampf, Kohlenstoffdioxid und sauerstoffreichen Gasgemischen führte zu einer vollständigen Kohlenstoffentfernung. Allerdings, im Brennstoffzellenbetrieb, zeigte nur der Regenerationsvorgang mit Wasserstoff und Wasserdampf eine zellschonende Wirkung. Kohlenstoffdioxid und Sauerstoff bewirkten eine weitere Degradation der Zellleistung und führten zur mechanischen Zerstörung der Zellmikrostruktur.

Hervorzuheben ist ein innovativer Ansatz zur Beseitigung der Kohlenstoffablagerungen: Die Beaufschlagung der Zelle mit einer Überspannung. Diese beschleunigt die Kohlenstoffentfernung und schützt die Brennstoffzelle vor ungewollter Degradation oder Mikrostrukturänderung. Der Einfluss der Überspannung unter verschiedenen Gasatmosphären auf die Zellperformance und Zellmikrostruktur wurde ausgiebig untersucht. Eine Überspannung unter CO_2-Atmosphäre ermöglichte eine schnelle und zellschonende Regeneration. Die Regeneration mit Wasserstoff unter Anlegen einer Überspannung senkte die Regenerationsdauer erheblich von 44 h auf nur 12 h. Das Aufbringen einer Überspannung ohne Gasversorgung zeigte ebenfalls gute Kohlenstoffentfernungsraten, allerdings wurde die Zellmikrostruktur beeinflusst und eine weitere Degradation der Zellleistung induziert. Der mikrostrukturelle Einfluss der Regenerationsmethode wurde anhand REM-Analyse aufgearbeitet. Die Leistungssteigerungen, sowie Verschlechterungen, konnten somit den mikrostrukturellen Veränderungen zugewiesen werden. Die in dieser Dissertation entwickelten Regenerationsmethoden ermöglichen eine vollständige Kohlenstoffentfernung und Wiederherstellung der ursprünglichen Leistung. Weiters sind auch die negativen Auswirkungen der nicht erfolgreichen Strategien beschrieben. Die dargestellten Methoden wurden weiter auf ihre industrielle Umsetzbarkeit überprüft.

Abstract

Solid oxide fuel cells (SOFCs) present an attractive and innovative technology for environmentally-friendly electricity generation. Their high operating temperatures and the excellent catalytic performance make SOFCs the most efficient fuel cell type, with a high level of fuel flexibility.

Within this thesis, detailed analyses of planar, anode-supported industrial-sized SOFCs were carried out. These cells were operated under conditions close to the real operating conditions and fuelled with both conventional and alternative fuels. Feeding the SOFCs with carbon-containing fuels carries the risk of carbon formation and its deposition on the anode, which can reduce cell activity, cause irreversible cell degradation, and decrease the cell's lifetime. In order to prolong the cell's lifetime and to ensure the undisturbed operation of SOFCs, an in-depth understanding of this degradation phenomenon is required.

As a first step towards gaining this understanding, a detailed in-situ electrochemical analysis based on electrochemical impedance spectroscopy (EIS) was performed. For this purpose, an appropriate equivalent circuit of the cells used was developed, and validated both experimentally and numerically. The combination of EIS technology and the distribution of relaxation times (DRT) method was identified as a promising technique for investigating critical operating conditions and as an online monitoring tool. Different occurring process mechanisms were successfully separated using this methodology without a reference electrode, which is of great importance for practical use.

Next, a complete investigation of carbon deposition mechanisms was carried out. Based on equilibrium calculations, the operating conditions under which carbon can be formed were defined. Diesel reformate was used as a fuel, with a typical gas composition as expected in auxiliary power units. The influence of methane in the reformate on carbon deposition was furthermore investigated. The use of electrochemical impedance spectroscopy, polarization curve measurements, temperature measurements, and gas analyses made an early detection of carbon formations possible. Subsequently, microscopic analysis confirmed the occurrence of the carbon identified via these methods.

Finally, different carbon removal processes were developed, with the aim of fully protecting the cell and regenerating its performance. At all times, the practicability of these methods for industrial application was considered. These strategies made use of: (1) gaseous components, for the gasification of carbon deposits, and (2) electrochemical methods, which remove carbon by means of current or voltage applied. Operation under hydrogen, water vapour, carbon dioxide, and oxygen-enriched gas mixtures allowed complete carbon removal. Nevertheless, under operation in a fuel cell mode, only the approach that combined hydrogen and water vapour removed carbon from the anode while also protecting it from further undesired degradation. Feeding the anode with carbon dioxide and oxygen showed high carbon removal rates but resulted in further deterioration of the cell performance, and eventually led to mechanical degradation. Both successful and unsuccessful approaches for carbon removal in a cell-protecting manner are presented within this work.

This thesis also considered a novel approach of applying overvoltage. This method shows high carbon removal rates and protects the cell from further degradation or microstructural modifications. In order to examine the impact of overvoltage, it was applied alongside various gas mixtures. Carbon dioxide with overvoltage led to fast and cell-protecting regeneration. When hydrogen and overvoltage were applied simultaneously, the regeneration time was significantly reduced, from 44 h to 12 h. Overvoltage without gas supply on the anode side also removed carbon, but had a negative impat on the cell microstructure and performance. All of the examinations performed were supported by microscopic imaging. The novel regeneration approaches developed in this thesis thus enabled complete carbon removal and a complete regeneration of cell performance.

Nomenclature

a	Constant
C	Ideal capacitance
$C_{Pj}(T)$	Temperature-dependent heat capacity for gaseous components j
e	Elementary charge
F	Faraday constant
f	Frequency
$f(s)$	Examined function
$g(t)$	Measured function g
g_i^σ	Noisy experimental data
I	Electric current
$Im(\underline{Z}(\omega))$	Imaginary part of complex impedance
i	Current density
i_0	Equilibrium exchange current density
i_{lim}	Limiting current density
$\underline{i}(t)$	Alternating current
j	Reactants, components
j	Imaginary number
K	Equilibrium constant
K_{NiO}	Equilibrium constant for NiO
$K(t,s)$	Kernel function
L	Inductance
m	Number of coefficients
N_A	Avogadro constant
n_C	Molecular quantity of atomic carbon
n^{el}	Number of electrons released due to fuel utilization
$\dot{n}^{el}$	Molar flow of the electrons

$\dot{n}_{fuel}$	Fuel molar flow
n_{H_2O}	Molecular quantity of water vapour
p	Total pressure
p_{H_2}	Hydrogen partial pressure
p_{H_2O}	Water vapour partial pressure
p_j	Partial pressure
p_{O_2}	Oxygen partial pressure
p_0	Standard pressure (1 bar)
P_{rev}	Reversible power
R	Overall resistance
R_{an}	Anodic resistance
$Re(\underline{Z}(\omega))$	Real part of complex impedance
R_{ca}	Cathodic resistance
R_{el}	Electrolyte resistance
R_g	Universal gas constant
R_{ion}	Ionic resistance
R_n	Resistance for element n
R_{ohmic}	Ohmic resistance
R_p	Polarization resistance
R_s	Series resistance
R_ω	Ohmic resistance
S_j	Entropy of any component j
Q	Non-ideal capacitance
t	Time
T	Temperature
U_{nernst}	Nernst voltage
U_{cell}	Cell voltage
U_{rev}	Reversible voltage
W_{rev}	Reversible electrical work
$\underline{u}(t)$	Alternating voltage
$x(t)$	Input signal of a time-invariant system
y_k	Actual value for each k=1,2,...,y_{k+1}

$y(t)$	Output signal of a time-invariant system
Z_{real}	Real part of complex impedance
Z_{imag}	Imaginary part of complex impedance
$\underline{Z}(\omega)$	Complex impedance

Greek letters

α	Transfer coefficient
β	Phase angel
$\Delta^r G$	Gibbs enthalpy
$\Delta^r H$	Reaction enthalpy
$\Delta^r S$	Reaction entropy
Δt	Time (or other variable) step
η_{act}	Activation losses
η_{conc}	Concentration losses
η_{ohmic}	Ohmic losses
η_r	Maximum efficiency
νj	Stoichiomettric coefficient of the reactants j
ϑ	Temperature in $^\circ C$
$\varphi(\omega)$	Frequency dependent phase shift
λ	Regularization parameter
σ_i	Error
ω	Angular frequency

Acronyms

Notation	Description
AC	alternating current
APU	auxiliary power unit
ASC	anode-supported
CeO_2	cerium oxide
CNF	carbon nanofibers
CPE	constant phase element
DC	direct current
DRT	distribution of relaxation times
EC	equivalent circuit
EDX	energy-dispersive X-ray spectroscopy
EIS	electrochemical impedance spectroscopy
FE-SEM	field emission scanning electron microscope
FTIRES	Fourier-transform infrared emission spectroscopy
Gd	gadolinium
LSCF	lanthanum strontium cobalt ferrite
MFC	mass flow controller
NDIR	non dispersive infrared detector
NIR	near-infrared thermal imaging

Notation	Description
OCV	open circuit voltage
PEM	polymer electrolyte fuel cell
S/C-ratio	steam/carbon ratio
SEM	scanning electron microscopy
SLPM	standard litre per minute
Sm	samarium
SOFC	Solid oxide fuel cell
TPB	three-phase boundary
XRD	X-ray diffraction
Y_2O_3	yttriumoxid
YSZ	yttria-stabilized zirconia
ZrO_2	zirconiumoxid

Contents

List of Figures

List of Tables

Introduction and Contribution of this Thesis to the SOFC Research Field

Imagine that you have one device. With it, you can illuminate an entire house. It produces enough power to heat your whole house. Or you may choose to run your vehicle with it. Then imagine that you can use any kind of fuel to run this device, because it permits the usage of various fuels. You can feed it with conventional or alternative fuels, the choice is up to you. Another thing about this device: if you connect of them to each other, you can supply entire factories and cities with electricity and high-quality heat. What a fantastic idea! Indeed, this device is no longer just an idea, it is technology we know as Solid Oxide Fuel Cells. This disruptive technology has many advantages, but in order to ensure the smooth operation and best performance thereof, there is still much research effort left to do. The overreaching goal of this work is to find suitable ways to prolong the lifetime of SOFC technology and to ensure its safe operation.

1.1 Motivation

A great share of electrical energy is produced from fossil fuels in conventional power plants, but their continued use contributes to the greenhouse effect. Alternatively, a certain amount of the energy demand could be fulfilled in a more environmentally friendly manner through the use of volatile renewable energy, but its integration into the energy system requires energy storage systems. In all cases, there are conversion steps between the primary energy and the end energy that further reduce the overall efficiency. Nonetheless, our increasing energy consumption requires new solutions that offer both high efficiency and clean energy generation. Solid oxide fuel cell systems appear to be a promising technology that provides direct conversion from electrochemical to electrical energy without additional conversion steps. SOFC systems enable a stable energy supply with high efficiency and low pollution

[9]. The heat losses that occur during operation at temperatures between $600°C$ and $1000°C$ can be used as high-quality heat energy. The overall efficiency is independent of the power plant scale since these systems are not Carnot limited [10]. This implies that SOFC systems can be considered for large-scale power generation, such as in MW-power plants, as well as for small-scale power generation, such as in households. [4]

In ecological terms, a fuel cell system is a low pollution system that produces neither fine particulate matter nor nonmetal oxides [9]. Emissions of nitrogen oxides (NO_x) are negligible because the oxidation and utilization of the fuel used occur at temperatures lower than those required for NO_x production [11]. Furthermore, since SOFC cells are sensitive to fuel impurities, such as sulphide, chloride and phosphide, which cause rapid degradation of the cell, the fuels used should contain no impurities [12--15]. Therefore, SOFC-operation does not lead to the emission of sulphur oxides (SO_x). Owing to their high efficiency, SOFCs require less fuel to achieve a target power, which means less CO_2 is emitted to the atmosphere. [7]

To effectively use SOFC-systems in the automotive industry or as a combined power-heat unit, the aim is to use available and favourable energy sources with high energy density. Since SOFCs are operated at high temperatures and have very good catalytic performance, they are suitable for internal reforming, and, if gaseous fuel is used directly, they often do not require the use of an external reformer [16]. Because of this, they are extremely flexible in terms of fuel. Generally, the fuels used can react catalytically in SOFCs, or can be reformed by means of steam- or dry-reforming. Nickel is the most commonly used material on the anode side because of its very good catalytic performance and high electrical conductivity [17--20]. Based on the high operating temperatures of SOFCs, nickel is highly appropriate as a catalyst for chemical and electrochemical reactions [21]. Nevertheless, the operation of Ni-cermet based ASC-SOFCs with fuels containing carbon includes the risk of carbon formation on the anode-side. Deposited carbon can block the pores on the fuel electrode, and thus obstruct the gas transport through the porous anode or cover the nickel-catalyst and three-phase-boundary; this can inhibit both the chemical and electrochemical reactions as well as current generation [22]. In some cases, carbon formation can cause irreversible degradation of the cell performance and damage the cell micro- and macrostructure [23]. Many researchers have investigated the impact of different fuels with carbon contents and have shown their degrading effect on cell performance [24--31]. Although it is clear that Ni in an anode encourages carbon formation and that the use of alternative materials could prevent carbon depositions, these have a negative effect on cell performance [32]. Instead of Ni, gadolinium (Gd)- and samarium (Sm)-stabilized ceria-based materials or conducting oxides are often investigated and used for anode fabrication [33--38]. Another option is the

use of copper, where hydrocarbon deposits fill the gaps between the metal particles, thus improving the anode conductivity and simultaneously reducing impedance, [39]. Although these materials have the ability to suppress carbon depositions, Ni offers both considerably better conductivity and electrocatalytic performance [40]. [5, 7]

1.2 Contribution of this Thesis to the SOFC Research Field

This work introduces new ideas, supported by detailed experimental investigations, for how to improve the lifetime of SOFCs as well as how to support their secure operation. Both carbon deposition and the possibility of its removal have a major impact on the safe operation of SOFC systems; these points are scrutinized in detail within this thesis.

This work will provide guidance regarding the problematic issue of carbonaceous deposits on industrial-sized, anode-supported solid oxide fuel cells. Many studies have investigated the phenomena of carbon deposits and their impact on cell performance; the deposits are mainly caused by methane whether as pure gas or in a gas mixture [24--27, 41]. To enable easy access to SOFCs in the form of auxiliary power units to the automotive market, the investigation of SOFCs fuelled with diesel reformate is of great relevance [42, 43]. For this purpose, the cells were supplied with a diesel reformate gas mixture, as expected in auxiliary power units (APUs), in order to induce carbon formation and deposits thereof. The Ni-YSZ anode structure was used in this work. It has the greatest tendency to adsorb carbon due to its excellent performance as a catalyst; however, this also means that it enables carbon formation reactions, which subsequently block the catalyst surface and the porous gas channels. The carbon formation process was examined on loaded cells, thus representing a practice-oriented case. In order to ensure the safe operation of SOFC systems, extensive in-situ and in-operando analyses of carbon deposits at early stages were performed, and their impact on the anode-stability and the electrochemical, mechanical and morphological cell properties were determined. A fast method for the in-situ identification of carbon deposits based on EIS is thus introduced. [6]

This work subsequently moves from the traditional concept of controlling or avoiding carbon formations to novel methods of carbon removal and performance restoring. Innovative regeneration approaches, which are of key importance for the SOFC community, are developed in this thesis. These new approaches facilitate the time-saving removal of carbon and restoration to the initial cell performance in a cell-protecting manner. Implementation of these regeneration methods, which were developed to completely remove carbon without causing cell damage, can ensure the safe, long-term operation of stationary or mobile SOFC systems and accelerate their commercialization.

This thesis also describes an entire electrochemical analysis of SOFCs, relevant for their industrial utilization, which has up to now been missing in the literature. A wide range of operating conditions was applied for this purpose. Different parameters, such as gas composition, humidity content, and load were varied in order to identify the specific cell behaviour and to create a base model that can be used for the detailed investigation of diverse degradation mechanisms as well as the identification of critical operating conditions. The temperature dependency of all processes involved is examined. The importance of the load during the impedance measurements, which simultaneously impacts the operating environment, is both discussed and analysed in detail. Different equivalent circuits (ECs) were also analysed and compared. Polarization curves were calculated based on the fit plots and subsequently verified by measured characteristic curves, thus evaluating single electric circuit elements and specifying the size of single loss mechanisms. This represents a method for the easy and fast identification of carbon deposits. Nonetheless, differentiating between the air electrode and the fuel electrode is a challenging and non-trivial approach if the measurements are performed for industrial-sized SOFCs without a reference electrode. In order to provide a detailed distinction between the anode and cathode processes, DRT is established. The DRT method was applied in order to separate the processes that occurred and to provide a basis for further investigation. DRT is already present in literature, but so far only for polymer electrolyte fuel cells (PEMs) or for SOFCs with small chemically active area ($\leq$16 cm^2). Altogether, literature on the topic lacks a detailed electrochemical analysis of cell behaviour, in addition to a sample approach to the early identification of adverse changes to cell performance caused by a wide variety of degradation mechanisms. This information is essential for the further investigation of solid oxide fuel cells. [8]

It is important to mention the size and shape of the cells used in the course of this thesis. Many studies have investigated the impact of various operating conditions on the performance of the solid oxide fuel cells, but they have mainly considered cells with a small active area that does not exceed 16 cm^2 and which are often button-shaped. The studies that have involved experiments with large-area, planar, single SOFCs, have shown that it is more difficult to reach optimal operating conditions and to achieve excellent cell performance due to a number of factors, including cell sealing, contacting, etc., when compared to small area button cells [44--46]. They also show that operating conditions strongly affect the electrochemical performance of large planar cells, and that the processes as well as fuel utilization and temperature differ along the cell. This makes the investigation of cells with a larger area much more complicated than the study of cells with small area. This work investigates large, planar, industrial-sized 10×10 cm^2 SOFCs with an active area of 81 cm^2, which are of great importance to SOFC research as candidates for the commercial use. [4]

2 Fundamentals

SOFCs represent a very attractive technology for clean-power generation through their conversion of the chemical energy of gaseous fuel into electricity. The major advantages of these cells include the high operating-temperatures and very good catalytic performance of the porous anode, which enables a high degree of fuel flexibility, in addition to the internal reforming of hydrocarbons. The ability to internally reform hydrocarbons means that SOFCs may be regarded as the fuel cells with the highest degree of fuel flexibility. Their high-efficiency and utilization of waste heat in order to improve overall-efficiency help make SOFCs suitable candidates for application in both small and large-scale generation systems [5, 11, 47, 48]. [5] This chapter provides a brief introduction to the basic principles of fuel cells. The working principle of this technology and typical loss mechanisms that detract from its maximum efficiency will also be described. The electrochemical characterization techniques and analysis methods used for the in-situ investigation of SOFCs are also introduced and discussed. Thus, this chapter will answer several basic questions: What are fuel cells? How do they work? And what are their major advantages in comparison with conventional power sources?

2.1 Fuel Cell Working Principle

Fuel cells are electrochemical conversion units that directly convert the chemical energy of a gaseous fuel and an oxidant into electrical energy. Two processes, oxygen reduction and fuel oxidation, occur on two spatially separated electrodes - the anode and the cathode. A physical representation of a planar ASC solid oxide fuel cell, showing the co-flow conditions, is provided in Fig. 2.1.

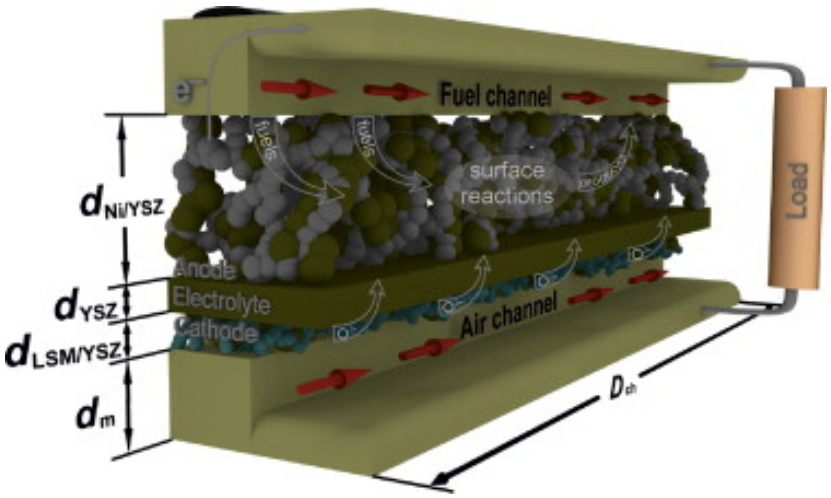

Figure 2.1: Illustration of a planar ASC-SOFC. [1]

Ideally, the fuel and the oxidant are not mixed and the gas-tightness between the electrodes is ensured. Further, the reactants and products are not mixed, and the maximum enthalpy of the reactant is available for energy production in cells. The maximum enthalpy of the products is thus transported from the cell. A further criterion is the reversible heat exchange between the fuel cell and an environment, which is based on their equal thermodynamic state. Operation under these mentioned conditions brings the cell into reversible operation, under which a fuel cell achieves maximum efficiency. The reversible electrical work (W_{rev}) achievable at this state is equal to the Gibbs enthalpy ($\Delta^r G$), as can be seen in Eq. 2.1. $\Delta^r H$ specifies the reaction enthalpy, where T is the operating temperature and $\Delta^r S$ represents the reaction entropy. [3, 47, 48]

$$W_{rev} = \Delta^r G = \Delta^r H - T \cdot \Delta^r S \tag{2.1}$$

The maximum efficiency (η_r) that can be reached at this state is given by Eq. 2.2 and represents the ratio between the Gibbs enthalpy and the reaction enthalpy.

$$\eta_r = \frac{\Delta^r G}{\Delta^r H} = \frac{\Delta^r H - T \cdot \Delta^r S}{\Delta^r H} \tag{2.2}$$

In the following explanation, the most simple fuel cell reaction - the oxidation of hydrogen will be discussed. Hydrogen oxidation occurs according to the reaction path in Eq. 2.3.

$$H_2 + \frac{1}{2} O_2 \rightarrow H_2O \tag{2.3}$$

In order to inhibit the direct combustion of fuel by oxygen, the key reactions - oxygen reduction and fuel oxidation occur on spatially separated electrodes, the anode and the cathode. Hydrogen is oxidized on the anode side according to Eq. 2.4 and the released

electrons are transported by electronic load to the cathode side. Simultaneously, the external load supplies the cathode with electrons, thus reducing oxygen to O^{2-} oxygen ion, as seen in Eq. 2.5.

$$H_2 \rightarrow 2H^+ + 2e^- \tag{2.4}$$

$$\frac{1}{2}O_2 + 2e^- \rightarrow O^{2-} \tag{2.5}$$

The oxygen ions produced are then conducted through the ceramic electrolyte to the anode, where the overall reaction occurs and the product, in this case water vapour, is formed according to Eq. 2.6.

$$2H^+ + O^{2-} \rightarrow H_2O \tag{2.6}$$

The electrons conducted from the anode to the cathode side represent electric current, which is a linear function of the molar flow of the electrons released by the fuel utilization, as shown in Eq. 2.7.

$$I = \dot{n}^{el} \cdot (-e) \cdot N_A = -\dot{n}^{el} \cdot F \tag{2.7}$$

I is the electric current, $\dot{n}^{el}$ is the molar flow of the electrons in $\frac{mol}{s}$, e is the elementary charge ($e = 1.60217733 \pm 0.00000049 \cdot 10^{-19}\, C$), N_A is the Avogadro constant ($N_A = 6.02214086 \cdot 10^{23}\, \frac{1}{mol}$), F is the Faraday constant ($F = 96485.309 \pm 0.029\, \frac{C}{mol}$).
Based on equations Eq. 2.1 and Eq. 2.7, the reversible power (P_{rev}) can be calculated as a product of the current (I) and the reversible voltage (U_{rev}), or as a product of the Gibbs enthalpy ($\Delta^r G$) and the molar flow of the fuel ($\dot{n}_{fuel}$). Reversible voltage is usually defined as the maximum available exergy obtained by fuel oxidation, without electron crossover, [47, 48].

$$P_{\text{rev}} = U_{rev} \cdot I = \dot{n}_{fuel} \cdot W_{rev} = \dot{n}_{fuel} \cdot \Delta^r G \tag{2.8}$$

According to equations 2.8 and 2.7, the reversible voltage can be calculated as:

$$U_{\text{rev}} = \frac{P_{rev}}{I} = \frac{\dot{n}_{fuel} \cdot \Delta^r G}{I} = -\frac{\dot{n}_{fuel} \cdot \Delta^r G}{\dot{n}^{el} \cdot F} = -\frac{\Delta G}{n^{el} \cdot F} \tag{2.9}$$

where n^{el}, according to Eq. 2.10, represents the ratio between the molar flow of the electrons and the molar flow of fuel. It can thus be defined as the number of electrons released due to fuel ionization.

$$n^{el} = -\frac{\dot{n}^{el}}{\dot{n}_{fuel}} \tag{2.10}$$

The detailed calculation of n^{el} for relevant SOFC fuels is shown in the following equations (Eq. 2.11, Eq. 2.12, Eq. 2.13):

$$H_2 \rightarrow 2H^{1+} + 2e^- \implies n^{el} = \frac{2}{1} = 2 \tag{2.11}$$

$$CO \rightarrow CO^{2+} + 2e^- \implies n^{el} = \frac{2}{1} = 2 \tag{2.12}$$

$$CH_4 \rightarrow CH_4^{8+} + 8e^- \implies n^{el} = \frac{8}{1} = 8 \tag{2.13}$$

As stated above, reversible fuel cell operation represents an ideal case. Under real operating conditions, the mixture of reactants and products on the anode side cannot be prevented. Thus, the theoretical voltage is reduced. This effect occurs due to a change in the partial pressure (p_j) of single gaseous components in the gas mixture [49]. The operating temperature (T) and total pressure (p) must also be considered for the correct calculations (Eq. 2.14).

$$\Delta^r G_{(T,p)} = \Delta^r H_{(T,p)} - T \cdot \Delta^r S_{(T,p)} \tag{2.14}$$

For the purpose of calculations for fuel cell systems, the assumption of the ideal gas is made, thus reducing Eq. 2.14 to Eq. 2.15 and calculating the entropy according to Eq. 2.16.

$$\Delta^r G_{(T)} = \Delta^r H_{(T)} - T \cdot \Delta^r S_{(T)} \tag{2.15}$$

$$S_{j(T,p)} = S_j^0 + \int_{T_0}^{T} \frac{C_{Pj}(T)}{t} dt - R_g \cdot \ln(\frac{p_j}{p_0}) \tag{2.16}$$

$C_{Pj}(T)$ specifies the temperature-dependent heat capacity for gaseous components j, whereas the pressure dependence is neglected in accordance to the assumption of the ideal gas. R_g is the universal gas constant (8,3144621 $\frac{J}{molK}$), whereas the term $\ln(\frac{p_j}{p_0}$ provides the logarithmic ratio between partial pressure of the component j and the standard pressure p_0. Based on Eq. 2.16, the reaction entropy can be calculated as presented in Eq. 2.17.

$$\Delta^r S_{(T,p)} = \Delta^r S_{(T)} - R_g \cdot \ln(K) \tag{2.17}$$

where K indicates the equilibrium constant, provided by Eq. 2.18. In the following equation, νj represents the stoichiometric coefficient of the reactants j.

$$K = \prod_j \frac{p_j}{p_0}^{\nu j} \tag{2.18}$$

In the context of the last four equations, the Gibbs' enthalpy change can be obtained by the following equation:

$$\Delta^r G_{(T)} = \Delta^r H_{(T)} - \Delta^r S_{(T)} - R_g \cdot \ln(K) = \Delta^r G_{(T)} - R_g \cdot \ln(K) \tag{2.19}$$

The maximum thermodynamic voltage of one fuel cell is stated as the Nernst-Voltage (U_{nernst}), which can be represented through Eq. 2.20. This value presents the ideal irreversible cell voltage without consideration of operation losses. Only at open circuit does the cell voltage or actual open circuit voltage (OCV) theoretically match the Nernst-Voltage:

$$U_{\text{nernst}} = -\frac{\Delta^r G_{\text{T,p}}}{n^{el} \cdot F} - \frac{R_g \cdot T}{n^{el} \cdot F} \cdot ln(K) = -\frac{\Delta^r G_{\text{T,p}}}{n^{el} \cdot F} - \frac{R_g \cdot T}{n^{el} \cdot F} \cdot \prod \frac{(\frac{p_{j,products}}{p_{0,products}})^{\nu_{j,products}}}{(\frac{p_{j,reactants}}{p_{0,reactants}})^{\nu_{j,reactants}}} \tag{2.20}$$

in which $j, reactants$ represents the reactant components and $j, products$ the product components. For the simplest case of hydrogen oxidation according to Eq. 2.3, the Nernst voltage can be calculated as given in Eq. 2.21.

$$U_{\text{nernst}} = -\frac{\Delta^r G_{\text{T,p}}}{2 \cdot F} - \frac{R_g \cdot T}{2 \cdot F} \cdot \ln(\frac{p^1_{H_2O}}{p^1_0} \cdot \frac{p^1_0}{p^1_{H_2}} \cdot \frac{p_0^{\frac{1}{2}}}{p_{O_2}^{\frac{1}{2}}}) \tag{2.21}$$

In Eq. 2.21 p_{O_2} is the oxygen partial pressure on the cathode, p_{H_2} is the hydrogen partial pressure on the anode, and p_{H_2O} is the partial pressure of water vapour as the product. As stated above, p_0 represents the standard pressure.

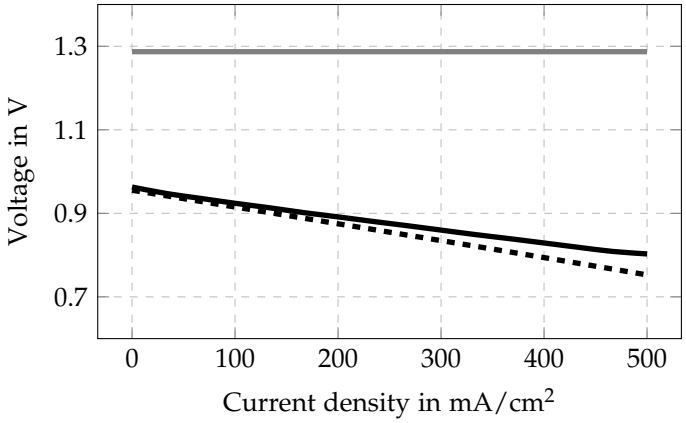

Figure 2.2: Voltage-current curves for $DR_{2.3}$: Nernst output voltage (——), Measured voltage (- - -), Thermal maximum voltage (——).

Fig. 2.2 shows the voltage measured (dashed black line) during operation with 2.4 SLPM of synthetic diesel fuel, including 2.3 vol% of methane (as given in Tab. 4.1 in Chapter 4) on the anode side and 2 SLPM air on the cathode side, compared to the calculated Nernst-voltage

(solid black line). The operating temperature was defined to be 800° C. It is evident that the measured OCV is almost the same as the Nernst-voltage. The difference amounts to 0.3%, which shows an operation almost without any leakage. In contrast, comparison with the theoretical voltage shows how operation with the defined gas mixture and dilution of fuel in 11 vol% of water vapour can strongly diminish the cell voltage and, consequently, the cell power. Still, the difference between the calculated Nernst-voltage and the measured voltage over the load range is not significant, which confirms very good cell contacting, as well as low activation losses due to the high operating temperatures. Detailed information about the test rig used is provided in Chapter 4.

2.2 Loss Mechanisms

As mentioned above, Nernst voltage represents the maximum possible irreversible thermodynamic voltage, and it cannot be practically achieved. There are multiple reasons behind this. All of the processes that occur in a fuel cell require some energy to drive them, thus reducing the total available energy of the system. Furthermore, the materials used are not superconductive, thus inducing ohmic losses under load. Gas transport and gas conversion can cause additional diffusion losses. The irreversible loss mechanisms in a fuel cell can generally be divided into: ohmic losses, activation losses, and concentration losses. When all possible loss mechanisms are taken into account, the real output voltage is significantly reduced compared to the Nernst voltage. The real voltage output for a fuel cell is represented in Eq. 2.22. [3]

$$U_{cell} = U_{nernst} - \eta_{act} - \eta_{ohmic} - \eta_{conc} \tag{2.22}$$

U_{cell} represents the cell voltage, η_{act} the activation losses, η_{ohmic} ohmic losses and η_{conc} concentration losses.

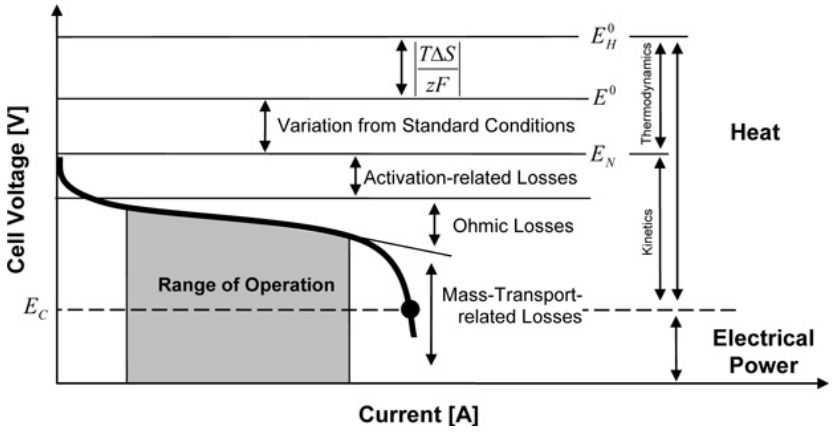

Figure 2.3: Illustration of typical losses occurring in a single fuel cell. [2]

Typical losses are illustrated in Fig. 2.3. The thermodynamic losses, which reduce the reversible voltage down to the Nernst voltage, are represented on the right hand side. The losses induced by cell operation, including activation, ohmic and mass-transport related losses, are also visible.

2.2.1 Ohmic Losses

Ohmic losses in SOFCs arise due to the internal resistance of the fuel cell, taking into account the electrolyte, the anode, and the cathode. Nevertheless, the ohmic losses are mainly related to the transport of O^{2-} ions through the electrolyte. The anode (R_{an}) and the cathode side (R_{ca}) are also responsible for ohmic losses, including both the ionic R_{ion} and electronic R_{el} charge transport resistance. Therefore, ohmic losses represent a voltage that must be applied to the transport charge defined by a specific current. The ohmic losses are proportional to the applied current density, as shown in Eq. 2.23.

$$\eta_{ohmic} = I \cdot \sum_{n} R_n = I \cdot R_{ohmic} = I \cdot (R_{el} + R_{ion}) = I \cdot (R_{an} + R_{el} + R_{ca}) \tag{2.23}$$

In SOFCs, ohmic losses are mostly caused by electrolytes. When different types of SOFCs are compared with one another, the ohmic losses are principally influenced by electrolyte thickness. Electrolyte resistance can simply be indicated by electrochemical impedance measurements. [47, 48, 50]

2.2.2 Activation Losses

Activation losses involve the energy required to overcome the barrier for activation electrochemical processes at each electrode and they are thus best visible in the low current range. Activation losses are commonly expressed by the Butler-Volmer-Equation (Eq. 2.24) [51]:

$$i = i_0 \cdot [\exp(\alpha \frac{n^{el} F \Delta\eta_{act}}{R_g \cdot T}) - \exp(-(1-\alpha) \cdot \frac{n^{el} F \Delta\eta_{act}}{R_g \cdot T})] \tag{2.24}$$

in which i describes the current density, i_0 the equilibrium exchange current density depending on the cell properties, such as material, construction, etc. Exchange current density is defined as the minimum current density required for the reaction. α is the transfer coefficient, usually defined as 0.5 for fuel cells, while n^{el} represents, as mentioned above, the number of electrons released in the overall reaction. η_{act} describes the activation losses and can be calculated from the Butler-Volmer equation shown. Simplification of the Butler-Volmer equation is possible for two extreme cases, when the activation losses are either very small or very large [3, 50]. For very large activation losses (approximately

50-100 mV at room temperature and essentially $i_0 < i$), the equation is simplified to the Tafel-equation (Eq. 2.25):

$$\eta_{act} = \frac{R_g \cdot T}{\alpha \cdot n^{el} \cdot F} \cdot \ln(\frac{i}{i_0}) \tag{2.25}$$

For very small activation losses (less than 15 mV at room temperature and $i \ll i_0$), this equation can further be simplified to Eq. 2.26 [3]:

$$\eta_{act} = \frac{R_g \cdot T}{\alpha \cdot n^{el} \cdot F} \cdot \frac{i}{i_0} \tag{2.26}$$

The overall cell activation losses are defined as the sum of the voltage losses on the anode and cathode. [52--54]

2.2.3 Concentration Losses

At high current densities, concentration or mass-transfer losses (η_{conc}) occur due to the inability of gases to diffuse at high rates. In this case, transport of the reactants to the triple-phase boundary is prevented, as is the removal the products from the cell. The concentration losses can be calculated according to Eq. 2.27:

$$\eta_{conc}(i) = \frac{R_g \cdot T}{\alpha \cdot n^{el} \cdot F} \cdot \ln(i_{lim} - \frac{i}{i_{lim}}) \tag{2.27}$$

in which i_{lim} refers to the limiting current density, defined as the maximum possible current density for the maximum possible reaction rate of the reactants. At high current density, a quick drop in voltage can also occur. This is due to the mass transport issue that the reactants cannot be delivered quickly enough to the catalyst sites, either due to the low porosity of the electrode, water flooding, or other factors that impede the flow of reactants. [50]

2.3 Polarization Curve and Cell Power

Investigations of electrochemical systems always begin with the measurement of a polarization curve, as it is the most ubiquitous electrochemical method, [55]. Polarization curves deliver information about the cell quality as well as the overall losses, thus comparing different cells based on their cell performance (voltage measured as a function of current density) and the available power. However, detailed information about single processes and the losses that occur cannot be obtained by simple direct current (DC) measurements. For an appropriate comparison of various fuel cell types, regardless of their size, current density, as available current per chemically active cell surface is used.

Correct interpretation and simulation of the polarization curve requires a complete analysis and use of the appropriate approaches. Reimer et al. [56] accelerated the degradation of high-temperature PEM and presented a simplified simulation model based on Tafel equation. As shown in their study, appropriate modelling requires some data, such as electrolyte resistance, which can be obtained only by electrochemical impedance spectroscopy. The power generated represents the product of the current and the voltage, and is often used to compare fuel cell performance.

2.3.1 Calculation of Single Losses and Simulation of the Polarization Curve

In order to graphically illustrate single loss mechanisms and their impact over the whole load range, the calculation and simulation of separate losses for ASC-SOFCs used in this work were carried out in MATLAB. For this purpose, the anode was fed with 2.4 SLPM of gas mixture, containing 25 vol% H_2 in N_2, while the cathode side was supplied with 1 SLPM synthetic air. More information about the cell characteristics can be found in Chapter 4. The chosen model generated was based on the study by Reimer et al. [56], in which an approximation of losses was based on a very common approach using the Tafel equation to calculate activation losses (Eq. 2.24) and Eq. 2.27 to calculate concentration losses. In the model used, the separate impact of single electrodes for detailed calculations was neglected, but the contribution of single electrodes was combined into one parameter. The model was thus significantly simplified, since the number of parameters required for modelling was minimized. Furthermore, the general quantification of activation, concentration, and ohmic losses was made possible. The exchange current density and the limiting current density were obtained from the experimental data and considered in the same way; only the combined overall influence of the electrodes and the electrolyte were taken into account.

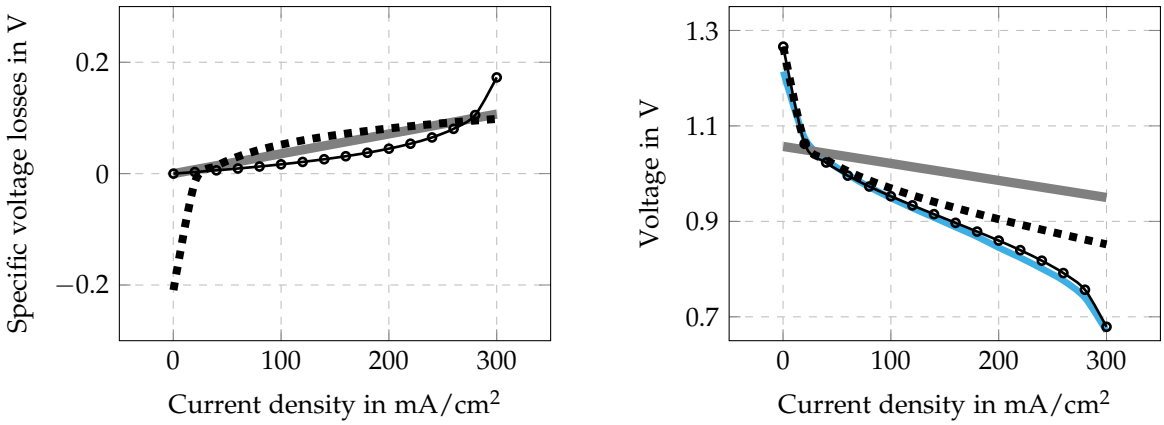

(a) Simulated losses

(b) Simulated polarization curves

Figure 2.4: Simulated loss mechanisms and polarization curve: Ohmic losses (▬), activation losses (▪▪▪), concentration losses (—o—), measured curve (▬).

In order to determine the ohmic losses according to Eq. 2.23, impedance measurements delivered information about the electrolyte resistance.

Fig. 2.4 illustrates the simulated losses for the SOFC cells tested (Fig. 2.4a) and the polarization curve calculated by subtracting single voltage losses from the Nernst voltage (Fig. 2.4b). According to the abovementioned model, the Nernst voltage is considered as a constant value that is equivalent to the OCV. Because of that, the cell voltage obtained by the reduction of OCV by ohmic losses (the grey solid line in Fig. 2.4b) represents a linear curve. The ohmic losses, indicated by the grey line in Fig. 2.4a, increase with the rising current density, and reach a value of approximately 0.11 V at the current density of 300 $\frac{mA}{cm^2}$. The dashed black line refers to the activation losses in Fig. 2.4a. Since the exchange current density is significantly lower than the maximum current density, the model described allows the Tafel approximation to be applied. It is clearly visible that the low current range is most affected by activation losses. The effect of the activation losses on the overall cell performance, especially at low current densities, is also noticeable in the calculated polarization curve (as the dashed black line in Fig. 2.4b). In contrast, the concentration losses dominate, especially at the high currents, while equal to zero at lower currents, as indicated by the black line with circles in both Figs. 2.4a and 2.4b. When compared with each other, the ohmic losses tend to dominate over the whole load range, while activation losses primarily occur in the low current range, and concentration losses at high current densities. Because of their high operating temperatures, the kinetic of reactions for SOFCs is enhanced and the activation losses are minimal, as represented in the literature [3, 47, 48]. However, in literature, the fuel used is always humidified. In the specific case represented in this section, dry hydrogen is supplied to the anode. This is the only way to achieve high activation losses since the oxidation of dry hydrogen requires a high amount of driving force energy [57]. A detailed description of this phenomenon is provided in Chapter 5. Taking all of the loss mechanisms into account, the overall fuel cell performance can be determined. Mathematically, this is demonstrated in Eq. 2.22. Having discussed a simplified simulation model, the predicted cell voltage (black dotted line) is in very good agreement with the measured voltage, depicted by the blue solid line.

2.4 Electrochemical Impedance Spectroscopy [1]

The dependence of voltage and current, as well as available power density, under the prevalent operating conditions is shown in Section 2.3. Indeed, this method only quantifies the cell's overall performance, which may also be used to monitor its degradation over time. [3, 8] In order to provide more detailed information about the loss mechanisms in-

[1] Segments of this section have already been published in [8].

volved, including ohmic, activation, and concentration losses, and to attempt an explanation of why the cell performs the way it does, electrochemical impedance spectroscopy is applied, [3].

Electrochemical impedance spectroscopy is a very important tool and a sophisticated technique for the online examination of cells and the evaluation of experimental results. Its usefulness lies in its ability to distinguish between the electrical and electrochemical properties of the fuel cells under investigation, and in the feedback it provides real-time processes such as cell performance changes. These can be, for example, cell degradation through carbon formation on the anode side, nickel oxidation, or cathode degradation. EIS is a non-intrusive, in-situ method, often used in laboratories, where tests are performed under a range of conditions, including accelerated stress test operation. Numerous studies have addressed the absolutely central importance of applying electrochemical impedance measurements to the field of fuel cell characterization techniques, [58--69]. Electrochemical impedance spectroscopy is also used as a powerful tool for the systematic analysis of solid oxide electrolysis cells (SOEC) and for the detection of SOEC degradation, [70--72]. Very interesting reviews about the relevance of electrochemical impedance spectroscopy and its wide range of the applications, such as for the purpose of mechanistic or kinetic study, are presented in [73, 74].

2.4.1 Impedance Representation

Impedance is often defined as a complex resistance ($\underline{Z}(\omega)$), which represents the ratio of the voltage to the current in an alternating current (AC) circuit in a defined frequency domain. It can be measured under OCV conditions, but also when an electrical circuit is driven with DC. In that case, AC signal is superimposed on the offset DC current. Impedance can be extracted from current/voltage measurements as shown in Eq. 2.28, below. In order to obtain information about on-going processes and the actual physical and functional cell configuration, multiple measurements must be conducted. For that purpose, the measurements must be performed over a wide load range.

$$\underline{Z}(\omega) = \frac{\underline{u}(t)}{\underline{i}(t)} = \frac{u_0(\omega)}{i_0(\omega)} \cdot e^{j \cdot \varphi(\omega)} = |\underline{Z}(\omega)| \cdot e^{j \cdot \varphi(\omega)} = Re(\underline{Z}(\omega)) + j \cdot Im(\underline{Z}(\omega)) \tag{2.28}$$

where ω represents the angular frequency ($\omega = 2 \cdot \pi \cdot f$) and $\varphi(\omega)$ is the frequency dependent phase shift between voltage and current.

The basic principle for impedance measurement is illustrated in Fig. 2.5. At defined DC

current, AC current is superimposed on the cell. If this AC signal is small enough, the system appears to be linear, thus fulfilling the basic requirements mentioned above. [3]

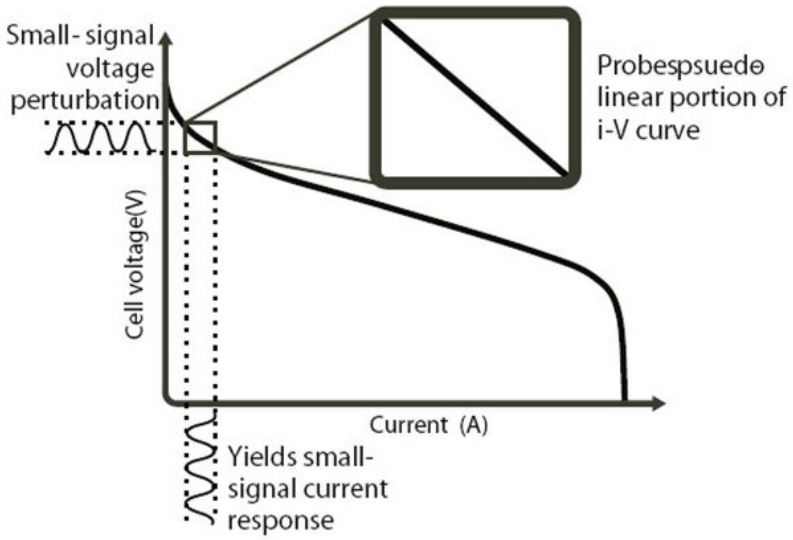

Figure 2.5: Impedance spectroscopy measurement principle. [3]

The measured impedance data are usually plotted as a Nyquist plot. The Nyquist plot illustrates two parts of the overall cell impedance: a real part, which is independent of frequency and represented on the x-axis, and an imaginary part, as a function of frequency and characteristic time-constants, respectively. The imaginary part is plotted on the y-axis. A 3D Nyquist plot for the SOFCs used in this work is illustrated for a wide current range in Fig. 2.6a. All of the diagrams shown in Fig. 2.6 are based on measurements taken during operation with 45 vol% H_2 in N_2, whereby the volume flow of the fuel was defined as 2.4 SLPM. Simultaneously, the cathode side was supplied with 4 SLPM synthetic air.

Bode plots provide an alternative way to illustrate the measured impedance. They express the magnitude of the impedance response of the system and a phase shift as a function of the frequency. These plots are used to provide detailed information about the system under investigation; from them, overall impedance and losses can be interpreted. Bode plots are mainly displayed on a logarithmic scale. [75, 76] Since the every single plot delivers limited information about the fuel systems under operation, only analysis of data observed in all mentioned plots together can provide complete information about the relations between the measurements carried out and permits an evaluation sufficient to validate and determine system characteristics as a function of operating conditions.

Both the magnitude of the impedance response and a phase shift for the cell operated under the above mentioned conditions are depicted in Figs. 2.6b and 2.6c as a function of frequency.

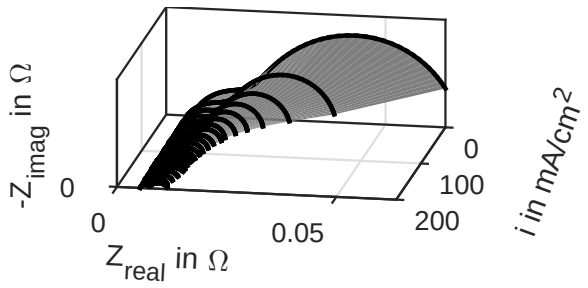

(a) 3D Nyquist plot

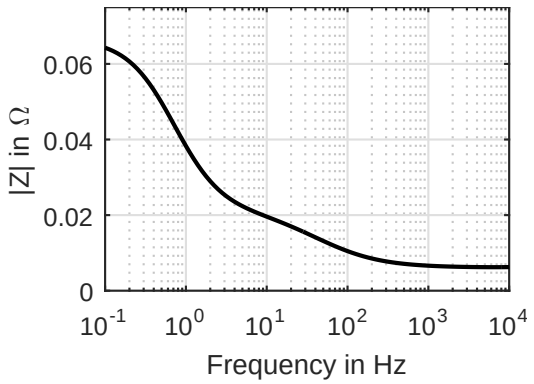

(b) Bode plot

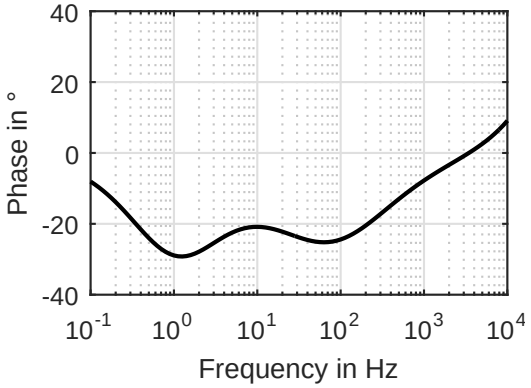

(c) Phase plot

Figure 2.6: Impedance representation as a Nyquist-, Bode magnitude- and phase-plot for the cell operated under 2.4 SLPM of fuel containing 45 vol% H_2 in N_2.

2.4.2 Equivalent Circuit Analysis

The fundamental advantage of the EIS-method is its ability to characterize cell behaviour, and enable the differentiation of the impact made by specific operating conditions. In order to correctly interpret the fuel cell behaviour, based on the EIS-measurements, and to model the specific process mechanisms the data obtained is commonly analysed by fitting it to an appropriate EC model. The fitted data must be consistent with the measured data. As the equivalent circuit becomes more complicated, the obtained data seems to be more correct. However, the complicated EC analysis does not always offer the correct interpretation of the investigated system, and a correct interpretation is still necessary in order to acquire the exact information about the mechanisms involved. Therefore, the EC should be modelled as simply as possible, while all relevant processes are introduced in the EC model developed. [3, 52, 75, 77, 78] In the following, the simple EC elements used in this work will be presented.

2.4.2.1 Ohmic Resistance

The resistor element (Fig. 2.7) is given to illustrate the ohmic resistance.

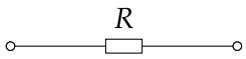

Figure 2.7: Ohmic resistance.

Ohmic resistance has a constant value that does not depend on frequency (Eq. 2.29) and which is measured on the real axis in a Nyquist plot, while its values are equal to zero on the imaginary axis. [79]

$$\underline{Z}(\omega) = R_{\Omega} \tag{2.29}$$

In a fuel cell system ohmic resistance is linked to internal cell resistance, including the anode, the cathode, and the electrolyte, as well as to the resistance of contact meshes and wires. It can be thus interpreted as a barrier for electronic and ionic conduction.

2.4.2.2 Inductance

The inductive impedance (Fig. 2.8) is dependent on frequency.

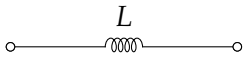

Figure 2.8: Inductance.

According to Eq. 2.30, it is noticeable in the high frequency range. In the Nyquist plot, it is visible as a vertical straight line in the imaginary positive part. In EC analyses of fuel cell systems, it is depicted as the impact of connectors and conducting cables, which develop inductance in very high frequency range. In a low frequency range, the inductive impact of connectors and cables is extremely small. [78]

$$\underline{Z}(\omega) = j \cdot \omega \cdot L \tag{2.30}$$

2.4.2.3 Capacitance

Capacitor C (Fig. 2.9) is a common electrical element, representing an ideal frequency dependent capacitor. The Nyquist plot of such an element corresponds to a vertical straight line in the imaginary negative part.

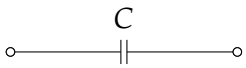

Figure 2.9: Capacitance.

The total impedance of a capacitive element can be calculated according to Eq. 2.31.

$$\underline{Z}(\omega) = \frac{1}{j \cdot \omega \cdot C} \tag{2.31}$$

2.4.2.4 Constant Phase Element

Constant phase element (CPE) (Fig. 2.10) is a frequency dependent equivalent circuit element, which illustrates non-ideal capacitor, thus modelling the behaviour of double-layer capacitance. This element is introduced in the electrochemistry to present the impact of surface roughness and the non-uniformly distributed properties of porous electrodes. [76, 80, 81]

Figure 2.10: Constant Phase element.

Mathematically, CPE is given by Eq. 2.32. Q has a numerical value of admittance (equal to $1/|Z|$), while β refers to phase angel. For the ideal capacitance, this value is 90°.

$$\underline{Z}(\omega) = \frac{1}{(Q \cdot j \cdot \omega)^{\beta_1}} \tag{2.32}$$

2.4.3 DRT-Analysis

DRT is an advanced complementary method, based on measured impedance spectra, which makes it possible for processes with different time constants to be isolated. It thus enables differentiation between anode and cathode processes. [82--84] The equivalent circuit analysis approach can be confusing, if it is not performed in a detailed manner and with regard to physical processes, since different equivalent circuits can result in the same response [52, 82, 85, 86]. When using the DRT method, a detailed equivalent circuit analysis is not required [82].

The DRT method is best explained by Eq. 2.33, [87]:

$$g(t) = \int_{s_{min}}^{s_{max}} K(t,s) f(s) ds + \sum_{j=1}^{m} a_j b_j(t) \tag{2.33}$$

in which $g(t)$ describes the measured function, the term $\int_{s_{min}}^{s_{max}} K(t,s)f(s)ds$ represents the Fredholm integral equation of the first kind and the term $\sum_{j=1}^{m} a_j b_j(t)$ gives the set of m coefficients, which are related to the measured function. $K(t,s)$ is the Kernel function of the given or measured function $g(t)$. The function to be calculated and which provides the required information about the system is $f(s)$. The solution of such an inverse function (ill-posed problem) is difficult and special methods must be used to find an appropriate solution. The most commonly method used is the Tikhonov regularisation. This method makes it possible to obtain data from the noisy experimental data, which, however, requires some constraints, as provided in Eq. 2.34:

$$V(\lambda) = \sum_{i=1}^{n} \frac{1}{\sigma_i^2} \cdot \left(g_i^{\sigma} - \left(\int_{s_{min}}^{s_{max}} K(t,s)f(s)ds + \sum_{j=1}^{m} a_j b_j(t) \right) \right)^2 + \lambda \|Lf\|^2 \tag{2.34}$$

where g_i^{σ} defines the noisy experimental data, σ_i the error, L is an operator ($Lf = f$) and λ is the regularisation parameter. The regularisation parameter must be appropriately defined for the system under investigation, in order to produce reliable data. For the calculations performed within this work, the program FTIKREG [87] and a MATLAB DRT Toolbox [84], based on the Tikhonov regularisation were used.

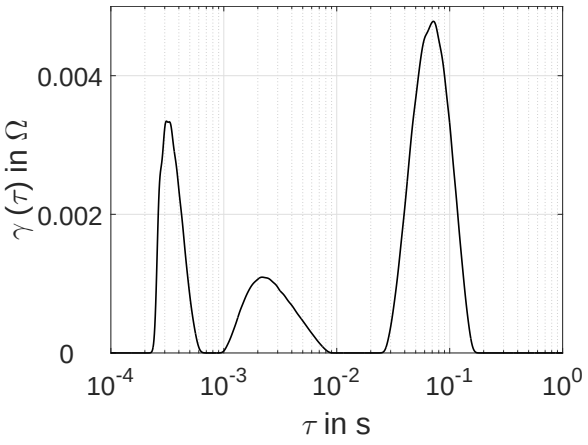

Figure 2.11: DRT-spectrum calculated for the cell operated under 25 vol% H_2 in H_2/N_2 gas mixture.

Fig. 2.11 shows an example DRT-spectrum, calculated for the ASC-SOFC cell, operated under 25 vol% H_2 in N_2. The volume flow of the fuel was set to be 2.4 SLPM, while the synthetic air on the cathode side was defined as 2 SLPM. The isolated peaks refer to single processes, which are described in detail in Section 5.1.

3

Theoretical Background and State-of-the-art of Carbon Depositions

Carbon deposition is a primary concern during the operation of solid oxide fuel cells when these are fuelled with carbon-containing fuels. [7] Carbon deposits block the gas pores, cover the catalytic active sites, and induce the microstructure and performance degradation of SOFCs. At the beginning of this chapter, possible reactions to carbon build-up are presented and the methods used to predict the carbon formation are demonstrated. This chapter is further intended to provide a brief overview of research on the subject of carbon deposition as well as options for its removal.

3.1 Fundamentals of Carbon Build-up Process [1]

Carbon formation on industrial Ni-catalysts for the reformation of methane is a well known phenomenon, and there is a large body of industrial experience referring to this issue. [21, 88--92] During the reforming process, methane is converted to carbon monoxide and hydrogen on the catalyst surface by means of steam (Eq. 3.1) or carbon-dioxide (Eq. 3.2).

$$CH_4 + H_2O \rightarrow 3H_2 + CO \tag{3.1}$$

$$CH_4 + CO_2 \rightarrow 2H_2 + 2CO \tag{3.2}$$

Hydrocarbons also react with steam over the Ni-catalyst, thus reforming in the following way [26]:

$$C_nH_m + nH_2O \rightarrow nCO + (n + \frac{1}{2}m)H_2 \tag{3.3}$$

[1] Segments of this section have already been published in [4].

To maximize the efficiency of the reforming process, the ratio of carbon to oxygen should be stoichiometric, if possible, [93]. Such operating conditions can still result in carbon formation on the catalyst, which induces its degradation. It is generally accepted that carbon can be formed through the dissociation of methane or long-chain hydrocarbons on the catalyst or supported materials. Direct carbon formation through methane dissociation (pyrolysis or cracking) is shown in Eq. (3.4), [94].

$$CH_4 \rightleftarrows C + 2H_2 \tag{3.4}$$

The cracking of hydrocarbons follows Eq. 3.5.

$$C_nH_m \rightleftarrows nC + \frac{m}{2}H_2 \tag{3.5}$$

Carbon monoxide, as a product of the steam or dry reforming, can be converted into carbon dioxide, according to the water-gas-shift reaction (Eq. 3.6), which is catalysed by Ni. [95]

$$CO + H_2O \rightleftarrows H_2 + CO_2 \tag{3.6}$$

However, the following undesirable reactions also occur: reversible steam gasification (Eq. 3.7) and the Boudouard reaction (Eq. 3.8). These reactions result in one mole of carbon, starting from one mole of CO.

$$CO + H_2 \rightleftarrows C + H_2O \tag{3.7}$$

$$2CO \rightleftarrows C + CO_2 \tag{3.8}$$

The equilibrium calculated for the Boudouard-reaction (Eq. 3.8) and methane-cracking (Eq. 3.2) as a function of temperature is shown graphically in Fig. 3.1. The amount of carbon formed due to methane cracking and the Boudouard rection is determined by the operating temperature, and represented in the diagram for the temperature range between 600 K and 1,200 K. In this diagram, as well as in all other equilibrium diagrams, the SOFC operating temperature range is marked with a grey coloured rectangle with grey points. Obviously, the rising temperature encourages the methane cracking, while the amount of carbon produced by the Boudouard-reaction reaches its maximum at significantly lower temperatures. The same impact of the two most significant carbon precursors - methane and carbon monoxide - on carbon formation was reported by Xiao at al. [32]. They observed a difference between the carbon formed by methane and the carbon formed by carbon monoxide. Thus, an important conclusion that can be drawn from that study is that if carbon is formed in methane by methane cracking, the amount of carbon deposited increases with rising temperatures, and such carbon cannot destroy the anode structure. On the other

hand, if carbon is formed in carbon monoxide, the amount of carbon deposited decreases with increasing temperature. [4, 6]

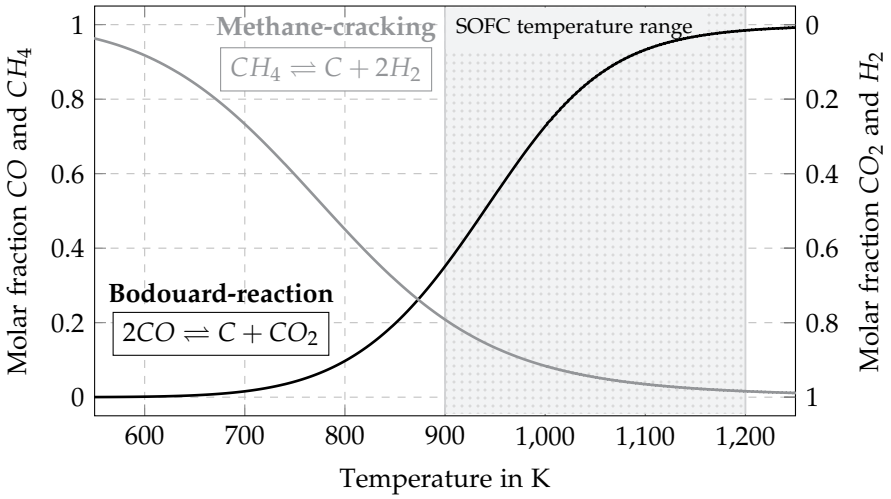

Figure 3.1: Calculated equilibrium: Boudouard-reaction (——), Methane-cracking (——). [4]

Detailed reaction paths for the carbon formation over Ni-YSZ anode are commonly given as represented in Eq. 3.9 for hydrocarbon cracking, Eq. 3.10 for hydrocarbon oxidation, and 3.11 for Boudouard reaction, [1]:

$$C_xH_y + (x+y)(Ni) \rightleftarrows xC_{Ni} + yH_{Ni} \tag{3.9}$$

$$C_xH_y + (y)O_{Ni} \rightleftarrows xC_{Ni} + yOH_{Ni} \tag{3.10}$$

$$xCO + x(Ni) \rightleftarrows \frac{x}{2}C_{Ni} + \frac{x}{2}CO_{2,Ni} \tag{3.11}$$

In the stated reactions, Ni represents a catalytic active nickel, either as surface or as bulk. The process of carbon formation mechanisms over industrial catalysts as well as Ni-YSZ SOFC anodes has already been well investigated, [96--99]. Bartholomew [99] states several types of carbon that can be formed through the steam reforming and methanation process; these are: graphitic, polymeric, adsorbed, vermicular or filamentous carbon as well as carbides. Further investigations, specified for SOFCs, have shown that the carbon formed under typical SOFC operating conditions depends on several aspects, such as the steam/carbon ratio (S/C-ratio), the microstructure of the anode, operating temperature, fuel mixture, etc. However, Yurkiv [1] summarized the available data and claimed that all of the carbon types mentioned can be identified with three major mechanisms: (1) heterogeneous carbon, similar to polymeric carbon, which is mainly formed under OCV conditions and covers the catalytic active Ni-site, thus disabling further reactions; (2) homogeneously/heterogeneously formed soot or pyrolitic carbon, which blocks the porous gas channels, thus increasing overall

resistance; and (3) again heterogeneously formed carbon at the anode surface, which further diffuses into Ni-particles and leads to destructive nickel dusting. Yurkiv [1] graphically represented the carbon formation path (Fig. 3.2), where it can clearly be seen that whether carbon is formed from CO or CH_4, its formation always originates on catalytic nickel.

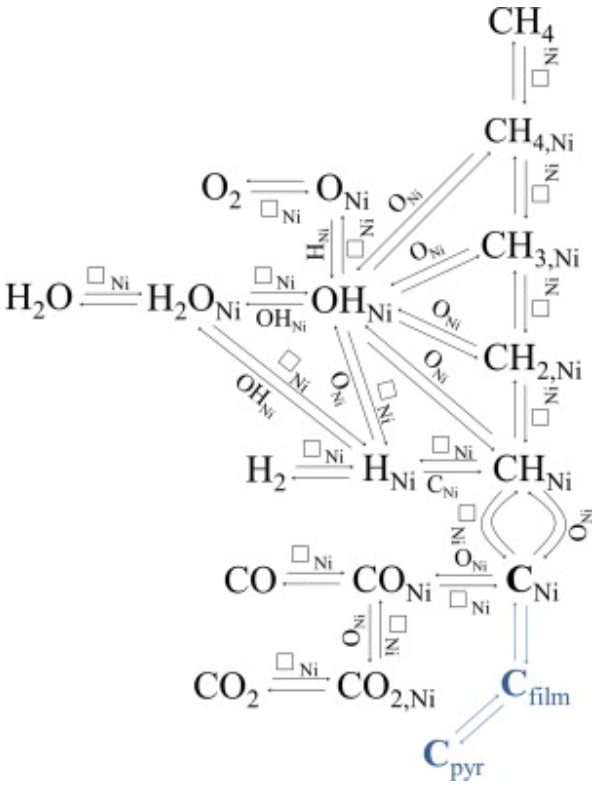

Figure 3.2: Schematic overview of carbon formation reaction mechanisms. [1]

Many studies have generally discussed the fact that carbon is firstly formed on the catalytic active sites, and, after the catalyst surface is covered, that carbon goes on to block the gas channels. Nevertheless, it has also been shown that purely SOFC-relevant oxides, such as yttria-stabilized zirconia (YSZ), yttriumoxid (Y_2O_3) and zirconiumoxid (ZrO_2), induce carbon-growth. These pure oxides efficiently promote methane dissociation and build different carbon species. They show high reactivity toward the adsorption of gaseous CO and CO_2 species as well, which diminish the performance of the utilized fuel cells. [100, 101] Uniform carbon formation, over both the Ni-catalyst and the oxide YSZ, is experimentally proven in this work. More details on this are presented in Chapter 5.

3.2 Prediction of Carbon Depositions

There are several parameters of significant importance to carbon build-up and its deposition onto the fuel electrode (anode). The key parameters that enable carbon prediction are: the

components involved in a used gas mixture, temperature, the steam/carbon-ratio, equilibrium state, and C-H-O ternary diagram.

This section presents all of the current carbon prediction methods, and analyses the basic calculation principles. For the detailed analysis of coking propensity, three diesel reformate mixtures with a composition shown in Tab. 3.1 were used. In order to examine the impact of water vapour on carbon deposition, the amount of H_2O in the fuel mixture was varied between 0 vol% (*Case a*), 11.3 vol% (*Case b*) and 20 vol% (*Case c*), which can be seen in Tab. 3.1. The gas mixtures used are thus presented in the same way, as *Case a*, *Case b* and *Case c* in further subsections. The S/C-ratio calculated for all three gas mixtures can also be seen in Tab. 3.1.

Table 3.1: Gas mixtures used for equilibrium calculations.

Species	H_2	CO	CO_2	CH_4	H_2O	N_2	S/C
Unit	vol%	vol%	vol%	vol%	vol%	vol%	-
Case a	15.4	13.7	9.8	20.3	0	40.8	0
Case b	15.4	13.7	9.8	20.3	11.3	29.5	0.33
Case c	15.4	13.7	9.8	20.3	20	9.8	0.58

For the purpose of the detailed analysis, thermodynamic equilibrium calculations are carried out for two different carbon types: graphitic carbon and carbon nanofibers (CNF).

3.2.1 Equilibrium Calculation [2]

When using carbon-containing fuels in SOFCs, thermochemical calculations are essential in order to establish the optimal operating conditions, if these can be varied. If the operating conditions are fixed, the thermodynamic equilibrium must be calculated. [102] The thermochemical calculations are an important step in determining the critical operating conditions because of the risk, when fuelling with carbon containing fuels, of solid carbon forming and of it being deposited on the anode. This in turn affects the nickel catalyst, and thus the electrochemical properties and gas transport of the cells in operations. The thermodynamic calculations in this work were performed using the program HSC Chemistry, for three different gas mixtures (as represented in Tab. 3.1), in a wide temperature range of 100°C to 1,000°C. This made it possible to scrutinize the fuel processing dependence on the operating temperature. The thermodynamic equilibrium composition is thus plotted dependent on a number of parameters that impact it - among others the fuel composition

[2] Segments of this section have already been published in [5].

and temperature. The applied parameters, such as pressure (in this case the standard pressure) and the amount of substance, are assumed from the real parameters applied in the experiment, while the results are represented as the amounts of the products. This method of showing results also makes it possible to present the amount of solid carbon formed and to compare it with the amount of gaseous product species [102]. The calculations are based on 1 mol of carbon (carbon-forming species). In their studies, Sasaki et al. [102] and Lee et al. [22] described the possibility of forming two different types of elementary carbon - graphite (C_{gr}) and carbon nanofibers (C_{CNF}). For the calculations performed in this work, both carbon types - carbon nanofibers and graphite - are considered. [5]

The equilibrium calculations were performed for three diesel mixture variations, the composition and S/C-ratio of which are shown in Tab. 3.1. Information on the amount of single species can be read from the y-axis in Fig. 3.3, which is represented as a function of the temperature. The temperature is thus plotted on the x-axis. Each diagram in Fig. 3.3 depicts not only the amount of single gaseous components but also the amount of solid carbon formed as graphite, indicated by the black dotted line, or as CNF, represented by the brown dotted line. Single species are indicated by solid lines in orange (H_2), green (CO), blue (H_2O), grey (CH_4), and pink (CO_2). When comparing the three first diagrams, it is clear that increasing the amount of water vapour intensifies steam-reforming, since the amount of H_2 and CO species increases simultaneously. Increasing the amount of water vapour significantly reduces the amount of carbon formed.

In the fourth diagram of Fig. 3.3, the formation trends of two carbon types as a function of temperature are compared with each other for the three gas mixtures. The coloured areas below the calculated curves in the fourth diagram show the amount of specific carbon that can form at different temperatures. Out of 1 mol of carbon-forming components, approximately 0.3 mol of graphite and 0.4 mol of CNF are formed at the typical ASC-SOFC operating temperature of 800 °C if the cell is fuelled with dry gas mixtures, specified as *Case a* (see Tab. 3.1) and in equilibrium conditions. Increasing the S/C-ratio, which indicates the rising amount of H_2O in the fuel, reduces the amount of carbon formed both as graphite and CNF. For S/C=0.33 (*Case b*), 0.2 mol C_{gr} and 0.23 mol C_{CNF} are formed at 800 °C, while S/C=0.58 (*Case c*) reduces C_{gr} to approximately 0.1 mol and C_{CNF} to almost 0.18 mol. For all three calculated cases, C_{gr} has a maximum value at 100°C, decreases significantly until 350 °C, and then has a constant value between 350 °C and 550 °C, after which it decreases further. This means that lower temperatures are favourable for graphite formation. By contrast, CNF is first formed at approximately 300°C, increasing above this temperature and peaking between 650°C and 700°C. With any further temperature increase, the amount

of CNF formed is reduced. In any case, both types of elemental carbon can be formed for the investigated fuel at SOFC operating temperatures between 600°C and 850°C. [5]

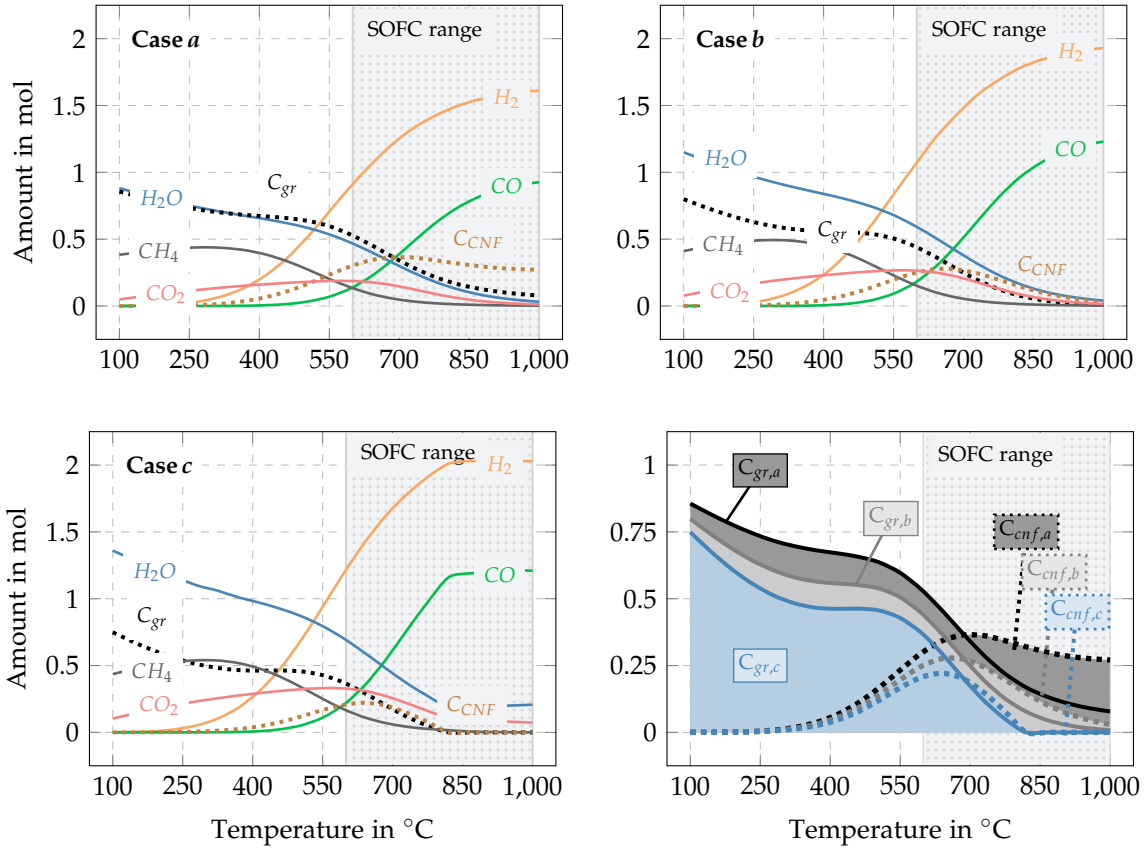

Figure 3.3: Equilibrium calculations for three different gas mixtures, as given in Tab. 3.1. [5]

Information regarding the catalytic aspects of the steam- and dry reforming of hydrocarbons as well as the oxidation both of hydrocarbons and carbon monoxide based on equilibrium calculations is presented in literature, [103--112]. It is important to note that the activity and effectiveness of the reactions mentioned strongly depend on the catalyst used. With this in mind, the performance of various metal oxides (Zr, Mg, Ni, Ce, La) in combination with Al_2O_3 as a support for rhodium catalysts, was examined in [103]. At the SOFC-relevant operating temperature of 700°C, thermodynamic calculations resulted in a methane conversion rate of 96.3%. In the absence of catalysts, a maximum of 2% of methane was converted. The application of catalysts, however, increased this rate to 72-89%. Of all the metals employed, Ni-Al_2O_3 was identified to be the best catalyst, and of significant relevance for use in solid oxide fuel cells. Nevertheless, it also showed the highest propensity towards carbon formation. The same applies to the auto-thermal reforming of hydrocarbons, in which case nickel reoxidation can occur as a negative side-effect, [110]. The choice of support is also of crucial importance to the reaction steps that occur within the catalytic process.

Depending on the catalyst and the support which are applied, steam reforming reactions and water-gas shift reactions can be either enhanced or inhibited, which thus affects the equilibrium state, [109, 113]. The contents of the components used in the support further impacts the activity in CO oxidation, [108]. For example, catalysts based on cerium or copper oxides promise the active and selective oxidation of carbon monoxide, but their particle size significantly diminishes catalytic activity. The addition of zirconium or lanthanum distinctly reduces the particle size and increases the catalytic active size. Therefore, the catalyst and the support used play an important role in the determination of reaction equilibrium, which thus often differs from the calculated thermodynamic equilibrium.

3.2.2 Steam/carbon Ratio

The steam/carbon-ratio represents the molar quantities ratio of molecular water vapour to atomic carbon in a fuel stream, [3] and is given by Eq. 3.12. In this context, it is important to note that not every carbon-containing component (such as CO_2) is considered for the purpose of this calculation, but rather only the components from which carbon is mainly formed, such as CO and CH_4.

$$\frac{S}{C} = \frac{n_{H_2O}}{n_C} \tag{3.12}$$

For example, if a gas mixture of 1 mol H_2O and 1 mol CH_4 is used, the calculated S/C-ratio ratio is 1. Many studies state that when a certain amount of water vapour is used to dilute a carbon-containing fuel, reaching a S/C-ratio higher than 2, no carbon should be formed, [114]. Otherwise, carbon formation and deposition can occur, [115, 116]. In this regard, S/C-ratios for the gas mixtures used are calculated and shown in Tab. 3.1. In all mentioned cases, the S/C-ratio is significantly lower than 2, which implies that carbon can be formed. On the other hand, the calculated equilibria in Fig. 3.3 show that the influence of the S/C-ratio on carbon formations is strongly dependent on the operating temperature. An S/C-ratio of 0.58, calculated for the defined gas mixture *Case c*, leads to carbon formation if the operating temperature is lower than 820 °C. This suggests that if the cell is operated at 800 °C with a steam-to-carbon ratio a little over 0.58 it may be possible to prevent carbon formation. [5]

The S/C-ratio for the gas mixture used can be derived for the equilibrium state at different operating temperatures. Varying S/C-ratios depending on the temperature range, for the three gas mixtures (*Case a*, *Case b*, *Case c*), can be seen in Fig. 3.4. If 2 is the minimum S/C-ratio that can suppress carbon formation, when considering the values calculated in Fig. 3.4, it is possible to see that carbon can be formed over the entire range of operating conditions. At temperatures higher than 550°C, which indeed represent the SOFC operating

range, the risk of carbon formation is particularly high. Between 550°C and 850°C, the S/C-ratio is depicted as an exponentially decreasing function, thus rapidly increasing the likelihood of carbon build-up.

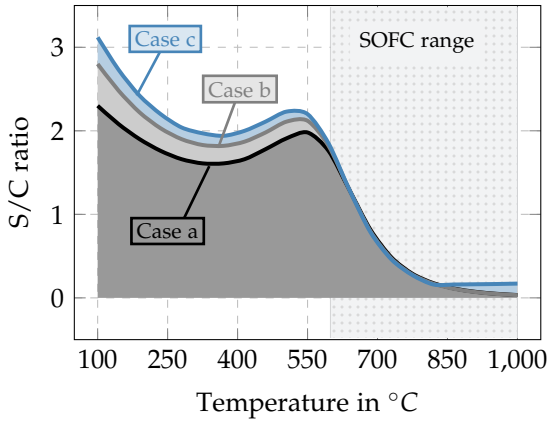

Figure 3.4: Equilibrium calculations for three different gas mixtures (with gas composition as given in Tab. 3.1).

The S/C-ratio should therefore not be considered as a constant value along the cell, since it must be specified for the set operating conditions as a function of the determined equilibrium state. The minimum S/C-ratios necessary to prevent carbon formation on the SOFC anode, operated under pure CO and CH_4, but also under a CO/CH_4 mixture, are reported in [117]. As described therein, when fuelled with CH_4 diluted in H_2O, the values of 0.16 at 100°C and 0.984 at 1,000°C were determined as required to inhibit the formation of graphite. Using CO as a fuel resulted in significantly higher graphite formation rates at lower temperatures, according to the Boudouard reaction. The maximum S/C-ratio was determined to be 2 at 100°C, and it decreased down to zero at 800°C. Therefore, within the SOFC operating temperature range, CH_4 is regarded as a more dangerous fuel component for graphite formation than CO. Finally, the calculations for the equimolar mixture of CH_4 and CO demonstrated the highest required S/C-ratio of 3.4 at 100°C for graphite and 0.92 at 650°C. The safest operation for the gas mixtures in question was reached at 800°C, where the ratio of 0.55 was seen to inhibit graphite formation. A slightly higher value is required to additionally impede the formation of carbon nanofibers. When only the build-up of filamentous carbon was examined, the most appropriate operating temperature was 300°C. At this point, a very low S/C-ratio of 0.26 was found to be adequate to guarantee safe carbon-free operation. However, this temperature is not relevant for the operation of SOFCs, which means that higher S/C-ratios are necessary for safe and carbon-free operation at higher temperatures.

3.2.3 C-H-O Ternary Diagram

Since the ratio of water, hydrogen or oxygen to carbon is a crucial factor that both impacts the formation of carbon and generally defines the operation conditions of cells employed, the presentation of these three components in one diagram - a ternary C-H-O diagram - is very important, [118]. C-H-O ternary diagrams represent the carbon deposition region as well as the region where carbon-free operation is ensured, thus allowing the potential hazard of carbon depositions to be determined. For every gas mixture utilized in SOFCs, operating points in the C-H-O diagram can be calculated for the equilibrium state, thus predicting if carbon deposition is being augmented or suppressed. The carbon deposition zone and the carbon free zone are presented depending on the temperature by demonstrating the relative amount of carbon, hydrogen, and oxygen, through a carbon deposition boundary line. Once the relative amount of these three components in the gas mixture is determined, it is possible to assume whether carbon will be formed on the cell surface. [5]

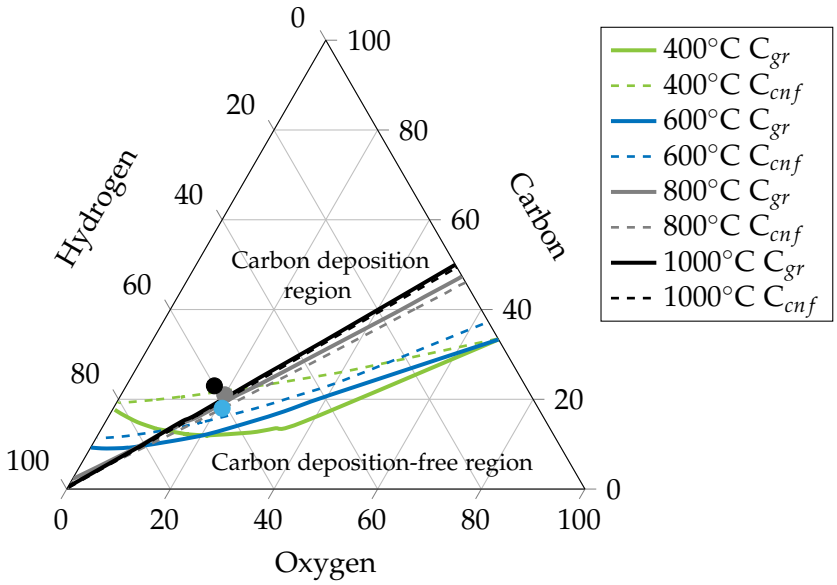

Figure 3.5: C-H-O Ternary diagram; Operating points - Case *a* (●), Case *b* (●), Case *c* (●) (gas composition is provided in Tab. 3.1).

Fig. 3.5 shows the defined carbon formation boundaries in the C-H-O diagram as a function of the four operating temperatures - from $\vartheta = 400\,°C$, indicated by the green line, up to $\vartheta = 1000\,°C$, indicated by the black line, with 200 °C steps. Solid lines represent the borderlines for graphite formation, while dashed lines illustrate carbon nanofibers. As can be seen in the diagram below, the difference between the formation boundaries for the two carbon types becomes significantly smaller as the temperature increases. The position of the diesel reformate mixture used, with varying water vapour concentrations, is also shown in the same diagram.

Operation under *Case c*, in which the diesel mixture contains 20 vol% H_2O (blue point), is represented as the most hydrogen-rich, and is positioned exactly at the boundary between the carbon-free and carbon-deposition region for both operating temperatures, $\vartheta = 800\,°C$ and $\vartheta = 1000\,°C$. The decreasing concentration of water vapour shifts the points more towards the carbon deposition region. The borderlines for the operating temperatures of 600 °C and 400 °C are still beneath all three gas mixtures, which means that the decreasing temperature promotes carbon deposition. Under the operating conditions defined in Tab. 3.1, it is clear that the cell is being operated in the carbon formation zone and that carbon deposition is expected.

3.2.4 Operating Current Density

Current density is an essential parameter that defines the amount of carbon formed during operation under carbon-containing fuels. According to the Faraday law (Eq. 3.13), increasing the current intensifies the reduction of oxygen to oxygen ions on the cathode side, which are subsequently conducted through the electrolyte to the anode. [94]

$$N_{O_2} = \frac{i}{4 \cdot F} \tag{3.13}$$

where N_{O_2} represents the oxygen molar flow density in $\frac{mol}{cm^2 \cdot s}$. The oxygen ions produced can oxidize the solid carbon. When operating under open circuit conditions, no oxygen ions are available, thus the probability of carbon formation significantly increases. Singh et al. [94] calculated the amount of carbon formed under fuelling with a mixture of 20 vol% CO, 15 vol% H_2, 10 vol% CO_2, 5 vol% H_2O, 2 vol% CH_4, and 48 vol% N_2 at 750°C. The maximum amount of carbon formed was determined to be 0.104 $\frac{mg}{s}$ at OCV, and monotonically decreased down to zero at 126 $\frac{mA}{cm^2}$.

3.3 The Phenomenon of Carbon Deposition in Literature [3]

The commonly used Ni-YSZ anode structure has the greatest tendency to adsorb carbon since its excellent catalyst performance promotes carbon formation reactions, such as those shown in Section 3.1. Conventional Ni-YSZ-based cermet was used for the anode material of the SOFC cells employed in this work. The carbon deposition degradation phenomenon can occur on either a microscopic or a macroscopic level, and can damage the catalyst surface and block the porous gas channels, thus preventing further power generation [41, 116, 119]. Many studies have investigated the phenomena of carbon depositions and their impact on

[3] Segments of this section have already been published in [4--7].

SOFC performance, mainly as caused by methane whether as pure gas or in a gas mixture [24--27].

Sameshima et al. [120] reported that carbon formation always occur in proximity to Ni, which is a very good catalyst for the steam- or dry-methane reforming, if a CH_4/CO_2 mixture is used as a fuel. The increase in methane concentration in the CH_4/CO_2 gas-mixture simultaneously increases the cell voltage. Similarly, the influence of an increasing CH_4 concentration on the cell stability, this time in a CH_4/H_2 mixture, was examined by Buchinger et al. [28]. In their study, however, an increment in CH_4 concentration was indicated by decreased voltage. Because of the rising CH_4 concentration, carbon formations occurred on the anode, blocking the gas channels and causing the mechanical degradation of the cell, due to the nickel degradation caused by deposited carbon tubes. The impact of methane on cell performance and carbon formation was also studied by Chen et al. [31]. In their study, Ni-YSZ anode-supported SOFCs were operated under diverse synthetic syngas mixtures. The methane concentration of the fuels used was varied in order to examine the cell behaviour. Increases in methane volume fraction accelerated performance deterioration and could even be seen to cause irreversible cell degradation; a critical methane volume fraction was, in this case, approximately 23 vol%. It has also been experimentally verified that the increased volume fraction of methane and decreased volume fraction of hydrogen and carbon monoxide in a gas mixture drastically changed the anode morphology and diminished cell performance. Mermelstein et al. [121] and Lorente et al. [30] studied the impact of the gasification syngas, containing tars, on the anode. This gas contained tars (toluene, benzene, and naphthalene) that led to both carbon deposition and cell degradation. The carbon deposits were also quantitatively analysed. In their investigations, Saunders et al. [122] and Kim et al. [123], considered carbon depositions from tars, injected directly into the cell as liquids, while Singh et al. [94] calculated the impact of gaseous tars on coke formation. They reported that carbon is formed more slowly with an increase in current density, and that after a critical current density is reached, no more carbon can be formed on the cell, see Section 3.2.4. The calculations performed in that study further showed that the concentration of steam required to eliminate carbon deposition increases with the rising concentration of the tars. For example, as the concentration of tars increases from 2% to 5% at OCV, the steam concentration required also increases from 14.7% to 42.8% [94].

As illustrated in Fig. 3.1, the Boudouard-reaction is not expected to be so prominent at the typical SOFC-operating temperatures compared to methane dissociation. The impact of carbon monoxide and hydrocarbons on carbon formation differs at the typical SOFC temperature of $800°C$; carbon monoxide forms the lowest amount of carbon, while the most carbon is formed during operation with methane [117, 124]. Based on [24, 31, 34, 95, 119, 125],

both operating temperature and the carbon-containing fuel introduced have a significant influence on the type and microstructure of the carbon formed. Snoeck et al. [126] claimed that the Boudouard reaction results in the formation of encapsulating carbon, which induces the gradual deactivation of the catalyst. Encapsulated carbon through methane cracking was formed only at the lower partial pressure of methane, and in the absence of hydrogen. Filamentous carbon was formed mainly during normal methane operation. Gunawarda et al. [127] claimed that the size and morphology of carbon formed depends on the size, shape, and composition of the metal particles on which they are deposited. In their experimental study, pre-oxidized Inconel 601 samples were exposed to several syngas mixtures in a temperature operating range between 550 and 750°C. The results showed that the amount of carbon formed is mainly a function of temperature and gas composition; however, increasing the temperature increased the amount of carbon formed. They also emphasized metal dusting as a negative side effect, initiated by the formation of whisker (filamentous) carbon. Helveg et al. [128] also addressed the destructive impact of carbon whiskers. They reported that whisker carbon includes different degrees of graphitization and morphologies of the graphene, and showed, by electron microscopy, the growth of multiple graphene layers as well as the encapsulation of Ni nanoparticles.

Carrying out a variety of in-situ optical studies made it possible for this investigation to gain an in-depth understanding of the carbon deposition process: vibrational Raman spectroscopy, Fourier-transform infrared emission spectroscopy (FTIRES) and near-infrared thermal imaging (NIR), [129--133]. The methods described in these studies were used for direct monitoring of the cell, in order to provide information about the gas-phase as well as adsorbed species during operation in real time, thus determining the structural and chemical changes of the SOFC anodes. In their studies, the authors showed that methane leads to very fast carbon formations in a wide temperature range, while carbon growth is reduced when the methane is diluted by CO_2. In order to better understand the carbon formation processes, a detailed description of SOFC mechanisms, and, especially of the internal reformation of methane - both dry and steam reforming and autothermal oxidation - as well as the water-gas shift reaction for a Ni-YSZ based anode can be found in [134--136]. The authors developed a comprehensive numerical model, which describes gas-surface interaction mechanisms. The mechanisms of carbon formation are furthermore described with elaborate detail in [46, 137].

Numerous studies have reported on the effect of carbon depositions, but these have mostly investigated SOFC-cells with a small active area ($\leq 16\,cm^2$), and especially button cells (approximately $1\,cm^2$). Only a few studies were found which investigated large planar cells. Hauth et al. [45] investigated the performance of large, planar, electrolyte-supported SOFCs;

they found that operation with hydrocarbons is critical for the performance of the cell and carbon formation. Lim et al. [44] analysed $10 \times 10\,cm^2$ anode-supported cells. Their study showed that many factors restrict the operation of large planar cells, without negatively affecting button cells. They investigated the influence of gas conversion overpotential on cell performance, and they showed that the operating conditions strongly affect the electrochemical performance of large planar cells. In general, large planar cells can achieve high power because of their large effective area, and this makes them relevant for commercial use. This is one of the reasons that the investigation of large planar cells is of such great importance. Nonetheless, both the large area of the investigated cells and their planar shape are also problematic for optimal cell operation, and responsible for losses in efficiency. [4] Although several studies have reported results related to large, planar SOFC-cells, detailed electrochemical analysis of this cell type in addition to the determination of the amount of carbon formed, even at an early-stage, is critically important in order to guarantee their safe operation, and to accelerate access to the market.

3.4 Carbon Removal in Literature [4]

The safe and carbon-free operation of large, planar SOFC cells under carbon-containing fuels can be ensured in several ways. The influence of the current density is, as mentioned, frequently scrutinized as a crucial factor for the carbon deposition rate, as shown in [41, 94, 138, 139]. To reduce carbon formation due to operation with carbon-containing fuels, Mermelstein et al. [139] suggest increasing the current-density and the steam content, while Singh et al. [94], showed in their simulation, mentioned above, that a critical current density exists, and that if this current density is achieved, carbon cannot be deposited on the cell surface. With regard to this, Alzate-Restrepo et al. [41] showed that the amount of carbon formed under load was around 100 times less than the amount of carbon formed at OCV, and that this carbon was also more reactive. Furthermore, not only the enhancement of current density is proposed for the minimization of carbon depositions, but also an increase of the water vapour concentration in the gas mixture used. Although this could reduce carbon formation, the increase of volume fraction of steam would dilute the fuel, and thus decrease the overall efficiency and power density of the fuelled cell. Increasing the concentration of CO_2 in the fuel gas could also minimize carbon formation [140]. Although many studies show how carbon formation could be minimized or even stopped, it is still a challenge to investigate and develop strategies that permit entire cell regeneration without diminishing cell performance or damaging the cell's microstructure. In order to prolong the lifetime of SOFCs, it is important to not only avoid the formation of carbon and remove carbon deposits when they do occur, but also to develop cell-protecting regeneration approaches.

[4] Segments of this section have already been published in [4--7].

This topic needs to be thoroughly addressed, having been given insufficient attention by the scientific community thus far.

Closer investigation of coke gasification in refineries and the gasification of carbonaceous species from metallic catalysts was performed in pioneering works from Figuerido [141, 142], Trimm [143, 144], Bernardo [145] and McCarty [146]. They suggest four main paths for gasification reaction, using four different gasification agents: (1) *hydrogen*, based on reversible methane dissociation (Eq. 3.4), (2) *steam*, for steam gasification (Eq. 3.7), (3) *carbon dioxide*, based on the reversible Boudouard reaction (Eq. 3.8) and (4) *oxygen*, which enables direct carbon gasification according to Eq. 3.14.

$$C + O_2 \rightarrow CO_2 \tag{3.14}$$

Figueiredo [141, 142] used two different catalyst types in order to gain more precise insight into the catalytic gasification of deposited carbon by hydrogen and water vapour. For this purpose, polycrystalline nickel foils and Al_2O_3 supported nickel catalyst were applied. The supported Ni-catalyst can thus be compared to the materials employed in the SOFC fabrication. When using water vapour for gasification, rates of gasification were found to be independent of the partial pressure of water vapour, amount of catalyst, and coke present for both catalyst types. However, the required activation energy for the gasification process was higher for pure Ni (32 $\frac{kcal}{mol}$) than for supported Ni/Al_2O_3 catalysts (18 $\frac{kcal}{mol}$). In both cases, the rate of gasification for nickel foils was nearly proportional to the amount of carbon formed. During the gasification with water vapour, CO_2 and H_2 were observed as the product gases, according to the following reaction (Eq. 3.15):

$$C + 2H_2O \rightarrow CO_2 + H_2 \tag{3.15}$$

When using hydrogen for carbon gasification, gasification rate was greatly reduced, since carbon reacts with hydrogen significantly more slowly, [141, 142]. Methane was measured as a gasification product in this case, which refers to the reaction given by Eq. 3.4. The required activation energy was measured to be of the same order of magnitude for both Ni-foils and supported catalyst (31-32 $\frac{kcal}{mol}$). [141, 142] Two different gasification mechanisms were introduced, which were determined by whether (1) reactant gas, or (2) carbon, that first interacted with the catalyst. When interaction between the reactant gas and the catalyst occurs first, the reactant gas is adsorbed on the catalyst surface. It further dissociates into atoms that migrate to the carbon. The second mechanism includes the dissolution of carbon and its transport to the catalyst-reactant gas, where the carbon gasification reaction takes place.

Bernardo and Trimm [145] examined the kinetics of carbon gasification by hydrogen and water vapour, as well as by carbon dioxide. The rate of gasification by CO_2 over Ni-foils was proportional to the initial carbon amount and showed significant dependence on the temperature. Increasing temperature noticeably increased the gasification rate, while at approximately $500°C$ the gasification rate decreased to zero. The gasification process took place according to the reversible Boudouard reaction (Eq. 3.8). Higher gasification rates were observed for the supported catalyst, where at approximately $500°C$, the gasification rate decreased to unity. The investigation of gasification with hydrogen and steam extended the results of Figuerido [141]. During the gasification process with hydrogen, methane was observed as the reaction product. Activation energy decreased with the increasing temperature, from 265($\pm$17) $\frac{kJ}{mol}$ below $550°C$ to 180($\pm$9) $\frac{kJ}{mol}$ between $550°C$ and $625°C$, further down to -82($\pm$5) $\frac{kJ}{mol}$ at temperature higher than $700°C$. The addition of methane to the gas decreased the gasification rate observed, since the product gas was thus available in a reactants mixture. When using water vapour as a gasification agent, the increasing temperature resulted in gasification rates similar to those obtained for carbon dioxide. Carbon gasification was favourable at higher operating temperatures.

Furthermore, the catalytic activity of various Ni-based catalysts was examined by Takenaka et al. [125, 147, 148]. Carbon depositions were produced due to methane utilization, based on methane decomposition, while the gasification process was performed using CO_2. For the purpose of detailed investigation, several cycles of carbon formation due to methane decomposition and the subsequent removal of the carbon deposits with CO_2 were repeated. The structural changes of Ni species influenced by the carbon deposits and their removal were examined after each cycle. Based on this examination, it was stated that catalytic activity and the microstructure of Ni changed after each newly performed cycle, which included, as already stated, methane decomposition and subsequent gasification with CO_2. A detailed analysis of the cell microstructure after repeating the coking and coke-removal processes was also performed with the aid of numerous scanning electron microscopy (SEM)-images and X-ray diffraction (XRD)-patterns. A very interesting fact represented in [125, 147, 148] is that the size of the CNF formed is dependent on the dimensions of the Ni-particles. [6]

Looking at the gasification of carbon deposits from the SOFC anode, Timmermann et al. [29] suggest operation with high water vapour concentration in order to remove carbon from the anode. The regeneration was performed with a mixture of 30% H_2O, 57% N_2 and 13%H_2 at 650°C for 30 minutes. No carbon particles were found on the cell after the experiment. Alzate-Restrepo et al. [41, 138] and Horita et al. [149] proposed oxygen ions and produced water vapor for fast SOFC anode regeneration due to their reaction with

the formed carbon. Kirtley et al. [150] employed in situ vibrational Raman spectroscopy in order to examine the rates of carbon deposits over the Ni-YSZ anode, and furthermore to detect the rates of carbon removal using pure H_2O, O_2 and CO_2 as gas phase reforming agents. H_2O was demonstrated to be the most effective at removing carbon, followed by O_2 and CO_2. Still, after carbon was removed, Ni was oxidized due to the excessive presence of O^{2-} ions from the agents used, thus inducing an increase to the anode volume and adding mechanical stress to the anode, which eventually leads to cell damage. Ni-oxidation was detected independent of the gasification agent used. This implies the need for continuous supervision of the carbon gasification and of ensuring an undisturbed anode supply. In any case, this study demonstrated that hydrogen, steam or carbon dioxide may gasify any carbon formed due to different reactions. Snoeck et al. [126] studied the gasification of filamentous carbon by CO_2, H_2 and H_2O, and showed both, a modelled and experimentally observed gasification rate. In their study, the gasification process was performed at 550°C, and it was shown that carbon gasification can differ depending on whether the carbon was formed by methane cracking or the Boudouard reaction. Nevertheless, none of these studies provided an electrochemical analysis of cell performance after the carbon removal process was complete, and it is not known, whether or not the initial SOFC electrochemical performance could still be achieved. The aim of the present thesis is to carry out carbon removal from the porous SOFC anode in a cell-protecting manner, in order to enable continued and efficient cell operation. This undertaking is intended to clarify whether carbon can be removed in such a way as to avoid limiting the operation of SOFCs, while increasing their potential lifetime.

4

Experimental Setup

This chapter describes (1) the design and the types of the cells used, (2) the measurement setup, and (3) the characterization techniques used for the detailed electrochemical and chemical analyses of the cell performance.

4.1 Single Cell Geometry

This work investigates anode-supported solid oxide fuel cells. The cells are 100 cm^2 (10 cm$\times$10 cm) in size, with an active electrode surface of 81 cm^2 (9 cm$\times$9 cm). This size is characterized as industrial-size since it is appropriate for commercial use in auxiliary power units. This type of fuel cell was used for the detailed electrochemical analysis in order to obtain data about individual loss-mechanisms and specific cell behaviour. The ASC-SOFCs were also used to scrutinize the degradation mechanisms based on carbon deposits, and to develop new strategies for carbon removal that both protect the cell and contribute to the regeneration of the cell performance.

As mentioned above, the anode-supported SOFC single cells have dimensions of $10\times10\,cm^2$. The anode substrate was a porous Ni-YSZ, and is between 200 μm and 500 μm thick. An anode functional layer (Ni/ZrO_2 with a thickness of approximately 10 μm) is applied directly onto the anode. The cathode functional layer, consisting of lanthanum strontium cobalt ferrite (LSCF), is approximately 30 μm thick with an active surface of 81 cm^2. The barrier layer, which is cerium oxide (CeO_2) of approximately 5 μm in thickness, was added between the cathode and the electrolyte as a buffer layer in order to inhibit chemical reactions between the cathode and the electrolyte materials. The geometry of the four ceramic layers stacked in one cell can be seen in Fig. 4.1.

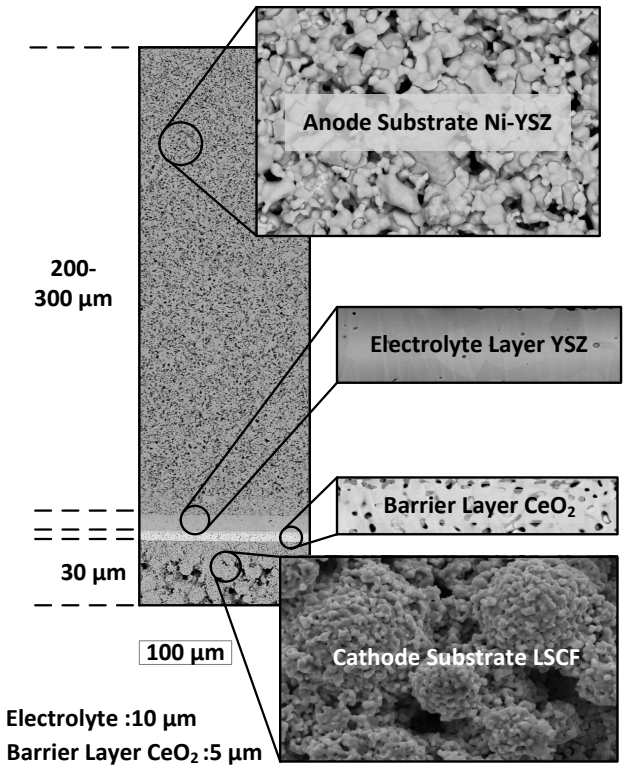

Figure 4.1: Geometry of a tested ASC-SOFC cell. [6]

During this work, two generations of the anode-supported cells were tested. The second generation of ASC-SOFCs used in this work returned results indicating that they were manufactured with and improved cathode. During the experiments with the later generation of SOFCs, significantly higher open circuit voltage was observed, but higher power density was also achievable under the same operating conditions.

4.2 Measurement Setup [1]

The test rig assembly used for the experimental investigations under ambient air pressure is shown in Fig. 4.2. A gas control system was equipped with 8 separate mass flow controllers (MFCs), which enabled the generation of various synthetic gas mixtures. The fuel mixture for the anode supply was produced by mixing pure gas component: N_2, H_2, CO, CO_2 and CH_4. A humidifier system based on the water bubbler principle was used for the humidification of the anode gas mixtures, whereby CO_2 was bypassed. Carbon dioxide was mixed together with the supplementary gases just after the humidifier in order to prevent carbon dioxide absorption through water. In case of emergency, if the gas supply was

[1] Segments of this section have already been published in [4--7].

interrupted, the cell would be flushed with a purge gas containing 5 vol% H_2 in N_2, in order to prevent the possible degradation, such as nickel reoxidation. One further MFC was installed for the regeneration gas mixture composed of O_2, CO_2 and N_2. The cathode side was fed with dry synthetic air via a separate air-line throughout the whole experiment. Both the fuel and air flow along the cell, in co-flow conditions.

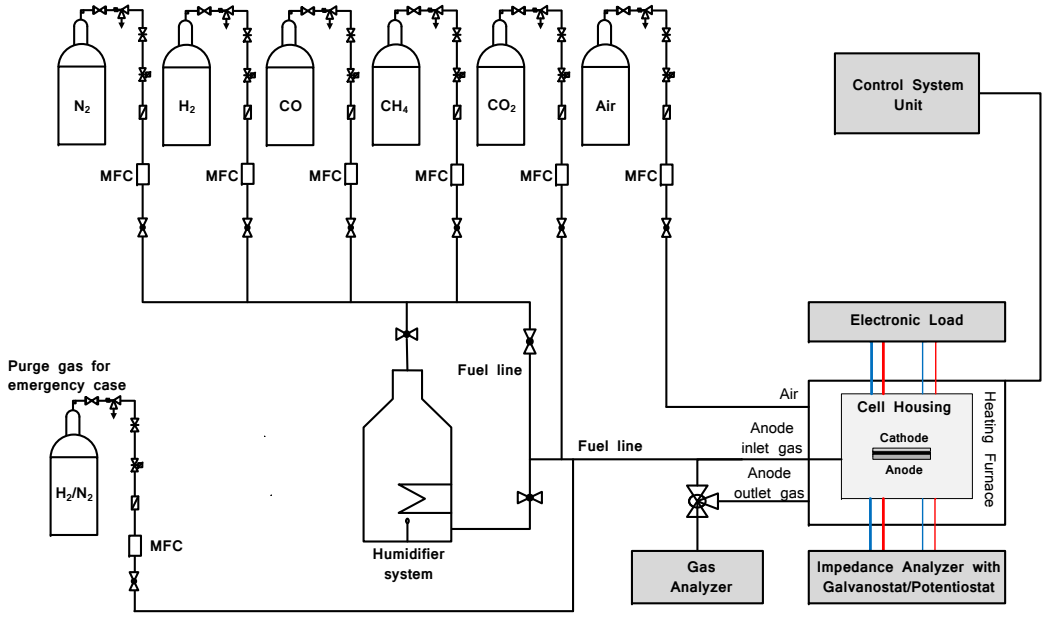

Figure 4.2: Test Rig. [7]

The cells analysed were embedded in alumina cell housing, appropriate for the testing of large area (10x10 cm^2) planar solid oxide fuel cells, which is shown in the style of the exploded-drawing in Fig. 4.3. The figure on the left-hand side depicts the front-view of the cell-housing positioned in the furnace, while the figure on the right-hand side shows the side-profile of the same housing. The anode side was contacted with nickel meshes. There are several reasons for using Ni as a current collector on the fuel electrode. First, the anode contains Ni as electron conductor with great catalytic performances. Second, Ni is relatively affordable compared to the noble metals. Third, two studies were identified, in which it was claimed that noble material such as platinum is a Ni-catcher because of the formation of Ni-Pt alloy on the platinum electrode after long-term operation, see Refs. [151, 152]. This phenomenon caused strong platinum degradation, and disqualified it for further application. Platinum was used to contact the cathode side because of its high catalytic activity, in addition to its very good chemical and electrochemical stability in oxidizing atmosphere and at high operating temperatures. For the same reason, the current and voltage supply wires were made from platinum. Four-wire sensing was applied in order to eliminate the lead

and contact resistance during the measurement process, as well as any drop in voltage due to the supply wires, thus enabling the accurate measurement of the low cell voltages. The same practice was used during the electrochemical impedance spectroscopy measurements to obtain accurate results.

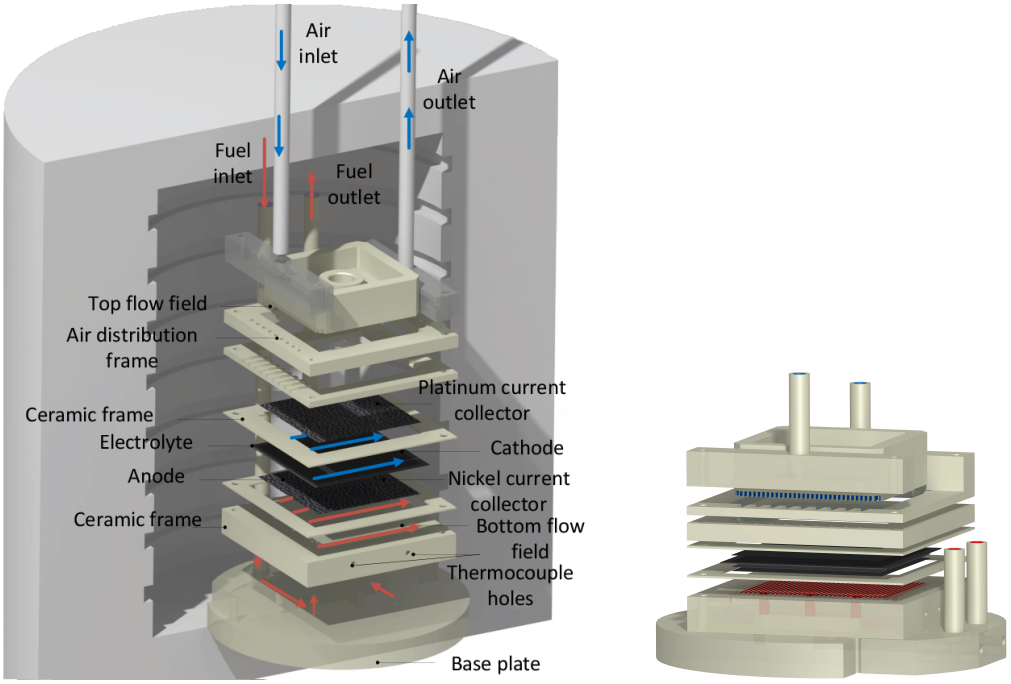

Figure 4.3: Ceramic cell housing.

The anode and the cathode gas chambers were separated from each other by a glass-ceramic sealant, thus minimizing leakage and undesired reactions on the electrodes.

4.2.1 Heating Procedure and NiO-reduction

After assembling the cell in the cell housing, it is necessary to perform the appropriate start-up procedure, which includes the controlled heating of the cell, while purging it, as appropriate with nitrogen. With regard to the thermal expansion coefficient of the aluminium oxide, of which the complete cell housing was made, the temperature gradient was not higher than 1 K/min. The temperature was taken via two thermocouples in the furnace, five thermocouples in the ceramic anode plate, which actually present the temperature distribution across the anode surface as well as two further thermocouples for the fuel inlet and fuel outlet. Taking the sealing schedule into account, the glass-ceramic sealant and the cell were heated from their respective ambient temperatures, up to 850°C, and then cooled down to 810°C. After the sealing procedure was finished, the operating temperature was set. According to the manufacturer, the optimal operating temperature

for the ASC-SOFC cells employed is defined as 800°C. At this temperature, nickel-oxide on the anode was also reduced. Because of large catalyst surface, the reduction process was time-consuming. It was performed under hydrogen, by slowly increasing the volume fraction of hydrogen in nitrogen. Initially, the anode was exposed to 5 vol% H_2 for 3 h, 10 vol% H_2 for 2 h and 20 vol% H_2 for 2 h. Finally, the anode was held in 45 vol% H_2 for 10 h. Throughout the anode reduction, the cathode side was supplied with dry synthetic air ($\vartheta_{O_2} = 20\,vol\%$, $\vartheta_{N_2} = 80\,vol\%$).

4.2.2 Operating Temperature and Gas Mixtures

Various operating conditions were applied in order to fulfil the objectives of this work; these objectives include carrying out a detailed electrochemical analysis in order to distinguish between single electrodes as well as the processes and loss mechanisms involved in carbon deposition and removal. Furthermore, this work aims to develop innovative strategies for the removal of carbon deposits in ways that protect the cell and promote performance regeneration. The electrochemical characterization tests were carried out in the temperature range between 750°C and 850°C, whereby several regeneration methods were applied between 500°C and 850°C.
The volume flow rate on the anode side was set to 2.4 SLPM, whereas the volume flow on the cathode side was varied between 2 SLPM and 5 SLPM. The volume flow on the air electrode was varied to obtain the data required for examination via electrochemical impedance spectroscopy. Most of the measurements were taken by supplying the cathode with 4 SLPM: therefore, the carbon deposition experiments were executed under this condition as well. At this stage, it is important to mention that a dry gas mixture of 45 vol% hydrogen in nitrogen was used for the reference measurements. Varying the concentration of H_2 and N_2 in a gas mixture made it possible to gain detailed insight into the nitrogen's impact on the cell performance. Additionally, the experiments scrutinized the influence of water vapour in the gas mixture on the cell performance as well as the determination of the activation losses depending on the single reagent and product components in the fuel mixture. In order to simulate real operating conditions, the cell was fuelled with a diesel reformate mixture. Conditions under which carbon can be formed were thus generated; the fuel mixtures used can be seen in Tab. 4.1.

4.2.3 Carbon Build-up and Deposition

As stated above, the phenomenon of carbon deposition was investigated during operation with carbon-containing fuels. For this purpose synthetic reformates were used, with the composition that would be expected and measured in auxiliary power units fuelled with diesel and modified diesel reformates, see Tab. 4.1. In order to obtain information about

cell performance degradation, such as critical operating times or degradation voltage, with the added benefit of accelerating the degradation phenomenon, the methane volume fraction in the fuel mixture used was varied between 2.3 vol% (as expected and measured in APUs), 9 vol%, 14 vol% and 20 vol%. The choice to vary the amount of methane was made because methane cracking is favored at high operating temperatures, whilst carbon formation by means of the Boudouard-reaction is not expected to be prominent at the operating temperature in question here. The theoretical background to the reactions (for example equilibrium calculations) is introduced in Chapter 3, in addition to the calculations for carbon predictions.

Table 4.1: Diesel reformate mixtures.

Species	H_2	CO	CO_2	CH_4	H_2O	N_2	S/C
Unit	vol%	vol%	vol%	vol%	vol%	vol%	-
$\boldsymbol{DR}_{2.3}$	15.4	13.7	9.8	2.3	11	47.8	0.7
$\boldsymbol{DR}_{9}$	15.4	13.7	9.8	9	11	41.1	0.5
$\boldsymbol{DR}_{14}$	15.4	13.7	9.8	14	11	36.1	0.4
$\boldsymbol{DR}_{20.3}$	15.4	13.7	9.8	20.3	11	29.8	0.3

4.2.4 Carbon Removal

A number of strategies were examined experimentally in order to find the best and most effective solution for technical application. The removal of solid carbon from the anode surface as well as the removal of gaseous products from the porous zone must be favourable under the applied operating conditions. For this purpose, the regeneration strategies introduced were based on two principles: (1) regeneration with the aid of possible gasification agents, and (2) electrochemical methods that represent the application of an external power source or power consumers that polarize the cell up to the required state. The parameters set during the regeneration process can be found in Tab. 4.2.

The regeneration approach, based on the application of gaseous species, was to combine the possible reaction paths with one another, according to equations shown in Chapter 3. Approaches $\boldsymbol{R}_1$ and $\boldsymbol{R}_2$ are based on catalytic gasification of solid carbon deposits by hydrogen and water vapour. The impact of both dry hydrogen and humidified hydrogen on the carbon removal process was examined. Pure water vapour was not used for the purpose of carbon removal because it can induce fast Ni-reoxidation, thus leading to the mechanical damage of the cells investigated. Nevertheless, in order to determine how a variety of concentrations of water vapour in a regeneration gas mixture impact the regeneration time,

the volume fraction of water vapour was increased in $\boldsymbol{R}_{2var}$. The critical concentration of H_2O in a defined regeneration gas mixture, which can lead to the reoxidation of Ni catalyst, was thus provided.

The removal of deposits was also studied using carbon dioxide as a gasification agent, which is presented as regeneration approach $\boldsymbol{R}_4$ in Tab. 4.2. The idea behind this strategy was the direct reaction of carbon with CO_2 by means of the Boudouard-reaction. Next, in order to prevent Ni-oxidation, CO_2 was mixed together with H_2 as well as H_2 and H_2O. All of the combinations with CO_2 are referred to as $\boldsymbol{R}_4$.

Conventional regeneration methods, based on pure gasification using gasification agents, were extended by means of innovative approaches, referred to within this work as electrochemical methods. The electrochemical methods based on current and voltage are mainly combined with various gas mixtures in an effort to meet the regeneration requirements. According to Eq. 3.13, the current is directly proportional to the oxygen current, thus accelerating oxygen transport through the anode, and, consequently carbon oxidation. The regeneration approach $\boldsymbol{R}_3$ specifies the gas mixture H_2/N_2 be applied on the polarized cell for the purpose of removing carbon from the porous anode and thereby regenerating cell performance. Both the current density and the operating time under the set current density were varied, in order to determine the optimal operating conditions.

In terms of electrochemical regeneration, the second option explored in this work is the application of overvoltage to the cell under operation, which constitutes a novel strategy for regeneration. This approach is also referred to as $\boldsymbol{R}_3$. In this sense, overvoltage represents the external voltage applied to the cell, thus theoretically leading the cell into the electrolysis mode. The overvoltage applied protects the cell from degradation on multiple levels. Elementary oxygen, especially near the electrolyte, removes carbon deposits and forces the desorption of gaseous species, preventing their further adsorption. Next, Ni-oxidation potential is significantly decreased thanks to the overvoltage applied, which moves oxygen and oxygenated species away from the catalyst surface. However, the regeneration strategies developed must meet the criterion set out for this work, of complete carbon removal in such a way as to both protect the cell and restore its performance. At the same time as the overvoltage was applied, the gas supply to both the anode and the cathode side was altered. Generally, three variants of the mentioned regeneration strategy were scrutinized in this work. Firstly, the gas supply both on the anode and the cathode was interrupted. Afterwards, the anode was supplied with a regeneration gas mixture as seen in strategy $\boldsymbol{R}_2$ while the cathode side was supplied with synthetic air. Secondly, only the cathode side was supplied with the synthetic air, while the anode side was not fuelled. Thirdly, the anode was

supplied with CO_2 for the purpose of carbon gasification, and the protecting overvoltage was applied to prevent damage to the microstructure and performance degradation. This method is specified as R_{4ov}.

The last method used to induce carbon removal included fuelling the anode with an oxygen-enriched gas mixture. It is referred to as $\boldsymbol{R}_{5var}$ in Tab. 4.2. Since oxygen is often used as a gasification agent in industrial settings, the possibility of using it in the SOFC-field was scrutinized in this thesis.

Table 4.2: Regeneration approaches.

	Parameters	Value	Unit
Regeneration approach $\boldsymbol{R}_1$			
	H_2	45	vol%
	N_2	55	vol%
Regeneration approach $\boldsymbol{R}_2$			
	H_2	45	vol%
	H_2O	11	vol%
	N_2	44	vol%
Regeneration approach $\boldsymbol{R}_{2var}$			
	H_2	30 vs. 45	vol%
	H_2O	variable	vol%
	N_2	rest	vol%
Regeneration approach $\boldsymbol{R}_3$			
	i	variable	mA/cm^2
	U	variable	V
	H_2	variable	vol%
	N_2	rest	vol%
Regeneration approach $\boldsymbol{R}_4$			
	CO_2	variable	vol%
	H_2	variable	vol%
	H_2O	variable	vol%
	N_2	rest	vol%
Regeneration approach $\boldsymbol{R}_{4ov}$			
	CO_2	25	vol%
	N_2	75	vol%
	U	1.4	V
Regeneration approach $\boldsymbol{R}_{5var}$			
	O_2	2 vs. 0.5	vol%
	CO_2	18.9 vs. 4.7	vol%
	N_2	rest	vol%

To examine the effects of individual carbon gasification methods and to determine the most suitable method for commercial applications, the regeneration strategies described

were applied to several cells. The strategy selected was carried out numerous times for each cell, so as to ensure its reproducibility. For the same purpose, the experiments were extended, and the efficiency of the strategy was tested on cells covered with carbon formed via exposure to four different carbon-containing fuel mixtures, as represented in Tab. 4.1. By this means, it was possible to establish whether the method was universally applicable. More information on the effects of the individual regeneration methods with regard to carbon removal and the restoration of performance can be found in Chapter 6.

4.3 Fuel Cell Characterization

Performing a complete analysis of cell behaviour using sophisticated characterization techniques makes it possible to gain deeper insight into cell performance, and, furthermore, enables differentiation between involved processes and loss mechanisms. This section describes the characterization techniques used for the experiments carried out in the present work.

4.3.1 Electrochemical Analysis [2]

The polarization curve was measured using an electronic load (TrueDatal-Load) from FuelCon, on a four-wire sensing principle, [153]. The measurements were carried out with the current density step of 10 $\frac{mA}{cm^2}$. The low limit for the cell voltage was defined as 0.7 V, in order to prevent Ni-reoxidation and to ensure stable operation over the whole load range. The general problem of Ni-oxidation under SOFC-operating conditions depending of the operating voltage was found in several references. Koch et al. [154] studied the performance of the cell under different operating conditions and concluded that a critical cell voltage exists. They suggested a limit in the proximity of 0.7 V at 850°C and 0.75 V at 750°C. Below these values, fast cell degradation was observed. In their study, the critical voltage is near the Nernst-voltage for Ni-oxidation, and, therefore they suggested investigating the correlation with Ni-oxidation. Frank [155] showed the degradation of the cell performance after nickel oxidation, which is explained by operation below the critical voltage. This critical Nernst voltage can be calculated using the oxygen partial pressure for the nickel oxidation equilibrium equation (Eq. 4.1), with the equilibrium constant $K_{NiO} = \frac{1}{p_{O_2}^{1/2}}$, which can be calculated as shown in Eq. 4.2. By combing these two equations, the minimum oxygen partial pressure for Ni-oxidation can be calculated. The use of these values in the Nernst equation (Eq. 4.3) makes it possible to determine the critical voltage, below which

[2] Segments of this section have already been published in [4].

nickel can be oxidized, due to the high oxygen partial pressure in the anode gas (Eq. 4.4). Frank proved that this critical voltage is 0.7 V at 850°C. [4]

$$Ni + \frac{1}{2}O_2 \rightarrow NiO \tag{4.1}$$

$$K_{NiO} = exp(-\frac{\Delta G}{R \cdot T}) \tag{4.2}$$

$$U_{nernst} = \frac{R \cdot T}{2 \cdot n^{el} \cdot F} ln(\frac{p_{O_{2,cathode}}}{p_{O_{2,anode}}}) \tag{4.3}$$

$$U_{nernst,NiO} = \frac{R \cdot T}{2 \cdot n^{el} \cdot F} ln\Big(p_{O_{2,cathode}} \cdot \big(exp(-\frac{\Delta G}{R \cdot T})\big)^2\Big) \tag{4.4}$$

Impedance measurements were carried out by means of a Bio-Logic impedance analyzer with a 80 A booster at OCV and under load in a frequency range from 10 kHz to 100 mHz, [156--158]. In order to analyse the performance of the polarized cells, the DC galvanostatic technique was applied, and an AC sinusoidal current was superimposed on the DC-offset current. The AC current amplitude was varied between of 10 mA and 80 mA peak-to peak so as to obtain the optimal signal values. For the purpose of this measurement, the aim is to cause the minimal perturbation of the fuel cell system and to reduce the number of errors occurring due to the performed measurements, thus retaining the linearity of the system under investigation. An in-situ electrochemical impedance spectroscopy method was used to investigate the impact of different parameters on the cell behaviour, such as partial pressure of single gas components, flow rate or humidity on anode side.

In order to separate the single processes, DRT-analysis by means of a Tikhonov regularisation was performed. A MATLAB toolbox, DRTTOOLS for computing distribution relaxation times, developed by Wan et. al [84], was used to analyse the measured impedance spectra. To obtain reliable data, impedance measurements were performed with 40 points per decade. The regularisation parameter was set to 10^{-4}. In their study, Sonn et al. [159] set the regularisation parameter to between 10^{-4} and 10^{-5}; they started from a high initial value for this parameter and decreased it until no systematic deviations were determined in the residuals obtained. The same procedure was applied in this thesis.

4.3.2 Gas Analysis

Gas analysis is a useful tool for determining the reactions that occur as well as the catalytic features of the cell. During the experiments performed, the concentrations of both the fuel at the anode inlet and the off-gas at the anode outlet were measured with an ABB gas analyser (ABB Advanced Optima 2005), [160]. The gas analyser used contained two

modules, Uras 14 and Caldos 17, for measuring H_2, CO, CO_2, O_2 and CH_4. The module Caldos 17 was responsible for hydrogen detection. This measurement technique is based on the thermal conductivity of the specific gases since the detector represents a thermal conductivity sensor. Uras 14 enables the detection of other gaseous components mentioned. It is based on two different principles: electrochemical cell for O_2 and non dispersive infrared detector (NDIR) for CO, CO_2 and CH_4. In addition to these components, the gas analyser further consists of a gas cooling unit and a gas pump. The gas cooling unit cools the measured gas at the entry down to approximately 2°C to avoid the condensation of water vapour in the downstream pipes and detectors. The measured gas concentrations are thus a depiction of the dry gas concentrations.

4.3.3 Post-Mortem Analysis

The post-mortem analysis of the cell microstructure is among the most important ex-situ characterization techniques, and contributes significantly to the correct evaluation of the measured results and interpretation of the cell performance. The data obtained regarding the catalyst, pore, and boundary layer microstructure provides information about the specific degradation effects and the degradation rates after fuelling with carbon-containing fuels as well as about the reversibility of those effects. Furthermore, the quality of the carbon removal and regeneration strategies applied can be evaluated.
The microscopic examination of the cell's surface and the cross-section view were both performed using a Zeiss Ultra 55 field emission scanning electron microscope (FE-SEM). The cell analysis was unobstructed, since no coating of the cell was necessary. The chemical characterization of the sample tested and detection of deposited carbon was carried out using energy-dispersive X-ray spectroscopy (EDX). The detailed examination of the microstructure of the carbon deposits was achieved by means of Raman spectroscopy, using a spectrometer Bruker ''EQUINOX 55'' and Bruker ''HYPERION 3000'' I-microsope.

5 Electrochemical Analysis of the SOFC

Failure modes such as carbon deposition must be avoided or controlled in order to ensure the safe operation of auxiliary power units running on diesel reformate or other carbon-containing fuels, [8]. Combined with the DRT method, electrochemical impedance spectroscopy technology and methodology is a promising technique for investigating the critical operating conditions for SOFC, and it plays a significant role in online monitoring. In this chapter, the sample anode-supported solid oxide fuel cells for industrial application are analysed and characterised with the aim of isolating anode processes and enabling the fast detection of carbon depositions. Different process mechanisms are successfully separated, and a detailed in-situ electrochemical analysis of the system under investigation is carried out. [8]

5.1 Validation of the Electrochemical SOFC-system and Process Identification [1]

Several requirements must be fulfilled in order to ensure the quality of the measurements performed; these include steady state, causality, linearity and time-invariance [73, 76]. Different fuel mixtures (as specified in Tab. 5.1) were used to supply the anode, in order to ensure that the required criteria were satisfied, and, for the purpose of the explicit electrochemical analysis, determination of single processes and separation of specific electrodes.

First, the amount of hydrogen in nitrogen was increased from 25 vol% to 100 vol% (a_{25-100}) in a constant gas mixture volume flow of 2.4 SLPM. The impact of the fuel dilution in nitrogen on the cell performance and the losses that occurred can thus be detected. Secondly, the amount of water vapour in a mixture of 45 vol% H_2 in N_2 was varied between 2.5 vol% and 11 vol%, in order to examine which changes could be observed. The fuel mixtures

[1] Segments of this section have already been published in [8].

mentioned are specified as $b_{2.5-11}$. Furthermore, the number of fuel components in a fuel mixture was increased. For this purpose, CO was added to a gas mixture $\boldsymbol{d}_{10}$, consisting of 25 vol% H_2 and 10 vol% H_2O in N_2, representing a mixture $\boldsymbol{c}$. Finally, the cell was supplied with different diesel reformate mixtures, specified as $\boldsymbol{e}_{2.5-9.5}$ in Tab. 5.1, which included three fuel components altogether - H_2, CO, and CH_4. The examinations were performed in a temperature range between 700°C and 800°C.

Table 5.1: Volume fraction of single gas components.

Gas mixture	H_2 vol%	CO vol%	CO_2 vol%	CH_4 vol%	H_2O vol%	N_2 vol%
$\boldsymbol{a}_{25-100}$	25-100	0	0	0	0	0-75
$\boldsymbol{b}_{2.5-11}$	45	0	0	0	2.5-11	44-52.5
$\boldsymbol{c}$	25	5	0	0	10	60
$\boldsymbol{d}_{10}$	25	0	0	0	10	65
$\boldsymbol{e}_{2.5-9.5}$	15.4	13.7	9.8	2.5-9.5	11	22.8-29.8

The fundamental requirements for an analysis of EIS data are steady state measurements performed while the working electrode is stable. These measurements were performed after the cell was in equilibrium in order to achieve a steady state after changing the operating conditions. Equilibrium was determined by monitoring the voltage and composition of all gas components. The measured voltage response was directly correlated to the sinusoidal waveform current input signal applied, thus fulfilling the causality criterion. The linearity requirement was satisfied for this case in that the amplitude of the input signal was small enough to result in the pseudo-linear output signal, and the measurements were performed in the linear part of the polarization curve, which excludes consideration of the concentration loss zones. In this work, a comparison of the electrochemical impedance spectra measured for various input amplitudes is made in order to prove the linearity criterion. The spectrum for all applied signal perturbation for such cases should be constant and free from significant deviations, [52, 76]. In summary, the impedance data of the system under investigation remains unchanged and independent from the size of the applied input amplitude, as long as the linearity criterion is fulfilled. All of the measurements were carried out several times during one experiment, and the same procedure was performed on a number of cells in order to ensure accurate, repeatable, and reproducible measurements.

The linearity requirement was satisfied for the cells investigated, as can be seen in Fig. 5.1a, which shows that the Nyquist plot did not change, whether 40 mA (blue line), 50 mA (green line), 60 mA (violet line), 70 mA (gray line) or 80 mA (black line) were used as the

input amplitude. It is important to note that Nyquist diagrams should always be plotted with abscissa and ordinates equal in size so as to graphically verify if the cell investigated represents the ideal connection of capacitance and ohmic resistance, or if it rather acts as a circuit of other electrochemical components. The same effect as seen in Fig. 5.1a is presented in the form of the Bode-plot in Fig. 5.1b, which represents an impedance magnitude as a function of the frequency. Fig. 5.1c illustrates the DRT-spectra calculated using the observed impedance data. DRT is calculated as a function of relaxation times, thus referring to the time constants of specific transport and kinetic mechanisms. The DRT-spectra seen here overlap, thus confirming the linearity criterion. The significance of the individual peaks will be discussed below.

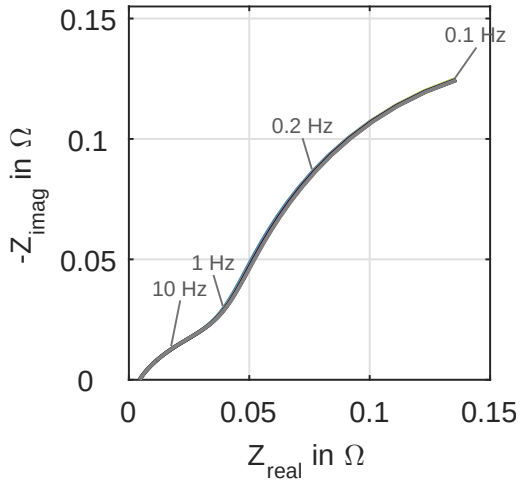

(a) Nyquist plots for varied amplitudes at OCV

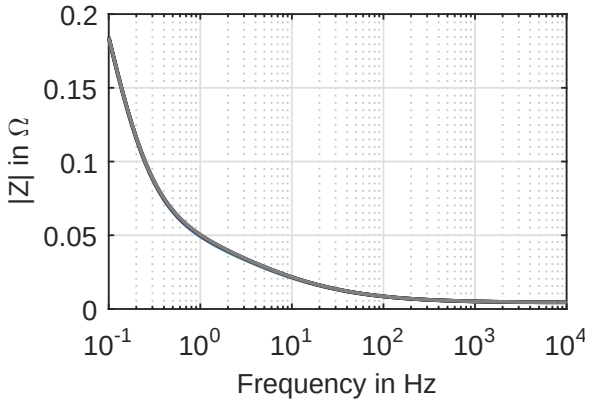

(b) Bode plot for varied amplitudes at OCV

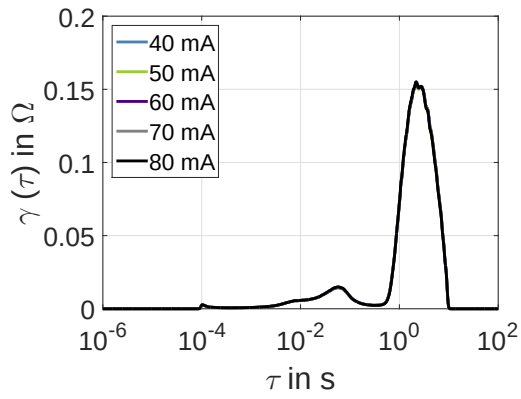

(c) DRT spectra for varied amplitudes at OCV

Figure 5.1: Linearity criterion for AC-amplitudes of 40 mA (—), 50 mA (—), 60 mA (—), 70 mA (—) and 80 mA (—) at OCV for validation of the investigated SOFC-system operated under gas mixture a_{45}.

In order to evaluate the performance of the investigated fuel cells and to be able to compare the results obtained during the total operating time, the next basic requirement for mean-

ingful measurements is time-invariance. The output signal of a time-invariant system does not depend on time, and can be demonstrated by Eq. 5.1 with the constant a.

$$y(t) = a \cdot x(t) \tag{5.1}$$

A fuel cell system needs to be operated with fuels under which equilibrium can be reached, if the time-invariance is questionable. If the operating conditions cause a change from the initial state, for example, if the cell is fed with a carbon-containing fuel under carbon-formation conditions - only fast measurements, rather than long-term measurements, must be carried out, for the purpose of proving time-invariance. Fig. 5.2 compares the impedance data plots measured while feeding the cell with gas mixture $\boldsymbol{a}_{45}$ under open circuit conditions over a time span of 5 hours. As can be seen in this figure, even after five-hours of operation (grey solid line), the cell performances, represented by the Bode- and phase plots, remained unchanged compared to their initial state (black solid line), thus confirming the time-invariance criterion.

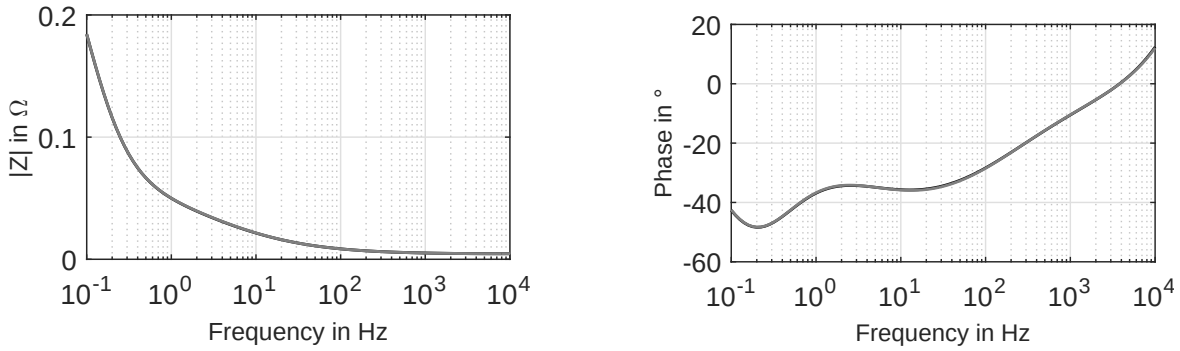

(a) Bode plot (b) Phase plot

Figure 5.2: Time invariance criterion examined for the gas mixtures a_{45} at 800°C under OCV operating conditions: Initial measurement (—), Measurement after 5 h (—). [8]

5.2 Equivalent Circuit Analysis [2]

The processes that occur in a fuel cell can be described with equivalent electrical circuit models. Initially, the SOFC-system is under investigation as an unknown system, and impedance spectra are measured and plotted. Subsequently, the data obtained are fitted to equivalent circuit models using a combination of several elements, such as resistors, capacitors, inductors, and less simple elements, such as constant-phase elements or Warburg impedances, as described in Section 2.4.2. Specific circuit elements indicate particular cell processes, including reaction kinetics, loss processes, or physical characteristics of the cell electrodes and the electrolyte. Certain equivalent circuits were constructed in order to

[2]Segments of this section have already been published in [8].

determine which processes become dominant as a function of the operating conditions and the elements used. The relevant equivalent circuits used for the fit procedure are RL-RC-RC (Fig. 5.3a), RL-RC-RQ (Fig. 5.3b) and RL-RQ-RQ (Fig. 5.3c). The electrical components used are R as resistor, L as inductor, C as capacitor and Q as constant phase element. More complicated ECs including elements such as the Gerischer element and a Warburg impedance, in combination with the elements already mentioned, as used in [161], showed poor fit quality when evaluated in terms of the very high relative error frequency between the measured data and the fit plots. For this reason, they were deemed to be inappropriate for the analysis of the planar industrial-sized, anode-supported SOFCs used in this work.

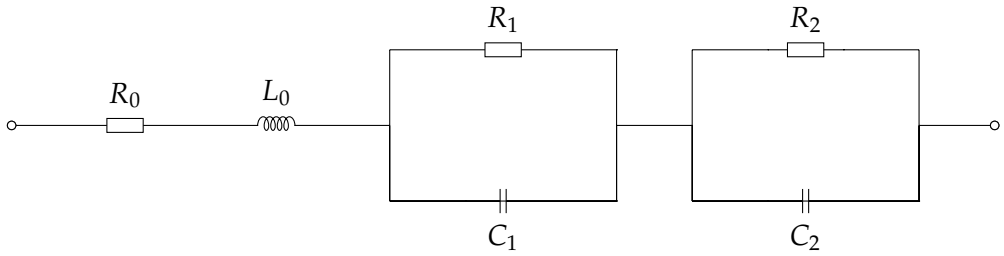

(a) Equivalent electrical circuit RL-RC-RC

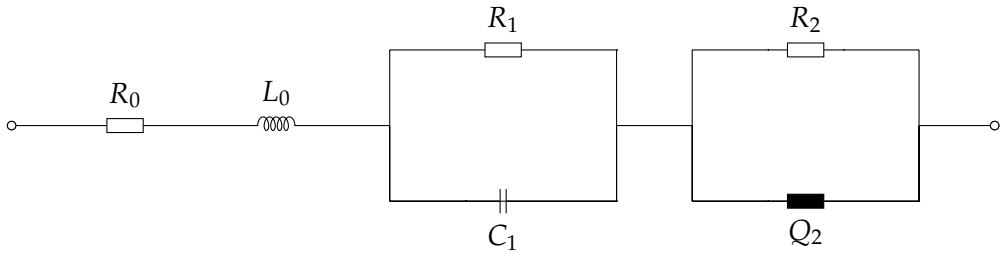

(b) Equivalent electrical circuit RL-RC-RQ

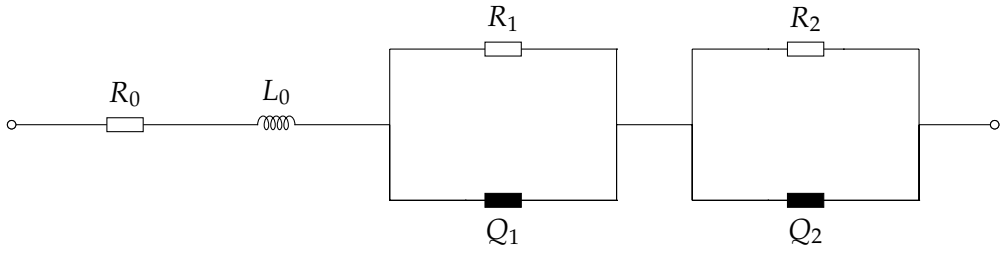

(c) Equivalent electrical circuit RL-RQ-RQ

Figure 5.3: Comparison of various equivalent electrical circuits. [8]

Figs. 5.4a, 5.4b, 5.4e and 5.4f illustrate different equivalent circuits used to analyse the cell operated under gas mixtures $\boldsymbol{a}_{25}$ and $\boldsymbol{d}_{10}$. Single blue points depict the measured plots, which are compared to the fit plots based on the three equivalent circuits already mentioned. The simplest equivalent circuit, RL-RC-RC, is indicated by a dashed violet line; the yellow dashed line depicts RL-RC-RQ, while the plots fitted using RL-RQ-RQ are indicated by a solid red line. Data contained within these figures are measured at OCV (Figs. 5.4a) and

150 $\frac{mA}{cm^2}$ (Figs. 5.4b) for gas mixture $\boldsymbol{a}_{25}$ and at OCV (Figs. 5.4e) and 100 $\frac{mA}{cm^2}$ (Figs. 5.4f) for gas mixture $\boldsymbol{d}_{10}$. The cell structure (which is made up of a porous two-phase composite Ni-YSZ anode layer containing the ionic- and the electronic-phase, the ionic YSZ electrolyte layer and a LSCF cathode layer with good electronic and ionic conductivity) does not validate the results obtained for the RL-RC-RC equivalent electrical circuit, independent of the operating conditions. This electrical circuit only depicts a simple capacitor consisting of two electrical conductive plates without porous structure, and therefore does not generate representative impedance plots for the cells used. Moreover, if the cell is operated under dry fuel conditions (such as in Figs.5.4a-5.4d) no difference exists between the measured values and the values fitted using the RL-RC-RQ and RL-RQ-RQ equivalent circuits. This difference only becomes obvious when the cell is fed with humidified fuel. In this case, the characteristics of the porous two-phase electrode layer of both the anode and the cathode takes on greater significance, thus establishing the chemical and physical properties of the system.

Selecting the correct equivalent circuit is important because the fitted circuit elements are used for the exact calculation of the single loss mechanisms. This is made possible by calculating the polarization curves based on ohmic resistance values observed through the fit process. First, different electrochemical circuits are used to find the best fit approach. On the basis of a comparison between the measured and the calculated curves, the optimal strategy can be determined, as indicated in Figs. 5.4b and 5.4f. Second, the chosen calculation method can be a further criterion for checking the accuracy of the fitting process used, as shown in Figs. 5.4d and 5.4h. Polarization curves calculated using different methods - the Euler implicit numerical integration (dashed red line), Euler explicit numerical integration (dashed yellow line) and trapezoidal function both in simple form (dashed violet line) and also fitted (green solid line) are shown in Figs. 5.4c and 5.4g. The four approaches used for the numerical analysis of the fit values to find the appropriate solution for the polarization curve were implemented in MATLAB. The approaches used are specified in Euler explicit or forward method (Eq. 5.2), Euler implicit or backward method (Eq. 5.3), and as trapezoidal rule (Eq. 5.4)):

$$\left(\frac{dy}{dt}\right)_k \approx \frac{y_{k+1} - y_k}{\Delta t} = -y_k^2 \tag{5.2}$$

$$\frac{y_{k+1} - y_k}{\Delta t} = -y_{k+1}^2 \tag{5.3}$$

$$\int_a^b y(x)dx = (b-a) \cdot \frac{y(a) + y(b)}{2} \tag{5.4}$$

where y_k is the actual value for each $k = 0, 1, ..., n$, y_{k+1} is the unknown value and Δt is time (or other variable) step. When using Euler explicit or forward method, the shown equation is explicit for y_{k+1}. In the Euler implicit or backward method, the implicit equation is given to find the solution for y_{k+1}. In the specific case for calculation of the polarization curve in this thesis, y gives the voltage and Δt gives the current steps, a and b are defined limit values. Since the impedance measurements, performed at different currents, give values for Ohmic resistance, the voltage is calculated for the purpose of numerical integration using the Ohmic law.

Compared to the measured values, the most appropriate and correct calculation method - the fitted trapezoidal function, which showed almost no discrepancy from the real curve - was chosen for the subsequent calculations. This strategy exhibited the smallest deviation from the measured values - of only 0.7 % while the discrepancy for the Euler explicit numerical integration method or forward integration amounted to as much as 5 %, when the cell was operated with the gas mixture $\boldsymbol{a}_{25}$, which does not contain water vapour. The Euler implicit numerical integration or backward integration gave better results compared to forward integration, but was still clearly inferior to the trapezoidal function. If a gas mixture contained water vapour the disagreement in the fitted values using these two methods can be neglected, as can be seen in Figs. 5.4g and 5.4h. The difference between the polarization curves for operation under humidified gas and water-free gas mixture is recognizable in the range of low current densities and may be explained by the combined effect of the Nernst voltage (Eq. 2.20) and the activation losses (Eq. 2.25). The partial pressure of water in the gas mixture used has a significant impact on the Nernst voltage, whereby the increasing amount of water vapour brings the polarization curve to the linear range. Both the measured U/i-curve (in Figs. 5.4c and 5.4d) and the electrochemical impedance spectra of the cell fuelled with dry hydrogen show that high activation losses occurred because dry hydrogen oxidizes with a large overpotential, [57]. Under low loads, a very small amount of water can be produced, which means that the activation overpotential for dry fuels is significantly higher than at higher current densities. If the cell is fed with a pre-humidified gas mixture, the product water is available, even under open circuit conditions, which considerably reduces the reaction rate [141], thus reducing the observed overpotential losses. As the load increased, the total difference in the available water vapour amount readily increases, and its constant rise is thus shown over the whole load range. However, the open circuit voltage is also lowered for this case because of the greater humidity. Operation with the humidified fuels thus brings the cell within the linear range and makes the applied fitting process far easier. Such a detailed electrochemical investigation and analysis of large planar ASC-SOFCs, using diverse parameters and applying different methods, cannot yet be found in literature.

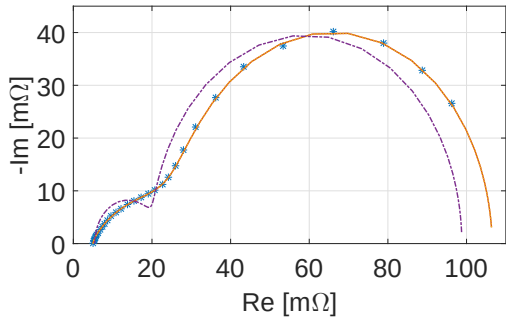

(a) Gas mixture $\boldsymbol{a}_{25}$ at 0 $\frac{mA}{cm^2}$

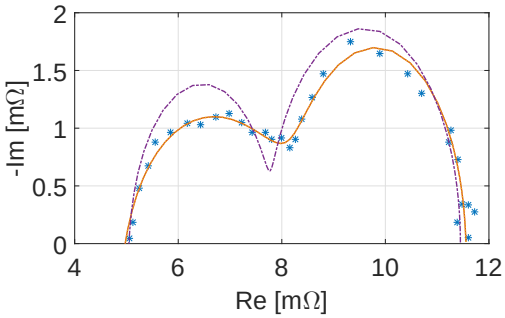

(b) Gas mixture $\boldsymbol{a}_{25}$ at 150 $\frac{mA}{cm^2}$

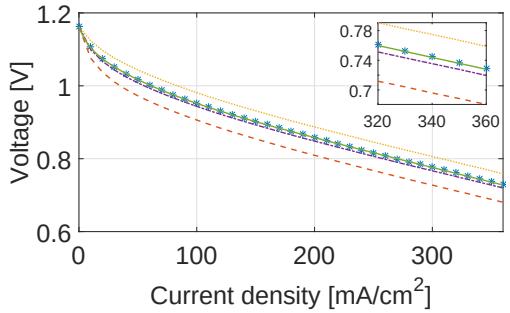

(c) U/i-curve - different integration methods for gas mixture $\boldsymbol{a}_{25}$

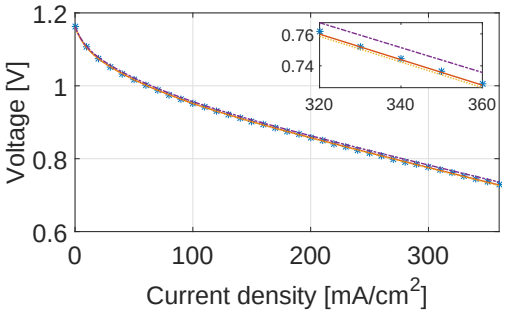

(d) U/i-curve - different equivalent circuits for gas mixture $\boldsymbol{a}_{25}$

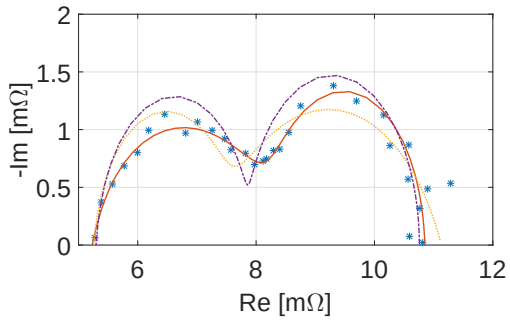

(e) Gas mixture $\boldsymbol{d}_{10}$ at 0 $\frac{mA}{cm^2}$

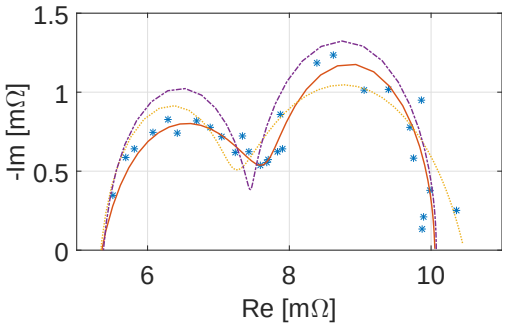

(f) Gas mixture $\boldsymbol{d}_{10}$ at 100 $\frac{mA}{cm^2}$

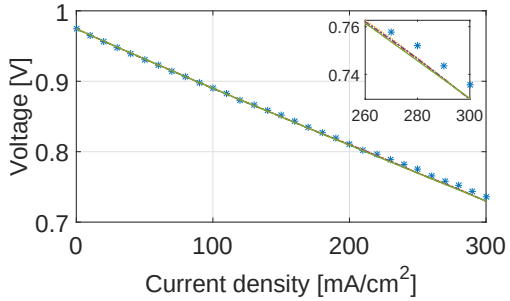

(g) U/i-curve - different integration methods for gas mixture $\boldsymbol{d}_{10}$

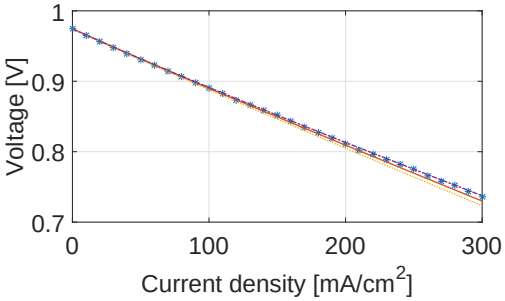

(h) U/i-curve - different equivalent circuits for gas mixture $\boldsymbol{d}_{10}$

Figure 5.4: Comparison of different equivalent circuits and methods for the calculation of the polarization curve for gas mixtures $\boldsymbol{a}_{25}$ and $\boldsymbol{d}_{10}$. *Nyquist plot*: measured values (*), EC RL-RC-RC (--), EC RL-RC-RQ (--), EC RL-RQ-RQ (—). *Polarization curve*: Euler explicit numerical integration (--), Euler implicit numerical integration (--), trapezoidal function (--), fitted trapezoidal function (—). [8]

The polarization curves are calculated not only to analyse the quality of the defined fitting process and the equivalent electrical circuit, but also and, in particular, to determine the specific loss sources, which depend on the electrolyte and the electrodes. These calculated losses represent the ohmic, kinetic, and diffusion losses. Fig. 5.5 separates the losses for operation under dry H_2/N_2 mixture (5.5a) and under humidified gas mixture (5.5b). The difference between the open circuit voltage, indicated by a black solid line, and the overvoltage based on the electrolyte resistance, represented by a red dashed line, indicates the ohmic losses. Furthermore, kinetic losses are represented through the subtraction of the red dashed and the yellow dashed lines, using the fitted R1 and R2 resistances showed in Fig. 5.3c. As described above, these losses become particularly apparent in the range of low current densities, when the cell is operated under dry hydrogen (Fig. 5.5). This effect is not visible if humidified fuel is used (Fig. 5.5b). The area between the yellow dashed line and the violet dashed line, superposed to the measured (blue points) values, represents diffusion overvoltage, caused by mass transfer and concentration losses. As can be seen in this figure, the concentration losses rise with increasing load.

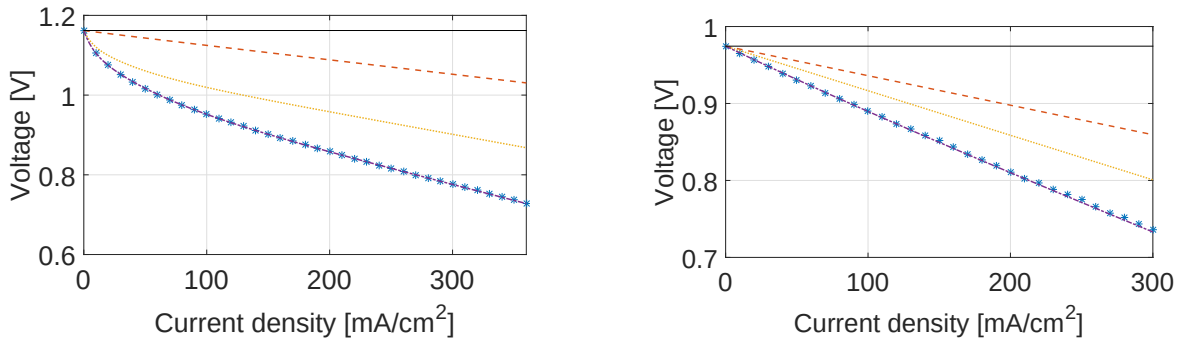

(a) Gas mixture $\boldsymbol{a}_{25}$ (b) Gas mixture $\boldsymbol{d}_{10}$

Figure 5.5: Comparison of overpotentials for the gas mixture $\boldsymbol{a}_{25}$ and the gas mixture $\boldsymbol{d}_{10}$: Nernst voltage (—), overvoltage 1 based on ohmic losses (--), overvoltage 2 based on kinetic losses (--), overvoltage 3 based on concentration losses (--), measured polarization curve (*). [8]

In order to prove the quality of the applied fit mechanism, the relative errors of both the real part (E_{rel} in Eq. 5.5) and the imaginary part (E_{im} in Eq. 5.6) were calculated. The relative errors or residuals (E) calculated for the cells investigated in this thesis are represented in Fig. 5.6. The observed errors are distributed uniformly over the frequency range between 100 mHz and 10 kHz. At frequencies lower than 10^3 Hz, the relative errors both for the real part (indicated by blue plus markers) and imaginary part (red circles) range between 0 % and 1 %, which is regarded as negligible. At higher frequencies, a slight deviation is generated due to cable inductance, thus representing an inductive artefact.

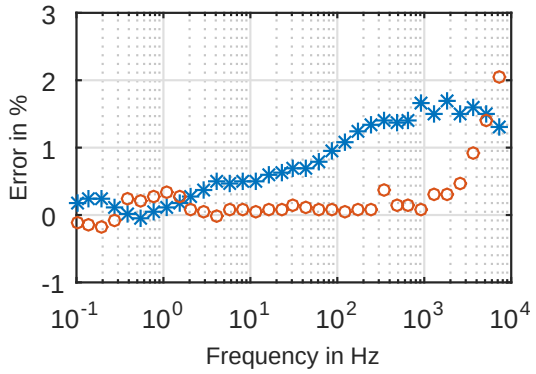

$$E_{rel} = \frac{Z'_{meas,rel} - Z'_{fit,rel}}{|Z(\omega)|} \cdot 100\% \quad (5.5)$$

$$E_{im} = \frac{Z'_{meas,im} - Z'_{fit,im}}{|Z(\omega)|} \cdot 100\% \quad (5.6)$$

Figure 5.6: Relative errors calculated for gas mixture $\boldsymbol{d}_{10}$ at 0 $\frac{mA}{cm^2}$: * - real part, o - imaginary part.

5.3 Fuel Variation

In order to identify the frequency range that best reflects the anode processes, the anode-supported cells tested were operated with various fuels, both humidified and dry (see Table 5.1). Special attention should be paid to the fact that humidity has a great impact on cell performance, and even significantly affects the evaluation of the measured impedance plot data, as shown in the following diagrams.

Fig. 5.7 compares the humidified gas mixtures $\boldsymbol{d}_{10}$ (black solid line), $\boldsymbol{c}$ (grey solid line) and $\boldsymbol{e}_{2.5}$ (blue solid line), in which the number of fuel components on the anode side was varied at a constant volume flow. The volume flow of the synthetic air on the cathode side also remained unchanged. The plots shown were obtained at OCV as well as under load of 100 $\frac{mA}{cm^2}$ and 200 $\frac{mA}{cm^2}$. In Fig. 5.8, a comparison is made between the dry hydrogen/nitrogen fuel, with hydrogen concentration varying between 25 vol% and 45 vol% ($\boldsymbol{a}_{25}$ and $\boldsymbol{a}_{45}$) and a gas mixture $\boldsymbol{d}_{10}$, containing 25 vol% H_2 and 10 vol% H_2O in N_2. In this respect, gas mixture $\boldsymbol{d}_{10}$ contains only one fuel component - hydrogen; gas mixture $\boldsymbol{c}$ contains two fuel components - hydrogen and carbon monoxide; and diesel mixture $\boldsymbol{e}_{2.5}$ includes three fuel components - hydrogen, carbon monoxide, and methane. Nyquist plots obtained at OCV (in Fig. 5.7a), under 100 $\frac{mA}{cm^2}$ (in Fig. 5.7b) and under 200 $\frac{mA}{cm^2}$ (in Fig. 5.7c), show significant differences mainly in their second arcs, which refer to changes on the anode side since only the composition on the anode side was changed. The increasing current density reduces the total impedance, but indicates diverse behaviour of the cell operated under gas mixture $\boldsymbol{e}_{2.5}$ than under gas mixtures $\boldsymbol{d}_{10}$ or $\boldsymbol{c}$. With increasing load, the series resistance of $\boldsymbol{e}_{2.5}$ becomes significantly higher than for two other mentioned gas combinations, while the magnitudes of the complex impedance almost do not vary with changing load, as shown in Bode plots in Figs. 5.7e and 5.7f. The magnitudes presented in Figs. 5.7d - 5.7f show the

variation of the absolute impedance only between 100 mHz and approximately 5 Hz thus referring to the processes on the fuel electrode. Increasing the number of fuel components and reducing the nitrogen quantity generally led to a reduction of the total impedance, as discussed in [159]. A detailed examination of the impact of the fuel dilution in nitrogen on the cell performance is represented in Section 5.4. The behaviour of the magnitude plots was observed to be similar for gas mixtures $\boldsymbol{d}_{10}$ and $\boldsymbol{c}$, independent of the load applied, while during the operation under the diesel fuel mixture $\boldsymbol{e}_{2.5}$ the measured trends changed significantly with the increasing loads. This fact can be assumed to be influenced by both the steam- and dry-reforming of methane, which represents a chemical reaction, and remains uninfluenced by current flow. The phase plots shown in Figs.5.7g-5.7i behave in a similar manner as the magnitude plots. They are identical on the frequency range between 0.1 Hz and 0.4 Hz and solely depict the influence of ohmic resistance. Since the phase plots differ in the low frequency range, the effect of capacitive elements and the increasing significance of AC-elements are thus well marked.

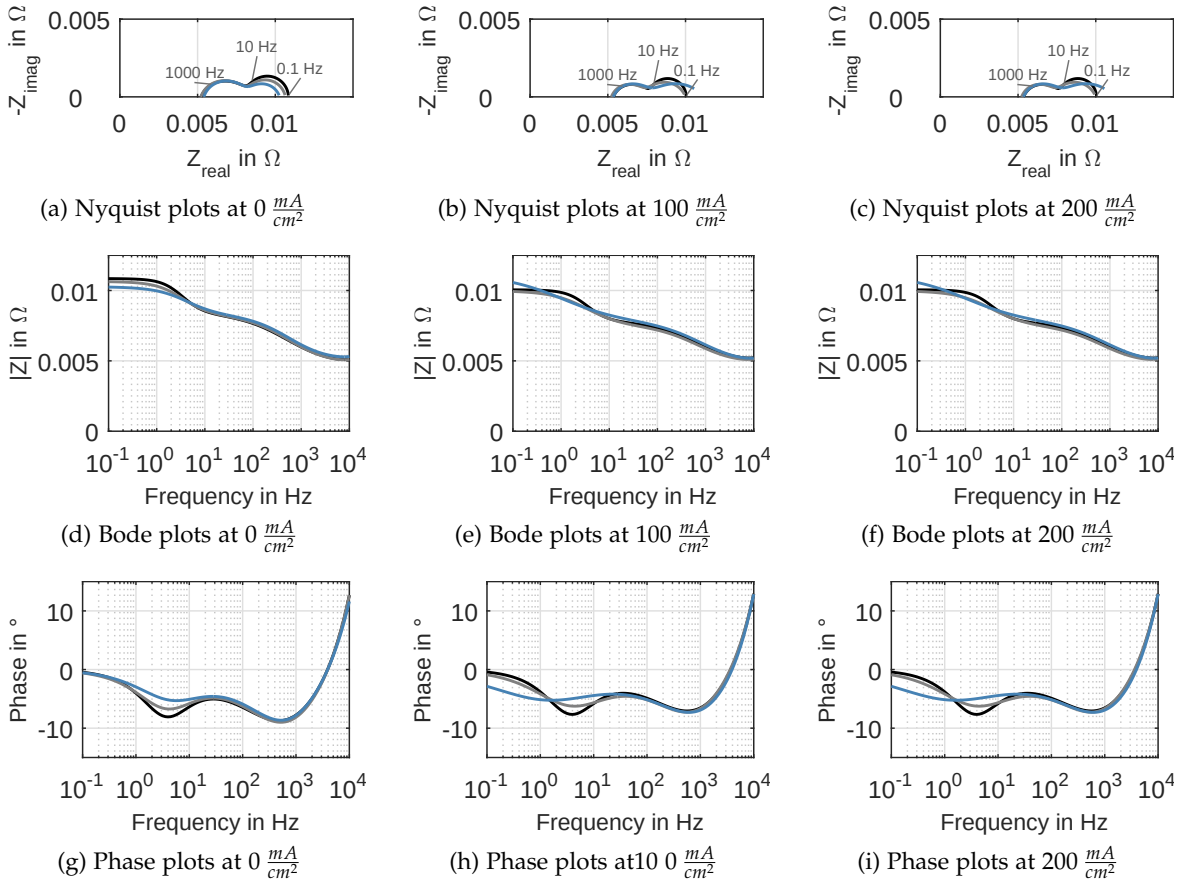

(a) Nyquist plots at 0 $\frac{mA}{cm^2}$ (b) Nyquist plots at 100 $\frac{mA}{cm^2}$ (c) Nyquist plots at 200 $\frac{mA}{cm^2}$

(d) Bode plots at 0 $\frac{mA}{cm^2}$ (e) Bode plots at 100 $\frac{mA}{cm^2}$ (f) Bode plots at 200 $\frac{mA}{cm^2}$

(g) Phase plots at 0 $\frac{mA}{cm^2}$ (h) Phase plots at10 0 $\frac{mA}{cm^2}$ (i) Phase plots at 200 $\frac{mA}{cm^2}$

Figure 5.7: Comparison of the electrochemical performances for gas mixtures used containing water vapour: gas mixture $\boldsymbol{d}_{10}$ (—), gas mixture $\boldsymbol{c}$ (—), gas mixture $\boldsymbol{e}_{2.5}$ (—). [8]

When feeding the cell with dry fuels (a_{25-100}), significantly higher polarization resistances were obtained, as shown in Figs. 5.8a-5.8c. Operation under OCV resulted in particularly widespread losses. The impedance value obtained under operation with the humidified d_{10} mixture, both in Nyquist and Bode plots, was negligibly small compared to the dry gas mixture. By increasing the current density, the obtained difference visibly decreased. This can notably be explained by the fact that electrochemical reactions are enhanced with increasing load. The amount of water vapour as a product of the electrochemical reaction thus increased. Next, the increased volume fraction of hydrogen in nitrogen, from 25 vol% (a_{25}) up to 45 vol% (a_{45}), reduced the overall impedance as well, which can be seen both in the Bode and Nyquist plots. As stated, this effect can be attributed to the decreasing amount of nitrogen, and thus the reducing dilution of the fuel mixture.

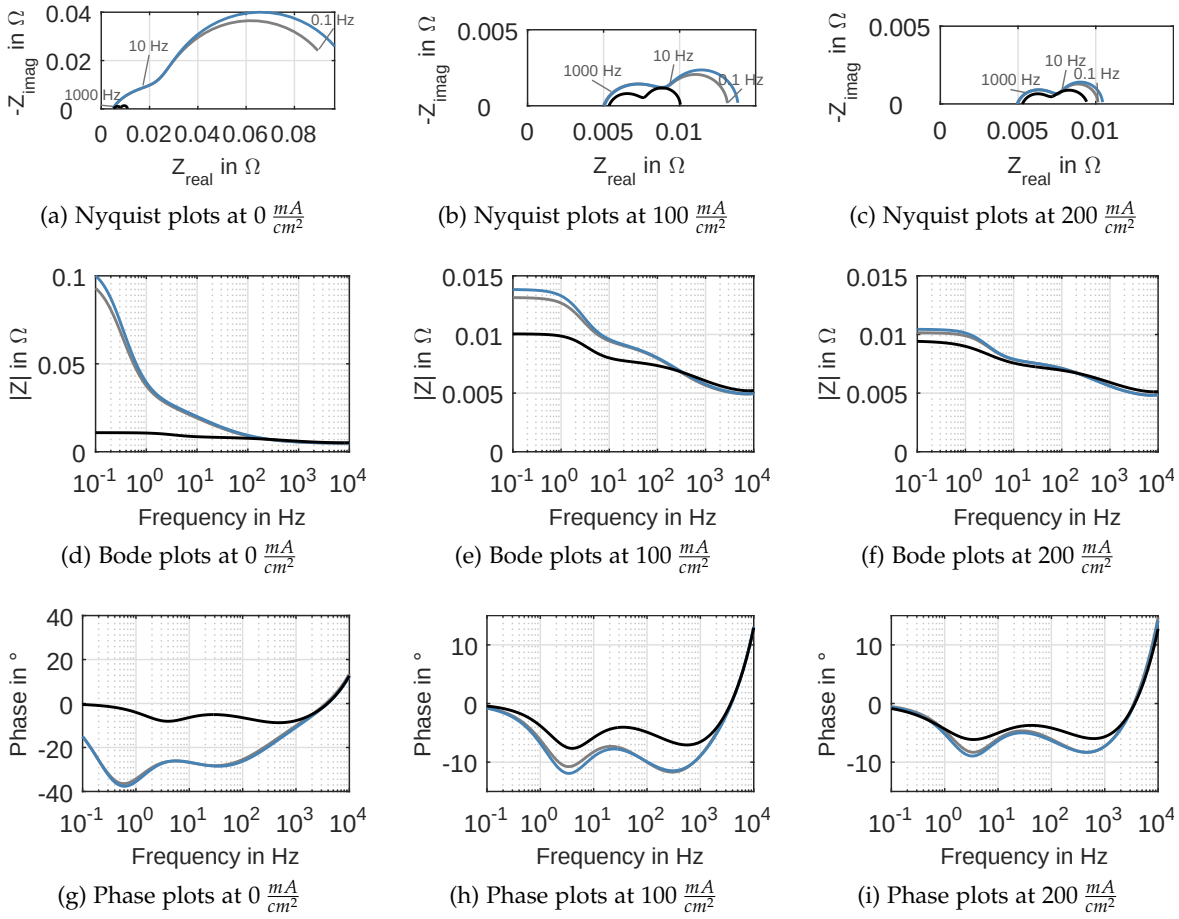

(a) Nyquist plots at 0 $\frac{mA}{cm^2}$ (b) Nyquist plots at 100 $\frac{mA}{cm^2}$ (c) Nyquist plots at 200 $\frac{mA}{cm^2}$

(d) Bode plots at 0 $\frac{mA}{cm^2}$ (e) Bode plots at 100 $\frac{mA}{cm^2}$ (f) Bode plots at 200 $\frac{mA}{cm^2}$

(g) Phase plots at 0 $\frac{mA}{cm^2}$ (h) Phase plots at 100 $\frac{mA}{cm^2}$ (i) Phase plots at 200 $\frac{mA}{cm^2}$

Figure 5.8: Comparison of the electrochemical performances for dry gas mixtures and one gas mixture containing water vapour: gas mixture a_{45} (—), gas mixture a_{25} (—), gas mixture d_{10} (—). [8]

Considering all the plots shown in Fig. 5.8, the same conclusion can be made as in Fig. 5.7; the fuel variation on the anode side always causes an impedance alternation in the low

frequency range. With rising load, the impedance difference between the cells fuelled with dry and wet gas mixtures drops significantly; the higher the load, the smaller difference, which is influenced by the available product gas in a gas mixture. Nevertheless, the observed effect of decreasing impedance with an increasing number of fuel components and increasing water vapour concentration does not completely agree with the resistance alternation calculated from the polarization curves, illustrated in Figs. 5.4c and 5.4g. The polarization curves indicate the best conductivity if the cell is operated with dry H_2/N_2 gas mixture. In this regard, reduced impedance, including decreased real and imaginary parts, does not refer to better conductivity, but does explain the behaviour of the theoretical electrical circuit if the cell is operated with more than one fuel component. In such cases, more processes (the oxidation of different fuels, methane reforming, water gas shift reaction, etc.) occur simultaneously, and, in a parallel circuit, the overall impedance is reduced.

5.4 Impact of Nitrogen on Cell Performance

In order to determine how fuel dilution by nitrogen impacts the processes on the anode side, series of data obtained under varying concentrations of hydrogen and nitrogen were recorded. The volume flow of all the gas mixtures used was kept constant at 2.4 SLPM. Since the volume flow of pure hydrogen does not remain constant in this case, further measurements were performed to investigate the effect of varying fuel volume flow.

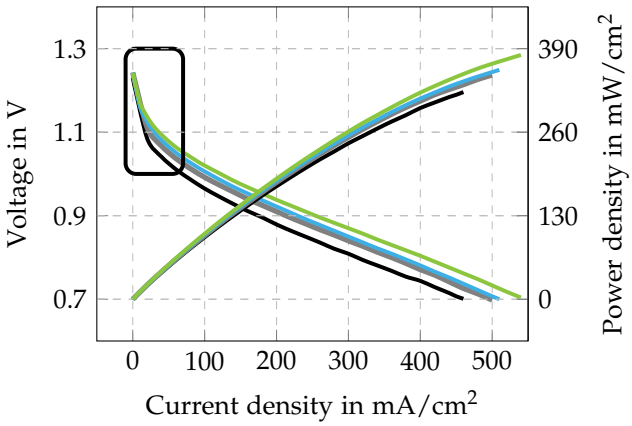

Figure 5.9: Comparison of the cell performance based on dilution of H_2 in N_2: a_{25} (—), a_{45} (—), a_{60} (—), a_{80} (—).

Fig. 5.9 compares the polarization curves measured under dry H_2/N_2 ($\boldsymbol{a}_{25-100}$ in Tab. 5.1) gas mixtures with hydrogen volume fraction varying between 25 vol%, 45 vol%, 60 vol% and 80 vol%. The nitrogen volume fraction was thus decreased from 75 vol% down to 20 vol%. The results observed clearly show that increasing the concentration of hydrogen and decreasing the amount of nitrogen, especially at low current densities (surface marked

with a black rectangle), reduces the activation losses and the overall ohmic losses.

When comparing impedance spectra, Fig. 5.10 illustrates the data observed during the electrochemical analysis performed for the H_2/N_2 $\boldsymbol{a}_{25-100}$ mixtures. As previously stated, the volume fraction of hydrogen was increased from 25 vol% to 100 vol%, simultaneously decreasing the nitrogen concentration. A constant volume flow of 2.4 SLPM was thus maintained. Depicted curves indicated by different colours refer to the varying amounts of hydrogen; black ($\boldsymbol{a}_{25}$), grey ($\boldsymbol{a}_{45}$), blue ($\boldsymbol{a}_{60}$), green ($\boldsymbol{a}_{80}$) and red ($\boldsymbol{a}_{100}$).

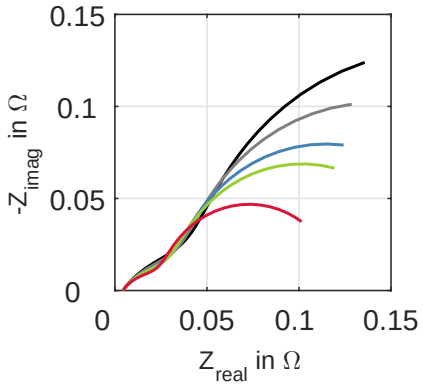

(a) Nyquist plots obtained at OCV

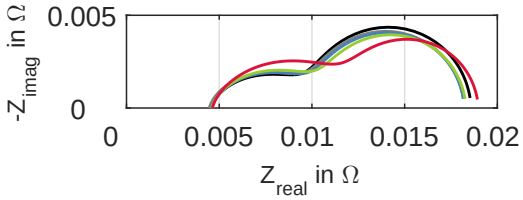

(b) Nyquist plots obtained at 50 $\frac{mA}{cm^2}$

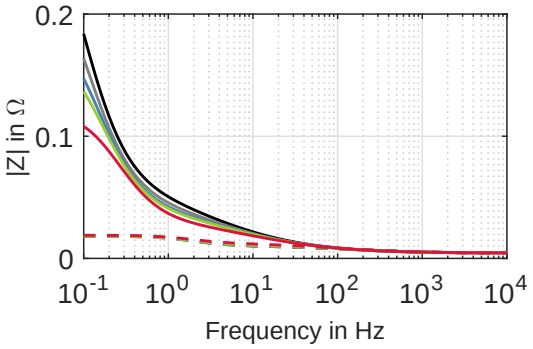

(c) Bode plots obtained both at 50 $\frac{mA}{cm^2}$ (dashed lines) and OCV (solid lines)

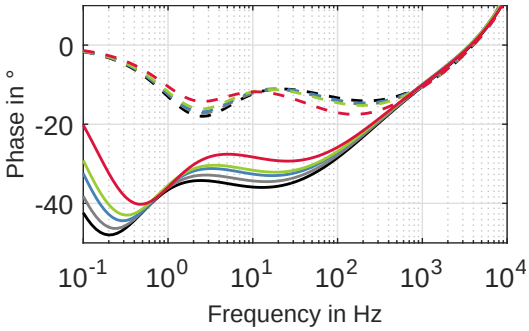

(d) Phase plots obtained both at 50 $\frac{mA}{cm^2}$ (dashed lines) and OCV (solid lines)

Figure 5.10: Electrochemical analysis of impact of H_2 dilution in N_2 on cell performance, performed at 800°C, both at OCV and 100 $\frac{mA}{cm^2}$: $\boldsymbol{a}_{25}$ (—), $\boldsymbol{a}_{45}$ (—), $\boldsymbol{a}_{60}$ (—), $\boldsymbol{a}_{80}$ (—), $\boldsymbol{a}_{100}$ (—), - OCV, -- 100 $\frac{mA}{cm^2}$.

Impedance spectra measured at OCV and under 50 $\frac{mA}{cm^2}$ can be seen in Figs. 5.10a and 5.10b, which generally show two separated arcs, a high frequency and a low frequency arc. The separate arcs can be assigned to the single electrodes, as described in Sections 5.2 and 5.3. The changes that occurred are more pronounced under the open circuit conditions in Fig. 5.10a. The low-frequency arc in the frequency range between 0.1 Hz und 1 Hz indicates

a significant increase in resistance with decreasing H_2 concentration and increasing N_2 concentration, while this dependence is less pronounced for the higher frequencies. When comparing the overall impedance for all of the $\boldsymbol{a}_{25-100}$ gas variations used, it can clearly be seen in Bode-plots in Fig. 5.10c that operation under pure hydrogen results in a reduction of the overall impedance of almost 50% compared to the overall impedance measured for 25 vol% H_2 in N_2.

It is possible to assume that increasing impedance, caused by the heavy dilution of fuel in nitrogen, disturbs hydrogen diffusion and activation of the fuel electrode. Increasing load, however, forces diffusion of reactants to the three-phase boundary (TPB)-sites. This effect is confirmed by comparing Fig. 5.10a with Fig. 5.10b. The overall impedance has substantially decreased since electrochemical reactions have occurred, and water vapour has been produced as a result. As stated, high activation losses arise during operation under dry hydrogen, since dry hydrogen oxidizes with a large overpotential, as addressed in [57]. Comparing the measured impedances of gas mixtures a_{45} in Fig. 5.10a and $b_{2.5}$ in Fig. 5.15a reveals approximately 50 times less impedance if water vapour is contained in a gas mixture. Nevertheless, the variation of nitrogen and hydrogen volume fraction in 2.4 SLPM shows that their impact is clearly visible in the same frequency range as activation losses. If the magnitude (Fig. 5.10c) and phase (Fig. 5.10d), both obtained at OCV and under a load of 50 $\frac{mA}{cm^2}$ are compared, it is obvious that the phase plot shows several break points, which refer to complex elements and processes occurring in the cell investigated. They are not visible in the magnitude diagrams.

The DRTs calculated from the impedance spectra obtained in Fig. 5.10 are shown in Fig. 5.11. DRT peaks obtained under OCV conditions show four peaks between 10^{-4} s and 10^{1} s. These peaks could refer to 4 processes and can be compared with the results obtained by Sonn et al. [159] for impedance spectra measured under OCV conditions. Obviously, the variation of nitrogen and hydrogen concentration is the most pronounced, with two peaks shown at approximately 1 s and 0.1 s. Increasing the nitrogen concentration significantly increases the peak value and shifts it to the right on the time axis, thus representing a very slow processes. Since diffusion is a very slow process, the peaks obtained at high relaxation time constants can be linked to the diffusion resistance. This peak is also visible for pure hydrogen, so diffusion resistance is shown in one peak for all species involved. The position of the peak on the x-axis shows that increasing the concentration of hydrogen accelerates the diffusion process, which can be well explained with the effect of the weaker fuel dilution and enhanced hydrogen diffusion to the TPB-sites. Since hydrogen molecules are significantly smaller, the diffusion process is faster when pure hydrogen must be transported to the active sites, as shown by DRT-spectra in Fig. 5.11a. The same effect as represented here,

decreasing peak value with an increasing amount of hydrogen, is obvious for the peak visible at 10^{-1} s, but the effect is not as strongly pronounced. Sonn et al. [159] connected the slower process with diffusive mass transport in the flow channels of the flow field, and the faster one with gas phase diffusion in the volume of the contact meshes. They further link two other peaks with the electro-oxidation of hydrogen. Under load, as shown in Fig. 5.11b, the processes run faster than expected because of external force. Diffusion, as the slowest process, is obtained between 10^{-2} s and 1 s, but in this case it is accelerated compared to OCV. The value on the y-axis significantly changed with varying gas mixtures, since the relaxation time remained almost unchanged, regardless of the hydrogen/nitrogen ratio. The highest peak, observable at OCV, almost disappeared under load. Therefore, it is reasonable to assume that this peak refers to activation losses that occur at OCV and very low current density when dry fuel mixture is used. As represented by Sonn et al. [159], peaks observed at lower times can be linked to hydrogen oxidation.

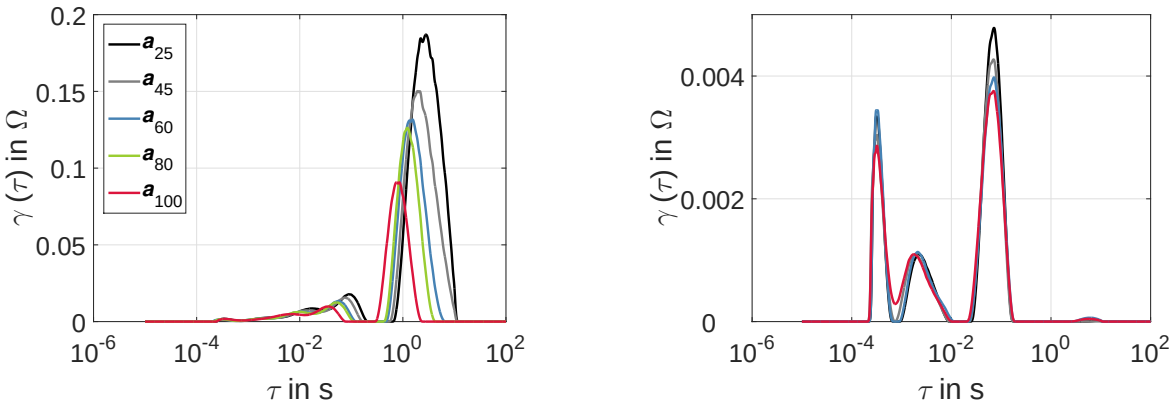

(a) DRT-analysis at OCV

(b) DRT-analysis at 100 $\frac{mA}{cm^2}$

Figure 5.11: DRT-analysis performed for impedance spectra measured at OCV and 50 $\frac{mA}{cm^2}$ for gas mixtures a_{25-100} with varying H_2/N_2 ratio: a_{25} (—), a_{45} (—), a_{60} (—), a_{80} (—), a_{100} (—).

Isolated single losses, calculated according to the same principle as described in Section 5.2, are represented in Fig. 5.12. Ohmic losses are represented as the difference between the measured open circuit voltage, indicated by a black line, and the voltage losses induced by electrolyte and contact resistance, depicted as a red dashed line. The difference between the red dashed line and the yellow dotted line indicates kinetic or activation losses, while the difference between the yellow dotted line and blue solid line refer to mass transfer and kinetic losses. In Figs. 5.12a and 5.12b, the obtained losses are compared for 25 vol% H_2 in N_2 (Fig. 5.12a) and 100 vol% H_2 (Fig. 5.12b). Obviously, the stronger dilution of hydrogen in nitrogen results in distinctly higher mass transfer losses.

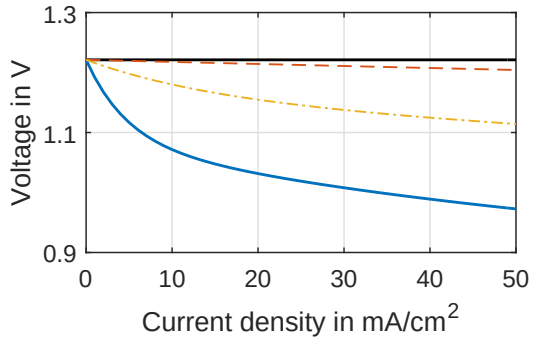

(a) Calculated losses based on impedance measurements during operation under gas mixture a_{25}

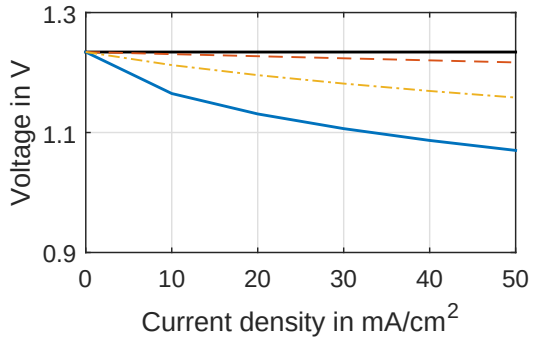

(b) Calculated losses based on impedance measurement during operation under gas mixture a_{100}

Figure 5.12: Comparison of single losses for varying H_2/N_2 ratio: overvoltage 1 based on ohmic losses (—), overvoltage 2 based on kinetic losses (—), overvoltage 3 based on concentration losses (—), OCV (—).

5.4.1 Impact of Fuel Volume Flow on Cell Performance

Further measurements were carried out in order to examine the impact of fuel volume flow on cell performance. Pure hydrogen was fed to the cell for this purpose, while its volume flow was varied between 1.8 SLPM and 2.4 SLPM in 0.2 SLPM steps. Increasing the volume of the hydrogen fuel on the anode side did not result in significant changes, as represented by the magnitude of the complex impedance in Fig. 5.13a both at OCV (solid lines) or under a load of 50 $\frac{mA}{cm^2}$ (dashed lines). Only a slight alternation was obtained in the phase plots, as shown in Fig. 5.13b. Since the peaks are shifted on the y-axis only, the ohmic resistance is demonstrated to be a function of the hydrogen amount. Thus, it is possible to summarize, that the shown volume flow alternation does not influence cell performance since enough fuel is available for electrochemical reactions to occur.

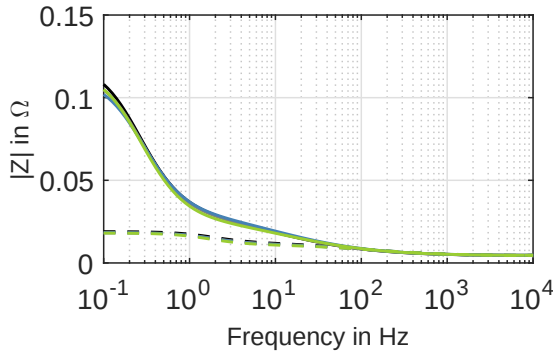

(a) Bode plots

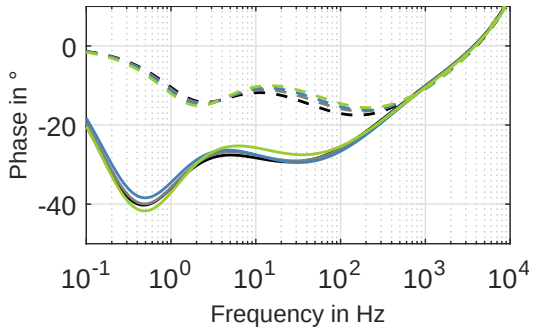

(b) Phase plots

Figure 5.13: Analysis of impact of varying hydrogen volume flow on the cell performance at 800°C: 2.4 SLPM (—), 2.2 SLPM (—), 2.0 SLPM (—),1.8 SLPM (—), - OCV, -- 50 $\frac{mA}{cm^2}$.

Based on this, the volume flow of pure hydrogen in the range where the fuel starvation does not occur has little impact on cell performance. Therefore, it is more probable that the cell's performance is influenced and diminished by hydrogen dilution in nitrogen than by volume flow alternation.

5.5 Impact of Water Vapour in the Gas Mixture on Cell Performance

The impact of water vapour in the fuel mixture on the cell performance and overall losses was also studied. For this purpose, the concentration of H_2O in H_2/N_2 mixture ($\boldsymbol{b}_{2.5-11}$) was varied between 2.5 vol% and 11 vol% (as shown in Tab. 5.1). As already stated, increasing load, and thus increasing water vapour concentration in the gas mixture, reduces the overall impedance, as obtained via the comparison of polarization curves in Fig. 5.14. Increasing the H_2O concentration considerably reduces the OCV as well as the overall performance, which is expected based on the calculation of the Nernst voltage (Eq. 4.3). The ohmic losses did not significantly change with the varying water vapour concentration. Nevertheless, the fact that operation under 2.5 vol% H_2O (black solid line) shows slight activation losses, smoothed with the increasing water vapour amount, is very important. The area where the activation losses are visible is marked with a black rectangle in Fig. 5.14.

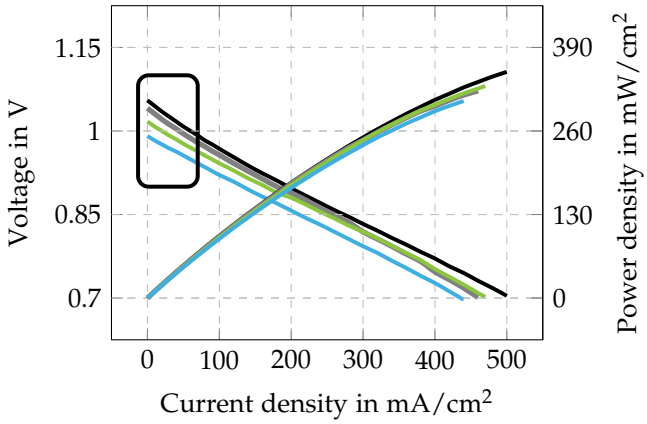

Figure 5.14: Comparison of the cell performance for varying amount of H_2O in H_2/N_2: $b_{2.5}$ (—), b_4 (—), b_7 (—), b_{11} (—).

Data obtained during the electrochemical impedance spectroscopy measurements are represented in Fig. 5.15. The Nyquist plots, observed at OCV (Fig. 5.15a) as well as under load of 50 $\frac{mA}{cm^2}$ (Fig. 5.15b), indicate the same performance behaviour with varying water vapour concentration. This implies that there is no significant difference between the impedance trend with varying load, as addressed during operation with dry gas mixtures because the

water vapour as a reaction product is already available in the fuel mixture used. In both diagrams, increasing the amount of water vapour from 2.5 vol%, indicated by the black line, up to 11 vol%, illustrated by the blue line, significantly decreased the second (low-frequency) arc.

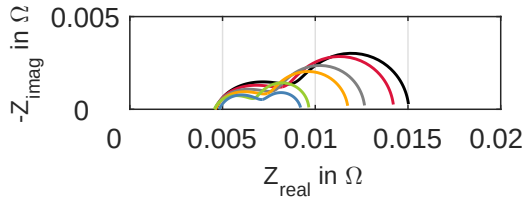

(a) Nyquist plots at OCV

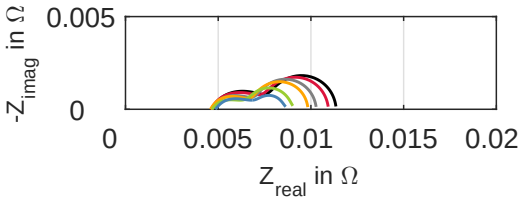

(b) Nyquist plots at 50 $\frac{mA}{cm^2}$

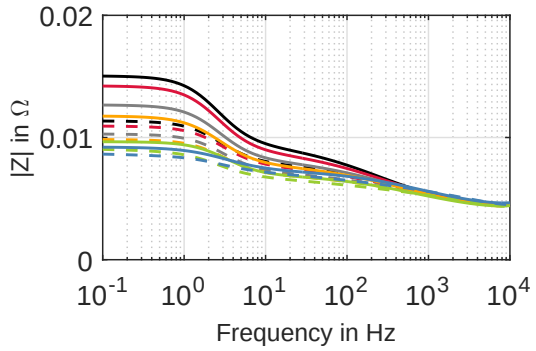

(c) Bode plots both at OCV (solid lines) and 50 $\frac{mA}{cm^2}$ (dashed lines)

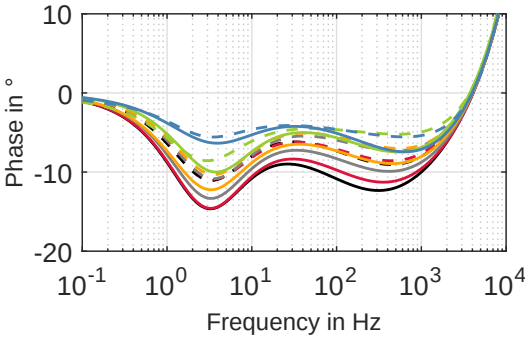

(d) Phase plots both at OCV (solid lines) and 50 $\frac{mA}{cm^2}$ (dashed lines)

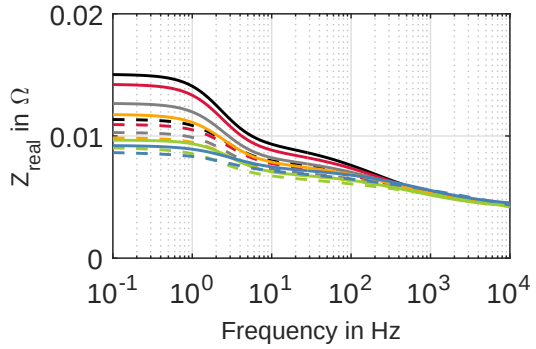

(e) Real part of complex impedance both at OCV (solid lines) and 50 $\frac{mA}{cm^2}$ (dashed lines)

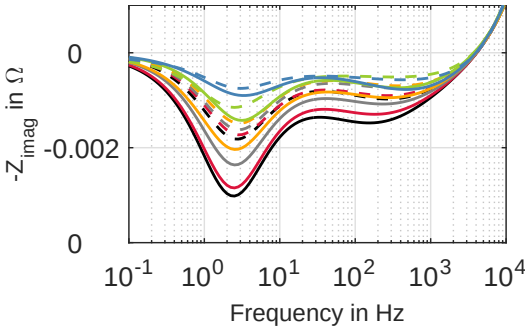

(f) Imaginar part of complex impedance both at OCV (solid lines) and 50 $\frac{mA}{cm^2}$ (dashed lines)

Figure 5.15: Impact analysis of varying water vapour concentration in the fuel mixture on the cell performance at 800°C, both at OCV and 50 $\frac{mA}{cm^2}$: $\boldsymbol{b}_{2.5}$ (—), $\boldsymbol{b}_3$ (—), $\boldsymbol{b}_4$ (—), $\boldsymbol{b}_5$ (—), $\boldsymbol{b}_7$(—), $\boldsymbol{b}_{11}$ (—).

The magnitude (Fig. 5.15c) and its real part (Fig. 5.15e) show the same trend and almost the same values depending on their frequency, which indicates the negligible impact of the imaginary part on the total cell impedance. The Bode-plots also provide that increasing concentration of water vapour in the fuel mixture results in the decreasing magnitude of the complex impedance. The increasing water vapour concentration thus reduces the absolute

difference in the overall impedance measured at OCV and under load. The same relation and an almost identical curve trend are obtainable through comparison with the phase plot (Fig. 5.15d) and the imaginary part of the overall impedance (Fig. 5.15f). The imaginary part is formed by an inductive or capacitive effect, and thus represents the AC processes. This can certainly simplify a basic interpretation of the cell behaviour, thus regarding or separately interpreting the real and imaginary part of the observed cell impedance.

DRT-spectra at OCV, observed for the gas mixtures containing water vapour significantly (Fig. 5.16) differ from the DRTs in Fig. 5.11a, which characterize operation under dry H_2/N_2 mixture. Compared to the dry gas mixture, where 4 peaks are visible, in this case only 3 peaks are obtained. The highest peaks, which refer to diffusion processes, are visible between 10^{-2} s and 1 s, and can thus be compared with the second diffusion peak for dry mixtures.

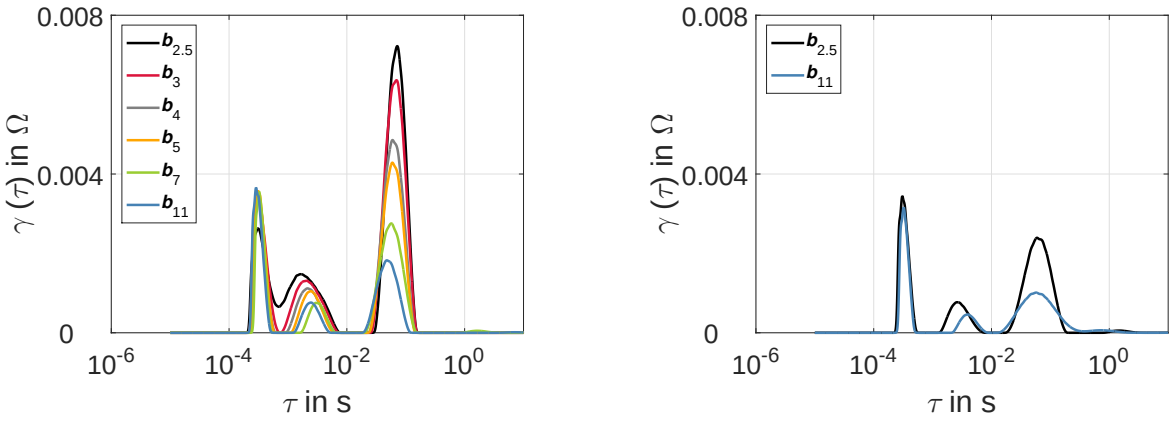

(a) DRT-analysis at OCV

(b) DRT-analysis at 100 $\frac{mA}{cm^2}$

Figure 5.16: DRT-analyses for examination of varying steam concentration in the fuel mixture on the cell performance at 800°C, both at OCV and 100 $\frac{mA}{cm^2}$: $\boldsymbol{b}_{2.5}$ (—), $\boldsymbol{b}_3$ (—), $\boldsymbol{b}_4$ (—), $\boldsymbol{b}_5$ (—), $\boldsymbol{b}_7$ (—), $\boldsymbol{b}_{11}$ (—).

The peak values in Fig. 5.16 are in the same range as in Fig. 5.11b, which represents the polarized cell operated under dry gas mixture, and is thus approximately 100 times smaller than under operation with dry mixtures $\boldsymbol{a}_{25-100}$ at OCV. Under load (during the cell polarization), water is produced, and the peaks obtained behave in the same way as when the anode is supplied with humidified fuel. With increasing water vapour concentration, the resistance decreases, whereas the relaxation times remain almost unchanged. The resistance of the process obtained between 10^{-3} s and 10^{-2} s, which can be related to hydrogen oxidation, also decreases with rising steam concentration, and, in parallel, the relaxation times decreases. The third peak, observed at the lowest relaxation time, is not affected by varied humidification. The same effect is noted under load in Fig. 5.16b, in which only the extreme

cases are illustrated; gas mixtures including 2.5 vol% and 11 vol% of H_2O. It is clearly visible that increasing steam content does not change the DRT trend, but only reduces the process resistance.

Separated losses obtained by calculating the polarization curve, in the same way as described in Sections 5.2 and 5.3, are represented in Fig. 5.17. The calculated losses are shown for gas mixtures $\boldsymbol{b}_{2.5}$ in Fig. 5.17a, containing 2.5 vol% of H_2O and in Fig. 5.17b for $\boldsymbol{b}_5$, in which the concentration of water vapour was increased to 5 vol%. It is clearly visible that increasing the amount of steam in a gas mixture significantly reduces the OCV. Otherwise, the overall losses do not show noticeable difference when the amount of steam is increased from 2.5 vol% to 5 vol%, only that with increasing water vapour concentration, the single loss curves become more linear. To sum up, it is possible to conclude that dry gas mixtures result in the highest losses at low current densities, which can be explained by the high activation energy required for the oxidation of dry hydrogen. However, detailed comparison of ohmic resistance shows that increasing the amount of steam reduces activation losses at lower current densities.

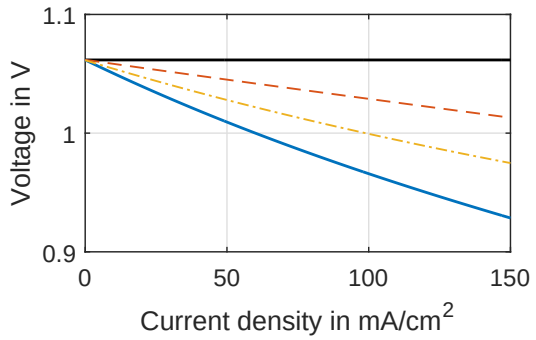

(a) Calculated losses based on impedance measurements during operation under $\boldsymbol{b}_{2.5}$

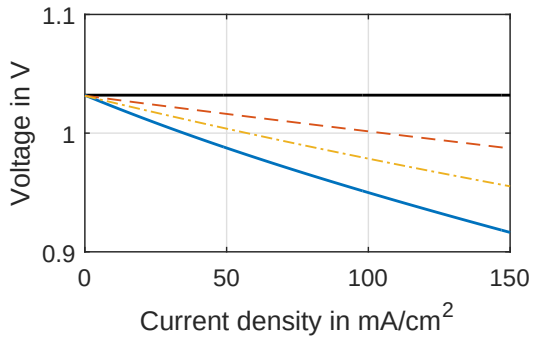

(b) Calculated losses based on impedance measurements during operation under $\boldsymbol{b}_5$

Figure 5.17: Comparison of single losses for varying water vapour concentration in gas mixtures $\boldsymbol{b}_{2.5-11}$: overvoltage 1 based on ohmic losses (—), overvoltage 2 based on kinetic losses (—), overvoltage 3 based on concentration losses (—), OCV (—).

5.6 Variation of the Operating Temperatures [3]

The operating temperature is a very important parameter, and has a significant impact on the cell behaviour. For a general case, in the context of the Nernst voltage, a lower operating temperature results in an increase in the open circuit voltage, since only chemical reactions are taken into account. If the cell is loaded, higher current densities at the operating voltage

[3] Segments of this section have already been published in [4, 8].

of 0.7 V can be reached at higher temperatures since the electrolyte conductivity increases with the increasing temperature, and, in general, the electrode materials used exhibit better performance at higher temperatures. Comparing the cell performance as measured at three operating temperatures (700°C (indicated by the blue line), 750°C (grey line) and 800°C (black line)) under fuel mixture $\boldsymbol{d}_{10}$ in Fig. 5.18 confirms that increasing the temperatures favourably affects the cell efficiency, while Nernst-voltage decreases at the same time. In the context of this correlation, it is important to consider that the voltage change also depends on the current density level. If the current density is lower than approximately 25 $\frac{mA}{cm^2}$, the cell voltage decreases with rising temperatures for the investigated cell. If the current density exceeds this value, the cell voltage increases, and the polarization curve becomes flatter with the increasing temperature. However, rising temperatures improve the cell performance – a temperature increase of 50°C leads to an increase in power density of almost 100 $\frac{mW}{cm^2}$ – and reach higher overall efficiencies and higher levels of fuel utilization at the operation voltage.

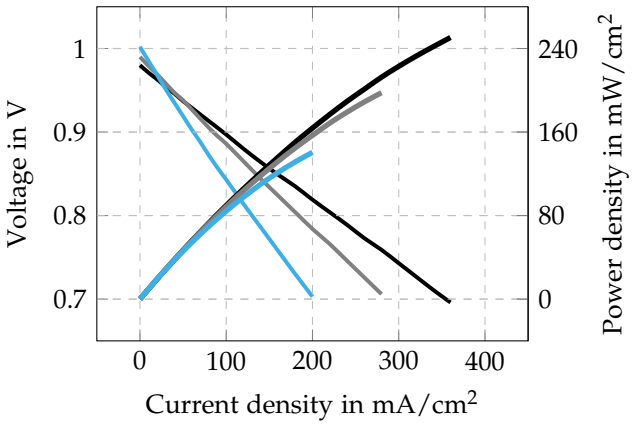

Figure 5.18: Comparison of the polarization curves measured under varied temperatures: 700°C (——), 750°C (——), 800°C (——).

The impedance measurements were also carried out at the temperatures of 700°C (blue), 750°C (grey) and 800°C (black) and under fuel mixture $\boldsymbol{d}_{10}$, which are shown in Fig. 5.19. The load impact was investigated in addition to the temperature variation, as can be seen in Fig. 5.19. The results are represented at 0 $\frac{mA}{cm^2}$, 60 $\frac{mA}{cm^2}$ and 120 $\frac{mA}{cm^2}$. The value of the electrolyte resistance can be seen at the beginning of the x-axis, where the y-value equals zero. It is obvious in the measured impedance spectra in Figs. 5.19a, 5.19b and 5.19c that the electrolyte resistance significantly decreases with a temperature increase and that the obtained cell impedance and cell losses, respectively, decrease as the temperature rises. The measured spectra thus support the results obtained through the measurement of the polarization curves, shown in Fig. 5.18. The trend of the impedance plots remains almost unchanged, but the magnitude is significantly affected by the temperature variation. The difference

between the values measured at the three temperatures mentioned is less pronounced when the load is higher since, as discussed, the polarization resistance is higher at lower load.

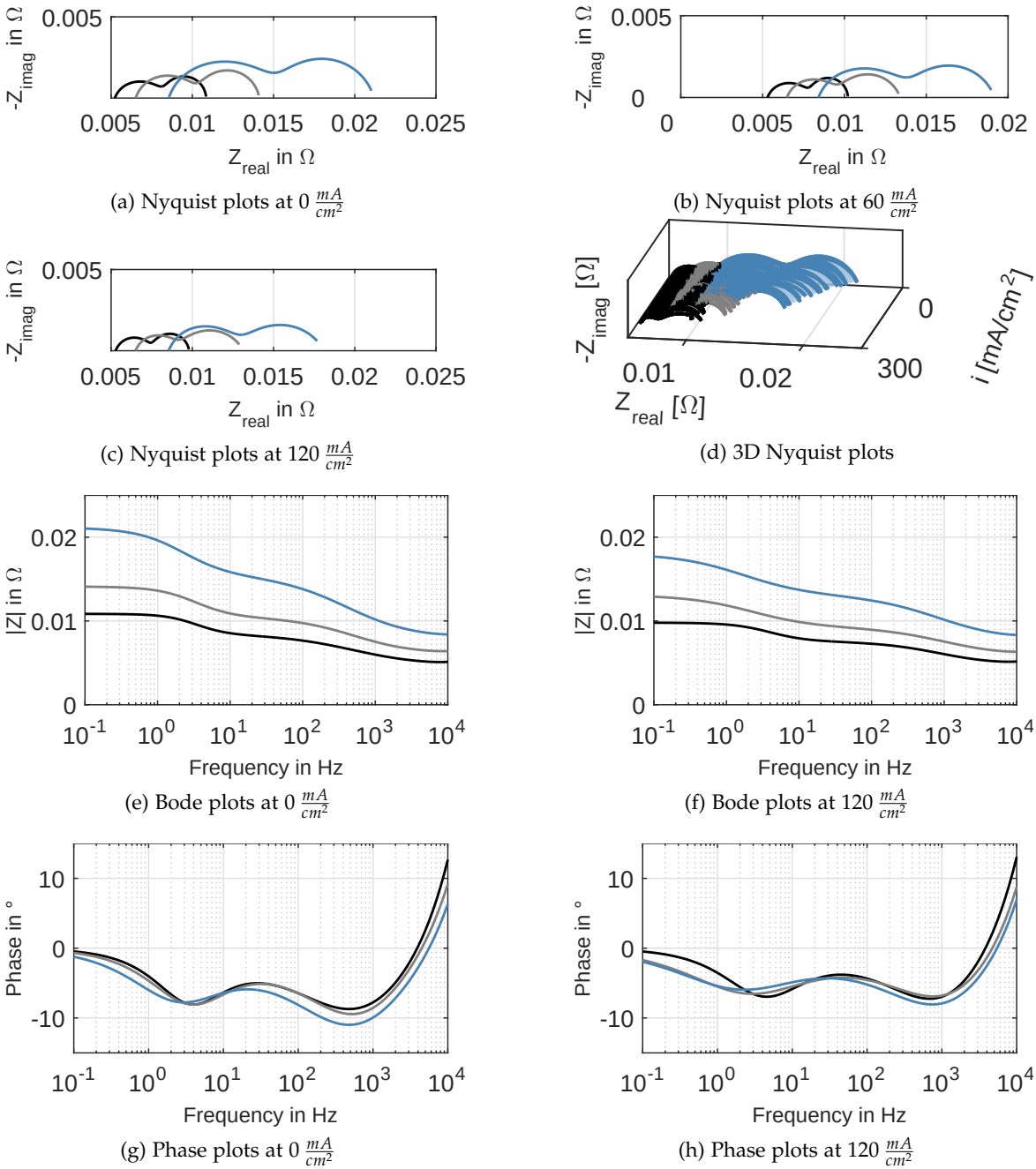

(a) Nyquist plots at 0 $\frac{mA}{cm^2}$

(b) Nyquist plots at 60 $\frac{mA}{cm^2}$

(c) Nyquist plots at 120 $\frac{mA}{cm^2}$

(d) 3D Nyquist plots

(e) Bode plots at 0 $\frac{mA}{cm^2}$

(f) Bode plots at 120 $\frac{mA}{cm^2}$

(g) Phase plots at 0 $\frac{mA}{cm^2}$

(h) Phase plots at 120 $\frac{mA}{cm^2}$

Figure 5.19: Comparison of the electrochemical data measured during operation under gas mixture $\boldsymbol{d}_{10}$, at varied temperatures: 700°C (—), 750°C (—), 800°C (—).

Furthermore, the electrochemical impedance spectra obtained also refer to the increased polarization impedance that occurred as the temperature decreased. To get a better overview

of the cell behaviour over the whole load range, Fig. 5.19d shows 3D impedance plots for the measured data mentioned above. Bode plots depicted in Figs. 5.19g and 5.19e represent the temperature-dependent overall impedance in the same manner as the Nyquist plots, while the phase plots exhibit identical cell behaviour, thus confirming that their equivalent electrical circuits are identical.

6

Carbon Deposition and its Effect on Cell Performance and Microstructure

The objective of this thesis is (1) to perform an electrochemical analysis of industrial-sized SOFCs and observe the separation of single electrodes and the processes that occur (addressed in the previous chapter); (2) to make advancements with regard to the early detection of degradation mechanisms, particularly carbon depositions; and (3) to develop innovative regeneration approaches that enable complete carbon removal and restore the cell's performance, in such a way as to protect the cell. The problematic of carbon deposition phenomenon, described in the preceding chapters, will be explained and supported with experimental results for industrial-sized solid oxide fuel cells in this chapter. In the course of the analysis of the mentioned phenomenon, the polarized industrial-sized planar single solid oxide fuel cells were fed with four different synthetic diesel reformate mixtures, thus representing realistic operating conditions. The operating conditions, under which carbon can be formed and deposited on the anode side were thus generated. The approaches that allow early identification of carbon build-up in order to avoid irreversible deterioration of cell performance and its microstructure were originated and they are provided within this chapter. The scanning electron microscopy was introduced to support the knowledge gained in the experimental analysis.

All of the investigations were undertaken several times on one cell, and the same procedure was repeated on a number of cells, thus ensuring the reproducibility and the repeatability of the characterisation principles applied and developed within this work.

6.1 Evaluation of Carbon Deposits [1]

The ability to detect and characterise carbon deposits at an early stage is of crucial importance in order to ensure the safe operation of SOFCs and to prevent undesired cell degradation. By assimilating the in-operando and post-mortem characterization techniques, it is possible to gain deeper insight into carbon formation mechanisms, which will help promote a greater understanding thereof.

In this work, the SOFCs tested were supplied with synthetic reformates, with compositions like those used in auxiliary power units fuelled with diesel and modified diesel reformates. The volume flow of the fuel mixture used was defined to be a constant 2.4 SLPM. Detailed information about the gas composition and the operating parameters can be found in Tab. 4.1 in Chapter 4. In order to obtain information about the degradation of cell performance, such as the critical operating time or degradation voltage, the methane volume fraction in the fuel mixture was varied between 2.3 vol% (as expected in APUs), 9 vol%, 14 vol% and 20.3 vol% (see Tab. 4.1). The choice to vary the amount of methane was made because methane cracking is favoured at high operating temperatures, whilst carbon formation via Boudouard-reaction is not expected to be prominent at the characteristic ASC-SOFC operating temperature of 800°C, as stated in Chapter 3. The experiments were performed on polarized cells in order to simulate more realistic operating conditions, as required for the operation of APUs. During carbon build-up, the current density was held as constant and the voltage was measured.

In order to accurately describe how carbon formation can be identified at an early stage, as well as which parameters lead to carbon deposits, the measurements performed under two different diesel mixtures ($DR_{2.3}$ and DR_{14}) are discussed in this section. These two fuel mixtures were selected for discussion because the effects observed during the coking experiment differed for $DR_{2.3}$, representing a slow carbon deposition process, but remained almost same for DR_9, DR_{14} and $DR_{20.3}$, thus providing an example of accelerated carbon formation.

Initially, the diesel fuel mixture $DR_{2.3}$ containing 2.3 vol% CH_4 was used as fuel, in order to produce carbon depositions. In Fig. 6.1, the measured curves for three consecutively performed carbon deposition experiments are plotted; these are termed as Experiment 1, 2 und 3, and the results both before carbon depositions (solid line) and after (dotted line). The same carbon deposition procedure was repeated three times in order to prove the reproducibility of the results obtained. At the beginning of the second and the third experiments,

[1] Segments of this section have already been published in [6, 7].

the cell's performance, including electrochemical measurements of the polarization curves and impedance spectra, as well as gas analysis, was compared to the cell performance from the first experiment to determine the same initial conditions. Exposure to diesel reformate with 2.3 vol% CH_4 influenced the cell resistance due to deterioration of the performance characteristics after fuelling with the aforementioned gas mixture. During fuelling, a period of 44 h was determined to be the critical operating time for carbon depositions. In all of the experiments performed, the cell performance changed in equal measure.

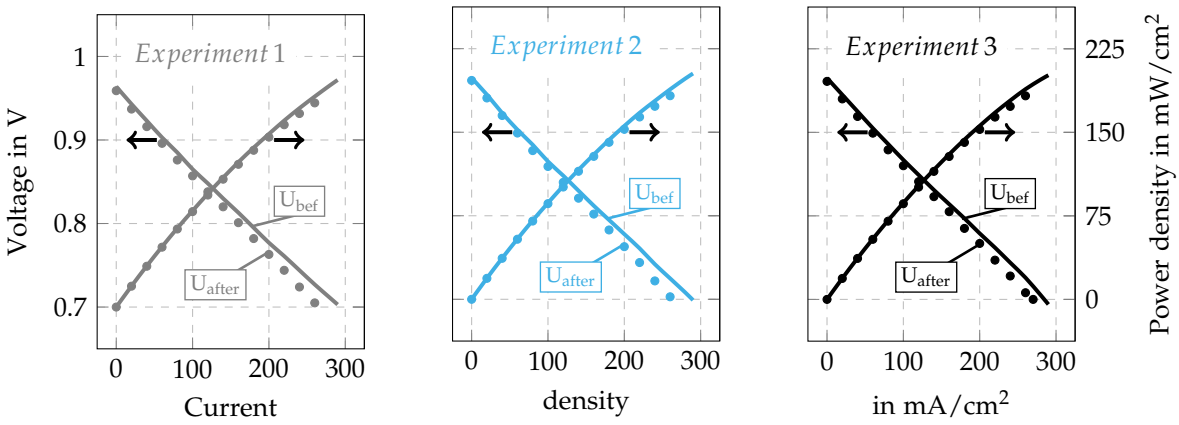

(a) Polarization curves

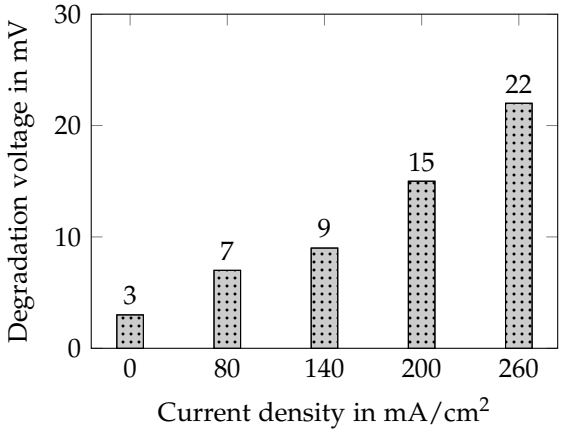

(b) Voltage degradation after 44 h operation with diesel reformate

Figure 6.1: Changes in electrochemical cell performances during fuelling with diesel reformate mixture $DR_{2.3}$. [7]

The initial current density of 290 $\frac{mA}{cm^2}$ at a voltage of 0.7 V could no longer be reached after the allotted time had passed; it decreased to 260 $\frac{mA}{cm^2}$. The OCV measured after the carbon deposition experiments also decreased, which indicates the change in the available fuel components and the catalytic surface when compared to the initial state. The partial pressure of the single gas components was thus varied, which impacted the measured

Nernst voltage or actually open circuit voltage. All of these facts suggest changes in the anode structure and the catalytic surface due to carbon depositions. Although operation with carbon-containing fuel caused the degradation of the cell performance, no continuous voltage fluctuations were observed during the measurement process, and cell stability was not affected in the same way. The cell performance deteriorated almost identically for each individual experiment, thus providing the reproducibility of the carbon formation. It is also important to mention that the initial state was reached after the regeneration methods were applied; these were used to remove deposited carbon, and are described in detail in Chapter 7. Thus, it is possible to claim both that the total regeneration of the cell was demonstrated, and that the reproducibility of the carbon deposits was proven, given that the cell performance for the second and the third tests, was almost identical to the initial results of the first experiment. Furthermore, the diagram in Fig. 6.1b depicts the difference in the measured voltage before and after the carbon deposition experiment for arbitrarily chosen current density values - $0, 80, 140, 200$ and $260\ \frac{mA}{cm^2}$, thus showing the exact degradation rate of the cell performance caused by carbon deposits after 44 h.
While feeding the set $DR_{2.3}$ fuel, simultaneous changes in voltage, gas, and temperature distribution ($\vartheta_1, \vartheta_2, \vartheta_3$) were detected in the anode chamber. The temperature distribution over the cell was measured over three zones ($\vartheta_1, \vartheta_2, \vartheta_3$), as shown in Fig. 6.2. The trend in temperature change can be seen in Fig. 6.3a.

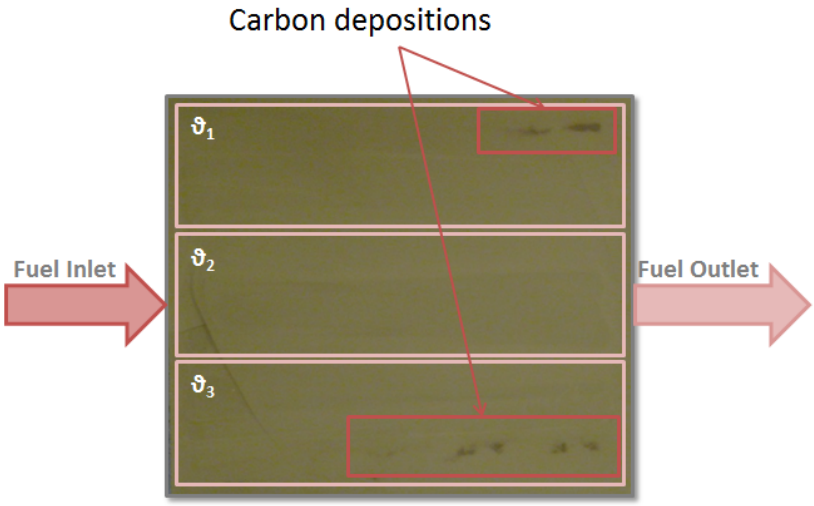

Figure 6.2: A photograph of the anode surface after the carbon deposition experiment. [7]

With the temperature change (Fig. 6.3a), the volume fraction of the single gas components (Fig. 6.3b) was also altered. Note that a gas analysis was performed for the dry gas, while water vapour was condensed to liquid state before reaching the gas analyser inlet. During the measured temperature increase, CO_2 volume fraction increased, whereas the volume fraction of the other gas components decreased. The change in gas outlet ratio, and the

increased volume fraction of CO_2 along with the decreased volume fraction of CO, which simultaneously altered the ratio of other gas components at the anode outlet, indicate the occurrence of the Boudouard reaction (Eq. 3.8). Since the Boudouard reaction (Eq. 3.8) is exothermic with regard to CO dissociation, the even temperature increase over the whole cell surface indicates carbon formation. Furthermore, the alternation of the species volume fraction at the anode outlet reduced the Nernst voltage, and therefore also the cell operating voltage. The voltage reduction depicted was present in every single repetition of the experiment, and always followed by the same behaviour; while the voltage decreased, the temperature in the anode chamber or exacter over the whole cell surface increased at the same time. This ''voltage decrease phenomenon'' occurred only in the course of operation with the diesel fuel $DR_{2.3}$, thus simulating the slow carbon formation process. Each time, it lasted approximately 15 minutes per appearance. By means of the data obtained, it is possible to assume that the ''voltage decrease phenomenon'' illustrates the process of carbon deposition. The available literature presents the CO_2-peaks during carbon formation as being due to operation with methane - both dry and humidified, [41] and [34]. Pomfret et al. [162] showed decreased temperature due to carbon deposits, but in their case it was for the cells fuelled with hydrocarbon, which can be explained by the endothermic catalytic cracking process.

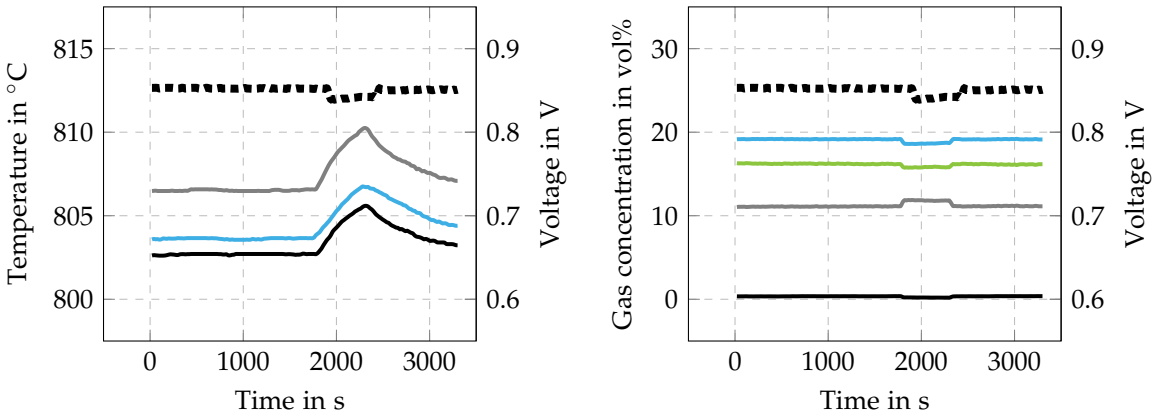

(a) Voltage (▪▪▪▪) and temperature (ϑ_1 (——), ϑ_2 (——), ϑ_3 (——))

(b) Voltage (▪▪▪▪) and gas analysis (H_2 (——), CO (——), CO_2 (——), CH_4 ——) during the carbon deposition

Figure 6.3: Cell voltage and temperature distribution in the anode plate. [7]

Information about the reactions that occurred while fuelling with $DR_{2.3}$ can be gleaned, from the subsequent gas analysis: gas volume fractions on the anode inlet and outlet depending on the load, both at the beginning of the experiment and after an estimated critical operating time of 44 h, as shown in Fig. 6.4. The volume fractions of single species at anode inlet under OCV are represented by single points, while lines represent the volume

fraction of single species as a function of current density. Solid lines provide information about the initial state of species trend and the dashed lines indicate species trend after the 44 h operation. Hydrogen species trend is plotted as a blue line, while the species trends of carbon monoxide, carbon dioxide, and methane are plotted as green, grey, and black lines, respectively. The trends in this figure show that the cell reforms very well, which can best be seen at OCV, where only chemical reactions occur. Electrochemical reactions are supported by external current flow. Due to the internal reforming of methane, an increase of the volume fraction of hydrogen and carbon-monoxide at the anode outlet, compared to the initial state at the anode inlet, is clearly recognizable at OCV; the methane and carbon-dioxide volume fraction shows a negative trend. The change in the methane volume fraction indicates a very high methane conversion rate. With the increasing load, the carbon monoxide and hydrogen volume fraction decreases, while the volume fraction of carbon dioxide as the reaction product rises compared to the initial state at the anode inlet. This fraction species trend proves occurrence of the water-gas shift reaction. Fig. 6.4 illustrates that the volume fraction of hydrogen and carbon monoxide has decreased after the estimated operating time of 44 h with $DR_{2.3}$, while the concentration of methane has increased. This indicates that Ni was covered with elemental carbon, and, therefore, the reforming reaction rate was inhibited. The increased concentration of carbon dioxide reveals that the Boudouard-reaction takes on greater significance and carbon is formed and deposited on the cell.

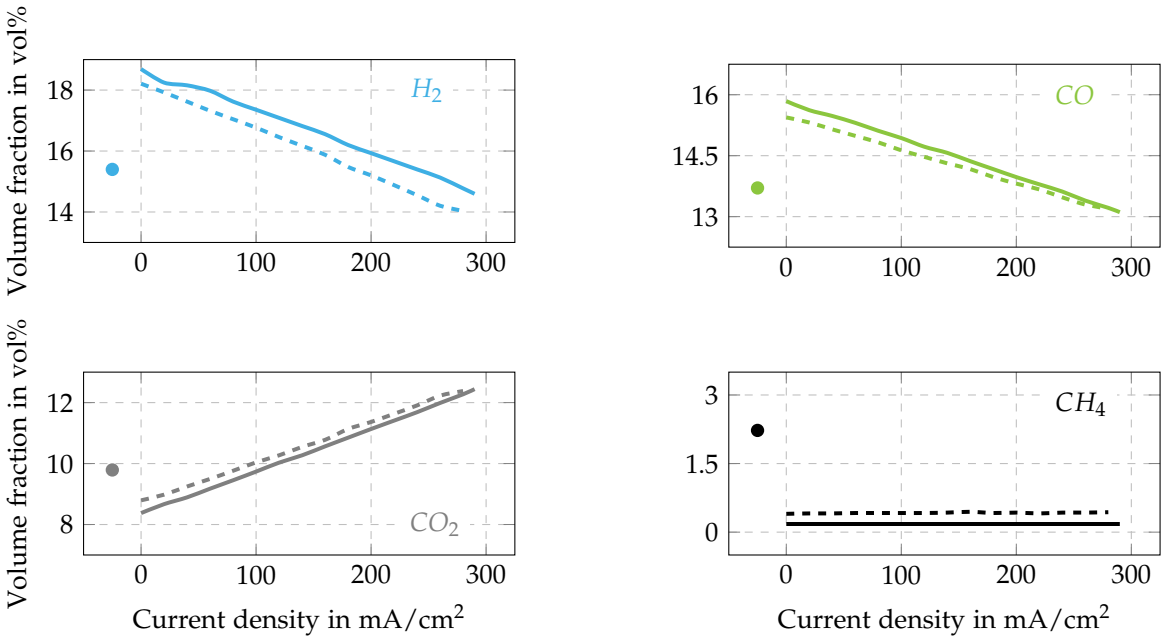

Figure 6.4: Gas volume fraction at the anode inlet (marked as point) and change of the gas volume fraction at the anode outlet depending of the load and time: 0 h (solid line), after 44 h fuelling with $DR_{2.3}$ (dashed line). [7]

In order to observe and investigate the phenomenon of fast carbon formation and deposition, the methane volume concentration in the fuel was increased, as seen in Tab. 4.1. For this purpose, the following discussion will be based on the cell behaviour obtained during operation under diesel reformate mixture DR_{14} containing 14 vol% CH_4. The results of occurred performance degradation caused by accelerated and enhanced carbon deposition process are outlined in Fig. 6.5. The voltage and power density, measured as a function of current density for a carbon-free anode and, indicated by a solid black line, are compared to an anode partially covered with carbon, depicted as a dashed black line, see Fig. 6.5a. Significant voltage and power losses were observed and the area between the two measured curves is hatched. Active catalyst sites on the fuel electrode are blocked by means of the coking effect, thus reducing the reforming activity of the cell. The loss of reforming activity can easily be detected by monitoring the methane concentration at the anode outlet. The methane volume fraction in the anode offgas, indicated by a black solid line, is represented on the left ordinate in Fig. 6.5b, while the methane conversion rate is shown on the right ordinate as a grey solid line. During the first three hours methane volume fraction at the anode outlet increased, and an overall increase of approximately 8 vol% was detected. It caused a significant decrease in the methane conversion rate. From almost 97 %, the converted methane was reduced down to 40 % for the blocked Ni-catalyst, as outlined in Fig. 6.5b. Interestingly, after approximately 3 hours, the methane conversion rate remained constant until the end of the experiment. At this state, equilibrium with carbon was reached, and no additional carbon was deposited onto the anode. The additional carbon deposition was therefore interrupted at this stage.

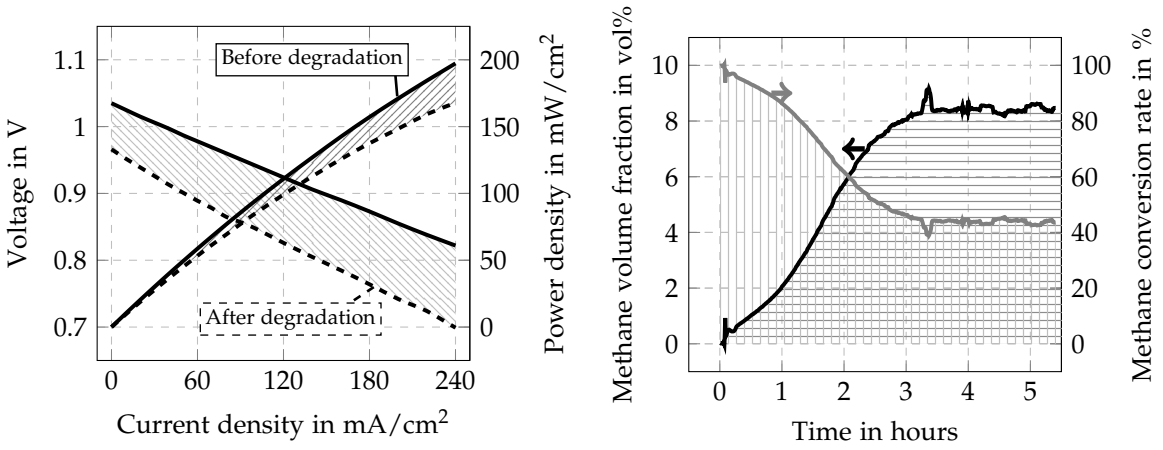

(a) Polarization curves measured before and after carbon deposition experiment

(b) Methane volume fraction at the anode outlet and methane conversion rate during the operation

Figure 6.5: Electrochemical cell performance obtained before and after carbon deposition experiment and methane reforming performance observed during the fueling with DR_{14}. [6]

Based on the information obtained from aforementioned experiments, several parameters important to the identification and investigation of cell degradation, as well as its prevention, are discussed. Fig. 6.6 shows how the changing volume fraction of methane in the fuel mixture impacts, and actually accelerates cell performance degradation. However, the change in the amount of methane does not just mean a change in one single variable; it also entails the simultaneous variation of a number of parameters, which depend on the methane concentration, such as S/C-ratio or CH_4/CO-ratio. The operating time, after which degradation of the cell performance was evident, during operation under specified diesel mixture and under constant load, is represented in Fig. 6.6a. A decisive criterion for the determination of the elapsed time was the achievement of the stationary state. This is explained as the state at which equilibrium with carbon is reached, as stated above. For example, when operated under modified diesel reformate including 9 vol% of CH_4, the voltage degradation rate of about 20 $\frac{mV}{h}$ was obtained. After this period, the degradation rate was reduced down to 5 $\frac{mV}{h}$ until no further degradation was observed. It can be assumed that, after this period, equilibrium with carbon was reached, and the amount of carbon formed equalled the amount of gasified carbon. This state is reached after 3 hours, if the cell is fuelled with the mentioned fuel mixture, including 14 vol% of CH_4. When diesel reformate, including 2.3 vol% of methane, was used as a fuel, no considerable impact on the cell performance was obtained until 44 hours, as already shown above. For this purpose, the cell was polarized to the higher current density, thus it was easy to observe the degradation rate under a higher load. However, during operation under fuel mixtures with a methane concentration equal to or higher than 9 vol%, degradation of the operating voltage was pronounced. As demonstrated in Fig. 6.6a, the estimated time for carbon deposition does not represent a linear function of the gas concentration, but is rather exponentially lowered with the increasing methane concentration in a fuel mixture.

In Figs. 6.6b, the degradation voltage is shown as a function of current density. The degradation voltage is calculated as the difference between the initial voltage and the voltage measured after the estimated time. The increasing amount of methane in the fuel mixture is represented by the rising intensity of the grey colour, from light grey (2.3 vol%) to black (14 vol%). Operation with the fuel mixture containing 20 vol% CH_4 resulted in massive carbon deposits after only 30 minutes. More information on this will be presented below. Next, it is apparent that the degradation voltage rate increases with increasing load. This effect occurs because the carbon deposited on the anode surface and within the porous structure, blocks the gas channels and the three-phase boundary, respectively. For this reason, both the fuel supply and the transport of oxygen ions through the anode are restricted, thus increasing the overall resistance, and diminishing the cell's performance. As result, electrochemical reactions are reduced with increasing current density. The degradation

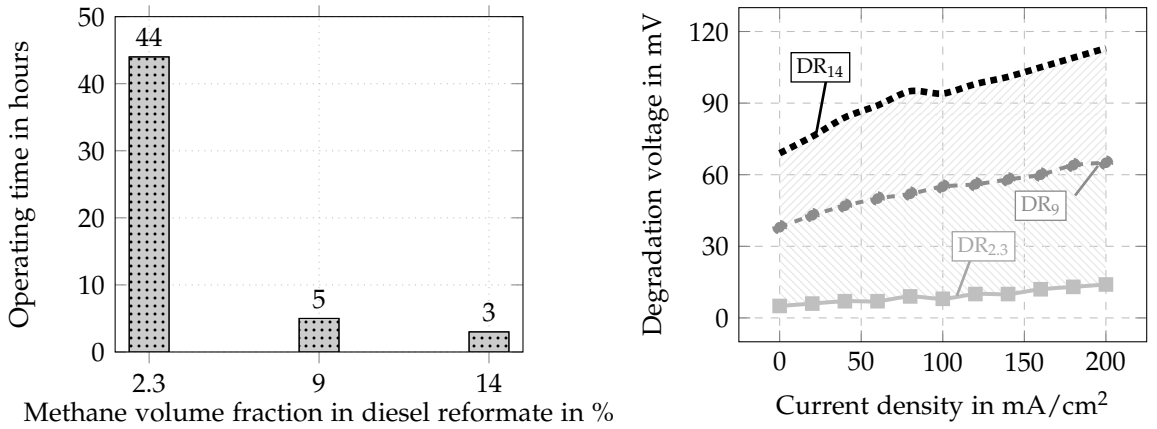

(a) Estimated operating times for different reformates

(b) Degradation voltage in mV after estimated operating time depending on the methane volume fraction

Figure 6.6: Degradation parameters depending on the methane volume fraction for diesel fuel mixtures $DR_{2.3}$, DR_9 and DR_{14}. [6]

voltage at 200 $\frac{mA}{cm^2}$, after fuelling with diesel reformate DR_9 including 9 vol% of methane for 5 h (grey line) rose as high as 80 mV, which represents a degradation rate of 9 %. The degradation rate increased up to 13 % or 118 mV, when the methane volume fraction in diesel reformate was set to 14 vol%, as illustrated by the black line, after an operating time of 3 hours. Furthermore, when the cell is operated under the fuel mixture with the lowest methane concentration of 2.3 vol%, as is typically used in APUs, the degradation voltage was detected to be between 1 mV and 8 mV in the current density range between 0 $\frac{mA}{cm^2}$ and 100 $\frac{mA}{cm^2}$, as can be seen in Fig. 6.6b, indicated by light grey line. When more power is drawn from the cell, the degradation effect was more pronounced, as explained above. Such a small amount of methane caused the slight deterioration of cell performance; the maximum degradation rate at 200 $\frac{mA}{cm^2}$ was 2 % (see Fig. 5.4d), or approximately 20 mV (Fig. 6.6b).

6.2 Impedance Spectroscopy for the In-operando Detection of Carbon Deposits at Early Stage

As discussed, under certain operating conditions, there is a risk of carbon deposits on the anode, which can cause the rapid degradation of the cell performance and microstructure. Increasing water vapour content in a fuel mixture can suppress carbon build-up. Nevertheless, this dilutes the fuel and significantly reduces both cell performance and overall efficiency. In order to maintain the desired cell performance, dilution of the utilized fuel with steam should be avoided. The critical operation points should be determined at an early stage, and appropriate regeneration techniques should be applied, thus preventing

rapid cell degradation. The carbon deposition processes that occurred inside the porous Ni-YSZ anode of the tested solid oxide fuel cells were obtained by means of in-situ electrochemical impedance spectroscopy. This characterization method made it possible to recognize the degradation process at an early-stage. The choice was made to represent the results obtained under different operating conditions as a function of various gas mixtures and varying polarization states.

6.2.1 Impedance Characteristics during Fuelling with DR_9 [2]

Electrochemical impedance spectroscopy measurements were applied during operation under modified diesel reformate, containing 9 vol% CH_4 (Tab. 4.1), in order to detect all of the performance variations caused by carbon depositions formed due to the mentioned fuel. The impedance spectra recorded at the initial state (solid black line) and after 0.5 h (blue line with blue points), 1 h (solid blue line), 1.5 h (dashed blue line), 4 h (dashed grey line) and 5 h (solid grey line) are depicted in Fig. 6.7. The spectra were measured at a current density of 120 $\frac{mA}{cm^2}$, in order to simulate realistic operating conditions.

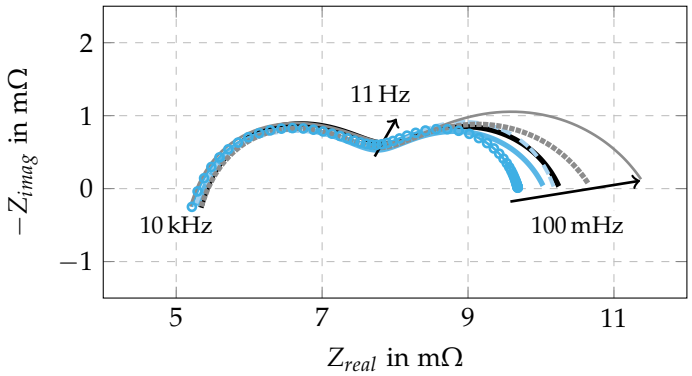

Figure 6.7: Electrochemical impedance spectra measured at 120 $\frac{mA}{cm^2}$ during the carbon deposition experiments using diesel reformate DR_9 including 9 vol% CH_4: initial state - 0 h (—), 0.5 h (—o—), 1 h (—), 1.5 h (– –), 4 h (·····), 5 h (——). [6]

The beginning of the carbon build-up process shown in spectra indicated by blue lines, is characterised by an improved cell conductivity compared to the initial state (black solid line) and decreased overall impedance, since a limited amount of carbon was formed over the anode-surface. After 0.5 h, the best conductivity was observed, as illustrated with the blue dotted line. Further operation and carbon deposition resulted in a slight loss in conductivity (blue solid line after 1 h), and finally, after 1.5 h, the initial state was achieved (blue dashed line). This effect is graphically illustrated in Fig. 6.9. Fig. 6.9a depicts the carbon free-anode, thus comparing it with the impedance spectra indicated by the black line. Grey sites

[2] Segments of this section have already been published in [6].

represent the catalytically active Ni, while the O^{2-} conducting YSZ is illustrated in blue. Obviously, Ni-particles are not completely connected with each other on the anode surface, thus decreasing the maximum electrical conductivity. When electrically conductive carbon particles (brown sites) partially cover the anode surface, thus better linking Ni-particles with each other, the overall conductivity increases, thus decreasing the measured impedance (as illustrated with blue lines in Fig. 6.7). The scanning electron microscopy images obtained at this level (Fig. 6.8a) show a thin carbon layer, accordingly to the illustration in Fig. 6.9b, which only covers the anode surface, but does not block the pores. The ability of carbon depositions to improve cell conductivity was also demonstrated in [115, 140]. In those studies, it was reported that a small amount of carbon deposited on the anode surface seems to connect the nickel particles together, thus improving conductivity.

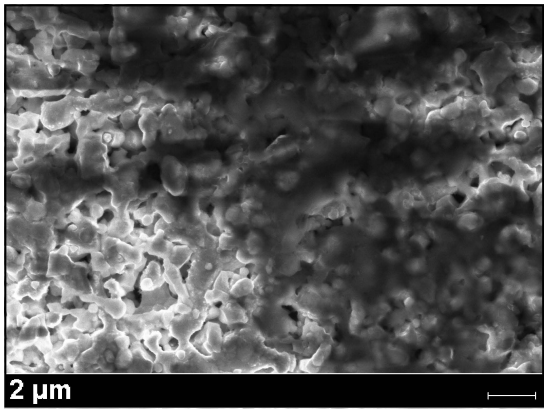

(a) Thin carbon layer on the anode surface

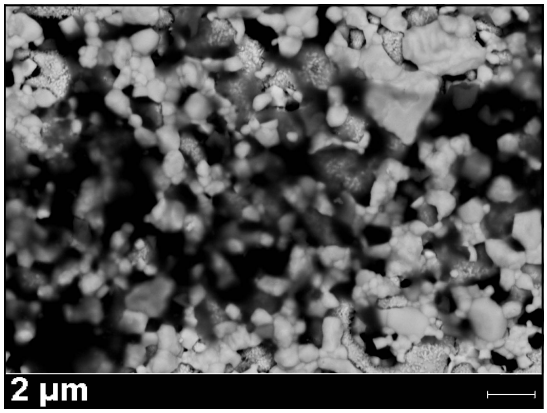

(b) Massive carbon deposits on the anode surface and in the gas pores

Figure 6.8: SEM-analysis of the anode surface after the estimated fuelling time of 5 h under DR_9 as fuel. [8]

Eventually, the additional formation and deposition of carbon led to the coverage of the fuel supply inlet manifold, gas pores, and active TPB sites, thus inhibiting the chemical and electrochemical reactions and preventing fuel distribution. This effect is detected by the rising impedance or cell resistance, as illustrated with the grey curve plots in Fig. 6.7. The dashed grey line refers to the state reached after 4 h of fuelling with DR_9 and the solid grey line demonstrates the cell impedance obtained after 5 h. The impedance spectra showed a rise in the anode-specific low frequency range, but also a slight increase in the high frequency range because the blocked pores disabled the undisturbed transport of oxygen ions through the anode, [5, 26, 163, 164]. This effect is also obvious in the microscopic images of the fuel electrode in Fig. 6.8b, where massive carbon depositions on the anode surface and in the porous structure can be seen. Below are graphic illustrations of different stages of carbon depositions in order to create a better understanding of the impact of massive carbon accumulation in gas channels (Fig. 6.9c).

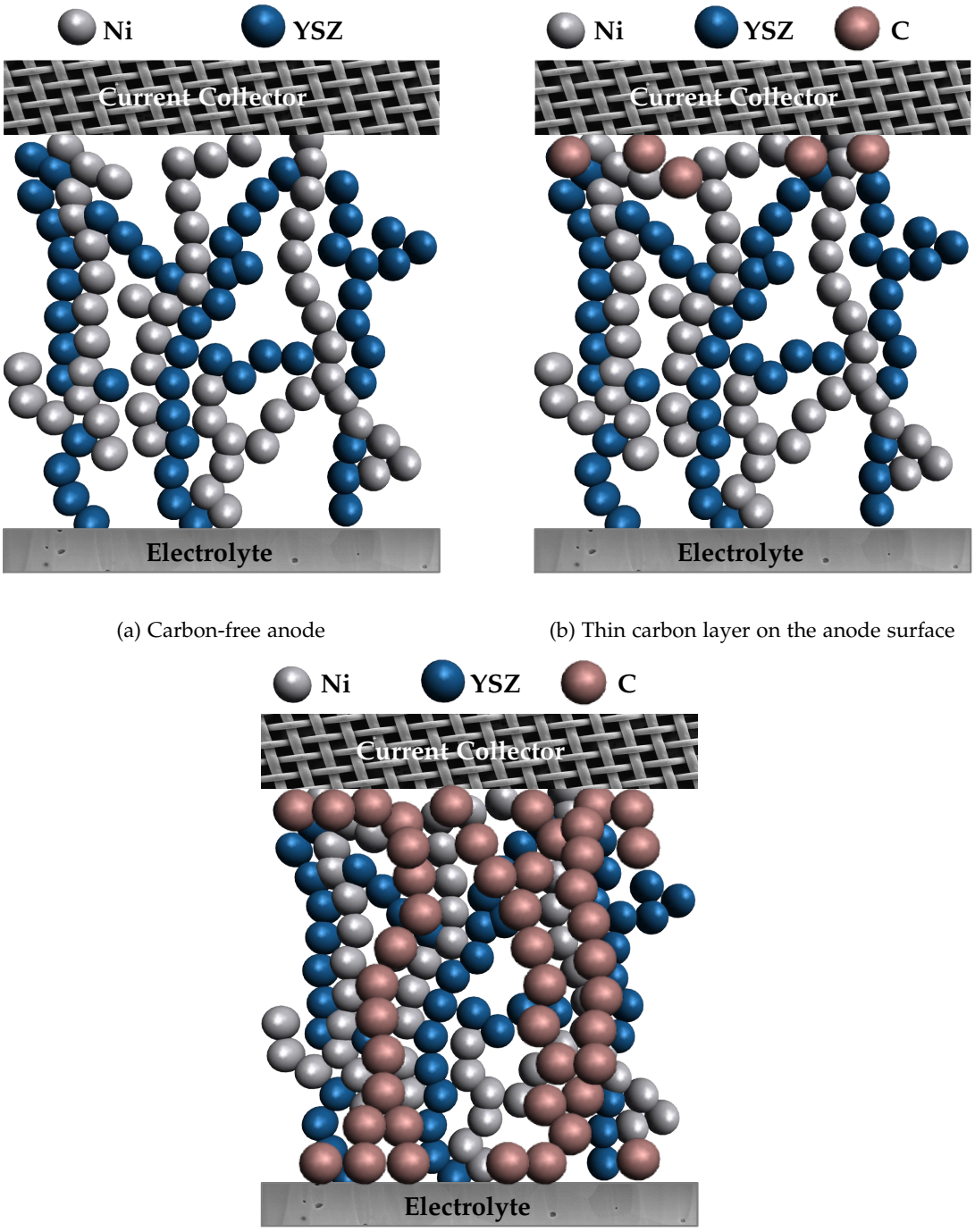

(a) Carbon-free anode

(b) Thin carbon layer on the anode surface

(c) Gas channels blocked with carbon

Figure 6.9: Graphical illustration of different carbon deposition stages.

6.2.2 Impedance Characteristics during Fuelling with $DR_{2.3}$ [3]

The performance of the ASC-SOFC as well as its resistance to carbon deposits during operation under diesel reformate $DR_{2.3}$ containing 2.3 vol% CH_4 and at OCV will be discussed in this section. For the purpose of the analysis under open circuit conditions, and to meet the criterion of having system stability for valid impedance measurements, the cell was fuelled with the dry gas mixture of 45 vol% of H_2 in N_2 (gas mixture $\boldsymbol{a}_{45}$ in Tab. 5.1) during the impedance analysis. The impedance spectra obtained at OCV, before (indicated by a black solid line) and after (indicated by a blue solid line) the carbon occurrence on the anode, are shown in Fig. 6.10. The EIS measurements show that there is no change in series resistance R_S (expressed through the high-frequency arc), but the polarization resistance R_P (as total resistance) decreases significantly after the carbon is deposited on the cell surface. The initial impedance spectra (indicated by a blue solid line) with total resistance of $Z_{real} = 0.137\,\Omega$ and $Z_{imag} = 0.0485\,\Omega$ was reduced to $Z_{real} = 0.118\,\Omega$ and $Z_{imag} = 0.039\,\Omega$ after the carbon deposition on the anode (blue dotted line). This result is in

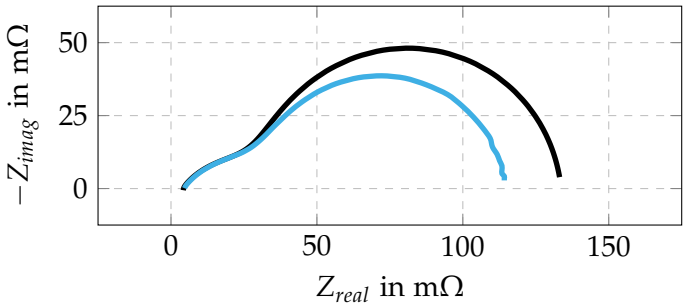

Figure 6.10: Electrochemical impedance spectroscopy: Impedance spectrum of the ''healthy'' cell (—), impedance spectrum of the cell covered with carbon after estimated fuelling time of 44 h (—). [7]

good accordance with Mermelstein et al. [139]. The measured impedance spectra in their study showed a decreased polarization resistance after exposing the cell to tars and a high steam concentration of 7.5 vol%, measured under open circuit voltage, and indicated that small deposits of carbon may temporarily increase anode conductivity. The distribution of carbon deposits (shown in Fig. 6.11) could also refer to the increased surface conductivity. It is apparent from the EDX mapping that carbon uniformly covered the catalyst Ni and YSZ particles. As already known, YSZ has dielectric performance and conducts only oxygen ions. Compared with this, besides being a very good catalyst, Ni is also a very good electric conductor and conducts electrons. Since carbon, which is also a good electrical conductor, covered not only Ni but also the YSZ surface (as can be seen in Fig. 6.11), this could have contributed to the increase in the surface conductivity.

[3] Segments of this section have already been published in [7].

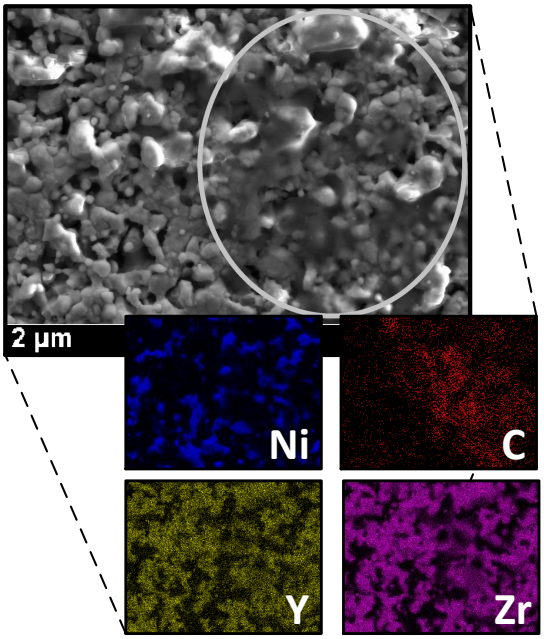

Figure 6.11: SEM micrograph and EDX-mapping of the anode surface after fueling with $DR_{2.3}$. [7]

The results observed in this case also allow for the following assumption. During the impedance measurements of the carbon-free cell, performed under H_2/N_2 mixture, only hydrogen was available as a fuel on the anode side. After the carbon deposition process, the impedance was measured under the same conditions as before, but the deposited carbon on the anode was able to react with O^{2-}-ions and thereby, to introduce a second fuel component: the gaseous product of carbon and oxygen. The additional fuel caused further overvoltage-losses and the additional current, according to the Butler-Volmer-Equation (Eq. 2.24). Since galvanostatic impedance measurements were carried out, the current density remained unchanged during the measurements. Thus, the increasing overvoltage-losses reduced the voltage response signal compared to the voltage response signal of the carbon-free cell. This effect is indicated by the lower measured values of the polarization resistance. It is assumed that this effect is exclusively possible at OCV, and only when the anode surface is partially covered with carbon, such as in this case. If the carbon deposits cover the whole anode structure - including the three-phase boundary and the gas channels - the polarization resistance increases, as described in the previous section, and this effect is well recognized under high load. Carbon depositions on the three-phase boundary, at which the electrochemical reactions occur, would decrease electrochemical activity, and the

blocking of the gas channels would hinder gas diffusion, and thus ion transport, as stated in Section 6.2.1.

6.3 Post-mortem Analysis of the Anode after Carbon Deposition[4]

All of the changes that occurred during the carbon deposition experiment were verified by means of a microscopic examination of the anode surface and cross-section. Fig. 6.2 shows a photograph of the anode surface after the fuelling with a diesel mixture containing 2.3 vol% CH_4. During the cooling-down process, the anode side was fed with nitrogen. The surface of the depicted cell is divided into three parts, marked by pink rectangles, which indicate the three zones where the temperature was measured. Carbon deposits, marked by red rectangles, can be only seen on the topside, and the bottom side of the cell, mainly near the anode outlet. In this regard, it is crucial to note that, during cell loading, it was observed that the temperature increased dramatically in the middle of the cell - obviously more than on the side. This implies that the most current flows through the area where the temperature strongly increased. The influence of the current density distribution on the carbon formation is a well-known fact. The higher the current density, the lower the carbon formation ratio [94], and, as mentioned, since the cell mid-area was under the highest load, no carbon was formed in this area. The post-mortem analysis of the cell demonstrated that the anode surface was covered with carbon after operation with the diesel fuel $DR_{2.3}$ under 100 $\frac{mA}{cm^2}$. The surface (Figs. 6.12a, 6.12b) and cross-section (Fig. 6.12c) microscopic analysis of the cell (sites marked with red rectangles on the top-right side) were performed in order to evaluate how carbon was distributed over the cell, and to determine if the cell structure was damaged thereby. After an estimated 44 hours of operation and exposure to the diesel fuel, the anode structure was still porous, and there was no change in structure except that carbon occurrence was detected. On the place marked in Fig. 6.12a, a large amount of carbon was detected via EDX-analysis (see Fig. 6.12d) through the appearance of the C-peak, while the elementary distribution for all chemical elements present - Ni, Y, Zi and C, can be seen in Fig. 6.11, which shows that carbon uniformly covered the Ni, Y and Zi particles, and thus covered not only the catalytic Ni, but also YSZ. It seems, from the detailed imaging of the surface (see Fig. 6.12b), that the carbon was not firmly connected to the anode structure, but only formed a thin layer, which covered a part of the anode surface. The morphology of the cell, which includes the anode as support layer and anode functional layer, electrolyte layer as well as barrier layer and cathode functional layer, shows no damage, and has the same properties as that of a healthy cell (when compared to the layer distribution of a new

[4]Segments of this section have already been published in [6, 7].

cell shown in Fig. 4.1). On one part of the anode surface a thin layer of carbon particles can be detected (site marked with a white rectangle), but there were no carbon deposits in the gas channels in the deeper anode structure or on the triple-phase boundary.

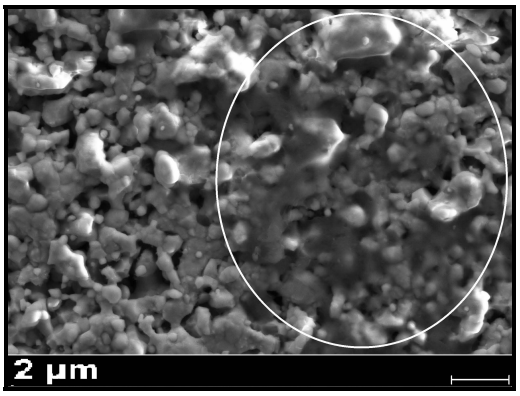

(a) Anode surface covered with carbon 2 μm

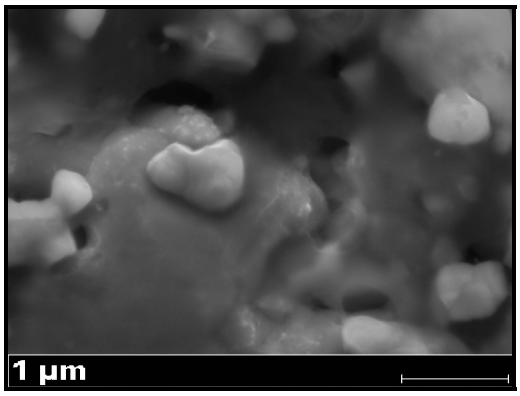

(b) Anode surface covered with carbon 1 μm

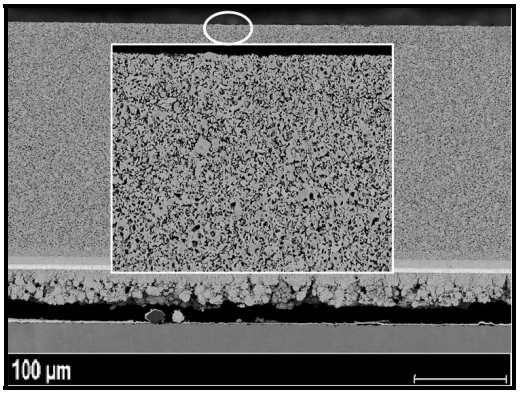

(c) Cross-section of the cell

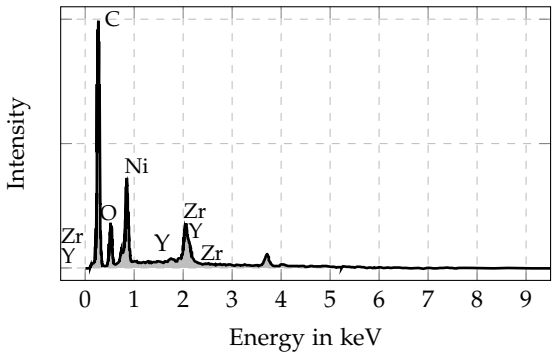

(d) EDX-analysis of the anode covered with carbon

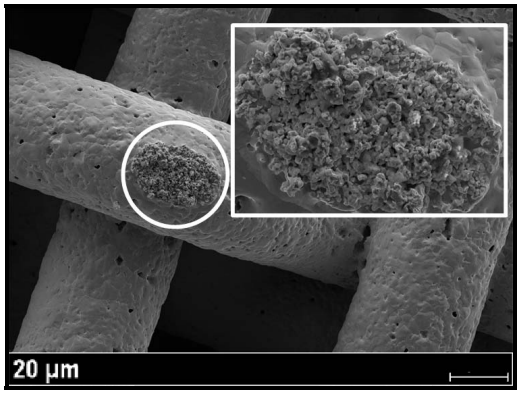

(e) Contact point of Ni mesh with the anode

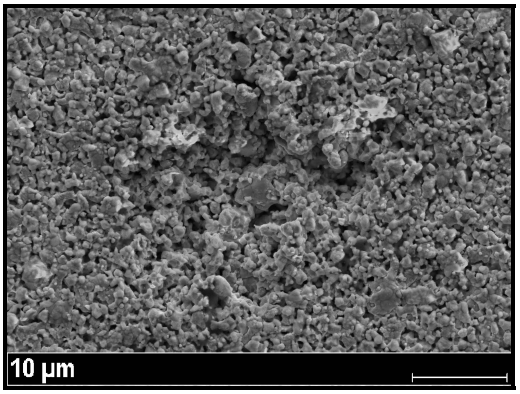

(f) Anode surface after contact with Ni mesh

Figure 6.12: SEM-analysis of the cell after feeding with diesel reformate $DR_{2.3}$. [7]

A topography of the contact surface between the Ni-mesh and the anode, after the carbon deposition process was finished and the cell had been cooled down in nitrogen, can be seen

in Figs. 6.12e and 6.12f. Once the experiment was finished and the cell had been removed from the cell housing, the Ni-mesh and the anode had to be separated from each other. The samples were then microscopically analysed. SEM-analysis showed damage at the contact points both on the nickel mesh (Fig. 6.12e) and on the anode surface (Fig. 6.12f) after the experiment, which proves that they had very good contacting with one another. There was carbon detected on the contact point between the nickel mesh and the anode, which confirms high catalytic activity on the contact points. This further implies that the same Ni-mesh should not be used for more than one experiment, in order to ensure good contacting and to prevent a possible reaction with the carbon deposited.

Additionally, Raman spectroscopy was observed on different points, both on the Ni-YSZ anode covered with carbon (the sites marked with both red rectangles in Fig. 6.2) and the carbon-free anode surface. The spectra are illustrated in Fig. 6.13. The Raman spectra of the areas covered with carbon in Fig. 6.2 show diffuse bands, of between $1600\,cm^{-1}$ and $1200\,cm^{-1}$ with a peak at $1350\,cm^{-1}$, which may indicate either a contamination with carbon or more generally with graphite. In the Raman spectrum, the bands for graphite should be at $1560\,cm^{-1}$ (G-band) and $1350\,cm^{-1}$ (D-band). It has been reported by [165--168] that the D band is related to amorphous carbon or graphite structures with defects, grain boundaries, or other non-crystalline structures, while the G band represents the carbon-carbon bonding within the graphitic structure. Since there is no observable G-band at $1560\,cm^{-1}$ in Fig. 6.13, and the peak centred at $1350\,cm^{-1}$ is very broad, it is hard to say from the Raman spectra whether these indicate graphite or a mixed phase, but, in any case, it is evidence of some disordered carbon structure. Sumi et al. [169] showed different Raman spectra obtained for two anode structures (Ni-YSZ and Ni-ScSZ), where two peaks were observed at $1350\,cm^{-1}$ (D-band) and $1580\,cm^{-1}$ (G-band), while Li et al. [170] reported only one band at $1540\,cm^{-1}$, represented as the aromatic ring systems. However, due to the difference in intensity of contamination, the obtained peaks at $1350\,cm^{-1}$ shown in Fig. 6.13 differ over the anode surface. The contamination intensity can also simply be inferred from the intensity of the black carbon deposits, as seen in Figs. 6.2 and 6.13. Furthermore, the spectra observed on the carbon-free anode surface show no peaks between $1600\,cm^{-1}$ and $1200\,cm^{-1}$, but only at approximately $600\,cm^{-1}$, which is typical of YSZ.

As previously mentioned, a microscopic analysis was carried out after every experiment, once for each of the four diesel reformate mixtures. Since no significant changes were observed with regard to carbon formed by feeding the cell with a methane concentration higher than or equal to 9 vol% in a diesel mixture (DR_9, DR_{14} and $DR_{20.3}$, as shown in Tab. 4.1), the following section presents results obtained after fuelling with DR_9. In this context, it is important to point out that the higher amount of methane in the fuel mixture

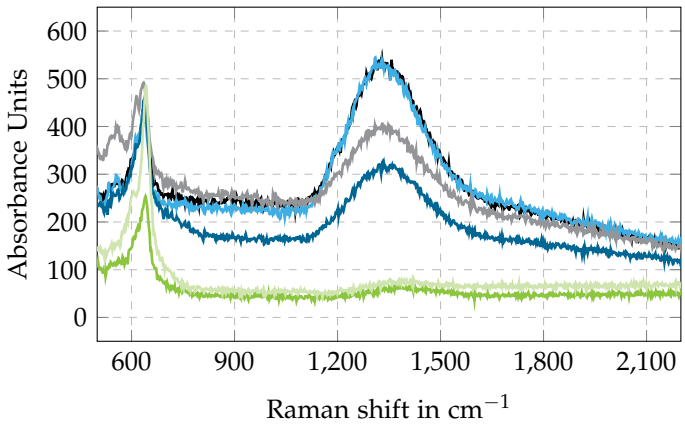

Figure 6.13: Raman spectra of different points on the Ni-YSZ anode covered with carbon: marked surface on the top right in Figure 6.2 (—— and ——), two points with different contamination intensity on the marked surface on the bottom right in Figure 6.2 (—— and ——), carbon-free anode surface (—— and ——). [7]

used led to the formation of filamentous carbon structure, since this occurrence was not observable for $DR_{2.3}$.

Fig. 6.14 provides detailed insight into the cell microstructure after carbon build-up, based on fuelling with DR_9 for 5 hours at 800°C. For the sake of the microscopic analysis, specific sites on the anode were marked and are referred to with the same number: Ni (1), YZS (2) and C (3). Fig. 6.14a shows the SEM-image of the carbon-free Ni-YSZ anode surface. After the experiments, the Ni-YSZ surface was permanently covered with carbon particles, as can be seen in Fig. 6.14b. A magnified view of the carbon-free anode surface is shown in Fig. 6.14c, while the deposited carbon is visible in Fig. 6.14d. The area in this figure marked with a black circle indicates mechanical damage on the anode surface. This represents the contact point with the Ni-mesh, and thus provides evidence of the very good contacting between the anode and the mesh. Damage of this kind can be seen over the entire anode surface and also occurs on the Ni-mesh. In view of this, as stated above, Ni-mesh should not be re-used for electrical contacting of the cells once it has been removed. Detailed microscopic investigations also showed that different types of carbon were found on the anode. The growth of amorphous carbon on the anode surface is depicted in SEM-image in Fig. 6.14e. This carbon was formed not only on the Ni-catalyst, but also uniformly covered the Ni-cermet and YSZ-sites. Amorphous carbon also induced Ni-YSZ microstructure degradation, which will be addressed in detail in Section 6.3.1. Furthermore, it is apparent from the cross-section overview in Figs. 6.14f that the carbon deposition on the electrolyte-anode boundary layer was formed as filamentous carbon nanofibers.

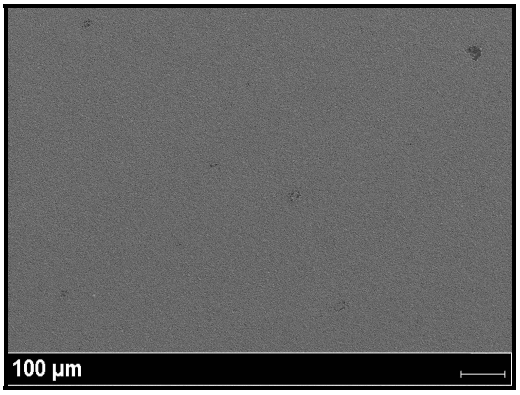

(a) SEM-micrograph of the carbon-free anode surface

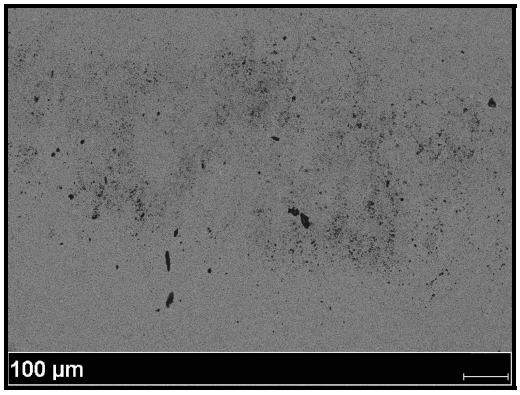

(b) SEM-micrograph of the anode surface after carbon deposition experiment

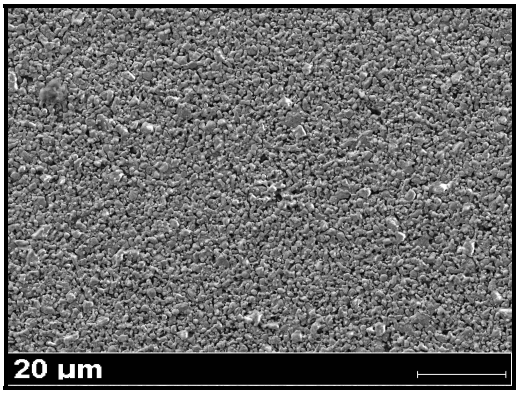

(c) Enlarged SEM-micrograph of the carbon-free anode surface

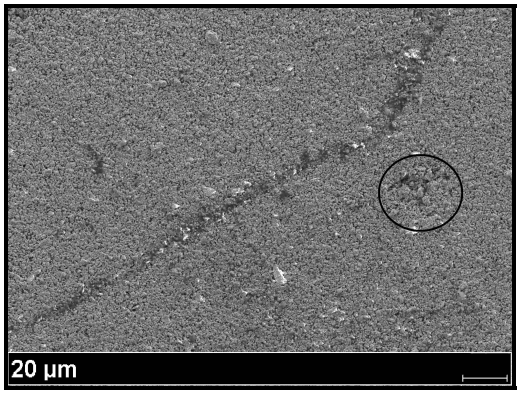

(d) Enlarged SEM-micrograph of the anode surface after carbon deposition experiment

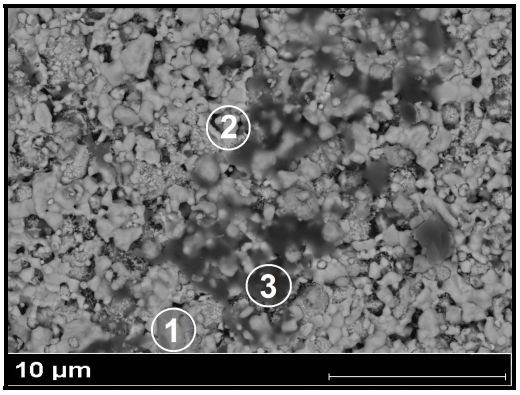

(e) Anode surface after carbon deposition experiment

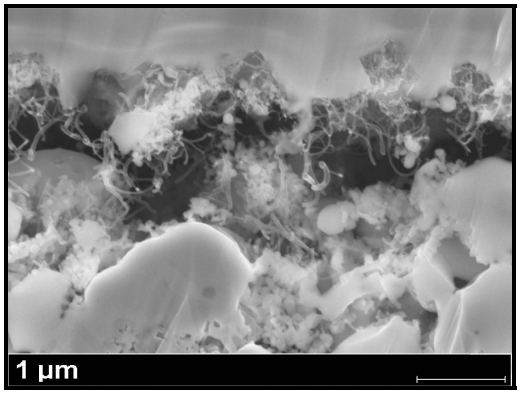

(f) Cross-section of the boundary layer after carbon deposition experiment [6]

Figure 6.14: SEM-analysis of the anode surface and cross-section view before and after carbon deposition experiment using DR_9 as fuel.

6.3.1 Anode Microstructure Degradation [5]

Much effort has been devoted to analysing carbon formation on the Ni-catalyst and its effect on the nickel microstructure. Many studies have discussed how carbon is first formed on the catalytic active sites and how, after the catalyst surface is covered, the gas channels will be blocked. The results of this work, based on experimental analysis and microstructure investigation, have certainly demonstrated that carbon was uniformly formed on Ni and YSZ, and its impact on the overall anode structure has been presented.

Fig. 6.15 shows the surface and cross-section of the Ni-YSZ sample before and after exposure to the modified diesel reformate fuel DR_9 (Tab. 4.1) including 9 vol% of methane. It thus shows the changes to the cell microstructure that occurred. The SEM-images are in the order of 1-10 μm in size. In all of the samples analysed, regardless of the amount of methane in the fuel stream, the presence of carbon induced the same degradation effect. The microstructural changes to Ni-YSZ were observed as the crushing of the YSZ-particles as well as their deposition on the Ni-catalyst; these observations were also confirmed by means of EDX-analysis and EDX-mapping. The Ni-YSZ microstructure of a cell before a carbon deposition experiment is shown in Fig. 6.15a. From the morphological point of view, the uniform distribution of Ni and YSZ, without a mixed-phase, is clearly apparent. The same effect is visible in the cross-section overview (see Fig. 6.15e) of the carbon-free anode sites. The structural distribution of Ni and YSZ particles for a carbon-free cell, investigated with the aid of EDX-analysis, can be seen in Fig. 6.15c.

When comparing these samples to the anode surface after carbon deposition is made, strong morphological changes are visible. It is clearly apparent that YSZ-particles are crushed into very small pieces, which cover the nickel particles (Fig. 6.15b), thus reducing the catalytic active surface. The two marked points, 1 and 2, in Fig. 6.15b, characterised with EDX-analysis (Fig. 6.15d), refer to clear deposition of ZrO_2 on Ni-particles. The same occurrence was also seen with the aid of a cross-section analysis, shown in Fig. 6.15f. Similar degradation behaviour of the Ni-YSZ-based anode structure is discussed by Novosel et al. [25] and Nikooyeh at al. [116].

[5] Segments of this section have already been published in [6].

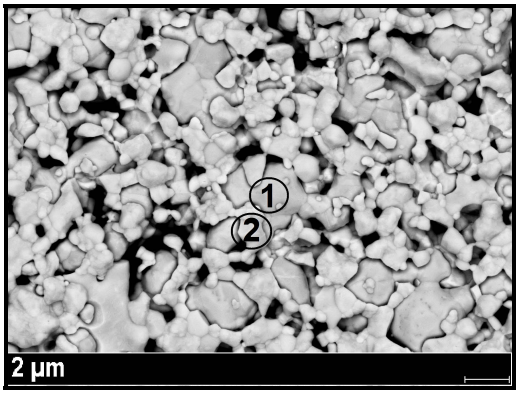

(a) Ni-YSZ anode surface before carbon build-up [6]

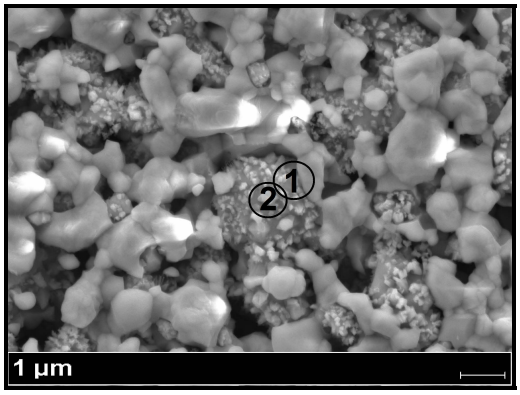

(b) Ni-YSZ anode surface after carbon build-up [6]

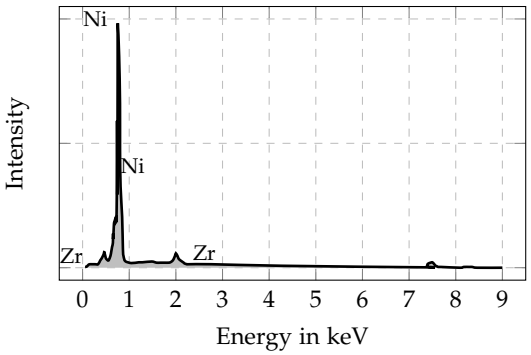

(c) EDX-analysis of the point 1

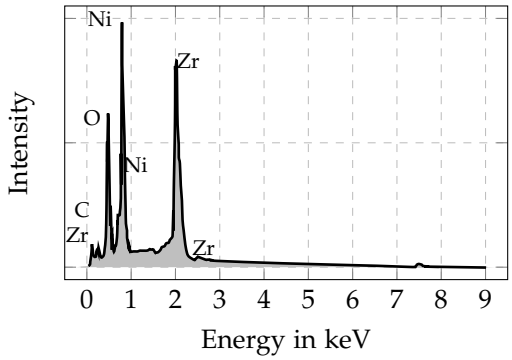

(d) EDX-analysis of the point 2

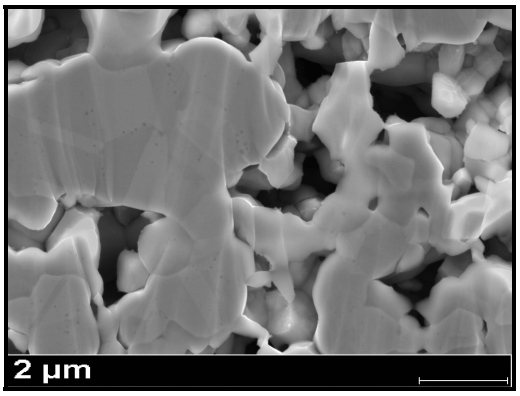

(e) Cross-section of the Ni-YSZ middle layer before carbon build-up

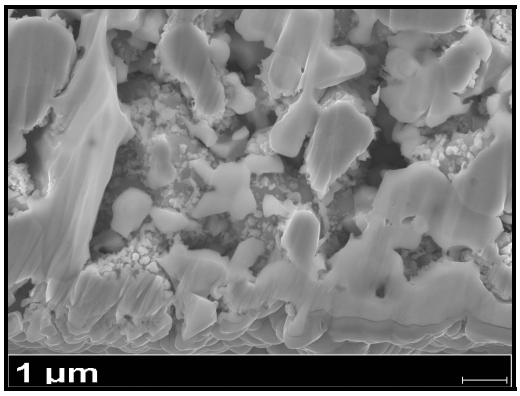

(f) Cross-section of the electrolyte-anode boundary layer after carbon-build up

Figure 6.15: SEM-analysis of the anode surface before and after carbon deposition using DR_9 as fuel.

In each case, amorphous carbon was identified as a dark layer without a clear structure, which covered the surface of the anode, as shown in Fig. 6.16a. Most of the surface showed the presence of the aforementioned degradation phenomenon. The presence of filament-like carbon is visible in Fig. 6.16b, and, interestingly, was detected only on the electrolyte-anode boundary layer. The morphologies visible in Fig. 6.16b represent crushed YSZ-particles,

which were not really deposited and sintered with Ni-particles, but rather exist as separate units. This investigation has shown that amorphous carbon is very destructive for the Ni-YSZ-structure, while carbon nanofibers also induce the degradation of YSZ particles, but not even lead to their deposition on the Ni-catalyst. However, they can lead to irreversible anode delamination. Sehestad [171] suggest that carbon nanofibers are one of the most destructive carbon forms. Rostrup-Nielsen and Trimm [91] claim that nickel-carbide is its preliminary stage. Because of possibility of irreversible damage to the anode, it is necessary to enable carbon degradation detection at an early stage, before carbon nanofibers are formed.

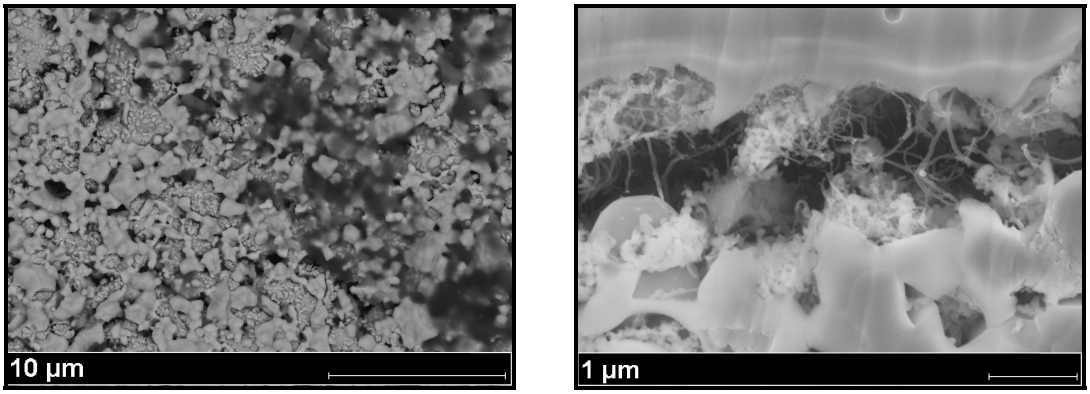

(a) Amorphous carbon on the anode surface

(b) Carbon nanofibers at the anode-electrolyte boundary layer

Figure 6.16: Differentiation of type of carbon deposition.

6.4 Concluding remarks

This chapter has demonstrated how the depositions of carbon on the porous Ni-YSZ anode can be induced, and scrutinized the impact of such deposits on cell performance. Moreover, strategies for the identification of carbon deposits at an early stage were provided. For the purpose of providing a detailed analysis, valid for a potential practical application, industrial-sized anode-supported solid oxide fuel cells were employed for this investigation. The cells were polarized, and fed with synthetic diesel reformate mixture containing 2.3 vol% CH_4, as typical in auxiliary power units, thus replicating real operating conditions. In order to examine the fast carbon formation process, modified diesel reformates with increased methane volume fraction were supplied to the fuel electrode. The methane concentration in modified diesel reformate was varied between 9 vol%, 14 vol% and 20.3 vol%.

The carbon build-up process on the Ni-catalyst, and, in fact, anywhere in the cell's fuel supply manifold, was detected at an early stage by means of electrochemical impedance spectroscopy, current/voltage measurement, and gas analysis. Methane, including the

decreasing steam/carbon ratio, was identified as having a major impact on the degradation rate at the typical operating temperature of 800°C for anode-supported solid oxide fuel cells. The critical operating time for carbon to form and be deposited on the anode was found to be strongly dependent on the amount of methane in the fuel mixture. For lower amounts of methane in the fuel mixture, such as 2.3 vol%, degradation of the cell performance was observed after 44 h. After accelerated carbon deposition process, due to an increase in the methane concentration of the gas mixture in use, the total critical operating time was reduced. In addition to the in-situ characterization techniques used, an ex-situ post-mortem analysis was performed, in order to obtain reliable and complete information about the cell microstructure after the carbon deposition process. A detailed microscopic investigation showed that carbon was uniformly formed over the Ni- and YSZ-sites. Massive carbon deposits not only caused the degradation of the cell performance, but also changed the Ni-YSZ structure. The crushing of YSZ-particles and their deposition on the Ni-catalyst were determined to be degradation phenomenona that occur if the carbon formation process in not interrupted at an early stage.

Development of Regeneration Strategies

In order to extend the lifetime of the cells used, various regeneration approaches were examined in this work. The primary and overriding goal of this thesis was to develop an effective and cell-protecting strategy for carbon removal and the restoration of electrochemical cell performance. The strategies employed were based on the use of hydrogen, water vapour, carbon dioxide and oxygen enriched gas mixtures. Detailed information about the gas composition and set parameters for the individual methods are listed in Tab. 4.2. A novel regeneration approach that involves the application of overvoltage was developed for the purpose of successful regeneration. The diverse gasification strategies employed, and their impact on cell performance, are summarized in this chapter. Moreover, several failure modes, such as Ni-oxidation and cathode degradation, were also induced. After the failure mode occurred, the effectiveness of the regeneration approaches as developed for specific cases was evaluated.

The volume flow of the regeneration gas mixture used was generally set to a constant 2.4 SLPM, unless otherwise stated. The cathode side was always supplied with 4 SLPM, except otherwise specified. Each of the regeneration strategies presented in this chapter were examined for the purpose of removing the carbon formed from the four diesel mixtures employed in this thesis, with their varying methane concentrations. To prevent changes to the operating temperature, thus avoiding thermal cycling, and to provide fast carbon removal, the operating temperature was kept constant at the optimal value of 800°C. However, in order to accommodate the detailed examination of several regeneration approaches, which involved the risk of Ni-reoxidation, the operating temperature was decreased to as low as 500°C.

7.1 Hydrogen- and Water Vapour-based Regeneration Strategies[1]

First of all, regeneration strategies $\boldsymbol{R}_1$ and $\boldsymbol{R}_2$ (Tab. 4.2) were combined and applied in order to improve the cell performance. Complete carbon removal and regeneration of the cell performance was achieved after approximately 44 hours. The regeneration approach $\boldsymbol{R}_2$, containing humidified H_2 in N_2, was applied for 24 hours. After this period, cell performance had not improved. To return to initial performance, the cell had to be operated for another 20 hours with the dry $\boldsymbol{R}_1$ regeneration gas mixture, thus combining what were originally two approaches into one successful strategy.

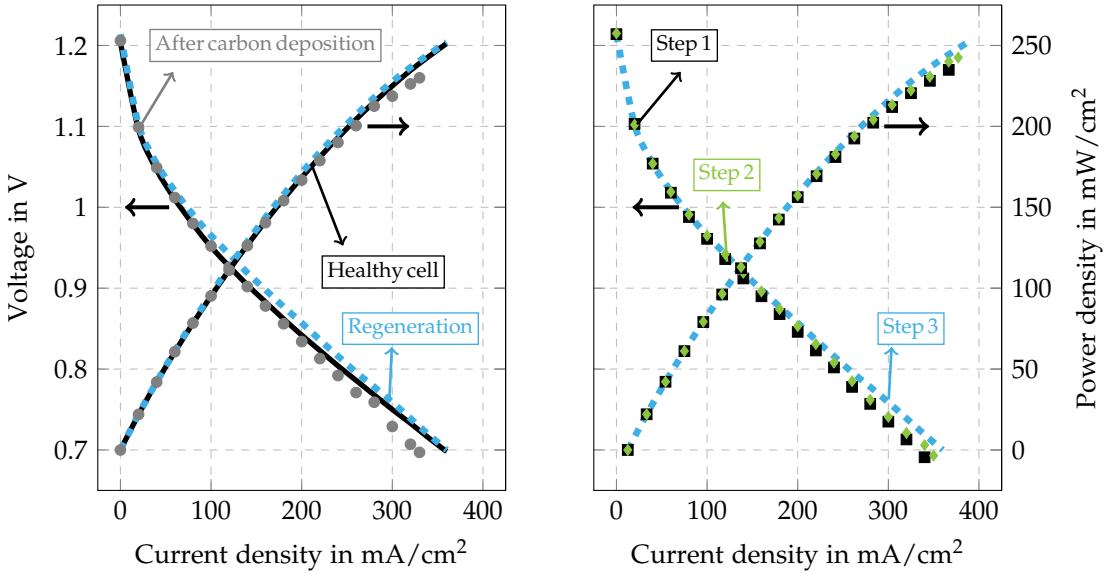

Figure 7.1: Change of voltage-current density and voltage-power density curves during the regeneration process. [7]

Fig. 7.1 shows the polarization and the power density curves of the tested cell before and after the operation with diesel fuel $DR_{2.3}$, as well as the changes in the cell performance as a result of the different regeneration steps. The deposition of carbon was induced by fuelling the anode with $DR_{2.3}$ for 44 h at 800°C, as described in detail in the previous chapter. After the formation of carbon on the anode side, the current density was decreased by 30 $\frac{mA}{cm^2}$ at the minimum voltage of 0.7 V, thus reducing the total cell power. When the cell was supplied with the $\boldsymbol{R}_2$ regeneration gas for 24 hours, the open circuit voltage reached an initial value of 1.214 V. The performance characteristics were improved over the whole current density range in this case, but the greatest performance enhancement was detected in the range of middle current densities (100-250 $\frac{mA}{cm^2}$). The dry reference gas enhanced the cell loading

[1]Segments of this section have already been published in [7].

and enabled further regeneration over the whole load range. Continued regeneration with the dry reference gas resulted in total cell regeneration. Over time, operation with the dry reference gas always led to better regeneration in the range of high current densities. Long-time operation with this gas mixture enabled the further activation of the cell, and revealed that the performance characteristics were improved in the range of high current densities versus the initial cell performances, due to the additional anode activation with dry hydrogen.

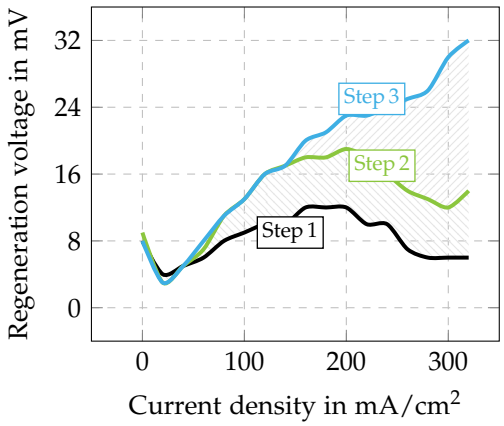

(a) Regeneration voltage after each regeneration step

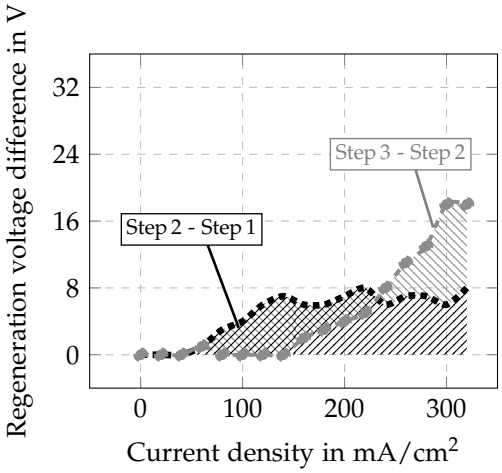

(b) Regeneration voltage difference

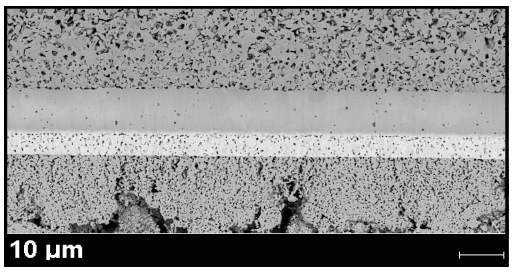

(c) SEM-micrograph of the cell cross-section

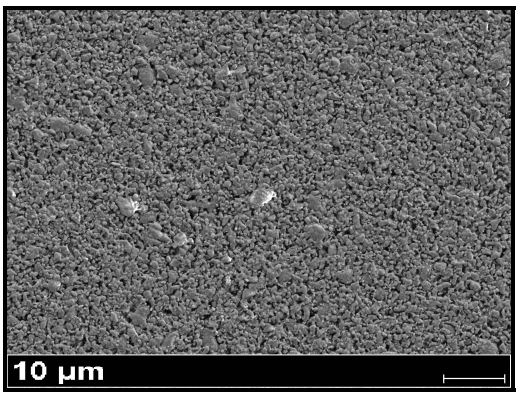

(d) SEM-micrograph of the anode surface

Figure 7.2: Electrochemical performance after single regeneration steps and cross-section SEM-micrographs after applying the defined regeneration strategy.

More precise information on the increasing voltage values after single regeneration steps, specified as regeneration voltage, is provided in Figs. 7.2a and 7.2b. The single regeneration steps are represented by the same colours as in Fig. 7.1. As previously noted, the first regeneration step brought about the highest performance enhancement in the middle-current range. This is because of carbon gasification from the anode surface, thus making the

three-phase boundary available. Fuelling with the dry $\boldsymbol{R}_1$ gas mixture specifically improved the performance in the range of higher current densities (200-300 $\frac{mA}{cm^2}$), as illustrated by the green and blue lines. The information obtained by means of microscopic examinations, after carbon removal and performance regeneration, is shown in Fig. 7.2c as a cross-section view of the electrolyte-electrodes boundary layer and in Fig. 7.2d as the anode surface. Based on the microscopic observations, the cell-protecting effect of the regeneration strategy can be estimated. The micrographs in both figures show a porous composite structure without carbon depositions or any other degradation phenomenon. Besides data observed by means of electrochemical analysis, the micrographs provide evidence of the success of the applied strategy with regard to performance restoration and protection of the cell microstructure.

After the regeneration process, the polarization resistance was increased towards the direction of the initial resistance value (represented in Fig. 6.10), Z_{real} increased to 0.138 Ω and Z_{imag} to 0.049 Ω, which indicates a slight increase of the total resistance versus the initial resistance. This is due to the fact that a thin carbon layer that had formed on the anode surface and which linked Ni-particles with each other, thus increasing the overall conductivity, was removed (described in detail in Section 6.2.1).

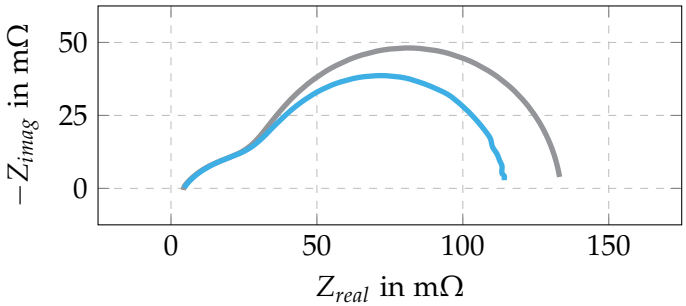

Figure 7.3: Electrochemical impedance spectroscopy: Impedance spectrum of the cell covered with carbon after estimated fuelling time of 44 h (—), impedance spectrum obtained after applied regeneration strategy (—). [7]

Although this method was very successful, the regeneration time required was approximately 44 h. In order to reduce the regeneration time and achieve the same result, several parameters were varied, including water vapour volume fraction, in regeneration approach R_{2var} and current or voltage in regeneration approach R_3, see Tab. 4.2. The selective variation of these parameters requires that the operation limits be taken into account, as some of these can induce undesired cell degradation, such as the critical volume fraction of water vapour or a voltage lower than 0.7 V, which can lead to Ni-reoxidation.

The data obtained by applying regeneration approach R_{2var}, consisting of 20 vol% H_2O and 45 vol% H_2 in N_2, are shown in Figs. 7.4a and 7.4b. The represented data were obtained

after fuelling with $DR_{2.3}$ for 44 h, and are shown here in order to make a meaningful comparison with the previously presented data. Fig. 7.4a represents the polarization curves measured on a cell covered with carbon (black solid lines) and, after 130 minutes, anode fuelling with the gas mixture R_{2var} (grey dashed lines). While the measurements were being taken, the cell was fuelled with the mentioned variant of a regeneration mixture R_{2var}. For a detailed analysis of the strategy's impact on performance improvement depending of the current density, representing the calculated voltage difference in the manner of Fig. 7.4b, specified as regeneration voltage, is indispensable. Comparing Fig. 7.4b with Fig. 7.2a, the same effect is recognizable; the humidified gas mixture R_{2var}, or water vapour concentration in H_2/N_2 mixture, enables performance regeneration mainly in the range of low and middle current densities. While increasing the amount of steam reduced the regeneration time with the humidified gas mixture, the complete gasification of all carbon deposits was not achieved. It may be thus concluded that feeding the anode with dry hydrogen is a necessary step in the regeneration process. The numerical investigation of combined R_1 and R_{2var} regeneration approaches, carried out in [172], showed that increasing the amount of steam in a gas mixture resulted in the formation of more CO_2 and less CO. This can be linked to the increased reaction rates of the water-gas shift reaction, thus shifting the equilibrium towards the product side. During regeneration, carbon monoxide desorbs quickly, which explains the measured CO peaks at the beginning of the regeneration process. For example, while fuelling the cell with 40 vol% H_2O and 30 vol% H_2 in N_2 for 2 hours, CO-peaks of 2 vol% were observed only at the beginning of the gasification process. Furthermore, the numerical study suggested that the number of vacant Ni sites increases with the increasing operating temperature. Thus, in order to prevent thermal stress and ensure the fastest and most efficient carbon removal process, the regeneration procedure was performed at the operating temperature of 800°C. This value was specified by the manufacturer as the optimal operating temperature for the cells used.

For further investigation, the amount of water vapour was gradually increased, and the hydrogen amount was decreased accordingly. The concentration of water vapour set to 40 vol% H_2O in 30 vol% H_2 and 30 vol% N_2, specified as R_{2var} in Tab. 4.2 led to the cell's degradation. The cell was operated under this regeneration gas mixture at OCV, since no further water vapour can be produced under these conditions. Nevertheless, only 2 hours of fuelling with the mentioned gas mixture resulted in the deterioration of the measured voltage by approximately 10 mV. The voltage degradation could indicate that some additional degradation mechanisms were occurring, which was verified when the cell was removed from the cell housing. The mechanical damage to the cell investigated occurred due to Ni reoxidation, which is visible in Fig. 7.4c.

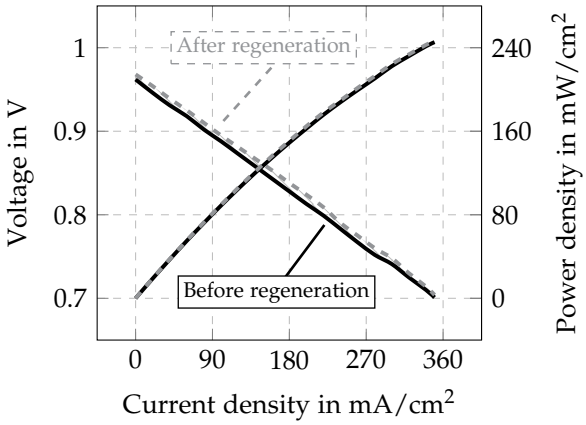

(a) Polarization curves measured before and after feeding with 20 vol% H_2 in R_{2var} for 130 minutes

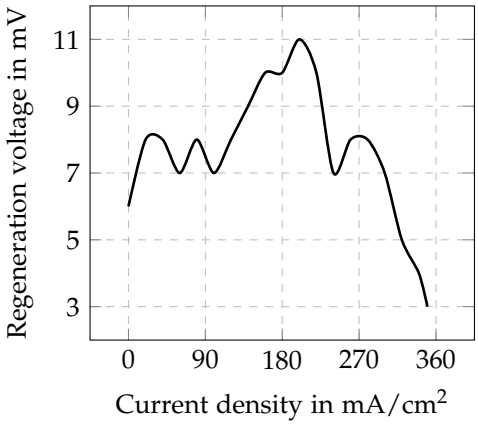

(b) Regeneration voltage difference after feeding with 20 vol% H_2 in R_{2var} for 130 minutes

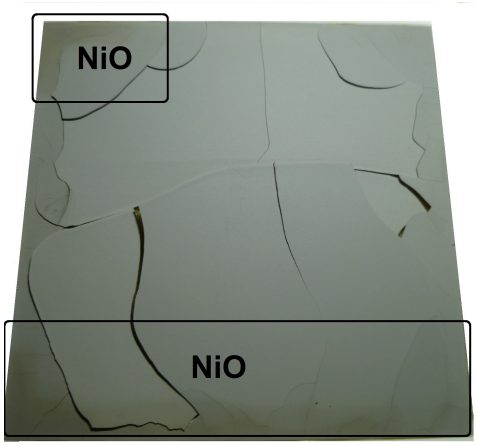

(c) Photograph of the anode surface after fueling with 40 vol% H_2O and 30 vol% H_2 in N_2

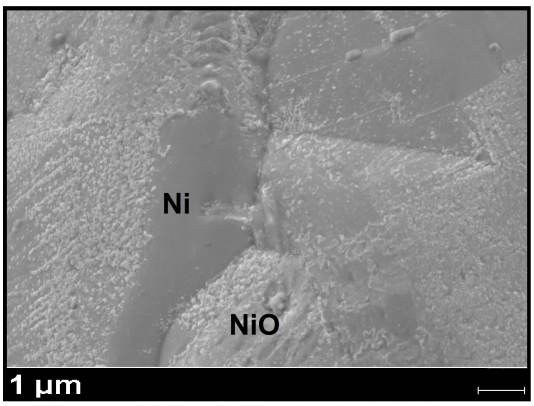

(d) SEM-micrograph of the contact Ni-mesh after fueling with 40 vol% H_2O and 30 vol% H_2 in N_2

Figure 7.4: Regeneration process depending on the amount of water vapour in a gas mixture R_{2var} fed to the anode at 800°C.

The strongest oxidation was recognized at the cell border (marked area) and was distributed from these points over the whole cell. The amount of water vapour used, and the obtained H_2/H_2O ratio also caused mechanical damage to the Ni current collector, which was observed via SEM-imaging and is shown in Fig. 7.4d. In summary, the combination of strategies $\boldsymbol{R}_1$ and $\boldsymbol{R}_2$ is a suitable method for the cell-protecting removal of carbon, but it is time-intensive. The gasification time can be reduced if a larger amount of steam is available in the gas mixture. In this case, the steam/hydrogen ratio must be lower than 1 in order to prevent the unwanted Ni-reoxidation and mechanical cell degradation. Moreover, while increasing the amount of steam may accelerate the regeneration process, complete carbon gasification and performance restoral was not achieved without feeding the cell

with dry hydrogen. Since the gasification of carbon from the metallic catalyst is a subject of great industrial relevance, the gasification of carbon on industrial metallic catalysts, such as nickel, iron, or alumina-supported nickel, was examined in pioneer works by Trimm [143, 144], Bernardo [145], McCarty [146] and Figueiredo [141, 142]. Figueiredo and Trimm [141] used both water vapour and hydrogen to gasify carbon from nickel foils and from the supported catalyst in a temperature range between 547°C and 747°C. Gasification with water vapour was found to be dependent on the operating temperature. At low temperatures, carbon could not be fully removed, and was left on the catalyst, but higher temperatures enabled complete carbon gasification. Figueiredo and Trimm [141] claimed that the rate of gasification by steam is independent of the partial pressure. For the Ni/Al_2O_3 catalyst, the gasification rate was also independent of amounts of catalyst and coke present, while the gasification rates for nickel foils were nearly proportional to the amount of carbon deposited. The same effect was observed using hydrogen as a gasification agent. In comparison, gasification using hydrogen resulted in a much slower gasification rate. The results obtained were extended to a temperature range between 475°C and 850°C for gasification with hydrogen and to 500°C-825°C for gasification with steam in the study by Bernardo and Trimm [145]. This study also suggests higher temperatures for carbon gasification using hydrogen and steam. At temperatures lower than 500°C, the carbon gasification rate using hydrogen was calculated to be almost zero. In his study [144], Trimm emphasized that the regeneration of the coked catalyst does not mean that the initial catalyst activity has been recovered. For this purpose, a detailed electrochemical and microscopic analysis of the solid oxide fuel cells investigated is required, which examines their state both before and after the removal process. The present work is thus of great importance to the SOFC-research field and contains significantly novel results.

7.2 Carbon Dioxide-based Regeneration Strategies[2]

This section demonstrates the potential of using carbon dioxide as a carbon gasification agent in SOFC systems. In order to obtain information about the possibility for fast carbon removal without changing the operating conditions, all of the investigations regarding the use of carbon dioxide were performed at 800°C, which is defined as the optimal operating temperature of the anode-supported single-cells used, as specified by the manufacturer. An additional reason for this is to prevent fast Ni-reoxidation on the fuel electrode. The oxidation potential, dependent on the gasification by carbon dioxide, significantly increases as the temperature decreases. Therefore, no thermal cycling was performed, and the aim was to investigate and to develop possible regeneration strategies based on CO_2 without varying the operating temperature. Several cells were used for the investigation of this

[2]Segments of this section have already been published in [6].

gasification method, which was carried out repeatedly for each cell, in order to ensure its reproducibility and repeatability. The deposition of carbon was induced by fuelling the cell with diesel mixture DR_9, containing 9 vol% CH_4.

As stated in Section 3.4, many studies have discussed carbon gasification using carbon dioxide as a gasification agent, [125, 126, 147, 148, 150]. However, an analysis of the electrochemical performance after the gasification processes cannot be found in literature. In this section, an approach to carbon removal using CO_2 as a gasification agent and its impact on the cell's performance are presented. It is important to note that, for this purpose, CO_2 was mixed with nitrogen and nitrogen/hydrogen. The regeneration approach used is specified as R_4 in Tab. 4.2. Water vapour was also added to this gas mixture for further investigation. The investigations carried out showed that whether hydrogen or water vapour was added to the gas mixture used, a high concentration of CO_2 induced further performance deterioration. The conclusion here is that a high concentration of carbon dioxide has a negative impact on cell activity. The diagrams in Fig. 7.5, however, outline the measurements carried out while using the CO_2/N_2 gas mixture, whereby the volume fraction of CO_2 was 25 vol% in N_2, in order to make a meaningful comparison with the results shown later in this work.

Bernardo and Trimm, [145] demonstrated that, when using CO_2 for carbon gasification from Ni-foils, carbon monoxide was measured as an off-gas. The CO concentration was closer to the predicted concentration, based on equilibrium calculations, when the temperature increased and the flow rates decreased. The highest gasification rate was observed at higher temperatures, while at approximately 550°C it appeared to be almost zero. During the gasification process performed in this work, CO-peaks were measured in the anode offgas. The greatest CO quantity of approximately 9 vol% was measured at the beginning of the gasification process, and this amount decreased even further, as can be seen in Fig. 7.5a. The gasification process was completed after 3 minutes, when the CO volume fraction decreased to zero. Although it was clear from the gas analysis that carbon had been gasified, degradation of the cell performance also occurred, as evident from the electrochemical analysis. Fig. 7.5b depicts the voltage and power density measured as a function of current density. The performance of a new cell, measured before the carbon deposition experiment, is represented by the black solid lines. Black dashed lines depict the diminished voltage and power density obtained after fuelling the cell with the mentioned diesel fuel mixture; as mentioned, these are seen to be most pronounced at higher current densities. Carbon gasification using CO_2 as a gasification agent induced further cell degradation, as clearly shown by the blue solid lines. The voltage degradation rate that occurred can be calculated as the difference between the voltages obtained after the carbon deposition and after gasification with CO_2. The degradation rate observed after the carbon gasification by

CO_2 ranges between 11 mV and 18 mV, depending on the cell load, while the maximum degradation voltage of the polarization curve measured before and after coking was 27 mV, as illustrated in Fig. 7.5c. The methane conversion rate was also significantly decreased following application of the carbon gasification strategy. CO_2 thus leads to significant performance degradation and cannot be used as a cell-protecting regeneration strategy.

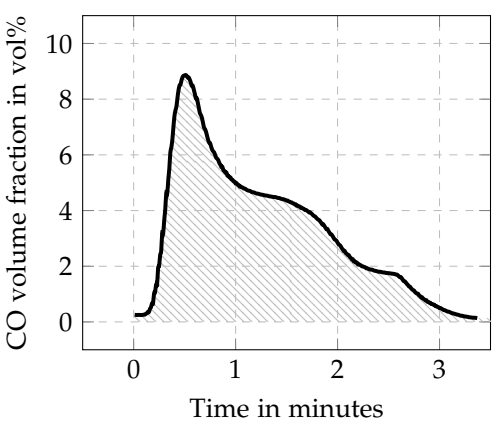

(a) CO volume fraction at the anode outlet

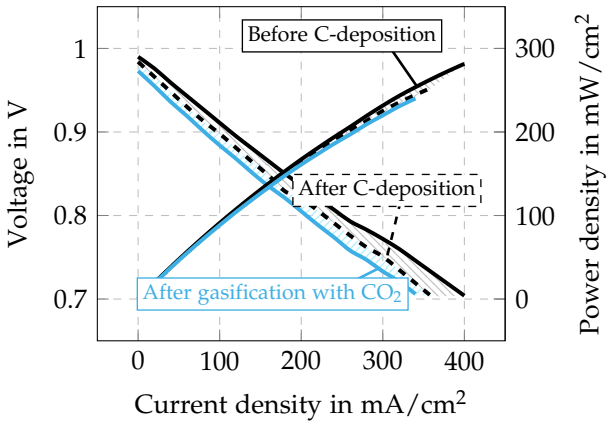

(b) Comparison of polarization curves

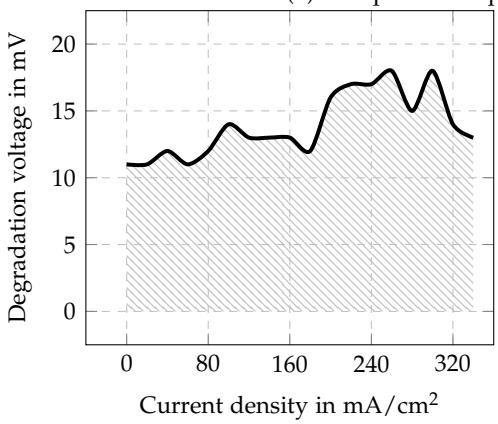

(c) Degradation voltage after gasification with CO_2

Figure 7.5: Off-gas measured during the regeneration process with 25 vol% CO_2 in N_2 and comparison of the electrochemical performance observed before and after the carbon deposition experiments with DR_9 as well as after gasification with the mentioned gas mixture. [6]

Using carbon dioxide as gasification agent, Kirtley et al. [150] observed the loss of carbon and afterwards the growth of nickel oxide, which surely caused the anode degradation. Maier et al. [173] developed detailed surface reaction mechanisms, in which they showed that carbon dioxide could both be adsorbed on the Ni-catalyst surface or decomposed on the anode surface. Decomposition of CO_2 on the nickel surface into carbon monoxide and oxygen leads to additional surface coverage. The experimental findings of this thesis con-

firmed the results obtained in [172], which analysed the surface conditions throughout this gasification strategy. Therein, several mechanisms are shown to be responsible for further performance degradation during the gasification process. First, elementary oxygen can be found on the anode surface, which increases the Ni-reoxidation potential and thus can be connected to the results obtained in [150]. Second, carbon monoxide is adsorbed on the anode surface and the regeneration strategy applied does not reduce that adsorbed amount. Third, carbon cannot be completely removed from the anode surface, but the remaining amount of the carbonaceous species is so small that it was not possible to measure it in the experimental study. The carbonaceous species were thus not completely gasified from the active nickel catalyst, which was also covered with adsorbed CO and O_2. This caused further performance degradation, thus also disabling methane reformation and reducing the overall methane conversion rate.

Nevertheless, CO_2 was combined with protective overvoltage in regeneration approach $\boldsymbol{R}_{ov}$. The value of the protective overvoltage was defined as 1.4 V, which lies below the upper limit for degradation of the materials' structures of SOFC cells. The overvoltage protects the cell from the destructive effects of gasification by CO_2 - described above - on multiple levels. Elementary oxygen removes carbon deposits, especially near the electrolyte, but more importantly, it functions as a means of cell protection in this regeneration method. The Ni-oxidation potential is significantly decreased due to the overvoltage, which pushes oxygen and oxygenated species back from the catalyst surface. The desorption of gaseous carbon monoxide and carbon dioxide species, which induce further cell degradation, is thus supported, and their further adsorption is not inhibited. Next, this voltage brings the cell into electrolysis mode and the input energy forces the reversible Boudouard reaction. This strategy ensured the gasification of carbonaceous species deposited on the catalytic active Ni, without causing further performance degradation or microstructure modifications. To the author's best knowledge, the combination of CO_2 and overvoltage is an entirely new method of removing carbon deposits from the anode surface and restoring cell performance. However, the application of overvoltage to enhance hydrogen diffusion through metals such as iron and palladium was presented by Andrews and Ubbelohde, [174]. The overvoltage was maintained constant by continued electrolysis in their work. A review of early studies of ion diffusion through solids can be found in a book by Barrer [175]. It is also worth noting that Petrakopoulou et al. [176] suggested triode fuel cell design, with an auxiliary circuit between the anode and the auxiliary electrode. The auxiliary circuit running in electrolytic mode induces overpotential, thus improving the stability and tolerance of the anode to carbon build-up, since a large amount of the carbon formed is gasified under the applied operating conditions. In the context of the experimental parameters set for the diagrams showed below, the volume fraction of CO_2 in nitrogen was 25 vol%. No further gaseous

components were used, apart from CO_2 and N_2. The input voltage was regulated, and the temperature was held constant at 800°C. One regeneration cycle was set to 30 s, but one cycle was not sufficient to completely remove the carbon and fully regenerate the electrochemical performance. Thus, several regeneration cycles were repeated in order to achieve the initial cell performance, as shown in Fig. 7.6a. The initial cell performance is depicted by a black solid line, whereas the diminished performance, obtained after the carbon deposition experiment which involved fuelling with CH_9, is always indicated by the dashed black curve. The grey and blue curves between these two curves plot single regeneration cycles. It is evident that stepwise improvement after every cycle ensured the complete regeneration of the cell performance. After applying this gasification and regeneration method for the first time (indicated by the solid grey line), the greatest improvement could be seen in the range of low current densities, and only slight enhancement was visible at higher current densities. Further cycles (2nd step as grey dashed line, 3rd step as blue solid line, and 4th step as dashed blue line) showed significant improvement at higher current densities. The efficiency of each individual regeneration step is also observed as the difference between the voltage after carbon deposition and after the applied regeneration method, which is depicted in Fig. 7.6b.

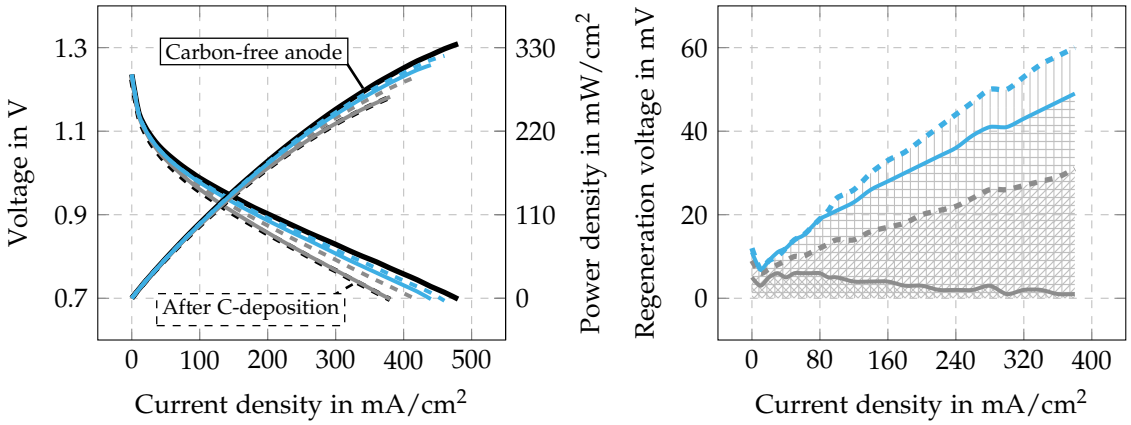

(a) Comparison of polarization curves before and after carbon deposition as well as after single regeneration cycle [6]

(b) Regeneration voltage after single regeneration cycles

Figure 7.6: Electrochemical cell performance and regeneration voltage measured after every regeneration cycle (1 (——), 2 (- - -), 3 (——), 4 (- - -)) with CO_2 and protective over-voltage.

The effect of current distribution at the beginning of the gasification process and corresponding to the time of the measured CO-peaks is visible in Fig. 7.7. Since the overvoltage forces the electrolysis mode, the current direction differs from the current direction in the load, and is thus shown as negative. The current measured at the beginning of the first regeneration

cycle is indicated by grey solid line, as in the diagram above. The first peak shown in the diagram represents the inrush or instantaneous input current, which accrues when the voltage is turned on. The real current distribution is actually depicted after those peaks, and the current change is given with an exponential function. The last regeneration cycle resulted in reduced current, which indicates that the catalytic anode surface is increased and thus less power is needed to remove the adsorbed species from the anode surface. This trend is represented by the blue dashed line. Furthermore, carbon gasification during the repeated regeneration cycles was proven by measured CO-peaks with the peak value of approximately 12 vol%, which had exhibited the same behaviour as the curve shown in Fig. 7.5a. The same procedure was repeated four times for each cell and was applied on several cells. This guaranteed the reproducibility of the strategy.

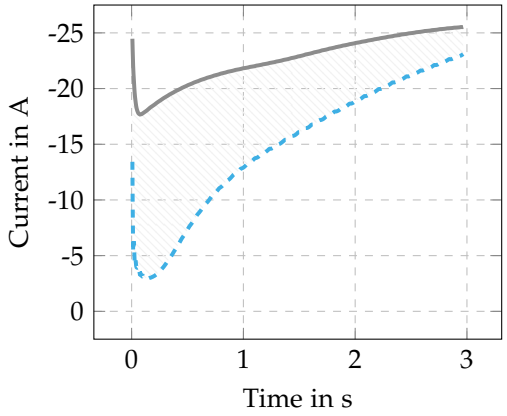

Figure 7.7: Current measured at the beginning of the gasification process under protective overvoltage: after first cycle (——), after fourth cycle (- - -). [6]

In order to prove that the applied regeneration strategy did not cause any morphological changes in the cell microstructure, and thus, to confirm the cell-protecting effect of the regeneration strategy applied, a post-mortem analysis was performed on the cells used. For this purpose, SEM-micrographs and an EDX-analysis were taken into consideration. In Fig. 7.8a, the SEM image shows the anode surface after the regeneration process. It is possible to see that the anode structure is composed of homogeneously distributed Ni and YSZ phases, and no degradation effects, such as YSZ-crushing into small particles and their deposition onto the Ni-catalyst, are observed. The fuel electrode's porosity does not seem to be affected. Two marked points were analysed in detail by means of EDX-analysis, and the results obtained are represented in Figs. 7.8b and 7.8c. Smaller grains, marked with 1, represent YSZ particles, while the Ni-catalyst grains are marked with 2. This morphology analysis showed that no significant changes were detected in the cell's microstructure since the anode structure remained porous and homogeneous.

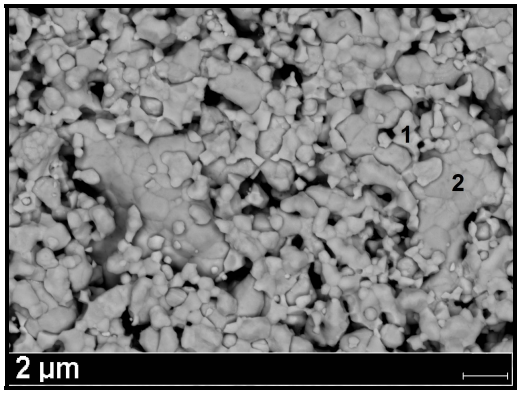

(a) SEM-micrograph of the Ni-YSZ surface after carbon gasification

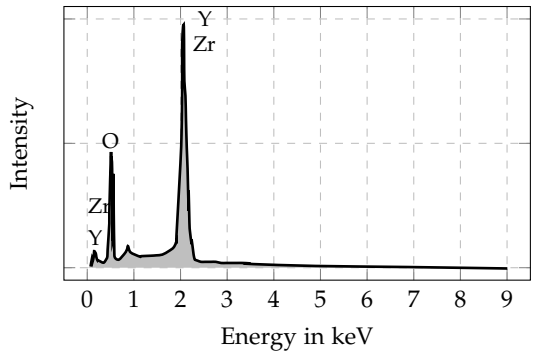

(b) EDX-analysis of the point 1

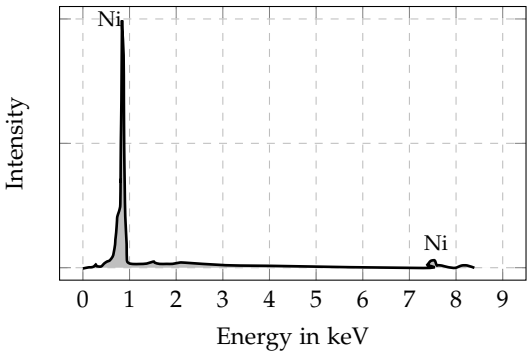

(c) EDX-analysis of the point 2

Figure 7.8: SEM- and EDX-analysis of the anode surface after carbon gasification using CO_2 and overvoltage. [6]

7.3 Electrochemical Methods of Carbon Removal

In order to exclude the necessity of using water vapour for carbon removal, and to use only dry gas mixtures for regeneration purposes, different electrochemical methods were applied, which are specified as $\boldsymbol{R}_3$ in Tab. 4.2. Their application was based on either cell operation in fuel cell mode or in theoretical electrolysis mode, which means that either the fuel cell was used as a power source, or it was supplied with power from an external power source. However, to avoid unwanted failure modes or destructive phenomena such as Ni reoxidation, which can occur during uncontrolled regeneration processes, critical current density or voltage had to be identified, and the limits for their application had to be considered.

For the purpose of the detailed investigation of this regeneration approach and for the definition of optimal operating conditions, both the fuel flow and synthetic air flow were varied, whereas the current output and voltage supply were controlled. The initial state

for the application of the regeneration approach was the cell covered with carbon after fuelling with diesel mixture DR_9, containing 9 vol% CH_4, whereby both the catalytic active Ni-sites and the porous gas channels were covered with carbon. The overall impedance thus increased after the completed carbon deposition experiment, as a result of the reduced conductivity.

7.3.1 Electric Load for Carbon Removal

Initially, the anode was supplied with dry hydrogen (as specified in the regeneration mixture $\boldsymbol{R}_1$) and the current density was set to 100 $\frac{mA}{cm^2}$ for the purpose of carbon removal and performance regeneration. The established current density enabled the controlled gasification of carbon. During the regeneration process, electrochemical impedance was measured every 20 minutes in order to capture the accrued changes. The results obtained by means of the application of this electrochemical method are shown in Fig. 7.9. Comparison of the polarization curves in Fig. 7.9a shows a slight improvement in the performance after 2 hours, but mainly in the range of the applied current density. Simultaneously, impedance spectra were measured every 20 minutes during the regeneration process. They reveal a decreasing trend. To simplify comparison, only impedance spectra obtained at initial state for the cell covered with carbon, and after 120 minutes operation under the given regeneration conditions, are depicted in Fig. 7.9b. Therefore, as expected, decreasing impedance from initial state (black solid line) to reduced impedance after 120 minutes (grey solid line) indicates increasing conductivity. Carbon was partially removed from the catalytic active Ni-sites and the gas channels making more active sites and surface available for electrochemical reactions and transport to occur. The overall losses were thus reduced and electrochemical reactions were enhanced. The changes are best detected at low-frequency arc, which reflects the anode-side, as shown in Chapter 5.

Based on observed impedance spectra, DRT-spectra were calculated and analysed. The DRT-spectra, calculated as a function of relaxation times, refer to the time dependent resistance of specific transport and kinetic mechanisms, as can be seen in Fig. 7.9c. The illustrated spectra represent values comparable to the represented impedance spectra, obtained at initial state (black solid line) and after 120 minutes (blue solid line) of regeneration under load. According to other studies, see Refs. [8, 159, 177, 178], slower process with diffusive mass transport can be seen at high relaxation time constants. Since fuel diffusion is a very slow process (addressed in Chapter 5), the peaks obtained between 10^{-2} and 1 s can be linked to the diffusion process. After 120 minutes of regeneration (indicated by the blue line), the peak is significantly reduced compared to the peak obtained for the cell covered with carbon (black solid line). Carbon removal increased the overall porosity of the cell

making gas channels available for gas transport. Next, due to the gasification process, the number of vacant TPB sites increased, thus enabling the oxidation of greater amounts of hydrogen. Hydrogen oxidation is a fast process, and the peaks observed at 10^{-4} s reflect this. Since more hydrogen is electrochemically converted, oxidation resistance accordingly increased up to 30%, as can be seen in the peaks observed at $\tau \approx 10^{-4}$.

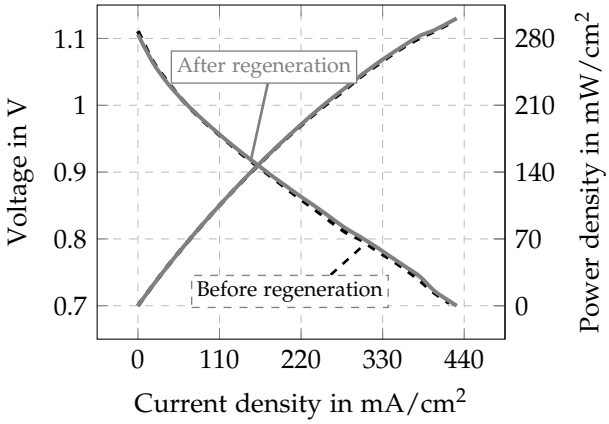

(a) Polarization curves measured before and after regeneration at 100 mA/cm² for 2 h in R_1

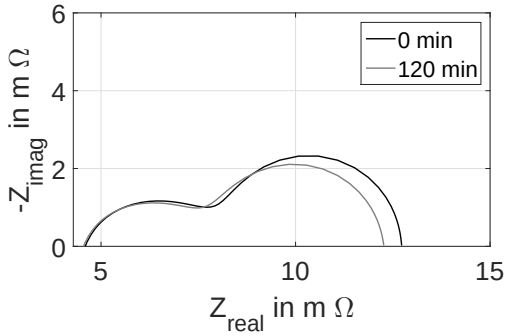

(b) Impedance spectra measured at initial state and after 2 h of regeneration with R_2 at 100 mA/cm²

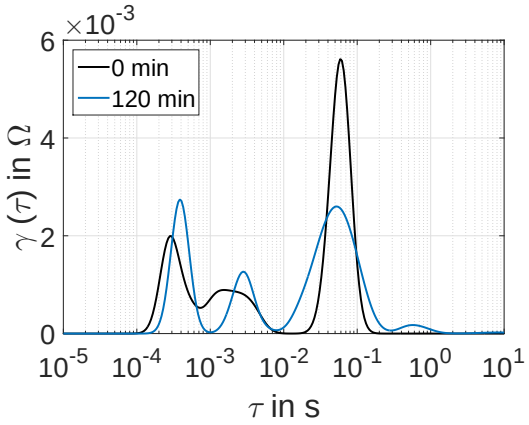

(c) DRT-analysis of the EIS-spectra measured at initial state and after 2 h

Figure 7.9: Regeneration using a regeneration approach R_1 at 100 $\frac{mA}{cm^2}$.

The cell was fuelled with a defined regeneration mixture at 100 $\frac{mA}{cm^2}$ for 44 h. However, the experimental investigation showed that complete regeneration via this method cannot be achieved within 44 hours, compared to the complete regeneration achieved within 44 h by combining regeneration approaches $\boldsymbol{R}_1$ and $\boldsymbol{R}_2$. This method is thus not appropriate for practical usage, and requires combined operation with a humidified gas mixture in order to reduce gasification time.

7.3.2 Overvoltage for Carbon Removal

Further electrochemical approaches were based on observations of the influence of overvoltage on the regeneration processes. The value of overvoltage with 1.45 V was chosen to be below the upper limit for degradation of the SOFC structure. During the application of overvoltage for the purpose of regeneration, the gas supply to both the anode and the cathode side was varied.
Firstly, the gas supply to both electrodes was interrupted for 20-40 s. During this period, the overvoltage of 1.45 V was applied. Afterwards, the polarization curve was measured, while the anode was supplied with a gas mixture $\boldsymbol{R}_1$ (see Tab. 4.2) with a constant volume flow of 2.4 SLPM. The cathode side was supplied with 4 SLPM of synthetic air. Further regeneration was performed under operation with a regeneration gas mixture as specified in $\boldsymbol{R}_1$. Secondly, the gas supply was interrupted only on the anode side, whereby the cathode was fed with air. For this purpose, the volume flow on the cathode side was varied between 1 SLPM and 4 SLPM. In the third method, CO_2 was used as gasification agent in combination with overvoltage. This method is described in detail in Section 7.2.

Fig. 7.10 provides information about the carbon removal process with overvoltage without gas supply both on the anode and the cathode side. The current measured during this process is illustrated in Fig. 7.10a. Due to the controlled overvoltage, the electrolysis mode is forced, thus inverting the current direction when compared to the direction in fuel cell mode. The inrush current was measured for the first 2 seconds, until the voltage reached a stationary value. The current measured during the first regeneration cycle is indicated by a blue solid line, a grey line represents the second regeneration cycle, and the third and final cycle is illustrated by a black line. The cycle time was set to 20 s. The same colours are used in Fig. 7.10b to compare the polarization characteristics before and after the regeneration procedure. After every cycle, the measured current decreased, thus indicating that a reduction in power is required to reach the voltage defined. This reveals that more active catalytic surface is available, since carbon was partially removed from the anode surface.

Comparison of the performances of polarized cells in Fig. 7.10b clearly shows the improvement from OCV up to the middle current density range, while at higher current densities, the overall performance diminished. In this case, the overvoltage applied enabled the removal of adsorbed gaseous species from the fuel electrode. Since the polarization curve shown was measured during feeding with DR_9, the increase in OCV refers to enhanced methane reforming. The results thus reflect an increase in the catalytic active surface and a number of vacant Ni sites. However, after carbon was removed from the anode surface and the desorption of gaseous species was finished, the voltage applied induced cell

degradation. This fact is supported by the voltage degradation observed at higher current densities. The voltage degradation reflects inhibited electrochemical reactions, impacted by a reduced number of TPB-sites, which may be caused by the degradation of the YSZ structure. Overvoltage can be assumed to induce the separation of oxygen from YSZ, when no gas is supplied to the cell and the carbon is gasified from the anode surface. In summary, the above described method makes it possible to remove carbon and restore cell performance in a controlled manner. This means that the carbon removal process needs to be closely monitored, and that, as soon as all deposits are removed, it is necessary to supply the cell with the appropriate gas mixture in order to prevent cell microstructure degradation. Taking this requirement into account, the industrial application of this method is possible. For this purpose, a detailed investigation and adjustment of the parameters for specific cell types is necessary.

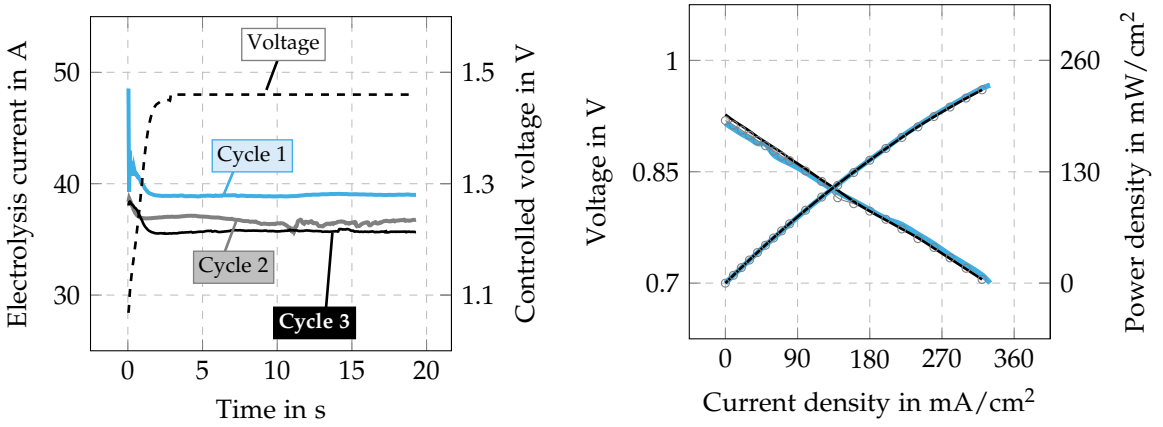

(a) Current measured during the regeneration process with a controlled overvoltage

(b) Comparison of polarization curves measured with DR_9 after every regeneration cycle

Figure 7.10: Regeneration using overvoltage without gas supply: cycle 1 (—), cycle 2 (—○—), cycle 3 (—).

This method was subsequently combined with regeneration approach $\boldsymbol{R}_1$. Only one cycle of 20 s was applied, in order to prevent the structural degradation of the cells used. Afterwards, the anode was fuelled with a 2.4 SLPM constant volume flow of 45 vol% H_2 in N_2, and the cathode side was supplied with both 2 SLPM and 4 SLPM synthetic air. The application of overvoltage for only 20 s reduced the overall regeneration time down to 12 h, when using a gas mixture as defined in a regeneration approach $\boldsymbol{R}_1$. It was not necessary to carry out additional operation with humidified hydrogen in order to achieve complete cell regeneration. Therefore, when using the combination of overvoltage applied for 20 s without gas supply on both electrodes and the dry H_2/N_2 mixture, total regeneration is possible. The reproducibility and repeatability of the presented method was confirmed. This method represents a cell-protecting and a time-saving solution.

Another variation of a regeneration approach $\boldsymbol{R}_3$ (see Tab. 4.2), in which only the cathode was supplied with synthetic air under forced electrolysis mode for the purpose of carbon gasification, achieved better results than when applying the overvoltage without gas supply. Total regeneration over the whole load range was reached, without additional degradation of the cell performance, as shown in Fig. 7.11. The polarization curves shown in this figure were measured during the fuelling with 45 vol% H_2 in N_2, with a constant volume flow of 2.4 SLPM. Strong performance degradation after carbon formation is obvious when the black solid line (new cell) and the grey solid line (cell partially covered with carbon) are compared. The voltage and power-density measured as a function of current-density after the applied regeneration strategy are indicated by blue points. The applied regeneration approach enables the continuous transport of oxygen ions, which then gasify the carbon, especially near the electrolyte along the anode functional layer. The applied voltage further induces the desorption of adsorbed gaseous species, such as carbon monoxide or carbon dioxide, thus making more catalyst area available for further reactions. The potential for Ni-oxidation to take place is decreased, while adsorbed carbon and gaseous species are available on the anode. The oxidation of vacant Ni-sites after complete carbon gasification and desorption of gaseous species may occur in this case, since no other gas is available on the anode side. However, the risk of undesired degradation after carbon removal by means of this strategy is significantly lower than for the previously described method. Therefore, the practical application of this method would also appear possible in a controlled-manner, which requires sophisticated monitoring equipment. This includes the online-monitoring of the gas measured at the anode outlet as well as determination of the need for carbon removal from the anode surface at an early stage, in order to ensure the anode a timely supply of the appropriate cell-protecting gas mixture.

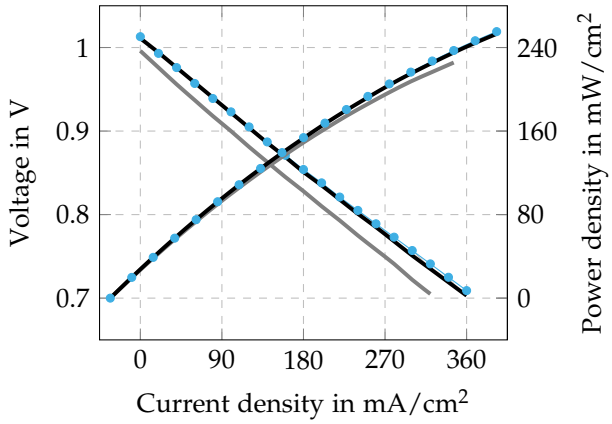

Figure 7.11: Regeneration using overvoltage during cathode supply: new cell (——), cell covered with carbon (——), after regeneration (—•—).

7.4 Carbon Removal Using Oxygen-enriched Gasification Mixtures

As a further possible carbon gasification agent, oxygen enriched mixtures $\boldsymbol{R}_{5var}$ (see Tab. 4.2) were also considered. Two variations of this gas mixture were applied. In the first variation, O_2, with a concentration of 2 vol% and CO_2, with 18.9 vol%, were mixed together in N_2. In the second variation, the gas mixture was diluted with nitrogen in order to obtain an O_2 concentration of 0.5 vol%. The CO_2 concentration was thus reduced down to 4.7 vol%. The volume flow on the anode side was held constant at 2.4 SLPM, while the cathode side was supplied with 4 SLPM synthetic air. The operating temperature for the applied regeneration approach was varied between 500°C and 800°C in order to prevent Ni reoxidation. This phenomenon results in crystallographic changes to the microstructure, which is accompanied by a bulk increase, and finally leads to the electrolyte cracking. The physical damage that occurs is irreversible. Nevertheless, the results demonstrated that Ni-oxidation cannot be prevented, regardless of the operating temperature, when the oxygen enriched mixture $\boldsymbol{R}_{5var}$ was applied.

With decreasing temperatures, the oxygen adsorption rate decreases, as a result of CO_2 decomposition. Ni oxidation caused by pure oxygen becomes more critical as the temperature increases. The regeneration time was controlled between 30 s and 10 minutes. Ni-oxidation occurred after only 30 s operation with a gas mixture diluted in N_2, including 0.5 vol% of O_2 and 4.7 vol% CO_2 but no irreversible degradation was seen. Afterwards, the cell was supplied with hydrogen for more than 10 hours to reduce the NiO formed, but the initial cell performance could not be regained. All other combinations caused irreversible mechanical damage to the cell, which can be seen in Fig. 7.12a. The green surfaces represent NiO. The SEM-image in Fig. 7.12b shows a completely changed catalyst surface. Ni-oxides, which have no catalytic activity, disabled chemical and electrochemical reactions, and blocked gas pores, which inhibit the transport of gaseous species. The marked points were characterized by EDX-analysis, and, as expected, point 1 represents the oxygen-conducting YSZ (Fig. 7.12c), while point 2 clearly refers to NiO (Fig. 7.12d). When applying this regeneration method, the exact position of the formed carbon has to be determined. In order to prevent the early oxidation of Ni, before the carbon is removed, only the sites covered with carbon should be fed with the defined gasification mixture. This is the only way to both remove carbon and prevent undesired Ni-oxidation.

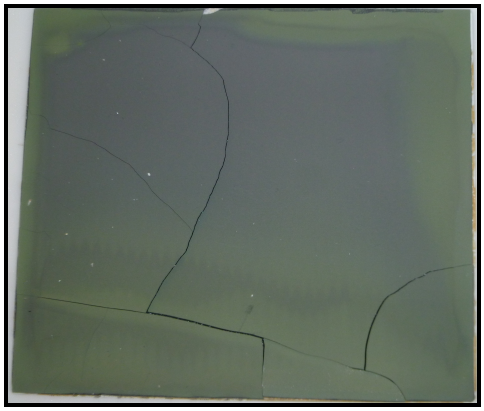

(a) A photograph of the anode surface

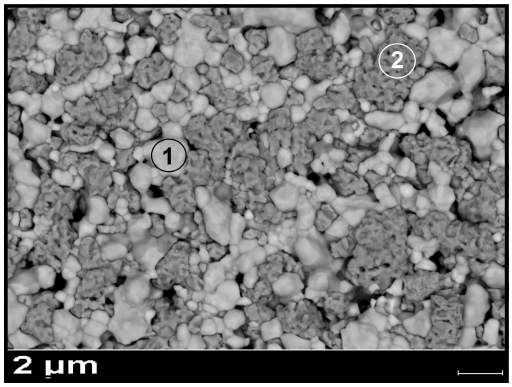

(b) SEM-micrograph of the anode surface

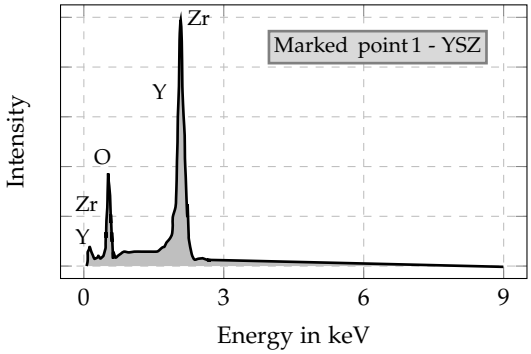

(c) EDX-analysis of the point 1

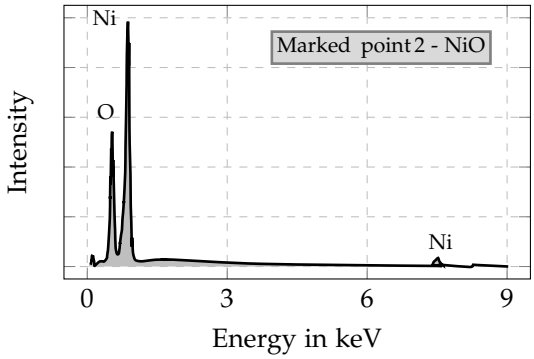

(d) EDX-analysis of the point 2

Figure 7.12: Anode surface after carbon gasification using the O_2-based regeneration approach $\boldsymbol{R}_{5var}$.

7.5 Analysis of Possibilities for Carbon Removal after Different Failure Modes [3]

This section demonstrates the feasibility of carbon removal from the porous anode, not only after carbon deposition experiments but also after this additional failure mechanism. For the removal of carbon, a cell-protecting strategy that involves a combination of regeneration approaches $\boldsymbol{R}_1$ and $\boldsymbol{R}_2$ was employed.The investigations undertaken in the course of this work determine that carbon can be fully removed from the anode surface after nickel oxidation, while cathode degradation makes the complete cell regeneration impossible.

To produce fast carbon deposits, the anode was fuelled with diesel reformate $DR_{20.3}$ containing 20.3 vol% CH_4 (see Tab. 4.1) at the current density of 60 $\frac{mA}{cm^2}$. The fuel volume flow was held constant at 2.4 SLPM, while the cathode side was supplied with 2 SLPM. The operating temperature was set to 800°C. Under the aforementioned operating condi-

[3] Segments of this section have already been published in [5].

tions, rapid performance degradation was observed after only 30 minutes. The voltage degradation trend is represented on the left y-axis in Fig. 7.13a. The same effect during the voltage degradation, based on strong voltage alternation, can be found in [135]. The rate of voltage degradation was not constant over a given period; after 15 minutes, the cell performance deteriorated significantly faster. Simultaneously, the volume fraction of methane, measured at the anode outlet, constantly increased, as shown by the right y-axis. This fact indicates that the catalytic active Ni-surface was covered with carbon, thus deactivating Ni for subsequent reforming reactions in such a way that the cell performance decreased. The measured polarization curves (Fig. 7.13b) and electrochemical impedance spectra (Fig. 7.13c) of a carbon-free cell (indicated by blue) and the cell with carbon depositions (indicated by grey) portray the decrease in cell activity after operation with diesel reformate containing carbon. Both in this figure and in all other diagrams in this section, the performance of the carbon-free cell is always indicated by the colour blue, while the cell performance after the carbon deposition experiments is represented by the colour grey. In this regard, solid lines represent the cell performance during the first procedure performed, while markers only refer to the second procedure carried out. The effects discussed above were signals that a certain amount of carbon had formed on the anode surface.

Electrochemical impedance measurements were used as a reliable method for the detection of changes to the cell performance. Fig. 7.13c represents the impedance spectra measured at open circuit voltage and under high load at 0.7 V. Impedance spectra showed the rising series and polarization resistance after the carbon deposition experiment, both at open circuit voltage as well as under load, since the imaginary part remained almost unchanged. The increasing ohmic resistance indicates the degradation of Ni- and TPB-active surface after they were covered with carbon and the gas pores were blocked. Subsequently, after the detection of carbon, the combination of $\boldsymbol{R}_1$ and $\boldsymbol{R}_2$ regeneration methods, as described above, was applied in order to remove the carbon formed in a cell-protecting manner. The applied regeneration method successfully removed the carbon and regenerated the cell, as illustrated in Fig. 7.13. To obtain reproducible results, the same procedure was repeated three times. In Fig. 7.13, the measured values of the two procedures are compared, in order to provide a simple overview.

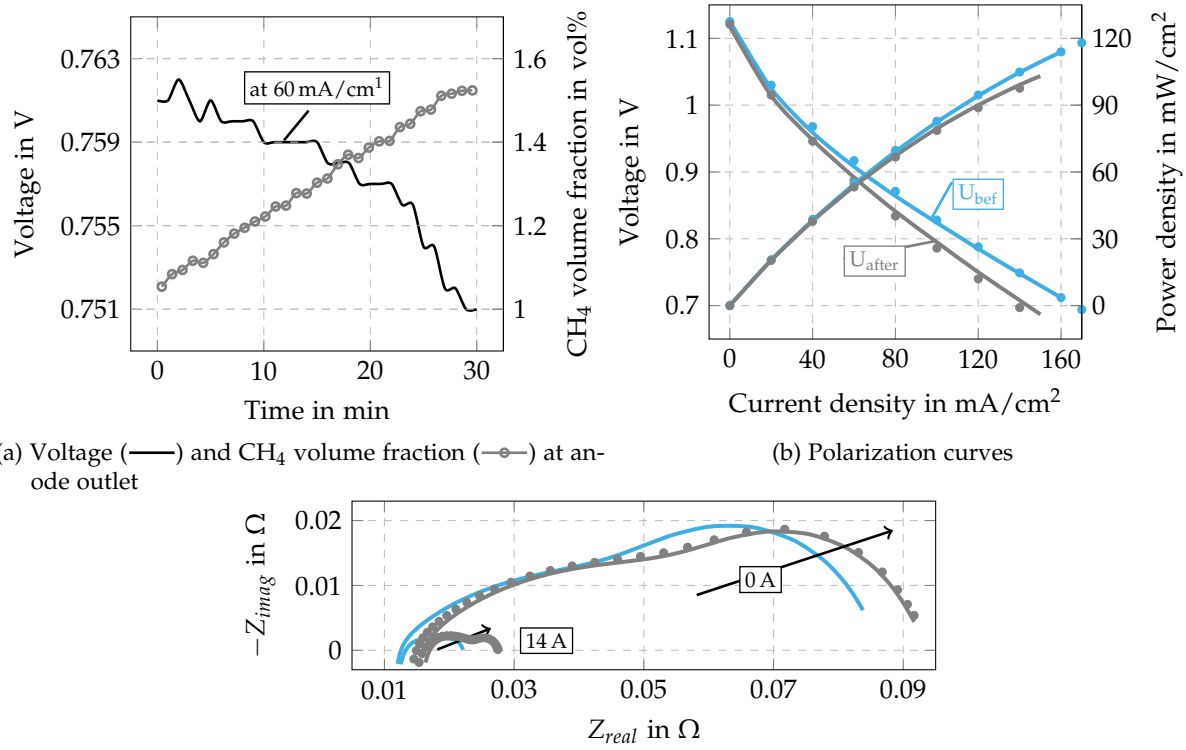

(a) Voltage (——) and CH_4 volume fraction (—○—) at anode outlet

(b) Polarization curves

(c) Electrochemical impedance spectra

Figure 7.13: Change of electrochemical performance of the cell before and after the first (—— and ——) and second (• and •) carbon deposition experiment. [5]

7.5.1 Removal of Carbon from the Ni-YSZ Anode after Cathode Degradation

The same procedure of eliciting carbon deposits by fuelling the cell with $DR_{20.3}$ was repeated. Subsequently, cathode degradation was induced through the use of compressed air containing impurities, in order to analyse the possibility of carbon removal after the failure modes of nickel oxidation and cathode degradation. Complete cell regeneration was not possible after this process. In Fig. 7.14, the performance of the cell after anode reduction and cell activation (solid blue), after complete regeneration (green points), and the degradation due to deposited carbon (marked as solid line in grey) are compared to the electrochemical cell performance of the cell after the cathode degradation effect (black points). The incomplete regeneration indicated by the cathode degradation was detected through the evidently irreversible deterioration of the cell performance, since the initial state could not be reached and regeneration was accomplished only up to a certain value. The series and polarization resistance decreased when compared to the impedance spectrum after the carbon deposition experiment (black solid line in Fig. 7.14). The imaginary part of the high-frequency arc reached the same value as the spectrum after the successful regeneration, but regeneration was not possible in the low-frequency arc.

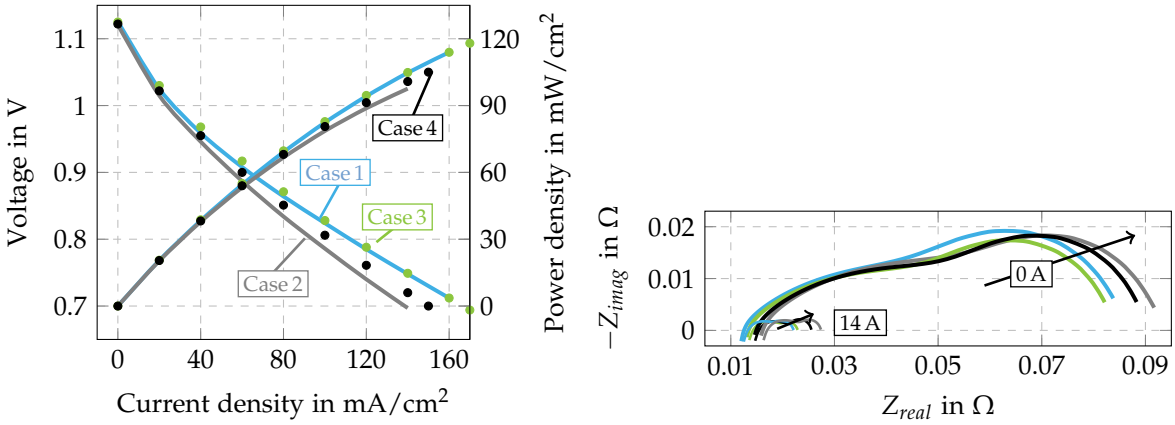

(a) Polarization curves

(b) Impedance spectra

Figure 7.14: Electrochemical cell performance before the carbon deposition experiment and after both the carbon deposition and regeneration experiments: Case 1: New cell; Case 2: After carbon deposition experiment; Case 3: After regeneration procedure; Case 4: After cathode degradation. [5]

The unsuccessful complete removal of carbon from the anode after the occurrence of the cathode degradation effect was confirmed by the appearance of carbon on the anode after the cell was removed from the cell housing following the experiment. Subsequently, it was also apparent during the post-mortem analysis, which allowed a complete analysis of the cell microstructure. As shown in Fig. 7.15a, the SEM-imaging and EDX-imaging showed massive carbon deposits, which thickly covered the anode surface and blocked gas pores. In Fig. 7.15b, the carbon-free anode surface and the surface covered with carbon are compared. The microstructure degradation phenomenon, discussed above in Section 6.3.1, was also obvious here. Significant changes to the microstructure of the anode surface covered with carbon, in the form of agglomerated Ni and YSZ particles, is easily observed. Thus, the catalyst active surface is reduced. Fig. 7.15a also depicts mechanical damage to the anode microstructure in the form of offprints over the whole surface, accrued on the contact points between the anode and the nickel mesh. The decomposition of LSCF to its single components destroyed the cathode microstructure, and thus made it impossible to completely remove carbon particles on the anode side (see Figs. 7.15c). Morphology changes on the cathode can also account for the irreversible degradation of the cell performance during the regeneration procedure. A layer of ferric oxide particles on the cathode surface as well as the strontium particles as units outsourced from the cathode unity are shown in Fig. 7.15d.

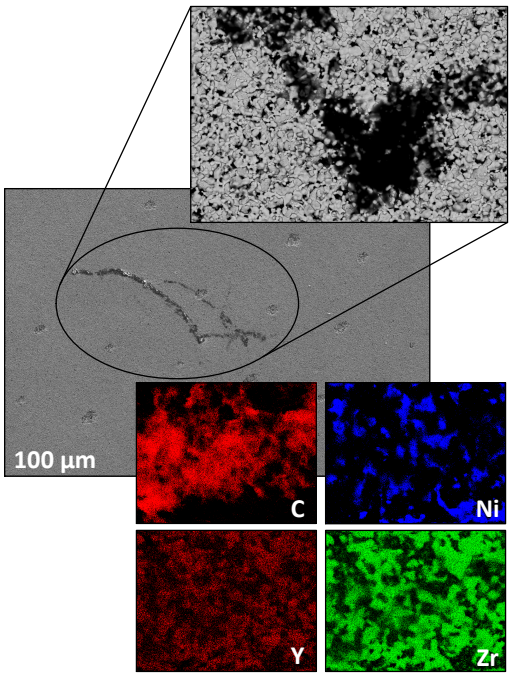

(a) Anode surface covered with carbon

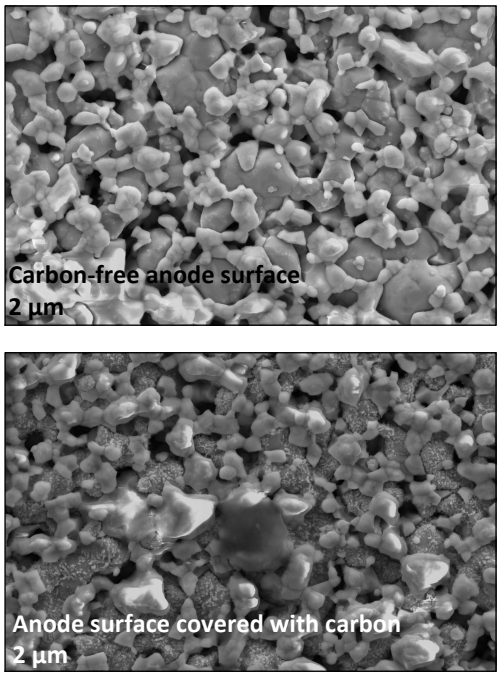

(b) SEM-micrograph of the anode surface

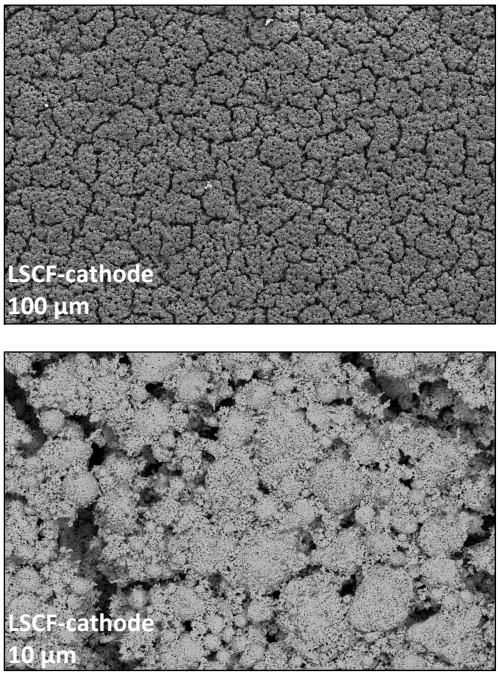

(c) LSCF-cathode

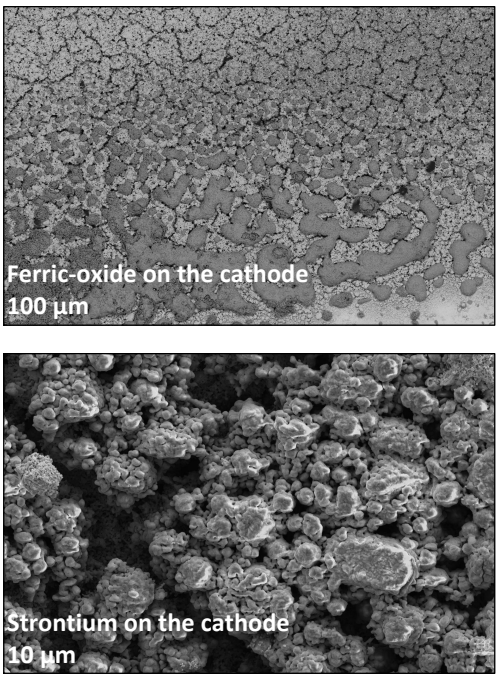

(d) Single cathode components

Figure 7.15: SEM-analysis of the anode and the cathode surface before and after cathode degradation. [5]

7.5.2 Regeneration of the Cell after Reoxidation of Nickel

One of the most important constraints and disadvantages of operating an Ni-YSZ-based SOFC is the reoxidation of nickel. After reoxidation the anode structure does not regain the initial structure of the prereduced anode; renewed oxidation causes bulk expansion and thus results in mechanical damage to the cell microstructure. [179--182]. Among others, the aim of this work was to investigate this phenomenon and its influence on carbon removal from the anode surface using a combination of regeneration approaches $\boldsymbol{R}_1$ and $\boldsymbol{R}_2$. For this purpose the gas, supply was interrupted for a short time (2-5 minutes) during the regeneration process in order to reoxidize the Ni cermet on the anode, after which the regeneration method was applied, as discussed above. This procedure was not applied until the effectiveness of the regeneration strategy without any additional failure modes had been proven. Firstly, as already mentioned, the cell was operated with $DR_{20.3}$ diesel fuel at 60 $\frac{mA}{cm^2}$ to produce carbon, and, subsequently, the aforementioned regeneration strategy was applied. It enabled the complete removal of carbon from the cell anode and returned the cell performance to its initial state. Afterwards, the coking process was repeated. During the second regeneration process, the fuel supply was stopped for a specific period in order to simulate this failure mode, and thereafter, the regeneration was continued. Fast nickel oxidation appeared, and, after the cell was removed from the cell housing, mechanical damage was detected: a narrow fracture over the length of the cell, from the fuel/air inlet to the fuel/air outlet, was clearly visible. The area adjacent to this cracking was slightly oxidized. Despite this, no carbon deposits were found on the cell, not even on the places described in Section 7.5.1 and shown in SEM-images in Fig. 7.15. Since the cell was slightly damaged, there is the possibility that the carbon formed was regenerated not only by the regeneration gas mixture, but also through appearance of air on the anode side. Thus, it was repeatedly proven that oxygen has a damaging effect on the cell microstructure and should not be used on the anode side.

Since the fuel interruption caused slight mechanical damage to the cell, carbon removal could not be precisely detected by the electrochemical methods applied. Nevertheless, Ni-oxidation can clearly be detected by means of different electrochemical methods, especially electrochemical impedance spectroscopy, which shows a unique change to the impedance spectra (see Fig. 7.16b). Reduced impedance, both real and imaginary, does not indicate the better conducting performance of the cell, but does show that more than one process occurs in parallel on the anode side, which means that the total impedance is reduced. However, some other interesting points can also be observed through the measured impedance spectra: the measurement at OCV reveals the decreasing resistance values over the whole frequency range. Compared with this, the measured impedance under high load showed decreased

impedance in the high frequency arc, while the low frequency arc increased in comparison to the measurements before the reoxidation of nickel. The electrolyte resistance remained unchanged for both cases. A further indication of the Ni-oxidation and cell degradation is the instability of the cell voltage, as seen in Fig. 7.16a. A variation of the voltage in the range of 20 mV was detected during cell operation. Furthermore, every change in the operational conditions (for example, concentration of the single gas components and their volume fraction) changed the cell performance - especially the open circuit voltage, while the volume fraction of hydrogen, measured at the anode outlet, decreased. Fig. 7.17 shows the spongy microstructure of the anode after nickel reoxidation, where the nickel surface appears with a higher porosity and many small pores compared to the dense nickel surface of the reduced anode.

As mentioned, neither the electrochemical measurements nor the gas analysis was able to indicate whether the cell was fully regenerated, since the failure occurrence caused irreversible and significant damage to the cell performance. After the cell was removed from the alumina housing, no carbon particles were found on the anode surface. Wang et al. found similar changes to the nickel structure after the reoxidation process [182]. Not only Ni on the anode surface, but also the Ni-mesh used for the anode contacting was irreversibly damaged by reoxidation. The SEM-images of the Ni-mesh before the operation as well as after long-term operation under high temperatures are compared with the same mesh after the Ni-oxidation. Long-term operation leads to a change of the Ni-microstructure, but does not cause degradation, while Ni-oxidation leads to delamination and irreversible degradation of the mesh used. Irreversible mechanical damage to the upper layer of the Ni-wires rules out the possibility of using the Ni-collector in further experiments.

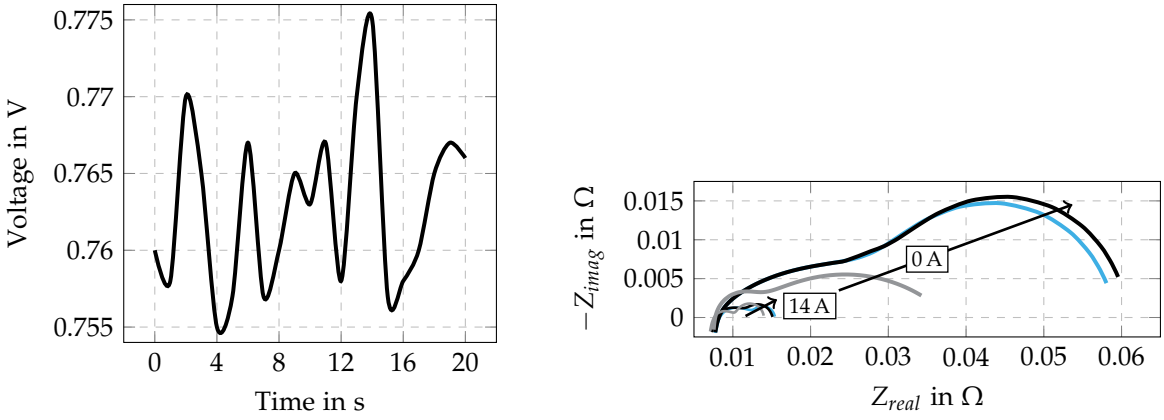

(a) Voltage fluctuation

(b) Impedance spectra

Figure 7.16: Change in cell performance before (—) and after (—) carbon deposition experiment and after occurred nickel reoxidation (—). [5]

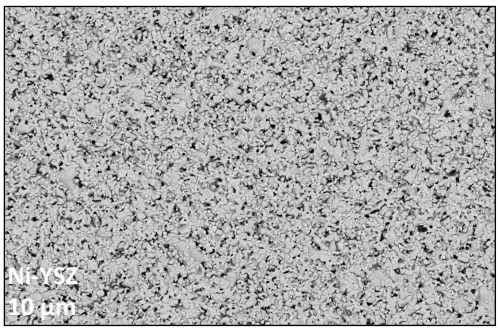

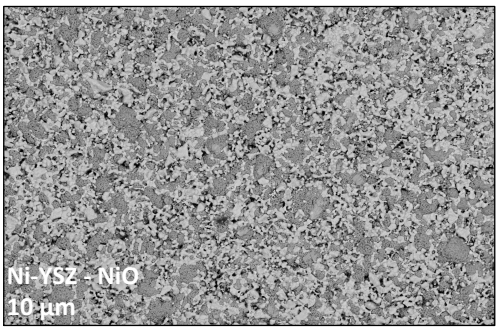

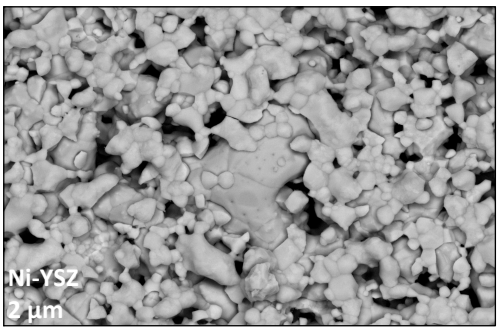

(a) Ni-YSZ anode surface 10 μm

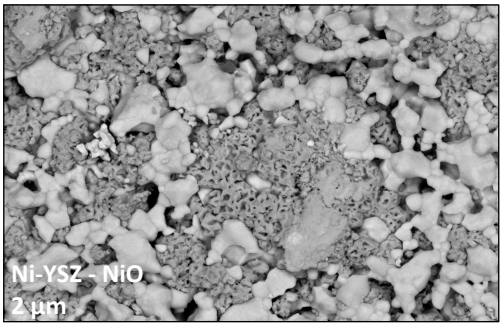

(b) NiO-YSZ anode surface 2 μm

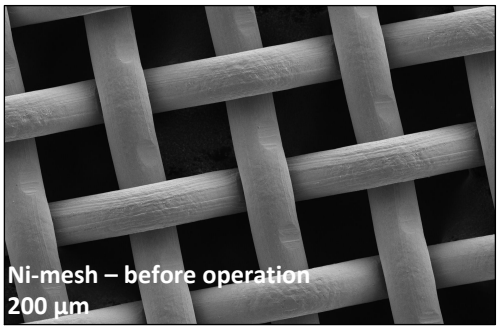

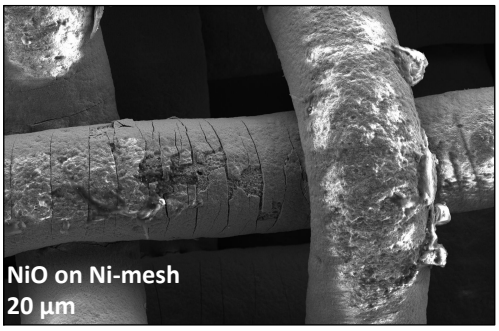

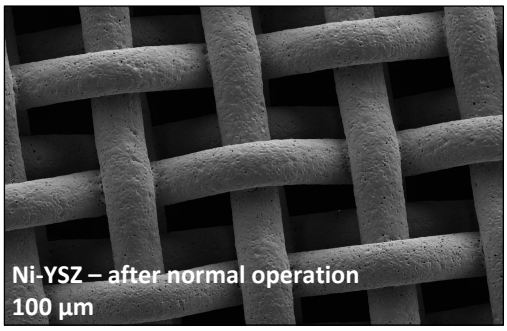

(c) Nickel-oxide on the anode surface 10 μm

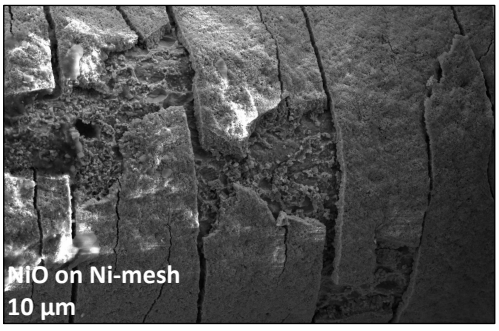

(d) Nickel-oxide on the mesh used 2 μm

Figure 7.17: SEM-analysis of the anode surface - before and after Ni reoxidation. [5]

7.6 Concluding Remarks

All of the regeneration approaches presented in this chapter were applied on the cells after fuelling with all four diesel reformate mixtures. This investigation was performed to examine the universal application of every single method developed. The reproducibility and repeatability of these methods were also proven, since every strategy was applied at least three times on each cell, and afterward on a number of cells. The regeneration time required, as well as the reusability of the strategy on one cell, and the cell-protecting effects of the single strategies used are summarized and listed in Tab. 7.1.

Table 7.1: Comparison of regeneration strategies applied and their influence on SOFC cells.

Regeneration approach	Regeneration time	Reusability	Cell-protecting effect
$\boldsymbol{R}_1$ and $\boldsymbol{R}_2$	$\sim$ 44 h	✓	✓
$\boldsymbol{R}_{3,at100\ \frac{mA}{cm^2}}$ and $\boldsymbol{R}_{2var}$	5-40 h	✓	✓
$\boldsymbol{R}_1$ and $\boldsymbol{R}_{3,overvoltage}$	$\sim$ 12 h	✓	✓
$\boldsymbol{R}_4$	1-10 min	×	×
$\boldsymbol{R}_{4ov}$	$\sim$ 200 s	✓	✓
$\boldsymbol{R}_{3,overvoltage,onlycathodesupply}$	40 s	1-2×	✓
$\boldsymbol{R}_{5var}$	30 s - 10 min	×	×

The combination of regeneration approaches $\boldsymbol{R}_1$ and $\boldsymbol{R}_2$ ensures complete and cell-protecting carbon removal as well as the regeneration of cell performance. In order to support complete regeneration, the two approaches must be combined. Otherwise, full regeneration is not possible. No external power sources are required for the application of this method; however, it is time-consuming, and complete regeneration is only possible after 44 h.

In order to reduce regeneration time, several operating parameters were varied. As first, the concentration of water vapour was increased, and this strategy was specified as $\boldsymbol{R}_{2var}$. This reduced the time required for regeneration, but not significantly. Furthermore, complete regeneration was not reached using only this strategy, but additional fuelling with dry H_2/N_2 mixture was necessary. When the amount of water vapour is increased, the hydrogen/oxygen ratio must be taken into consideration. Otherwise, the risk of Ni-oxidation and the subsequent physical damage of the cell is high.

Another method, specified as electrochemical method $\boldsymbol{R}_3$, involved either power supply or power consumer into operation. Therefore, the flow of oxygen ions through the anode

was forced, thus enhancing the carbon removal. Electric load supported the regeneration process, but complete regeneration was not achieved, even after operating for 44 h.

A novel regeneration strategy was developed in this work, based on the application of overvoltage. Overvoltage was always defined so as not to exceed the critical degradation voltage. For this purpose, the gas supply was varied on both the anode and the cathode side. When applying the overvoltage without gas supply, the regeneration must be performed in a controlled-manner, in order to protect the cell microstructure. For complete regeneration, several cycles with an approximate cycle time of 20 s must be applied. However, the cell-protecting effect was achieved when one cycle was applied and the cell was then supplied with regeneration mixture $\boldsymbol{R}_1$. The application of overvoltage and simultaneous supply of synthetic air to the cathode minimized the risk of microstructure degradation. Further regeneration strategy based on combined CO_2 and overvoltage, specified as $\boldsymbol{R}_{4ov}$, must be highlighted. Complete carbon removal and cell-protecting performance regeneration was achieved after several 20 s cycles. In comparison, the fuelling with CO_2 or other oxygen-enriched mixtures without external power sources led to the rapid degradation of cell performance and mechanical damage.

8 Conclusion

This work has addressed several important challenges faced by the SOFC research field: (1) how to detect cell degradation at an early-stage, (2) how to remove carbon and regenerate cell performance in a cell-protecting manner, and (3) how to separate single processes specified for characteristic electrodes, without using a reference electrode for this purpose.

Anode supported SOFC cells with an industrial relevant size of 10x10 cm^2 were employed for the experimental investigation. Large planar cells differ significantly from small button cells, with an active area of approximately 1 cm^2; this means that there are many differences with regard to temperature and current-distribution along the cell, reforming performance, sealing challenges and many others. This study's utilization of the examined cells must therefore be highlighted, because it means that the finding of this investigation are applicable to the industrial use of SOFC.

For meaningful characterisation of the cells used, an advanced electrochemical analysis was performed in order to determine how every single alternation of the cell performance can be analysed and interpreted at a sufficiently early stage, in addition to determining on which electrode the problem has occurred. This, in turn, allows the problem to be counteracted in a timely manner, or the opportunity for regeneration to be scheduled. The cells were operated under various operating conditions. The number of the fuel components was steadily increased in order to ensure a detailed analysis of their impact on the impedance spectra. This work determined that increasing the number of fuel components induced a reduction of the total impedance. This was explained by means of additional processes that occurred simultaneously to the already running processes, since a parallel electrical circuit of multiple elements reduces the overall impedance. This work also outlined how complex systems like SOFC systems can be analysed, and presented different possibilities for the evaluation of the results obtained, such as the polarization curve, Nyquist plots, Bode

plots and phase plots, all of which are equally important for a meaningful and accurate analysis of the system. Next, this work demonstrated how the chosen approaches can be evaluated, for example, by means of comparison of the polarization curves calculated from the measured impedance data with the measured curves. This work also addressed how to be sure that the equivalent circuit chosen is the ideal solution for the interpretation of the system investigated. The calculation of polarization curves enabled the separation of specific loss sources, such as ohmic, kinetic and diffusion losses. No less important is the distribution of relaxation times method, which allows an advanced analysis of the impedance data. This method encourages the use of other strategies to differentiate the electrode-specific frequencies and the frequency range, and exemplifies how to separate the individual loss mechanisms and associate single processes with the specific frequency range. This work also presented how some degradation mechanisms such as carbon deposits, could be detected during operation by means of simple impedance spectroscopy measurements. This offers an early identification method for this mechanism, which can result in the irreversible deterioration of cell performance and mechanical damage the cell microstructure. [8]

For the purpose of the detailed electrochemical analysis, as well as the carbon deposition experiments and the development of novel approaches to their removal, the anode was supplied with both hydrogen and diverse carbon-containing fuels. It is important to highlight that the measurements were carried out under diesel reformate and syngas, which are of great importance for the use of SOFCs in the automotive industry as an auxiliary power unit (APU) as well as for stationary usage as a combined power-heat unit. Operation under carbon-containing fuel mixtures can result in carbon deposition, however, which can induce irreversible degradation and cell delamination. The thermodynamic equilibrium calculations (including S/C-ratio and C-H-O diagrams) were performed in the course of this work. The amount of carbon formed is thus shown as a function of operating temperature and the applied steam-to-carbon ratio. The formation and deposition of carbon as graphite, as well as the formation of carbon nanofibers on the catalytic active Ni-surface, was observed. Thermodynamic equilibrium calculations showed that lower temperatures are favourable to the formation of graphite while the amount of carbon nanofibers formed peaked at temperatures between 600 and 700 $^{\circ}C$, depending on the operating conditions. However, if the system is not in equilibrium, a number of other factors must be considered such as current density, reaction kinetics, etc., which also define the carbon formation process. [5]

The effect of carbon deposition on the Ni-YSZ anode was also examined by means of electrochemical and chemical analyses. The carbon build-up process on the Ni-catalyst, and in fact, anywhere in the cell fuel supply manifold, was detected at an early stage. Methane and thus a decreasing steam/carbon ratio were identified as having a major impact on the

degradation rate. The critical operating time for carbon deposition thus strongly depends on the amount of methane in the fuel mixture. For lower concentrations of methane in the fuel mixture, such as 2.3 vol%, which is typical for APUs, degradation of the cell's performance was observed after 44 h. In order to accelerate the carbon deposition process and to reduce the total operating time, the methane concentration in the gas mixture used was increased. The estimated time for carbon depositions was thus decreased down to 5 h when feeding the cell DR_9, 3 h for DR_{14}, while the methane concentration of 20.3 vol% reduced the operating time down to 30 minutes. Detailed microscopic investigation showed that carbon was formed uniformly over the Ni- and YSZ-sites. Carbon deposits caused not only the deterioration of the cell performance, but also changes to Ni-YSZ structure. The crushing of YSZ-particles and their deposition on the Ni-catalyst were also determined to be a degradation phenomenon. [6]

The present work advances from a traditional practice of attempting to control or avoid carbon formation to novel methods of carbon gasification and performance regeneration. A number of different approaches for successful carbon removal were presented in this thesis, and a detailed experimental analysis, based on chronopotentiometry, electrochemical impedance spectroscopy, gas analysis and microscopic examination of the utilized cells, was carried out. The stability of the porous Ni-YSZ anode, which was operated on different regeneration gas mixtures and in various electrical modes, was verified. The use of hydrogen in combination with steam has proved to be a very good option for cell protecting carbon removal and restoring cell performance. The experimental study showed that complete regeneration is possible within 44 hours. In order to achieve the optimal gasification time, the water vapour concentration in a gas mixture must be adjusted. Attention must be paid to the critical concentration of water vapour in a gas mixture, in order to prevent undesired Ni oxidation. The methods described were further extended by introducing external power sources, which lead the cell into theoretical electrolysis mode, or by electric load, thus using the cell as a power source. The application of overvoltage, defined by external power source, significantly reduced the regeneration time. However, there is a risk of undesired cell microstructure degradation. Therefore, when applying the overvoltage, regeneration must be carried out in a controlled manner. Interestingly, when applying the overvoltage of 1.45 V for only 20 s, complete regeneration with dry hydrogen/nitrogen was observed after only 12 h. This implies that overvoltage significantly reduces the regeneration time and excludes the requirement for water vapour usage. For further investigation, CO_2 was also introduced as a possible gasification agent. It was found to enable carbon gasification, but also induced further performance degradation. This negative effect was inhibited by the application of overvoltage during the gasification process, meaning that a complete regeneration in a cell-protecting manner was ensured by this method. Based on this finding, a novel approach

of using overvoltage was successfully applied with various gas mixtures in order to gently remove carbon deposits from fuel electrodes. Moreover, the use of oxygen enriched gas mixtures emerged as a fast method of removing carbon deposits, but they also proved to be a fast method of oxidizing catalytic active Ni sites, thus leading to mechanical damage and the cracking of both electrolyte and electrodes. It is thus possible to conclude that the industrial use of several regeneration methods is possible. Although all of the strategies mentioned led to the removal of carbon through gasification, several strategies also induced further degradation of the cell performance or the cell microstructure. In order to avoid the inducing additional undesired degradation phenomena, regeneration must be carried out in a controlled manner. In order to enable the time-saving and cell-friendly application of these methods in auxiliary power units, however, they must be tested on specific SOFC cell types and stacks in order to determine the exact mass flows of the gasification agents used, as well as gas distribution, the applied voltages, and the gasification time required.

Bibliography

[1] V. Yurkiv, ''Reformate-operated {SOFC} anode performance and degradation considering solid carbon formation: A modeling and simulation study,'' *Electrochimica Acta*, vol. 143, pp. 114 -- 128, 2014.

[2] G. C. Institute, ''III.2 fuel cell technology,'' 2016.

[3] R. O'Hayre, S.-W. Cha, W. Colella, and F. B. Prinz, ''Fuel cell fundamentals,'' in *Fuel Cell Fundamentals*, New Jersey: John Wiley and Sons, 2009.

[4] V. Subotić, C. Schluckner, and C. Hochenauer, ''An experimental and numerical study of performance of large planar esc-sofcs and experimental investigation of carbon depositions,'' *Journal of the Energy Institute*, pp. --, 2015.

[5] V. Subotić, C. Schluckner, H. Schroettner, and C. Hochenauer, ''Analysis of possibilities for carbon removal from porous anode of solid oxide fuel cells after different failure modes,'' *Journal of Power Sources*, vol. 302, pp. 378 -- 386, 2016.

[6] V. Subotić, C. Schluckner, B. Stoeckl, V. Lawlor, H. Schroettner, and C. Hochenauer, ''Strategy for carbon gasification from porous ni-ysz anodes of industrial-sized asc-sofc and effects of carbon growth,'' *Journal of the Electrochemical Society*, vol. 163, no. 4, pp. F1515 -- F1522, 2016.

[7] V. Subotić, C. Schluckner, M. Joerg, J. Rechberger, H. Schroettner, and C. Hochenauer, ''Anode regeneration following carbon depositions in an industrial-sized anode supported solid oxide fuel cell operating on synthetic diesel reformate,'' *Journal of Power Sources*, vol. 295, pp. 55--66, 2015.

[8] V. Subotić, C. Schluckner, J. Strasser, V. Lawlor, J. Mathe, J. Rechberger, H. Schroettner, and C. Hochenauer, ''In-situ electrochemical characterization methods for industrial-sized planar solid oxide fuel cells part I: Methodology, qualification and detection of carbon deposition,'' *Electrochimica Acta*, vol. 207, pp. 224 -- 236, 2016.

[9] C. Song, ''Fuel processing for low-temperature and high-temperature fuel cells: Challenges, and opportunities for sustainable development in the 21st century,'' *Catalysis Today*, vol. 77, no. 1–2, pp. 17 -- 49, 2002.

[10] J. Milewski and K. Świrski, ''Artificial neural network-based model for calculating the flow composition influence of solid oxide fuel cell,'' *Journal of Fuel Cell Science and Technology*, vol. 11, no. 2, pp. 021001--1--021001--5, 2014.

[11] D. Stolten and B. Emonts, *Fuel Cell Science and Engineering - Materials, Processes, Systems and Technology - Volume 1.* Weinheim: WILEY-VCH Verlag GmbH&Co. KGaA, 2012.

[12] T. S. Li, H. Miao, T. Chen, W. G. Wang, and C. Xu, ''Effect of simulated coal-derived gas composition on h2s poisoning behavior evaluated using a disaggregation scheme,'' *Journal of The Electrochemical Society*, vol. 156, no. 12, pp. B1383 -- B1388, 2009.

[13] K. Haga, S. Adachi, Y. Shiratori, K. Itoh, and K. Sasaki, ''Poisoning of SOFC anodes by various fuel impurities,'' *Solid State Ionics*, vol. 179, no. 27–32, pp. 1427 -- 1431, 2008.

[14] A. Martinez, K. Gerdes, R. Gemmen, and J. Poston, ''Thermodynamic analysis of interactions between Ni-based solid oxide fuel cells (SOFC) anodes and trace species in a survey of coal syngas,'' *Journal of Power Sources*, vol. 195, no. 16, pp. 5206 -- 5212, 2010.

[15] K. Haga, Y. Shiratori, K. Ito, and K. Sasaki, ''Chlorine poisoning of SOFC Ni-cermet anodes,'' *Journal of The Electrochemical Society*, vol. 155, no. 12, pp. B1233 -- B1239, 2008.

[16] U. D. o. E. O. o. F. E. N. E. T. L. National Technical Information Service, *Fuel Cell Handbook*. Morgantown, West Virginia: EG&G Technical Services, Inc., 2004.

[17] J. B. Goodenough and Y.-H. Huang, ''Alternative anode materials for solid oxide fuel cells,'' *Journal of Power Sources*, vol. 173, no. 1, pp. 1 -- 10, 2007.

[18] W. Chueh, Y. Hao, W. Jung, and S. Haile, ''High electrochemical activity of the oxide phase in model ceria-Pt and ceria-Ni composite anodes,'' *Nature Materials*, vol. 11, no. 2, pp. 155 -- 161, 2012.

[19] T. W. Napporn, X. Jacques-Bedard, F. Morin, and M. Meuniera, ''Operating conditions of a single-chamber SOFC,'' *Journal of the Electrochemical Society*, vol. 151, no. 12, pp. A2088 -- A2094, 2004.

[20] S. Savoie, T. W. Napporn, B. Morel, M. Meunier, and R. Roberge, ''Catalytic activity of Ni-YSZ anodes in a single-chamber solid oxide fuel cell reactor,'' *Journal of Power Sources*, vol. 196, no. 8, pp. 3713 -- 3721, 2011.

[21] J. R. Rostrup-Nielsen, ''Activity of nickel catalysts for steam reforming of hydrocarbons,'' *Journal of Catalysis*, vol. 31, pp. 173 -- 199, 1973.

[22] W. Y. Lee, J. Hanna, and A. F. Ghoniem, ''On the predictions of carbon deposition on the nickel anode of a SOFC and its impact on open-circuit conditions,'' *Journal of The Electrochemical Society*, vol. 160, no. 2, pp. 94 -- 105, 2013.

[23] I. Kang, Y. Kang, S. Yoon, G. Bae, and J. Bae, ''The operating characteristics of solid oxide fuel cells driven by diesel autothermal reformate,'' *International Journal of Hydrogen Energy*, vol. 33, no. 21, pp. 6298 -- 6307, 2008.

[24] J. Maček, B. Novosel, and M. Marinšek, ''Ni–YSZ SOFC anodes—minimization of carbon deposition,'' *Journal of the European Ceramic Society*, vol. 27, no. 2–3, pp. 487 -- 491, 2007.

[25] B. Novosel, M. Marinšek, and J. Maček, ''Deactivation of Ni–YSZ material in dry methane and oxidation of various forms of deposited carbon,'' *Journal of Fuel Cell Science and Technology*, vol. 9, no. 6, pp. 061003--1 -- 061003--6, 2012.

[26] J.-H. Koh, Y.-S. Yoo, J.-W. Park, and H. C. Lim, ''Carbon deposition and cell performance of ni-ysz anode support sofc with methane fuel,'' *Solid State Ionics*, vol. 149, no. 3–4, pp. 157 -- 166, 2002.

[27] A. Lanzini, P. Leone, C. Guerra, F. Smeacetto, N. Brandon, and M. Santarelli, ''Durability of anode supported solid oxides fuel cells (SOFC) under direct dry-reforming of methane,'' *Chemical Engineering Journal*, vol. 220, pp. 254 -- 263, 2013.

[28] *Operating Micro-Tubular SOFC Containing Nickel Based Anodes with Blends of Methane and Hydrogen*, IEEE, 2007.

[29] H. Timmermann, W. Sawady, D. Campbell, A. Weber, R. Reimart, and E. Ivers-Tiffee, ''Coke formation and degradation in SOFC operation with a model reformate from liquid hydrocarbons,'' *Journal of the Electrochemical Society*, vol. 155, no. 4, pp. B356 -- B359, 2008.

[30] E. Lorente, M. Millan, and N. Brandon, ''Use of gasification syngas in SOFC: Impact of real tar on anode materials,'' *International Journal of Hydrogen Energy*, vol. 37, no. 8, pp. 7271 -- 7278, 2012.

[31] T. Chen, W. G. Wang, H. Miao, T. Li, and C. Xu, ''Evaluation of carbon deposition behavior on the nickel/yttrium-stabilized zirconia anode-supported fuel cell fueled with simulated syngas,'' *Journal of Power Sources*, vol. 196, no. 5, pp. 2461 -- 2468, 2011.

[32] J. Xiao, Y. Xie, J. Liu, and M. Liu, ''Deactivation of nickel-based anode in solid oxide fuel cells operated on carbon-containing fuels,'' *Journal of Power Sources*, vol. 268, pp. 508 -- 516, 2014.

[33] S. Wang, T. Kobayashi, M. Dokiya, and T. Hashimoto, ''Electrical and ionic conductivity of Gd-doped Ceria,'' *Journal of The Electrochemical Society*, vol. 147, no. 10, pp. 3606 -- 3609, 2000.

[34] H. He and J. M. Hill, ''Carbon deposition on Ni/YSZ composites exposed to humidified methane,'' *Applied Catalysis A: General*, vol. 317, no. 2, pp. 284 -- 292, 2007.

[35] E. Ramirez-Cabrera, A. Atkinson, and D. Chadwick, ''The influence of point defects on the resistance of ceria to carbon deposition in hydrocarbon catalysis,'' *Solid State Ionics*, vol. 136–137, pp. 825 -- 831, 2000.

[36] H. Kim, C. Lu, W. L. Worrell, J. M. Vohs, and R. J. Gorte, ''Cu-Ni cermet anodes for direct oxidation of methane in solid-oxide fuel cells,'' *Journal of The Electrochemical Society*, vol. 149, no. 3, pp. A247 -- A250, 2002.

[37] S. Park, J. M. Vohs, and R. J. Gorte, ''Direct oxidation of hydrocarbons in a solid oxide fuel cells,'' *Lett. Nature*, vol. 404, pp. 265 -- 267, 2000.

[38] M. S. Khan, S.-B. Lee, R.-H. Song, J.-W. Lee, T.-H. Lim, and S.-J. Park, ''Fundamental mechanisms involved in the degradation of nickel–yttria stabilized zirconia (Ni–YSZ) anode during solid oxide fuel cells operation: A review,'' *Ceramics International*, vol. 42, pp. 35--48, Jan. 2016.

[39] S. McIntosh, J. M. Vohs, and R. J. Gorte, ''Role of hydrocarbon deposits in the enhanced performance of direct-oxidation SOFCs,'' *Journal of The Electrochemical Society*, vol. 150, no. 4, pp. A470 -- A476, 2003.

[40] H. He, J. M. Vohs, and R. J. Gorte, ''Carbonaceous deposits in direct utilization hydrocarbon SOFC anode,'' *Journal of Power Sources*, vol. 144, no. 1, pp. 135 -- 140, 2005.

[41] V. Alzate-Restrepo and J. M. Hill, ''Effect of anodic polarization on carbon deposition on Ni/YSZ anodes exposed to methane,'' *Applied Catalysis A: General*, vol. 342, no. 1–2, pp. 49 -- 55, 2008.

[42] J. Lawrence and M. Boltze, ''Auxiliary power unit based on a solid oxide fuel cell and fuelled with diesel,'' *Journal of Power Sources*, vol. 154, no. 2, pp. 479 -- 488, 2006.

[43] J. Rechbergeer, M. Reissig, and M. Hauth, ''AVL SOFC systems on the way of industrialization,'' *ESC Transactions*, vol. 57, no. 1, pp. 141 -- 148, 2013.

[44] H.-T. Lim, S. C. Hwang, and J. S. Ahn, ''Performance of anode-supported solid oxide fuel cell in planar-cell channel-type setup,'' *Ceramics International*, vol. 39, Supplement 1, pp. S659 -- S662, 2013.

[45] M. Hauth, W. Lerch, K. Koenig, and J. Karl, ''Impact of naphthalene on the performance of SOFCs during operation with synthetic wood gas,'' *Journal of Power Sources*, vol. 196, no. 17, pp. 7144 -- 7151, 2011.

[46] C. Schluckner, V. Subotić, V. Lawlor, and C. Hochenauer, ''Three-dimensional numerical and experimental investigation of an industrial-sized SOFC fueled by diesel reformat – part I: Creation of a base model for further carbon deposition modeling,'' *International Journal of Hydrogen Energy*, vol. 39, no. 33, pp. 19102 -- 19118, 2014.

[47] S. C. Singhal and K. Kendall, ''Preface,'' in *High Temperature and Solid Oxide Fuel Cells* (S. C. Singhal and K. Kendal, eds.), pp. xv -- xvi, Amsterdam: Elsevier Science, 2003.

[48] K. Kendall and M. Kendall, *High-temperature Solid Oxide Fuel Cells for the 21st Century: Fundamentals, Design and Application*. Elsevier, 2016.

[49] W. Winkler, *Brennstoffzellenanlagen*. VDI-Buch, Springer Berlin Heidelberg, 2002.

[50] A. Leonide, *SOFC Modelling and Parameter Identification by means of Impedance Spectroscopy*. PhD thesis, Universitaet Karlsruhe, 2010.

[51] D. Noren and M. Hoffman, ''Clarifying the butler–volmer equation and related approximations for calculating activation losses in solid oxide fuel cell models,'' *Journal of Power Sources*, vol. 152, pp. 175 -- 181, 2005.

[52] M. E. Orazem and B. Tribollet, *Electrochemical Impedance Spectroscopy*. A John Wiley and Sons, Inc., Publication: A John Wiley and Sons, Inc.,Publication, 2008.

[53] A. Bard and L. Faulkner, *Electrochemical Methods: Fundamentals and Applications*. Wiley, 2000.

[54] M. Bieber, *Messmethoden zur Untersuchung der Kohlenstoffablagerung an nickelhaltigen SOFC-Anoden beim Betrieb mit Methan*. PhD thesis, Technische Universitaet Muenchen, 2010.

[55] M. Stern and A. L. Geary, ''Electrochemical polarization i. a theoretical analysis of the shape of polarization curves,'' *Journal of the Electrochemical Society*, vol. 104, no. 1, pp. 57 -- 63, 1957.

[56] U. Reimer, B. Schumacher, and W. Lehnert, ''Accelerated degradation of high-temperature polymer electrolyte fuel cells: Discussion and empirical modeling,'' *Journal of the Electrochemical Society*, vol. 162, no. 1, pp. F153 -- F164, 2015.

[57] R. Das, *Kinetic studies of anode materials for solid oxide fuel cells (SOFC)*. PhD thesis, The University of Alabama, 2013.

[58] A. A. Kulikovsky, ''A model for SOFC anode performance,'' *Electrochimica Acta*, vol. 54, no. 26, pp. 6686--6695.

[59] M. J. Jørgensen, S. Primdahl, and M. Mogensen, ''Characterisation of composite SOFC cathodes using electrochemical impedance spectroscopy,'' *Electrochimica Acta*, vol. 44, no. 24, pp. 4195--4201.

[60] T. Jacobsen, P. V. Hendriksen, and S. Koch, ''Diffusion and conversion impedance in solid oxide fuel cells,'' *Electrochimica Acta*, vol. 53, no. 25, pp. 7500--7508, 2008.

[61] C. Fu, K. Sun, N. Zhang, X. Chen, and D. Zhou, ''Electrochemical characteristics of LSCF–SDC composite cathode for intermediate temperature SOFC,'' *Electrochimica Acta*, vol. 52, no. 13, pp. 4589--4594.

[62] A. Barbucci, M. Viviani, P. Carpanese, D. Vladikova, and Z. Stoynov, ''Impedance analysis of oxygen reduction in SOFC composite electrodes,'' *Electrochimica Acta*, vol. 51, no. 8–9, pp. 1641--1650.

[63] J. Nielsen, T. Jacobsen, and M. Wandel, ''Impedance of porous IT-SOFC LSCF:CGO composite cathodes,'' *Electrochimica Acta*, vol. 56, pp. 7963--7974, Sept. 2011.

[64] J. Nielsen and J. Hjelm, ''Impedance of SOFC electrodes: A review and a comprehensive case study on the impedance of LSM:YSZ cathodes,'' *Electrochimica Acta*, vol. 115, pp. 31--45, Jan. 2014.

[65] Q.-A. Huang, M. Liu, and M. Liu, ''Impedance Spectroscopy Study of an SDC-based SOFC with High Open Circuit Voltage,'' *Electrochimica Acta*, vol. 177, pp. 227--236, Sept. 2015.

[66] D. E. Vladikova, Z. B. Stoynov, A. Barbucci, M. Viviani, P. Carpanese, J. A. Kilner, S. J. Skinner, and R. Rudkin, ''Impedance studies of cathode/electrolyte behaviour in SOFC,'' *Electrochimica Acta*, vol. 53, no. 25, pp. 7491--7499, 2008.

[67] M. Lang, C. Auer, A. Eismann, P. Szabo, and N. Wagner, ''Investigation of solid oxide fuel cell short stacks for mobile applications by electrochemical impedance spectroscopy,'' *Electrochimica Acta*, vol. 53, no. 25, pp. 7509--7513, 2008.

[68] G. J. Offer, P. Shearing, J. I. Golbert, D. J. L. Brett, A. Atkinson, and N. P. Brandon, ''Using electrochemical impedance spectroscopy to compensate for errors when measuring polarisation curves during three-electrode measurements of solid oxide fuel cell electrodes,'' *Electrochimica Acta*, vol. 53, pp. 7614--7621, Nov. 2008.

[69] Q.-A. Huang, R. Hui, B. Wang, and J. Zhang, ''A review of AC impedance modeling and validation in SOFC diagnosis,'' *Electrochimica Acta*, vol. 52, no. 28, pp. 8144--8164, 2007.

[70] A. Nechache, M. Cassir, and A. Ringuedé, ''Solid oxide electrolysis cell analysis by means of electrochemical impedance spectroscopy: A review,'' *Journal of Power Sources*, vol. 258, pp. 164 -- 181, 2014.

[71] J. Schefold, A. Brisse, and F. Tietz, ''Nine thousand hours of operation of a solid oxide cell in steam electrolysis mode,'' *Journal of the Electrochemical Society*, vol. 159, no. 2, pp. A137 -- A144, 2012.

[72] J. Schefold, A. Brisse, and H. Poepke, ''Long-term steam electrolysis with electrolyte-supported solid oxide cells,'' *Electrochimica Acta*, vol. 179, pp. 161 -- 168, 2015.

[73] D. D. Macdonald, ''Reflections on the history of electrochemical impedance spectroscopy,'' *Electrochimica Acta*, vol. 51, no. 8–9, pp. 1376 -- 1388, 2006.

[74] D. D. Macdonald, ''Review of mechanistic analysis by electrochemical impedance spectroscopy,'' *Electrochimica Acta*, vol. 35, no. 10, pp. 1509 -- 1525, 1990.

[75] E. Barsoukov and J. R. Macdonald, *Impedance Spectroscopy Theory, Experiment, and Applications*. A John Wiley and Sons, Inc., Publication: A John Wiley and Sons, Inc.,Publication, 2005.

[76] D. Vladikova, ''The technique of the differential impedance analysis part I: Basics of the impedance spectroscopy,'' pp. L8.1 -- L.828, 2004.

[77] A. Weber, *Entwicklung von Kathodenstruktur für die Hochtemperatur-Brennstoffzelle SOFC*. PhD thesis, Universitaet Fridericiana Karlsruhe, 2002.

[78] V. F. Lvovich, *Impedance spectroscopy Applications to Electrochemical and Dielectric Phenomena*. Hoboken, New Jersey: A John Wiley and Sons, Inc.,Publication, 2012.

[79] B. S. Instruments, *BT-Lab and EC-Lab Data Analysis and Processes*, 2015.

[80] J. R. Macdonald, ''Impedance spectroscopy,'' *Annals of Biomedical Engineering*, vol. 20, no. 3, pp. 289--305, 1992.

[81] T. Pajkossy and L. Nyikos, ''Impedance of fractal blocking electrodes,'' *Journal of the Electrochemical Society*, vol. 133, no. 10, pp. 2061 -- 2064, 1986.

[82] M. Saccoccio, T. H. Wan, C. Chen, and F. Ciucci, ''Optimal regularization in distribution of relaxation times applied to electrochemical impedance spectroscopy: Ridge and lasso regression methods - a theoretical and experimental study,'' *Electrochimica Acta*, vol. 147, pp. 470 -- 482, 2014.

[83] F. Ciucci and C. Chen, ''Analysis of electrochemical impedance spectroscopy data using the distribution of relaxation times: A bayesian and hierarchical bayesian approach,'' *Electrochimica Acta*, vol. 167, pp. 439 -- 454, 2015.

[84] T. H. Wan, M. Saccoccio, C. Chen, and F. Ciucci, ''Influence of the discretization methods on the distribution of relaxation times deconvolution: Implementing radial basis functions with DRTtools,'' *Electrochimica Acta*, vol. 184, pp. 483 -- 499, 2015.

[85] D. Vladikova, Z. Stoynov, A. Barbucci, M. Viviani, P. Carpanese, J. Kilner, S. Skinner, and R. Rudkin, ''Impedance studies of cathode/electrolyte behaviour in sofc,'' *Electrochimica Acta*, vol. 53, no. 25, pp. 7491 -- 7499, 2008.

[86] ''Strongly heteroscedatic nonlinear regression,'' *Commun. Stat. Simulat.*, vol. 20, no. 4, pp. 843 -- 886, 1991.

[87] J. Weese, ''Ftikreg: A program for the solution of fredholm integral equations of the first kind user manual,'' *Computer Physics Communications*, vol. 69, p. 99, 1992.

[88] J. R. Rostrup-Nielsen, ''Equilibria of decomposition reactions of carbon monoxide and methane over nickel catalyst,'' *Journal of Catalysis*, vol. 27, pp. 343 -- 356, 1972.

[89] J. R. Rostrup-Nielsen, ''Activity of nickel catalysts for steam reforming of hydrocarbons,'' *Journal of Catalysis*, vol. 31, no. 2, pp. 173 -- 199, 1973.

[90] J. R. Rostrup-Nielsen, ''Coking on nickel catalysts for steam reforming of hydrocarbons,'' *Journal of Catalysis*, vol. 33, no. 2, pp. 184 -- 201, 1974.

[91] J. Rostrup-Nielsen and D. L. Trimm, ''Mechanisms of carbon formation on nickel-containing catalysts,'' *Journal of Catalysis*, vol. 48, no. 1–3, pp. 155 -- 165, 1977.

[92] F. Besenbacher, I. Chorkendorff, B. Clausen, B. Hammer, A. Molenbrock, J. Nørskov, and I. Stensgaard, ''Design of a surface alloy catalyst for steam reforming,'' *Science*, vol. 279, no. 5358, pp. 1913--1915, 1998.

[93] H. Bengaard, J. Nørskov, J. Sehested, B. Clausen, L. Nielsen, A. Molenbroek, and J. Rostrup-Nielsen, ''Steam reforming and graphite formation on Ni catalysts,'' *Journal of Catalysis*, vol. 209, no. 2, pp. 365 -- 384, 2002.

[94] D. Singh, E. Hernández-Pacheco, P. N. Hutton, N. Patel, and M. D. Mann, ''Carbon deposition in an SOFC fueled by tar-laden biomass gas: a thermodynamic analysis,'' *Journal of Power Sources*, vol. 142, no. 1–2, pp. 194 -- 199, 2005.

[95] T. Takeguchi, Y. Kani, T. Yano, R. Kikuchi, K. Eguchi, K. Tsujimoto, Y. Uchida, A. Ueno, K. Omoshiki, and M. Aizawa, ''Study on steam reforming of CH4 and C2 hydrocarbons and carbon deposition on Ni-YSZ cermets,'' *Journal of Power Sources*, vol. 112, no. 2, pp. 588 -- 595, 2002.

[96] D. Mogensen, J.-D. Grunwaldt, P. Hendriksen, K. Dam-Johansen, and J. Nielsen, ''Internal steam reforming in solid oxide fuel cells: Status and opportunities of kinetic studies and their impact on modelling,'' *Journal of Power Sources*, vol. 196, no. 1, pp. 25 -- 38, 2011.

[97] B. R. Alexander, R. E. Mitchell, and T. M. Gür, ''Modeling of experimental results for carbon utilization in a carbon fuel cell,'' *Journal of Power Sources*, vol. 228, pp. 132 -- 140, 2013.

[98] S. Park, J. M. Vohs, and R. J. Gorte, ''Direct oxidation of hydrocarbons in a solid-oxide fuel cell,'' *Letter to Nature*, vol. 404, pp. 265 -- 267, 2000.

[99] C. H. Bartholomew, ''Carbon deposition in steam reforming and methanation,'' *Catalysis Reviews: Science and Engineering*, vol. 24, no. 1, pp. 67 -- 112, 1982.

[100] E.-M. Köck, M. Kogler, T. Götsch, B. Klötzer, and S. Penner, ''Structural and chemical degradation mechanisms of pure YSZ and its components ZrO2 and Y2O3 in carbon-rich fuel gases,'' *Physical Chemistry Chemical Physics*, vol. 18, no. 21, pp. 14333--14349, 2016.

[101] M. Kogler, E.-M. Köck, L. Perfler, T. Bielz, M. Stöger-Pollach, W. Hetaba, M. Willinger, X. Huang, M. Schuster, B. Klötzer, and S. Penner, ''Methane Decomposition and Carbon Growth on Y2o3, Yttria-Stabilized Zirconia, and ZrO2,'' *Chem. Mater.*, vol. 26, pp. 1690--1701, Feb. 2014.

[102] K. Sasaki and Y. Teraoka, ''Equilibria in fuel cell gases: I. equilibrium compositions and reforming conditions,'' *Journal of The Electrochemical Society*, vol. 150, no. 7, pp. 878 -- 884, 2003.

[103] A. Drif, N. Bion, R. Brahmi, S. Ojala, L. Pirault-Roy, E. Turpeinen, P. K. Seelam, R. L. Keiski, and F. Epron, ''Study of the dry reforming of methane and ethanol using Rh catalysts supported on doped alumina,'' *Applied Catalysis A: General*, vol. 504, pp. 576 -- 584, 2015.

[104] W. Yang, R. Zhang, B. Chen, N. Bion, D. Duprez, and S. Royer, ''Activity of perovskite-type mixed oxides for the low-temperature CO oxidation: Evidence of oxygen species participation from the solid,'' *Journal of Catalysis*, vol. 295, pp. 45 -- 58, 2012.

[105] J. S. Moura, J. da Silva Lima Fonseca, N. Bion, F. Epron, T. de Freitas Silva, C. G. Maciel, J. M. Assaf, and M. do Carmo Rangel, ''Effect of lanthanum on the properties of copper, cerium and zirconium catalysts for preferential oxidation of carbon monoxide,'' *Catalysis Today*, vol. 228, pp. 40 -- 50, 2014.

[106] F. Diehl, J. Barbier, D. Duprez, I. Guibard, and G. Mabilon, ''Catalytic oxidation of heavy hydrocarbons over Pt/Al2O3. oxidation of C10+ solid hydrocarbons representative of soluble organic fraction of diesel soots,'' *Applied Catalysis A: General*, vol. 504, pp. 37 -- 43, 2015.

[107] A. Wootsch, C. Descorme, S. Rousselet, D. Duprez, and C. Templier, ''Carbon monoxide oxidation over well-defined pt/zro2 model catalysts: Bridging the material gap,'' *Applied Surface Science*, vol. 253, no. 3, pp. 1310 -- 1322, 2006.

[108] J. Fonseca, S. Royer, N. Bion, L. Pirault-Roy, M. do Carmo Rangel, D. Duprez, and F. Epron, ''Preferential CO oxidation over nanosized gold catalysts supported on ceria and amorphous ceria–alumina,'' *Applied Catalysis B: Environmental*, vol. 128, pp. 10 -- 20, 2012.

[109] F. Aupretre, C. Descorme, and D. Duprez, ''63 steam reforming catalysts for H2 production from ethanol,'' in *Science and Technology in Catalysis 2002: Proceedings of the Fourth Tokyo conference on Advance Catalytic Science and Technology* (M. O. Masakazu Anpo and H. Yamashita, eds.), vol. 145 of *Studies in Surface Science and Catalysis*, pp. 303 -- 306, Elsevier, 2003.

[110] S. Ayabe, H. Omoto, T. Utaka, R. Kikuchi, K. Sasaki, Y. Teraoka, and K. Eguchi, ''Catalytic autothermal reforming of methane and propane over supported metal catalysts,'' *Applied Catalysis A: General*, vol. 241, no. 1–2, pp. 261 -- 269, 2003.

[111] M. C. Bradford and M. A. Vannice, ''Catalytic reforming of methane with carbon dioxide over nickel catalysts i. catalyst characterization and activity,'' *Applied Catalysis A: General*, vol. 142, no. 1, pp. 73 -- 96, 1996.

[112] M. C. Bradford and M. A. Vannice, ''Catalytic reforming of methane with carbon dioxide over nickel catalysts ii. reaction kinetics,'' *Applied Catalysis A: General*, vol. 142, no. 1, pp. 97 -- 122, 1996.

[113] F. Auprêtre, C. Descorme, and D. Duprez, ''Bio-ethanol catalytic steam reforming over supported metal catalysts,'' *Catalysis Communications*, vol. 3, no. 6, pp. 263 -- 267, 2002.

[114] K. Yamaji, H. Kishimoto, Y. Xiong, T. Horita, N. Sakai, M. E. Brito, and H. Yokokawa, ''Catalytic methane decomposition on nickel-based model anodes of SOFCs fabricated on various oxide ion conductors,'' *Solid State Ionics*, vol. 179, no. 27–32, pp. 1526 -- 1530, 2008.

[115] H. Sumi, K. Ukai, Y. Mizutani, H. Mori, C.-J. Wen, H. Takahashi, and O. Yamamoto, ''Performance of nickel–scandia-stabilized zirconia cermet anodes for SOFCs in 3no. 1–4, pp. 151 -- 156, 2004.

[116] K. Nikooyeh, R. Clemmer, V. Alzate-Restrepo, and J. M. Hill, ''Effect of hydrogen on carbon formation on Ni/YSZ composites exposed to methane,'' *Applied Catalysis A: General*, vol. 347, no. 1, pp. 106 -- 111, 2008.

[117] C. Schluckner, V. Subotić, V. Lawlor, and C. Hochenauer, ''Carbon deposition simulation in porous SOFC anodes: A detailed numerical analysis of majojr carbon precursors,'' *Fuel Cell Science and Technology*, vol. 12, pp. 051007--1 -- 051007--12, 2015.

[118] K. Sasaki and Y. Teraoka, ''Equilibria in fuel cell gases: II. the C-H-O ternary diagrams,'' *Journal of The Electrochemical Society*, vol. 150, no. 7, pp. 885 -- 888, 2003.

[119] G. Bae, J. Bae, P. Kim-Lohsoontorn, and J. Jeong, ''Performance of SOFC coupled with n-C4H10 autothermal reformer: Carbon deposition and development of anode structure,'' *International Journal of Hydrogen Energy*, vol. 35, no. 22, pp. 12346 -- 12358, 2010.

[120] S. Sameshima, N. Furukawa, Y. Hirata, and T. Shimonosono, ''Cell performance of SOFC using CH4/CO2 mixed gases,'' *Ceramics International*, vol. 40, no. 4, pp. 6279 -- 6284, 2014.

[121] J. Mermelstein, M. Millan, and N. Brandon, ''The impact of carbon formation on ni–ysz anodes from biomass gasification model tars operating in dry conditions,'' *Chemical Engineering Science*, vol. 64, no. 3, pp. 492 -- 500, 2009.

[122] G. Saunders, J. Preece, and K. Kendall, ''Formulating liquid hydrocarbon fuels for sofcs,'' *Journal of Power Sources*, vol. 131, no. 1–2, pp. 23 -- 26, 2004.

[123] H. Kim, S. Park, J. M. Vohs, and R. J. Gorte, ''Direct oxidation of hydrocarbons in a solid-oxide fuel cell,'' *Journal of the Electrochemical Society*, vol. 148, no. 7, pp. A693 -- A695, 2001.

[124] C. Schluckner, V. Subotić, V. Lawlor, and C. Hochenauer, ''Numerical SOFC anode catalyst occupation study: Internal reforming of carbonaceous fuel mixtures,'' *Journal of the Electrochemical Society*, vol. 163, no. 7, pp. F761 -- F770, 2016.

[125] S. Takenaka, E. Kato, Y. Tomikubo, and K. Otsuka, ''Structural change of Ni species during the methane decomposition and the subsequent gasification of deposited carbon with CO2 over supported ni catalysts,'' *Journal of Catalysis*, vol. 219, no. 1, pp. 176 -- 185, 2003.

[126] J.-W. Snoeck and G. Froment, ''Steam/CO2 reforming of methane. carbon filament formation by the boudouard reaction and gasification by CO2, by H2, and by steam: Kinetic study,'' *Ind. Eng. Chem. Res.*, vol. 41, pp. 4252 -- 4265, 2002.

[127] P. S. Guanawardana, T. T. M. Nguyen, J. C. Walmsley, and H. J. Venvik, ''Initiation of metal dusting corrosion in conversion of natural gas to syngas studied under industrially relevant conditions,'' *IEC research Industrial and Engineering Chemistry Research*, vol. 53, pp. 1794 -- 1803, 2014.

[128] S. Helveg, J. Sehestad, and J. Rostrup-Nielsen, ''Whisker carbon in perspective,'' *Catalysis Today*, vol. 178, pp. 42 -- 46, 2011.

[129] J. D. Kirtley, M. B. Pomfret, D. A. Steinhurst, J. C. Owrutsky, and R. A. Walker, ''Toward a working mechanism of fuel oxidation in SOFCs: In situ optical studies of simulated biogas and methane,'' *The Journal of Physical Chemistry C*, vol. 119, pp. 12781 -- 12791, 2015.

[130] M. B. Pomfret, D. A. Steinhurst, and J. C. Owrutsky, ''Methanol and ethanol fuels in solid oxide fuel cells: A thermal imagingn study of carbon deposition,'' *energyfuels*, vol. 25, pp. 2633-- 2642, 2011.

[131] M. B. Pomfret, J. C. Owrutsky, and R. A. Walker, ''In situ studies of fuel oxidation in solide oxide fuel cells,'' *Analytical Chemistry*, vol. 79, no. 6, pp. 2367 -- 2372, 2007.

[132] M. B. Pomfret, D. A. Steinhurst, and J. C. Owrutsky, ''Ni/YSZ solid oxide fuel cell anodes operating on humidified ethanol fuel feeds: An optical study,'' *Journal of Power Sources*, vol. 233, pp. 331 -- 340, 2013.

[133] B. C. Eigenbrodt, M. B. Pomfret, D. A. Steinhurst, J. C. Owrutsky, and robert A. Walker, ''Direct, in situ optical studies of Ni-YSZ anodes in solid oxide fuel cells operating with methanol and methane,'' *The Journal of Physical Chemistry C*, vol. 115, pp. 2895 -- 2903, 2011.

[134] K. M. Walters, A. M. Dean, H. Zhu, and R. J. Kee, ''Homogeneous kinetics and equilibrium predicitions of coking propensity in the anode channels of direct oxidation solid-oxide fuel cells using dry natural gas,'' *Journal of Power Sources*, vol. 123, pp. 182 -- 189, 2003.

[135] M. Pillai, Y. Lin, H. Zhu, R. J. Kee, and S. A. Barnett, ''Stability and coking of direct-methane solide oxide fuel cells: Effect of CO2 and air additions,'' *Journal of Power Sources*, vol. 195, pp. 271 -- 279, 2010.

[136] C. J. Moyer, N. P-Sullivan, H. Zhu, and R. J. Kee, ''Polarization characteristics and chemistry in reversible tubular solid-oxide cells operating on mixtures of h2, co, h2o, and co2,'' *Journal of The Electrochemical Society*, vol. 158, no. 2, pp. B117 -- B131, 2011.

[137] C. Schluckner, V. Subotić, V. Lawlor, and C. Hochenauer, ''Three-dimensional numerical and experimental investigation of an industrial-sized SOFC fueled by diesel reformat – part II: Detailed reforming chemistry and carbon deposition analysis,'' *International Journal of Hydrogen Energy*, vol. 40, no. 39, pp. 10943 -- 10959, 2015.

[138] V. Alzate-Restrepo and J. M. Hill, ''Carbon deposition on Ni/YSZ anodes exposed to CO/H2 feeds,'' *Journal of Power Sources*, vol. 195, no. 5, pp. 1344 -- 1351, 2010.

[139] J. Mermelstein, M. Millan, and N. Brandon, ''The impact of steam and current density on carbon formation from biomass gasification tar on Ni/YSZ, and Ni/CGO solid oxide fuel cell anodes,'' *Journal of Power Sources*, vol. 195, no. 6, pp. 1657 -- 1666, 2010.

[140] C. Mallon and K. Kendall, ''Sensitivity of nickel cermet anodes to reduction conditions,'' *Journal of Power Sources*, vol. 145, no. 2, pp. 154 -- 160, 2005.

[141] J. Figueiredo and D. Trimm, ''Gasification of carbon deposits on nickel catalysts,'' *Journal of Catalysis*, vol. 40, no. 2, pp. 154 -- 159, 1975.

[142] J. Figueiredo, C. Bernardo, and J.J.M.Orfao., *Gasification of carbon deposited on metallic catalyst*, pp. 269 -- 287. Dordrecht: Springer Netherlands, 1986.

[143] D. L. Trimm, ''The formation and removal of coke from nickel catalyst,'' *Catalytic Reviews*, vol. 16, no. 2, pp. 155 -- 189, 1977.

[144] D. L. Trimm, *The Regeneration of Coked Catalysts*, pp. 543 -- 555. Dordrecht: Springer Netherlands, 1986.

[145] C. Bernardo and D. Trimm, ''The kinetics of gasification of carbon deposited on nickel catalysts,'' *Carbon*, vol. 17, no. 2, pp. 115 -- 120, 1979.

[146] J. McCarty and H. Wise, ''Hydrogenation of surface carbon on alumina-supported nickel,'' *Journal of Catalysis*, vol. 57, no. 3, pp. 406 -- 416, 1979.

[147] S. Takenaka, T. Shimizu, and K. Otsuka, ''Complete removal of carbon monoxide in hydrogen-rich gas stream through methanation over supported metal catalysts,'' *International Journal of Hydrogen Energy*, vol. 29, no. 10, pp. 1065 -- 1073, 2004.

[148] S. Takenaka, Y. Tomikubo, E. Kato, and K. Otsuka, ''Sequential production of H2 and CO over supported ni catalysts,'' *Fuel*, vol. 83, no. 1, pp. 47 -- 57, 2004.

[149] T. Horita, K. Yamaji, T. Kato, H. Kishimoto, Y. Xiong, N. Sakai, M. E. Brito, and H. Yokokawa, ''Imaging of CH4 decomposition around the Ni/YSZ interfaces under anodic polarization,'' *Journal of Power Sources*, vol. 145, no. 2, pp. 133 -- 138, 2005.

[150] J. Kirtley, A. Singh, D. Halat, T. Oswell, and J. M. Hill, ''In situ raman studies of carbon removal from high temperature Ni-YSZ cermet anodes by gas phase reforming agents,'' *The Journal of Physical Chemistry*, vol. 117, pp. 25908 -- 25916, 2013.

[151] A. K. M. S. Chowdhury, S. A. Akbar, S. Kapileshwar, and J. R. Schorr, ''A Rugged Oxygen Gas Sensor with Solid Reference for High Temperature Applications,'' *Journal of The Electrochemical Society*, vol. 148, pp. G91--G94, Feb. 2001.

[152] D. F. Lupton, J. Merker, and F. Schölz, ''The Correct Use of Platinum in the XRF Laboratory,'' 1997.

[153] FuelCon, *TrueData-Load*, 2010.

[154] *Solid Oxide Fuel Cell performance under severe operating conditions*, 6th European Solid Oxide Fuel Cell Forum, 2004.

[155] N. P. Frank, *Umsetzung von Kohlenwasserstoffen in DOFCs*. PhD thesis, Technische Universitaet Muenchen, 2009.

[156] B. S. Instruments, ''Ec-lab electrochemistry,'' 2016.

[157] B. S. Instruments, *VSP Installation and Configuration Manual*, 2007.

[158] B. S. Instruments, *EC-Lab Software User's Manual*, 2007.

[159] V. Sonn, A. Leonide, and E. Ivers-Tiffée, ''Combined deconvolution and cnls fitting approach applied on the impedance response of technical Ni8YSZ cermet electrodes,'' *J. Electrochem. Soc.*, vol. 155, no. 7, pp. B675--B679, 2008.

[160] B. S. Instruments, *ABB Advance Optima 2000*, 2005.

[161] A. Kromp, A. Leonide, A. Weber, and E. Ivers-Tiffée, ''Electrochemical Analysis of Reformate-Fuelled Anode Supported SOFC,'' *J. Electrochem. Soc.*, vol. 158, pp. B980--B986, Aug. 2011.

[162] M. B. Pomfret, D. A. Steinhurst, D. A. Kidwell, and J. C. Owrutsky, ''Thermal imaging of solid oxide fuel cell anode processes,'' *Journal of Power Sources*, vol. 195, no. 1, pp. 257 -- 262, 2010.

[163] C. A. Lozano, M. Ohasi, S. Shimpalee, J. W. V. Zee, and P. Aungkavattana, ''Comparison of hydrogen and methane as fuel in micro-tubular sofc using electrochemical analysis,'' *Journal of the Electrochemical Society*, vol. 158, no. 10, pp. B1235 -- B1245, 2011.

[164] A. Leonide, A. Weber, and E. Ivers-Tiffee, ''Electrochemical analysis of biogas fueled anode supported sofc,'' *ESC Transactions*, vol. 35, no. 1, pp. 2961 -- 2968, 2011.

[165] M. Yoshinaga, H. Kishimoto, K. Yamaji, Y.-P. Xiong, M. E. Brito, T. Horita, and H. Yokokawa, ''Deposited carbon distributions on nickel film/oxide substrate systems,'' *Solid State Ionics*, vol. 192, no. 1, pp. 571 -- 575, 2011.

[166] H. Sumi, P. Puengjinda, H. Muroyama, T. Matsui, and K. Eguchi, ''Effects of crystal structure of yttria- and scandia-stabilized zirconia in nickel-based SOFC anodes on carbon deposition and oxidation behavior,'' *Journal of Power Sources*, vol. 196, no. 15, pp. 6048 -- 6054, 2011.

[167] J. Millichamp, T. J. Mason, N. P. Brandon, R. J. Brown, R. C. Maher, G. Manos, T. P. Neville, and D. J. Brett, ''A study of carbon deposition on solid oxide fuel cell anodes using electrochemical impedance spectroscopy in combination with a high temperature crystal microbalance,'' *Journal of Power Sources*, vol. 235, pp. 14 -- 19, 2013.

[168] J. Kirtley, A. Singh, D. Halat, T. Oswell, and J. M. Hill, ''Raman spectroscopy of graphite,'' *Phil. Trans. R. Soc. Lond. A*, vol. 362, pp. 2271 -- 2288, 2004.

[169] H. Sumi, Y.-H. Lee, H. Muroyama, T. Matui, and K. Eguchi, ''Comparison between internal steam and co2 reforming of methane for ni-ysz ans ni-scsz sofc anodes,'' *Journal of The Electrochemical Society*, vol. 157, no. 8, pp. 1118 -- 1125, 2010.

[170] W. Li, Y. Shi, Y. Luo, Y. Wang, and N. Cai, ''Carbon deposition on patterned nickel/yttria stabilized zirconia electrodes for solid oxide fuel cell/solid oxide electrolysis cell modes,'' *Journal of Power Sources*, vol. 276, pp. 26 -- 31, 2015.

[171] J. Sehestad, ''Four challanges for nickel steam-reforming catalysts,'' *Catalysis Today*, vol. 111, pp. 103 -- 110, 2006.

[172] C. Schluckner, V. Subotić, V. Lawlor, and C. Hochenauer, ''Cfd-simulation of effectice carbon gasification strategies from high temperature sofc ni-ysz cermet anodes,'' *International Journal of Hydrogen Energy*, 2016.

[173] L. Maier, B. Schaedel, K. H. Delgado, S. Tischer, and O. Deutschmann, ''Steam reforming of methane over nickel: Development of a multi-step surface reaction mechanism,'' *Top Catal.*, vol. 54, pp. 845 -- 858, 2011.

[174] J. Andrews and A. Ubbelohde, ''Overvoltage and diffusion through iron and palladium,'' *Proc. Royal Soc.*, vol. 253, pp. 6 -- 15, 1959.

[175] R. M. Barrer, *Diffusion in and through solids*. New York: The Macmillan Company, Cambridge, England: At the University Press: Cambridge University Press, 1941.

[176] F. Petrakopoulou, Y. D. Lee, and G. Tsatsaronis, ''Simulation and exergetic evaluation of co2 capture in a solid-oxide fuel-cell combined-cycle power plant,'' *Applied Energy*, vol. 114, pp. 417 -- 425, 2014.

[177] A. Kromp, H. Geisler, A. Weber, and E. Ivers-Tiffée, ''Electrochemical impedance modeling of gas transport and reforming kinetics in reformate fueled solid oxide fuel cell anodes,'' *Electrochimica Acta*, vol. 106, pp. 418--424.

[178] Q. Fang, L. Blum, and N.H.Menzler, ''Performance and degradation of solid oxide eleectrolysis cells in stack,'' *Journal of The Electrochemical Society*, vol. 162, no. 8, pp. F907 -- F912, 2015.

[179] M. Cassidy, G. Lindsay, and K. Kendall, ''The reduction of nickel-zirconia cermet anodes and the effects on supported thin electrolytes,'' *Journal of Power Sources*, vol. 61, no. 1–2, pp. 189 -- 192, 1996.

[180] T. Klemenso, C. Chung, P. Larsen, and M. Mogensen, ''The mechanism behind redox instability of anodes in high-temperature sofcs,'' *Journal of The Electrochemical Society*, vol. 152, no. 11, pp. 2186 -- 2192, 2005.

[181] Y. Zhang, B. Liu, B. Tu, Y. Dong, and M. Cheng, ''Understanding of redox behavior of ni–ysz cermets,'' *Solid State Ionics*, vol. 180, no. 36–39, pp. 1580 -- 1586, 2009.

[182] Z. Wang, Z. Lü, B. Wei, K. Chen, X. Huang, W. Pan, and W. Su, ''Redox of Ni/YSZ anodes and oscillatory behavior in single-chamber sofc under methane oxidation conditions,'' *Electrochimica Acta*, vol. 56, no. 19, pp. 6688 -- 6695, 2011.